Simulation of a Permian climate and analysis of atmospheric transport and mixing processes

DISSERTATION

Zur Erlangung des Grades
“Doktor
der Naturwissenschaften”

am Fachbereich Physik, Mathematik und Informatik
der Johannes Gutenberg-Universität
in Mainz

STEVEN SCHNEIDER
geb. in Gifhorn

Mainz, den 13. September 2018

1. Berichterstatter: [redacted]
2. Berichterstatter: [redacted]

Tag der mündlichen Prüfung: 21. Januar 2019

Contents

Abstract

The modelling of palaeoclimates allows to analyse the environment of a certain period in the past. Additionally, it can give insight to the behaviour of specific atmospheric processes under altered circumstances. The Permian (299-251 mya) provides promising topographical and atmospheric conditions for palaeoclimate studies. The supercontinent of Pangaea predominated the topography which is one of the best known reconstructed topographies of the Palaeozoic and Mesozoic. Its extensive landmass comprised almost all of the present-day continents and stretched nearly from pole to pole. In the course of that period the atmospheric carbon dioxide content increased significantly to a multiple of the present-day concentration and induced global warming.

The application of the established atmosphere-ocean general circulation model EMAC-MPIOM to simulate the palaeoclimate of the Middle Permian requires the estimation of boundary conditions, like e.g. the fraction of greenhouse gases and the astronomical setting, as well as the generation of a full land surface data set. The response stage of atmosphere and upper ocean layers to the changed conditions is in the magnitude of a few years, whereas it lasts several thousand years of simulation for deep ocean layers. The found equilibrium shows only a small net radiation imbalance and the equilibrium state turns out to be unique and independent of initialisation.

The simulated mean climate for the Middle Permian is characterised by warm temperatures, especially in high latitudes, extreme saisonality and dry conditions in the continental interior. There is no permanent sea ice coverage on both hemispheres and the vicinity of the Tethys Ocean is subjected to a monsoonal climate. The geographic distribution pattern of associated biomes matches well the pattern derived from lithological and floral data in the Southern Hemisphere and in the low latitude range of the Northern Hemisphere. The higher resolution of the model results in warmer temperatures and increased precipitation in these areas compared to the climate simulated by other

models on coarser grids. However, northern mid- and high latitude regions generally tend towards cooler and drier conditions due to weak northward heat transport by the ocean. Further sensitivity studies deal with how the simulated Permian climate depends on atmospheric carbon dioxide concentration, vegetation distribution, fluctuations of solar irradiation in the course of the Milankovitch cycles, and the parameterisation of convection.

Effects on atmospheric stability and vertical transport are evaluated with regard to the altered temperature and moisture distributions and the continuous forcing by nudging techniques. The analyses include the impact on the frequency of unstable conditions in the lower, middle, and upper troposphere. Furthermore, the impact on frequency and intensity of triggered convection events is examined as well as the response of the tropopause height. The comparison between the Permian and the present-day scenario focusses on mean meridional effects. In contrast, the analysis of the nudging impact on processes in the present-day atmosphere allows to extract regional effects and the impact of the single nudged prognostic variables is eventually separated.

Zusammenfassung

Das Modellieren und Simulieren von Paläoklimaten ermöglicht einerseits die Untersuchung der Klima- und Umweltbedingungen im damaligen Erdzeitalter. Andererseits kann aber auch das Verhalten verschiedener atmosphärischer Prozesse unter veränderten Bedingungen analysiert werden. Die topographischen und atmosphärischen Bedingungen im Perm (vor 299-251 Millionen Jahren) bieten eine vielversprechende Umgebung für paläoklimatische Untersuchungen. Die Topographie wird durch den Superkontinent Pangäa dominiert und ist eine der am besten rekonstruiertesten Topographien des Paläozoikums und Mesozoikums. Die ausgedehnte Landmasse Pangäas bestand aus fast allen heute bekannten Kontinente und erstreckte sich nahezu von Pol zu Pol. Der Kohlenstoffdioxidgehalt der Atmosphäre stieg im Laufe des Perms auf ein Vielfaches des heutigen Wertes und erzeugte globale Erderwärmung.

Die Abschätzung verschiedener Randbedingungen, wie z.B. der Anteil an Treibhausgasen und die astronomische Konstellation, sowie die Erzeugung eines vollständigen Oberflächendatensets sind notwendig, um das Paläoklima des Mittleren Perms mit dem etablierten Atmosphäre-Ozean-Zirkulationsmodell ECHAM-MPIOM simulieren zu können. Die Reaktionszeit der Atmosphäre und der oberen Ozeanschichten auf die veränderten Bedingungen liegt in der Größenordung mehrerer Jahre, während tiefere Ozeanschichten eine Reaktionszeit mehrerer Jahrtausende aufweisen. Der resultierende Gleichgewichtszustand zeigt nur kleine Abweichungen vom Strahlungsgleichgewicht und erweist sich als eindeutig und unabhängig von der Initialisierung.

Das simulierte mittlere Klima für das Mittlere Perm zeichnet sich durch warme Temperaturen, insbesondere in den hohen Breiten, extreme Saisonalität sowie sehr trockene Verhältnisse im Kontinentinnern aus. Es gibt keine permanente Meereisbedeckung in beiden Hemisphären und die Umgebung der Tethyssee ist einem Monsunklima ausgesetzt. Für die Südhalbkugel wie auch die niedrigen Breiten der Nordhalbkugel stimmt die

geographische Verteilung der assoziierten Biome gut mit der auf lithologischen und botanischen Daten basierenden Verteilung überein. In diesen Gebieten führt die höhere Auflösung tendenziell zu wärmeren Temperaturen und erhöhtem Niederschlag verglichen mit den Simulationen anderer Modelle, bei denen zumeist niedrigere Auflösungen verwendet wurden. Aufgrund des schwächeren Ozeanwärmetransports nach Norden neigen die mittleren und hohen Breiten der Nordhalbkugel dagegen eher zu zu kälteren und trockneren Bedingungen. In Sensitivitätsstudien werden die Abhängigkeit des simulierten Klimas von dem Kohlenstoffdioxidgehalt der Atmosphäre, der Vegetationsverteilung, Strahlungsschwankungen im Zuge der Milankovic-Zyklen sowie der Parametrisierung der Konvektion behandelt.

Effekte auf atmosphärische Stabilität und vertikalen Transport werden im Hinblick auf die veränderten Temperatur- und Feuchteverteilungen im Perm und das kontinuierliche Forcing durch Anwendung von Nudging-Techniken untersucht. Die Analysen beinhalten den Einfluss auf die Häufigkeit instabiler Verhältnisse in der unteren, mittleren und oberen Troposphäre. Weiterhin wird die Auswirkung auf Häufigkeit und Intensität konvektiver Ereignisse wie auch der Reaktion der Tropopausenhöhe betrachtet. Dabei konzentriert sich der Vergleich zwischen dem Perm und der heutigen Atmosphäre auf mittlere meriodionale Effekte, während die Analyse der durch Nudging verursachten Veränderungen auch regionale Effekte miteinbezieht und den Einfluss der einzelnen Variablen separiert.

1 Introduction

1.1. Motivation

The atmosphere is essential to all life on Earth. On the one hand it provides oxygen that is vital for most organisms. On the other hand it enables more-balanced conditions by transporting heat from areas of strong insolation near the equator to areas of weak insolation in polar ranges and moisture from the ocean onto the continents. Its state determines to a great extent our environment and influences the way we live. The atmosphere is a very mutable system whose equilibrium state depends on multiple factors, like its composition, the input energy in form of incoming solar radiation, but also the properties of the ground. That is why the understanding of the processes that affect the global and regional climate as well as the local weather is of large significance.

The investigation of the atmosphere is onerous, however. Flight campaigns allow *in situ* measurements of various processes, but they are expensive and only cover the specific situation at the respective places for the time of the measurement. The comprehensive observation of the atmosphere by means of satellites and ground-based measurements is very expensive as well, especially in unpopulated areas. Moreover, the spatial and temporal resolution is too coarse for studying small-scale processes. The major difficulties are generally the reproducibility of the measurements and the predefined environmental conditions that prevent the variation of parameters to study dependencies. In contrast to observations, simulations allow to freely change the environmental conditions and they can be executed several times with exactly the same conditions. Moreover, quantities that can not be accessed by measurements directly can be computed for each simulation time step and give insight into specific processes. Global and long-term simulations are computationally expensive as well, but the resolution of the numerical grid and the size of the simulation area can be varied according to the requirements of the investigation.

The simulation of weather, climate, and numerous specific processes within the atmosphere is well established. General circulation models (GCM) are employed to simulate

the state of atmosphere and the ocean on a global scale, whereas regional models and different cloud-resolving models are used to study specific regions or specific small-scale processes in more details. In most cases the underlying equations are solved numerically on three-dimensional grids and subgrid-scale processes are included by means of parameterisation. This procedure requires optimal tuning of the parameters to achieve realistic results. Comparison with observational data allows to evaluate the model results and to optimise the parameters. In addition data assimilation techniques can be applied to make the simulations match observations.

The employment of atmospheric models for present-day conditions allows the comprehensive validation of the model results as well as the optimisation of the model parameters by means of observed data. However, the models are not limited to the present-day atmosphere. Since the environmental and boundary conditions can be varied freely, the models can also be applied to simulate past or prospective climates, extraterrestrial atmospheres, and other extreme conditions. Due to the current climate change, the short- and midterm development of the climate is of particular interest to be prepared for changing conditions on Earth. Simulations with unusual parameter values or boundary conditions lead to extreme states of the models far from the well-tuned and validated model settings. That is why it is difficult to estimate the validity of model results for model states that deviate strongly from the present-day state. Simulating palaeoclimates, i.e. climates of past periods of the Earth's history, provides information about how the model behaves for environments that differ entirely from the present day. The density of the geological record indicating past climates is considerably smaller compared to data based on present-day observations, but it is still sufficient to validate the simulation results in many cases, at least for certain regions.

The prevailing climatic conditions of the respective period are reconstructed by means of proxies, i.e. physical, chemical, and biological materials that are preserved within the geologic record and correlated with climate or environmental parameters in the modern world. The choice of proxy depends on how far the respective period goes back. Tree rings or atmospheric gases trapped in ice cores can give information on relatively young palaeoclimates during the last millenials, whereas many other proxies, like e.g. plant macrofossils, sediment compositions, or isotope measurements in shells and corals, reflect the paleoclimate of periods several millions of years ago. On the one hand these climate indicators serve the validation of the simulated palaeoclimates. On the other hand the simulations provide a more comprehensive reconstruction of the respective palaeoclimates and help to investigate the history of the Earth. Parameter studies allow to estimate the most likely boundary conditions by comparing the simulated climate to the climate indicated by the proxies. That way, the assumed composition of the atmosphere, the assumed values of obliquity and eccentricity of the Earth's orbit, as well as the assumed orographic configurations can be evaluated, for example. The analysis of the simulation results not only allows to examine the climate, however, but also allows to analyse the behaviour of specific processes within the atmosphere at specific conditions.

The Permian (299-251 mya) is the last period of the Palaeozoic era (542-251 mya) and exhibits entirely different conditions compared to the present-day Earth. The reconstruction of the Permian climate and the examination of the Permian atmosphere are especially instructive due to the special topographic constellation of that period, the strong increase of carbon dioxide in the atmosphere within a relatively short time, and the concomitant induced warming.

The Permian topography is predominated by the very extensive landmass of the supercontinent of Pangaea and the surrounding Panthalassic Ocean. Apart from some small microcontinents, all of the present-day continents have been part of Pangaea forming a large 'C' and stretching nearly from pole to pole. Hence, the topography represents an extreme case of the land-sea distribution. Palaeomagnetic data of all present-day continents prove the existence of Pangaea and indicate their positions at that time [1–3]. That is why the Permian topography is one of the best known reconstructed topographies of the Palaeozoic and Mesozoic and thus well-suited for palaeoclimate studies.

At the beginning of the Permian, the carbon dioxide concentration of the atmosphere is similar to the preindustrial concentration of the present-day Earth [4, 5], the mean global temperature is in the present-day range [6], and both polar regions are covered with ice. The conditions change from icehouse to hothouse climate in the course of the Permian and they are far more extreme at the end of the period. The carbon dioxide concentration is increased four- to eightfold [4, 5], the mean global temperature is about 6 K warmer than at the present day [6], and the polar regions are ice-free during summer. Anoxic and euxinic conditions prevail in the oceans of the Late Permian and the Permo-Triassic boundary is marked by the most severe extinction event of Earth's history. Within a few million years about 95% of all marine species [7] and about 70% of terrestrial life [8] was extinguished. The causes of the extinction are still under debate. Simulating the Permian palaeoclimate as realistic as possible allows to examine the climatic contributions to the extinction, however, and can provide information about the atmosphere of that time.

The major sources of moisture, carbon dioxide, and many other aerosols are at the Earth's surface. Their global distribution as well as their transport to higher altitudes generally depends on atmospheric mixing. Water vapour, carbon dioxide, and other aerosols provide an indirect effect on the climate by means of radiative forcing. However, their lifetime in the atmosphere varies strongly with their altitude. That way, the transport and mixing properties of the atmospheric flow affect the local climate and the quality of the air. Moreover, the availability of atmospheric moisture is directly correlated to the amount of precipitation.

The stability of the atmosphere inhibits the three-dimensionality of the flow in most parts of the troposphere, and especially in the stratosphere, in many cases. Three-dimensional turbulences are therefore confined primarily to the lowest layer of the troposphere, i.e. the Planetary Boundary Layer (PBL). Vertical mixing in higher layers is related

to convective clouds and turbulences resulting from dynamical instabilities. Although horizontal displacements are usually much larger, vertical displacements are crucial for the mixing of the atmosphere and the global distribution of the aerosols.

Instabilities of the vertical stratification generally depend on the moisture content and the vertical temperature gradient of the considered air column. Hence, the altered conditions of the warmer Permian climate as well as the aridity and extreme continental character due to the extensive landmass of Pangaea are assumed to significantly affect the atmospheric mixing. The application of data assimilation techniques using observed and reanalysed data is common practice for simulations of present-day conditions. The forcing of the model variables towards the data constitutes an non-physical impact to the model dynamics, however. The model consequently reacts by rebalancing to return to an equilibrium state again. Since this rebalancing is particularly realised in form of atmospheric and oceanic motion, the assimilation also affects the simulated atmospheric mixing.

1.2. Overview

This work deals with the simulation and evaluation of the palaeoclimate of the Middle Permian (Kazanian Stage, 270-260 mya). The simulation is performed with the coupled atmosphere-ocean general circulation model EMAC-MPIOM. The model boundary conditions are set to best estimates for the Permian environment and the model orography and other surface parameters are adapted accordingly. Due to the unknown initial conditions for the Permian oceans, spin-up simulations of several thousands of years are required to find the equilibrium of the coupled atmosphere-ocean system with respect to the prescribed boundary conditions of the Permian Earth. The simulated palaeoclimate is analysed in detail and evaluated by means of further sensitivity studies. These studies consider the variation of atmospheric carbon dioxide concentration, solar luminosity and other astronomical parameters, the vegetation distribution, and convection parameterisation. Moreover, the simulated Permian palaeoclimate is compared to climate indications of the geological record as well as to simulations by other models for validation. The analysis of atmospheric mixing processes in the Permian atmosphere focusses on vertical transport and convection in particular. At first this study considers the propensity to unstable conditions as well as the degree of stability at different layers of the troposphere to examine the preconditions for convection. The frequency and the intensity of the triggered convection events are evaluated in a second step. The approved procedure is subsequently applied to evaluate the impact of nudging on atmospheric vertical transport for simulation of EMAC in a present-day environment.

In the following the structure of the atmosphere and atmospheric transport processes are summarised in Section 1.3. Chapter 2 provides an overview of the Permian. The Permian is described in terms of the chronology of the Earth's history. The topography,

the astronomical constellation, and the composition of its atmosphere are outlined. Moreover, the chapter compiles climate indications of the geological record and the simulation results by other models that are used for validation. Chapter 3 describes the employed coupled atmosphere-ocean model EMAC-MMPIOM and the convection parameterisation schemes by Tiedtke, and Zhang-McFarlan-Hack. The simulation procedure is explained in Chapter 4. This includes the generation of the prescibed dataset of orography and other land surface parameters the Permian Earth as well as other model settings and the grids for atmosphere and ocean. Furthermore, this chapter deals with the initialisation of the simulation and the spin-up simulations up to the equilibrium state. Chapter 5 presents the simulated Permian palaeoclimate. First, the mean climate is characterised in terms of surface temperature, precipitation, wind, and ocean circulation. Second, the sensitivity of the simulated climate to the variation of atmospheric carbon dioxide concentration, orbital forcing, self-established vegetation, and different convection parameterisation schemes is evaluated and uncertainties are estimated. The simulated climate is additionally compared to data of the geological record and other simulations for validation. Chapter 6 analyses the atmospheric mixing in the Permian atmosphere. The frequency of unstable conditions and the degree of stability is compared to the present-day reference for different layers of the troposphere. Moreover, the chapter considers the frequency and intensity of triggered convection events and the lifting of the tropopause. Chapter 7 evaluates the impact of nudging on atmospheric vertical transport. Different approaches of data assimilation are summarised and it is outlined how data assimilation is realised in EMAC. Furthermore, the impact of nudging on atmospheric stability, the frequency and intensity of convection events, as well as the tropopause height is analysed. Chapter 8 eventually concludes the procedure and the results of this work.

1.3. Atmospheric Transport

1.3.1. Structure of the Lower Atmosphere

The atmosphere of the Earth is not a homogeneous gas envelope around the solid planet but structured into different layers due to different radiative, chemical, and thermodynamical processes. The layers differ by thickness, composition, and predominating processes. The definition of the boundaries between the different layers is generally based on distinct changes of the vertical temperature gradient, although additional definitions in terms of other atmospheric properties exist as well. Moreover, the boundaries do not necessarily represent continuous surfaces and vary depending on the latitude and the season. The main characteristics are essentially determined by the way of energy input.

The lowest layer, i.e. the troposphere, is distinctly affected by the Earth's surface by means of friction, injection of water vapour and aerosols, as well as energy input in form of heat from the surface. The incoming short-wave radiation of the Sun, that lies

primarily within the ultraviolet, visible, and near-infrared range of the spectrum, hardly interacts with the atmosphere in this layer. A small fraction of the radiation is absorbed by carbon dioxide and other aerosols, but the bulk of the radiation is eventually absorbed by the ground. The warm surface then transfers heat by conduction and long-wave radiation to the overlying air. The surface warming also induces the evaporation of water and injects additional energy to the atmosphere in form of latent heat. Hence, in the troposphere the major heat input is at the ground and the temperature consequently decreases with height. The density and pressure of the air are generally largest near the surface due to gravitation and both also decrease with height. This behaviour of temperature, density, and pressure enables the vertical adiabatic ascent of warmed and less dense air from the surface to higher levels, i.e. convection (see Section 1.3.3). Water vapour that is carried by the ascending air from the surface to higher altitudes can induce the generation of clouds and precipitation.

Both turbulences and convection contribute to the vertical exchange within the troposphere and lead to a well-mixed state. The lowest layers are most strongly affected by the surface. A boundary layer builds up that is separated from the overlying free atmosphere by a capping inversion. Within the boundary layer convective activity is generally subjected to a diurnal cycle due to the variation of solar radiation between day and night (see Section 1.3.3). Shallow convection is restricted to the boundary layer, but deep convection penetrates into the free atmosphere and injects moisture. In higher altitudes the impact of the surface warming decreases. The stratification gets more stable and the temperature remains rather constant with height. This prevents most convective motion to proceed to higher altitudes and thus constitutes a distinct boundary, the tropopause. The tropopause determines the maximal level to vertical exchange and only very energy-rich convection is able to overshoot. That is why higher levels are significantly dryer and clouds merely appear for very cold conditions. The tropopause is defined more exactly as the level where the temperature gradient is less than 0,2 K per 100 m (WMO definition [9]). It is located at a height of about 16 km near the equator and 6-9 km near the poles.

The stratosphere is the layer above the tropopause. It is characterised by a very dry and stable air mass that is well stratified. The absorption of ultraviolet radiation by ozone releases heat and makes the temperature increase with height. The absence of water vapour and the increasing temperature profile suppress any vertical motion and lead to the very stable layering. However, the horizontal atmospheric flow is very strong. The stratosphere reaches up to the stratopause at an altitude of about 50 km.

1.3.2. Atmospheric Stability

The stratification of the atmosphere generally determines its stability and decides whether vertical transport is either encouraged or suppressed. The most simple description considers the behaviour of an air parcel in equilibrium within a vertical air column.

For unstable conditions the air parcel experiences positive buoancy, i.e. a small vertical displacement of the air parcel is enhanced and the parcel is accelerated. In contrast, the air parcel is decelerated under stable conditions and negative buoancy leads to oscillations around the equilibrium level.

Both gravitational force and hydrostatical pressure impact on the air parcel within the atmospheric fluid and balance each other in equilibrium on the large scale. Assuming the parcel to be initially at rest the equilibrium is described by the hydrostatic equation:

$$\frac{\partial p}{\partial z} + g\rho = 0 \tag{1.1}$$

where p is the pressure of the air parcel, ρ its density, g the gravitational acceleration of the Earth, and z denotes the vertical axis. For small vertical displacements from the equilibrium the parcel experiences buoancy, since both forces are not balanced any more. The equation of motion in terms of the vertical velocity of the parcel w reads as:

$$\frac{dw}{dt} = -\frac{1}{\rho}\frac{\partial p}{\partial z} - g \ . \tag{1.2}$$

The environment can be assumed to be in hydrostatic equilibrium with density ρ^*. The equation of motion can be rewritten:

$$\frac{dw}{dt} = g\ \frac{\rho^*(z) - \rho(z)}{\rho(z)} = g\ \frac{T^*(z) - T(z)}{T(z)}\ , \tag{1.3}$$

where ρ is the density of the parcel and the pressure difference between the parcel and the environment is assumed to be negligibly small. That is why the density is directly related to the temperature T according to the ideal gas law.

The temperature of the air parcel as well as its density and pressure are not constant during the ascent. The ascent velocity is significantly faster than heat exchange with the environment, however, and the parcel's motion can be therefore considered adiabatic:

$$dU + pdV = 0\ , \tag{1.4}$$

where U is the internal energy of the parcel. The temperature of the air parcel follows the dry-adiabatic lapse rate Γ_{dry} when there is no condensation:

$$\Gamma_{\text{dry}} = -\left(\frac{dT}{dz}\right)_{\text{adiabatic}} = -\frac{g}{c_p} = -0.00981\ \frac{\text{K}}{\text{m}}\ , \tag{1.5}$$

where c_p is the specific heat at constant pressure. If the air parcel contains any moisture, however, the cooling induces condensation of the contained water vapour. The addition of latent heat that is released during the phase change lets the parcel cool more slowly, though the actual moist-adiabatic lapse rate Γ_{moist} depends on the moisture content of the air parcel.

Temperature and pressure are generally not well-suited to characterise the air parcel due to their mutual dependency and their dependency on altitude. These dependencies prevent the direct comparison of different air parcels at different levels and complicates the evaluation of buoancy and atmospheric stability. The proper description requires the consideration in terms of a conserved quantity during the ascent of the air parcel. The potential temperature θ is conserved for dry-adiabatic changes by definition and thus it is constant for ascending and descending air parcels when condensation is neglected. According to the adiabatic state equations the potential temperature is defined as:

$$\theta = T \left(\frac{p_0}{p}\right)^{\frac{R}{c_p}} , \tag{1.6}$$

where p_0 is a standard reference pressure, typically $p_0 = 1000$ hPa, and $R/c_p = 0.286$ for air. The potential temperature is a measure for the potential and internal energy of the air parcel and represents the temperature that an air parcel would have when it is moved adiabatically to a reference level with pressure p_0.

The constraint to dry air is not a realistic assumption, however, since tropospheric air is commonly enriched by moisture and condensation and evaporation are most likely to happen during ascending and descending. The equivalent potential temperature, or pseudo-equivalent potential temperature, θ_e is conserved during moist-adiabatic processes and includes the exchange of latent heat in case of condensation and evaporation. The consideration is not straightforward because of the description of the pseudo-adiabatic processes during condensation and different approaches exist [10, 11]. Bolton [11] defines the equivalent potential temperature "to be the final temperature θ_e which a parcel of air attains when it is lifted dry adiabatically to its lifting condensation level, then pseudo-wet adiabatically (with respect to water saturation) to a great height (dropping out condensed water as it is formed), then finally brought down dry adiabatically to 1000 mb". Ice formation, however, is not considered. The equivalent potential temperature can be determined approximately by:

$$\theta_\mathrm{e} = T \left(\frac{p_0}{p}\right)^{0.2854(1-0.28\cdot 10^{-3} r)} \cdot \exp\left[\left(\frac{3.376}{T_L} - 0.00254\right) \cdot r(1 + 0.81 \cdot 10^{-3} r)\right] , \tag{1.7}$$

where r is the mixing ratio and T_L is the temperature that the parcel would attain if lifted adiabatically to its condensation level. This temperature can be computed by means of the is the relative humidity ϕ (%):

$$T_L = \frac{1}{\frac{1}{T-55} - \frac{\ln(\phi/100)}{2840}} + 55 . \tag{1.8}$$

The first factor of Equation 1.7 represents the potential temperature. However, Bolton [11] additionally takes account of the variation of the specific heat c_p with respect to temperature and pressure.

The above considerations allow to rewrite the equation of motion of the air parcel (Eq. 1.5) in terms of the (equivalent) potential temperature. The temperature change of the ascending parcel can be obtained by the adiabatic lapse rate:

$$T(z) = T_0 - \Gamma \Delta z \ , \tag{1.9}$$

where T_0 is the temperature at the start level. The temperature of the environment at the respective level can be determined similarly by means of the actual lapse rate γ:

$$T^*(z) = T_0 - \frac{dT^*}{dz}\Delta z = T_0 - \gamma \Delta z \ . \tag{1.10}$$

The equation of motion then transforms to:

$$\frac{dw}{dt} = g\frac{\gamma - \Gamma}{T^*}\Delta z = \frac{g}{\theta^*}\frac{d\theta^*}{dz}\Delta z \ . \tag{1.11}$$

Hence, the buoancy of the air parcel basically depends on the potential temperature of the environment and its vertical gradient. The previous consideration generally applies for both dry-adiabatic and moist-adiabatic ascents when either the potential or equivalent potential temperature are used.

Equation 1.11 has the form of the differential equation of harmonic oscillations. The behaviour of the deviated air parcel depends on the vertical gradient of the potential temperature, since g is constant and the potential temperature θ itself is always positive by definition. Three different cases can occur: When the gradient is negative the motion of the parcel is represented by oscillations with frequency ν:

$$\nu^2 = \frac{1}{4\pi^2}\frac{g}{\theta}\frac{d\theta}{dz} \ , \tag{1.12}$$

that is also denoted as Brunt-Väisälä frequency. Displacements of the air parcel from the start level are balanced by a restoring force and the parcel is merely induced to oscillate, i.e. the stratification is absolutely stable. The lapse rate of the environment is smaller than the dry- and moist-adiabatic lapse rates, $\Gamma_{\mathrm{dry}} > \Gamma_{\mathrm{moist}} > \Gamma_{\mathrm{env}}$, convection is suppressed, and cloud formation is generally very unlikely. This situation is common for temperature inversions. When the gradient vanishes identically the displaced air parcel is still in equilibrium and remains at the place it has been moved to. This case represents neutral stratification. Positive vertical gradients of the potential temperature lead to unstable stratification. Here, the displacement of the parcel is not restored, but the parcel is further accelerated and lifted. However, the air parcel can be lifted either dry-adiabatically or moist-adiabatically and the stability depends on its saturation. When the lapse rate of the environment is greater than the dry-adiabatic lapse rate, $\Gamma_{\mathrm{env}} > \Gamma_{\mathrm{dry}} > \Gamma_{\mathrm{moist}}$, the stratification is absolutely unstable and convection and cloud formation is very likely. When the lapse rate of the environment is between the dry- and moist-adiabatic lapse rate, $\Gamma_{\mathrm{dry}} > \Gamma_{\mathrm{env}} > \Gamma_{\mathrm{moist}}$, the stratification is conditionally unstable. That means the stratification is unstable for saturated air but stable for unsaturated air.

An air parcel that is exposed to an unstable environment directly starts ascending triggered by small displacements or it is accelerated further when it is already in motion. Alternatively, the parcel can also be located within a stable layer and larger displacements are required to bring the parcel to an unstable environment. There are several processes that induce destabilisation of the atmosphere. On the one hand the air parcel itself can be warmed over a warm surface or displaced to a different environment. This can be caused by topographic lifting, when the air is forced up at a topographic barrier like hills and mountains, convergence, and by lifting at the fronts of extratropical cyclons. Lifting to an unstable layer, that takes place commonly along cold fronts, triggers convection and often results in the formation of cumulus or cumulonimbus clouds. In contrast, lifting to a stable layer occurs commonly along warm fronts and is related to the formation of stratus and nimbostratus clouds since any further ascent is suppressed. On the other hand the environment around the air parcel can change due to advection, surface heating, or cooling effected by irradiation of infrared radiation. The cooling of air in higher levels as well as the advection of cooler air aloft also lead to unstable conditions.

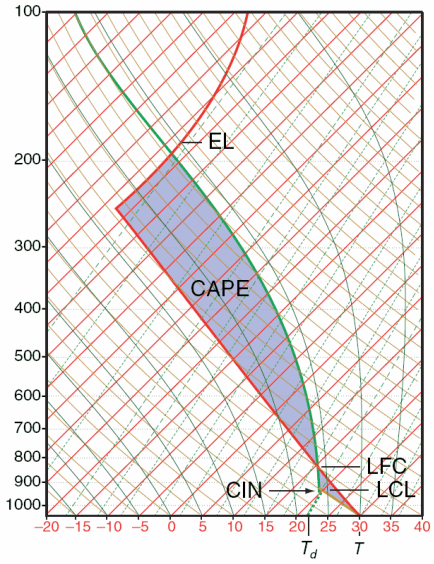

Figure 1.1.: Example of CAPE and CIN in a skew-T-p diagram plotting the pressure (hPA) logarithmically over the temperature (°C). The brown lines denote the dry-adiabatic lapse rate following the isentropes, the green line denotes the moist-adiabatic lapse rate following the pseudo-isentropes, and the red line represents the actual lapse rate of the atmosphere. (source: `http://www.atmos.umd.edu/~dkleist/aosc431.html`)

The stability of the atmosphere significantly affects the strength of the convective motion and thus the growth of cumulus clouds and the convective cloud top-height. Convective inhibition (CIN) is the energy threshold that has to be overcome to reach an unstable environment, the level of free convection (LFC). This threshold is often related to a capping stable layer of inversion. The convective available potential energy (CAPE)

summarises the energy that is related to the positive buoancy within this unstable layer. Both depend on the vertical profile of the actual lapse rate of the atmosphere and can be derived easily from a skew-T-p diagram by atmospheric sounding (see Fig. 1.1). The air parcel needs to be lifted initially by an external force (see above). The state of the air parcel changes dry-adiabatically during the lifting. It expands and its temperature changes according to the dry-adiabatic lapse rate (Eq. 1.9). Condensation of the contained water vapour starts when the relative humidity reaches 100%, at the level of condensation (LCL), and the temperature of the parcel begins to follow the moist-adiabatic lapse rate. The level of free convection is reached when the buoancy balances the gravitational force and the lapse rate of the environment becomes larger than the moist-adiabatic lapse rate. The parcel continues to ascent to the equilibrium level (EL) when the gravitational force balances buoancy again and the lapse rate of the environment is again smaller. CIN is then given by the area in the skew-T-p diagram confined between the dry- and moist-adiabatic lapse rate and the lapse rate of the environment until the LFC, while the area between the lapse rate of the environment and the moist-adiabatic lapse rate between LFC and EL represents CAPE. CAPE can be computed by:

$$\mathrm{CAPE} = \int_{\mathrm{LFC}}^{\mathrm{EL}} \left(\frac{T_v - \overline{T_v}}{\overline{T_v}} g \right) dz \ , \tag{1.13}$$

where T_v is the virtual temperature of the air parcel and $\overline{T_v}$ the virtual temperature of the environment. Here, the virtual temperature is the temperature that dry air would have corresponding to a sample of moist air with equal pressure and density. The size of CIN and CAPE generally vary according to the stability of the atmospheric stratification. This consideration represents the situation for conditional instabilities. In case of absolutely unstable conditions the temperature of the environment decreases rapidly with height and CAPE becomes very large, where the atmospheric lapse does not intersect with the moist-adiabatic lapse rate for absolutely stable conditions.

1.3.3. Atmospheric mixing

The interaction of the atmosphere with the surface is the primary trigger for atmospheric mixing processes and that is why the mixing is strongest in the PBL. Rapid changes in the free atmosphere above the PBL, like e.g. the passage of fronts related to extratropical cyclons, affect the mixing as well. Mixing acitivity in the PBL is generally subjected to a characteristic diurnal cycle, though strong cloud coverage, region-specific effects due to terrain or nearby land-sea contrasts, and passages of fronts can distinctly impact upon this pattern.

The ground cools significantly faster than the overlying atmosphere at night, dense cloud coverage, or wintertime without any additional warming due to irradiation of heat. This also cools the near-surface layers of air and leads to a rather stable temperature profile

within the PBL. Moreover, the PBL is separated from the overlying free atmosphere by a capping inversion layer in many cases. This situation is characterised by large CIN and very low CAPE. During the day the solar radiation heats up the ground and warms the overlying air when cloud coverage is weak enough. The warming from the ground generates thermal instabilities and makes the stratification of the lowest layers more unstable. Convection brings warmer air to higher layers and a shallow convective mixed layer builds up which has potential temperature and humidity nearly constant with height. Varying surface properties, like albedo and vegetation coverage, lead to non-uniform heating of the near-surface air. Turbulences emerge due to the different vertical velocities. On the one hand convection tends to stabilise previous instabilities and ensures warming of the entire mixed layer. On the other hand the continuous heating increases CAPE of the triggered convection and deepens the convective layer. Consequently, the nocturnal stable layer is gradually dissipated and the convection penetrates into the overlying residual layer, the remnants of the mixed layer of the previous day. This layer is merely weakly stable and convection rapidly reaches the capping inversion at the top of the PBL. When solar heating is not sufficient any more to maintain buoancy in the late afternoon, convection and turbulence collapse and become restricted to near-surface layers again.

The capping inversion at the top of the PBL provides a barrier for the ascending air and restricts the maximal convective cloud top-height. These conditions favour shallow convection that is basically restricted to the PBL. Cumulus humulus and stratocumulus clouds are characteristic for this situation. When CAPE is large enough or additional lifting is caused by advection or topography, the buoancy is able to overcome the capping inversion and the convection overshoots into the free atmosphere. The free atmosphere is usually well stratified and separated from the PBL since turbulences break at the inversion layer. Horizontal transport predominates. However, deep convection that overshoots from the PBL injects moisture and destabilises the atmospheric stratification. The convection is able to penetrate through the entire troposphere up to the tropopause when CAPE is large enough and the convection lasts sufficiently long. Deep convection is generally characterised by the formation of cumulus congestus and cumulonimbus clouds. It requires high buyoant energies. That is why deep convection is very common in the tropics, forming the ITCZ due to the maximum of incoming solar radiation. It also occurs frequently near cold fronts of extratropical cyclons in mid-latitudes where large temperature differences between warm and cold air masses induce strong buoancy. The temperature inversion at the tropopause provides a very strong barrier and only very energy-rich convection is able to overshoot into the lower stratosphere. The lifting of moist and warm air masses to the LFC, e.g. by means of a warm front of an extratropical cyclon, induces mid-level or elevated convection that is rooted above the PBL.

The surface also interacts with the overlying air layers by means of friction. The strength of the friction basically depends on the texture of the surface. Friction increases with surface roughness which is related to vegetation coverage, surface waves of the oceans, and small orographic structures. The effect of the surface friction is especially strong for

windy conditions and decreases with height. This causes wind shear turbulences that are usually smaller in size than the ones produces by buyoant air. These turbulences also contribute to the mixing within the PBL and predominate for very windy conditions as well as within the stable nocturnal surface layer. Above the Ekman layer, i.e. the layer affected by surface friction, the geostrophic wind is balanced by the Coriolis force and the pressure gradient force and follows the isobars. The additional drag due to surface friction within the Ekman layer impacts in the direction against the real wind. This slows the wind down and deflects it in the direction of the pressure gradient force.

2

The Permian

The simulation of the Permian palaeoclimate is a major part of this thesis. The description of the results and their evaluation in the context of this period of Earth's history requires a certain knowledge of the geographical and geological circumstances of that time. This Chapter summarises the main points and reviews shortly the state of the art of palaeoclimate simulations of the Permian in literature. Section 2.1 describes briefly the Permian in terms of the chronology of the Earth's history and surveys the essential evolutions in the course of this period. The geographical configuration of land and ocean is outlined in Section 2.2, and the composition of the atmosphere is dealt with in Section 2.3. The planetary orbit and other astronomical features are discussed in Section 2.4. The data-based reconstruction of the Permian climate by means of geological finds that indicate the climate is explained in Section 2.5 and the results are reported in short. Section 2.6 gives an overview of climate simulations of the Permian in literature and elaborates the results that are used for validation in Chaptre 5.

2.1. Chronological Survey

Since its formation at around 4,600 mya, the Earth has experienced numerous geological, climatic, and evolutionary changes in the course of its history that all left traces in the geological records. Tectonic processes like volcanism or continental drift, and the evolution of flora and fauna have had a tremendous effect on the climate. However, the carbon-silicate[2] cycle has stabilised the mean global temperature to a narrow interval between 0 to 60°C for at least 3,500 my [12].

[2]The carbon-silicate cycle describes the transformation of silicate rocks to carbonate rocks by weathering and sedimentation. The transformation of carbonate rocks back to silicate rocks is driven by metamorphism and magmatism. It affects the carbon dioxide concentration of the atmosphere.

Palaeozoic		Mesozoic		Cenozoic	
Age [mya]	Period	Age [mya]	Period	Age [mya]	Period
542-488	Cambrian	251.0-201.6	Triassic	65.6- 23.0	Palaeogene
488-444	Ordovician	201.6-145.5	Jurassic	23.0- 2.6	Neogen
444-416	Silurian	145.5- 65.5	Cretaceous	2.6- 0.01	Pleistocene
416-359	Devonian			0.01- 0	Holocene
359-299	Carboniferous				
299-251	**Permian**				

Table 2.1.: Geologic time scale for Phanærozoic eon, according to Walker and Geissman [13]. See Appendix A for more detailed subdivisions of periods.

Table 2.1 surveys the divisions of the current geological eon, i.e. the Phanærozoic. The beginning of the Phanærozoic eon at 542 mya marks the appearance of abundant animal and plant life on Earth, at first in form of diverse hard-shelled animals. The first era of the Phanærozoic is named Palaeozoic and stretches from 542 to 251 mya. During this time complex life forms evolved, first in the ocean and later on the continents. Fishes and the first land plants appear by the Silurian. By the Devonian the first amphibians and trees evolved, and reptiles first came up by the Carboniferous and Permian. Three mass extinction events are known for the Palaeozoic era. Marking the transition from Palaeozoic to Mesozoic, the last event occured at the Permo-Triassic boundary and is known to be the most severe exitinction event in Earth's history. The Mesozoic is dominated by the dinosaurs that lived until the beginning of the Cenozoic. The first birds evolve by the Jurassic and the first mammals appear by the late Cretaceous dominating life in the Cenozoic.

The Permian is the last period of the Palaeozoic and extends from 299 to 251 mya. It is named after the Perm Governorate of the former Russian Empire by Murchison who first described this system after findings on an expedition to the west Ural Mountains [14]. The geological subdivisions of the Permian period are listed in Table 2.2.

By the latest Carboniferous the supercontinent of Pangaea accreted. In the course of continental drift it occured several times that all landmasses were united to a single supercontinent that comprised almost all landmasses of the present-day Earth, but, Pangaea is the youngest of these. The Permo-Carboniferous is characterised by vast tropical swamplands and extensive glaciation in Southern Pangaea [15]. The continental ice sheets extended from the pole as far as 40°S and deposits indicate glaciation until the Middle Permian about 265 mya [16, 17]. However, there is no evidence for extended ice sheets in the Northern Hemisphere. In the course of the Permian the atmospheric carbon dioxide content increased and the climate gradually warmed. The ice sheets melted and swamplands as well as extensive inland seas formed in southern high latitudes by the late Middle Permian. The continental interior got very dry and deserts spread out [15].

[1] International Commission on Stratigraphy

Age [mya]	Epoch	Stage
299-297	Early Permian	Asselian
297-284		Sakmarian
284-276		Artinskian
276-271		Kungurian
271-268	Middle Permian*	Roadian
268-266		Wordian
266-260		Capitanian
260-254	Late Permian	Wuchiapingian
254-251		Changhsingian

* Other Stages (Europe): Kazanian 270-260 mya

Table 2.2.: Time scale of Permian geological subdivisions, according to the Geological Society of America, 2009, Walker and Geissman [13]. The table includes all official ICS[1] subdivisions. Further local subdivisions, like the Kazanian in Europe, are possible.

The Permo-Triassic boundary is marked by the most severe extinction event of Earth's history. Within a few million years about 95% of all marine species [7] and about 70% of terrestrial life [8] was extinguished. After this dramatic loss of biodiversity the ecosystem needed about 30 my to recover [18]. The causes of the extinction are presumably diverse. There is still an ongoing debate about the exact extinction mechanism. Kidder and Worsley [19] propose decline and collapse of ocean circulation due to warm conditions in polar latitudes. This suspended sinking of cold and nutrient-rich water. Anoxic and euxinic conditions became widespread and evaporation in shallow shelf seas intensified this effect. Geologic records evidence anoxic and euxinic conditions both in shallow seas and deep ocean [20, 21]. Furthermore, ocean models confirm weak circulation and possible anoxia for warm polar waters [22, 23]. Sustained heat and aridity affected terrestrial life significantly. High atmospheric carbon dioxide concentration caused acid rainfall that leached soil nutrients and stunted plant growth [24]. By the end of the Permian atmospheric greenhouse gas concentrations were considerably increased by degassing of the Siberian Traps that were created by one of the largest known volcanic eruptions of the Phanærozoic. Release of methane amplified the greenhouse effect and led to depletion of stratospheric ozone [24, 25]. The resulting increase of UV-B radiation could provide another mechanism for the extinction of terrestrial life. There is no evidence for extraterrestrial impacts, like nearby supernovae or meteors [7]. These mechanisms seem unlikely due to different regional extinction patterns [26].

2.2. Topography

The Permian topography is dominated by the supercontinent of Pangaea and the surrounding Panthalassic Ocean. The huge Pangaean landmass nearly stretches from

pole to pole and, in simple terms, has the shape of a large 'C'. The topography was not static in the course of the Permian. Pangaea moved northwards by about 10° of latitude during this time span and the small microcontinents changed their location as well (see Figure2.1). In the Early Permian the south of Pangaea extended across the South Pole. In constrast, in the Late Permian the South Pole was not covered by a continent any more and the north of Pangaea approached the North Pole. The movement of Pangaea not only induced a movement of climate zones but it also affected the direction of ocean streams and thus the climate of certain regions. When the pole is free of land, there is a circumpolar current that cannot exist in the case when the polar region is blocked by a continent. Winguth et al. [27] showed that the existence of a circumpolar current joined by a warm eastward current of middle latitudes causes enhanced sea-to-air heat flux in high latitudes. This significantly increases polar surface air temperatures at the adjacent coasts, although the total meridional ocean overturning circulation is slightly reduced.

It is not part of this work to analyse the climate variations affected by continental drift. Furthermore, the time intervall used for the time slice simulations of our study is far shorter than the geological time scales that are relevant for continental movements. Therefore, we choose an intermediate topography of the time of the Kazanian stage (Middle Permian, 270-260 mya). At this time the southernmost tip of Pangaea was still close to the South Pole so that mapping onto the model grid results in continental grid cells at the pole (see Section 4.2). The topography of this work is based on reconstructions by Scotese and McKerrow [1], Ziegler, Hulver, and Rowley [2], and Ziegler, Gibbs, and Hulver [3]. It is depicted in Figure 2.1.

In the following the different continents that are part of Pangaea and the oceans of the Permian Earth are explained in more detail. The terminology introduced here will be used in the discussions of the following chapters for exact specification of the different parts of Pangaea and surrounding oceans.

Gondwana. In itself, Gondwana is likewise a supercontinent that comprises in its core the present-day continents of South America, Africa, Madagascar, India, Antarctica and Australia [1]. It emerged around 520-510 mya and existed nearly during the entire course of the Palaeozoic. During this time it was located exclusively in southern latitudes and it extended over the South Pole at many times. Several series of ribbon continents broke off Gondwana and amalgamated with Euramerica or Cathaysia after crossing the Paleo-Tethys Ocean [28]. Cimmeria rifted away from Gondwana at the beginning of the Permian and opened the Tethys Ocean [1, 29]. After the collision with Laurasia at the end of the Carboniferous Gondwana constituted the southern half of Pangaea [1, 29]. It existed until its breakup in the Late Jurassic when the South Atlantic Ocean started to open and Eastern Gondwana started to separate from its western part.

Baltica. This terrane corresponds to the northeastern part of modern Europe [30]. In modern terms it is limited by the Ural Mountains in the east, as far as the British Isles and Scandinavia to the west, and Central Europe to the south. By the collision with

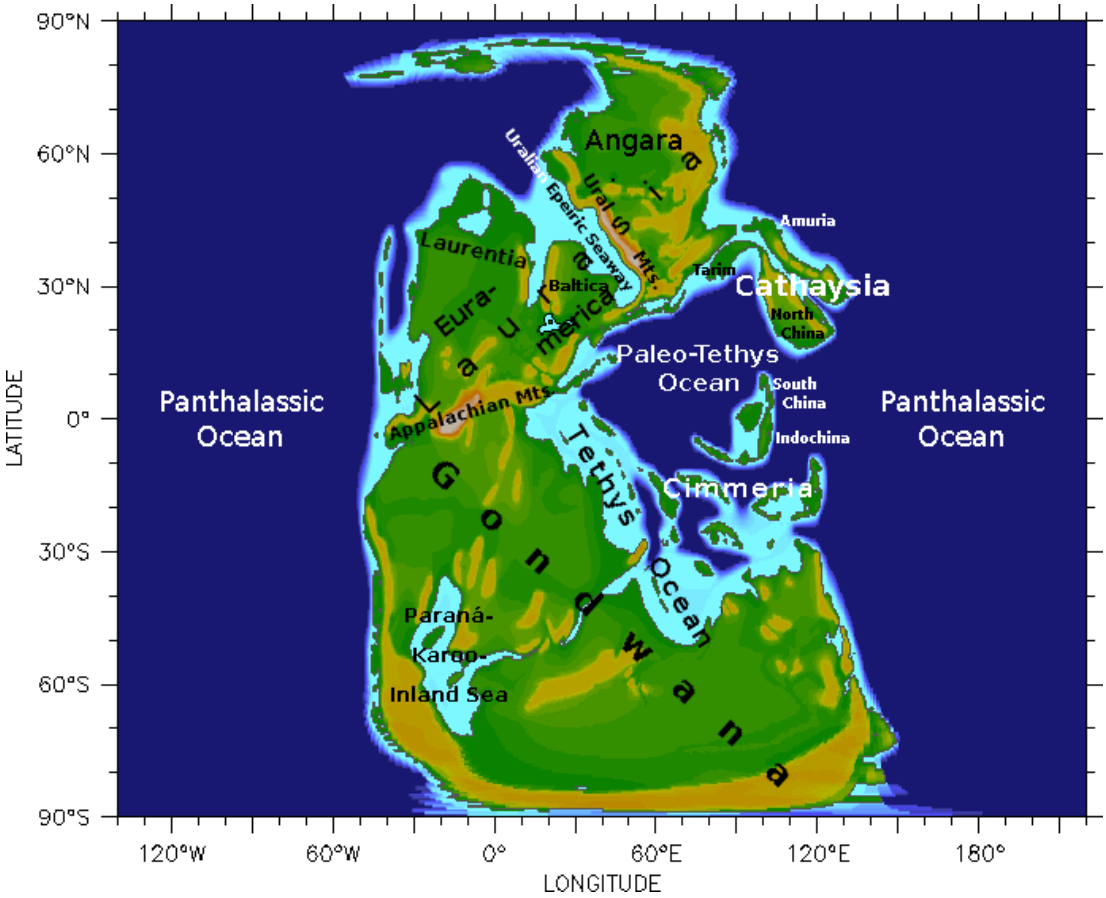

Figure 2.1.: Topography of Permian Earth at Kazanian stage (270-260 mya). The map shows the supercontinent of Pangaea and the surrounding Panthalassic Ocean, as well as the marginal Tethys Ocean and the embedded ribbon continents. The different subcontinents that form Pangaea are labelled as well as the most important mountain chains, inland seas and seaways. This denotation of the different regions will be used in the discussion in the following chapters.

Laurentia in the Silurian the continent of Euramerica was formed, and the mountains of Scandinavia and the British Isles were build in the Caledonian Orogeny [30].

Laurentia. Laurentia makes up the North American palaeocontinent and further includes modern Greenland as well as parts of Alaska, Ireland, and Scotland [1, 30]. The terrane originated from the breakup of a former supercontinent in the Precambrian and was an independent continent until the collision with Baltica in the Silurian.

Angara. Angara also originated from separation of a former supercontinent in the Precambrian. It corresponds to modern Siberia and parts of Central Asia that split off Gondwana and emerged with Siberia in the course of the Palaeozoic [1]. The collision with Euramerica started during the Late Carboniferous. Angara was finally welded to Baltica by the end of the Triassic [28] forming the continent of Laurasia that constitutes

the northern half of Pangaea. This collision triggered the Ural orogeny that built the Ural Mountains in Western Angara and generated the shallow Uralian epeiric seaway.

Laurasia. Laurasia emerged from the collision of Euramerica with Angara in the Late Carboniferous. At the same time it merged with Gondwana near the equator [30]. This collision triggered the Variscan orogeny that built, *inter alia*, the Appalachian Montains in North America and the Anti-Atlas in Africa. Laurasia existed until the breakup of Pangaea and the opening of the North Atlantic Ocean in the Jurassic [28].

Cimmeria. The ribbon continent of Cimmeria seperated from Gondwana in the Early Permian and opened the Tethys Ocean. Its terranes include modern Turkey, Iran, Tibet, and parts of Southeast Asia. The continent crossed the Paleo-Tethys Ocean and merged with Pangaea during the Middle to Late Triassic [1].

Cathaysia. The Cathaysian terranes include Tarim, Amuria, North China, South China, and Indochina [31]. These terranes rifted away from Gondwana in the Middle Palaeozoic. By the Permo-Carboniferous Tarim started to collide with Angara. North China and Amuria had merged by the Late Permian, and the Qinling Ocean between North and South China was closed by the Late Triassic [31]. This block joined the evolving Asian continent by the Late Triassic/Early Jurassic in the course of the Indonesian Orogeny [1].

Panthalassic Ocean. "Though it made up nearly two-thirds of the Earth's surface, virtually nothing is known about Panthalassa." (Scotese [32]). The Panthalassic is the all encompassing ocean of the Permian Earth. Similar to the present-day Pacific Ocean it is dotted with small islands and encircled by a ring of active subduction zones, the Pangaean Rim. The Pangaean Rim is characterised by volcanic island arcs and Andean-type mountains along the western margin of Pangaea [2, 31]. All of the oceanic lithosphere has subducted beneath both the western and eastern margins of Pangaea [31]. The only remnants are preserved in volcanic seamounts along the Pangaean Rim. Therefore, there is no information known about the bathymetry of the ocean and the location of ocean ridges that undoubtedly existed.

Paleo-Tethys Ocean. The Paleo-Tethys Ocean opened in the Silurian with the separation of some ribbon continents of Northern Gondwana [28]. In the Permian the Paleo-Tethys lay southeast of Laurasia and separated the terranes of Cathaysia and Cimmeria. Due to the northward drift of Cimmeria, the ocean closed rapidly in the latest Permian and Triassic. For the sake of convenience the Paleo-Tethys Ocean and the Tethys Ocean will be referred to as 'Tethys' in the discussion in the following chapters.

Tethys Ocean. The Tethys Ocean, also named Neotethys Ocean, opened when Cimmeria had separated from Gondwana in the Early Permian. In combination with the Paleo-Tethys Ocean it separates the northern and the southern part of Pangaea in the east of the supercontinent and constitutes a marginal ocean basin to the Panthalassic Ocean. The basin of the Mediterranean Sea, Black Sea and Caspian Sea are remnants of the Tethys Ocean.

The orography of Pangaea is generally dominated by widespread plains, yet the Appalachian and Ural Mountains as well as the remnants of ranges of former orogenies traversed the continent. Located along the equator and built in the course of the Variscan orogeny, the Appalachian Mountains were highest during the Early Permian and already started to collapse by the Late Permian [31]. Their maximum elevation is controversial, as, for example Hatcher et al. [33] assume a Himalayan-size range. However, Pitman and Golovchenko [34] showed that the degradation of such a mountain chain would take 450 my and, thus, Ziegler, Hulver, and Rowley [2] assume a more moderate elevation in their reconstructions of Permian topography. The Ural Mountains resulted from the collision of Euramerica with Angara in the Permo-Carboniferous. The Uralian epeiric seaway to the west remained open until the end of the Permian but was steadily filled with erosional matter of the rising foldbelt [2]. Another salient mountain range is the Andean-type range in the south and southwest of Gondwana that will be named South Gondwanan Mountains in the following. These mountains were not as high as the Appalachian and Ural Mountains, but they still constituted a distinct wind barrier.

The increase in temperature in the course of the Permian induced the total melting of the great southern ice cap [31] (see Section 2.1). Subsequently, thick peat swamps [29] and giant freshwater lakes [31] replaced the widespread glaciation that dominated in the earliest Permian. Yemane [35] and Kutzbach and Ziegler [36] showed that the existence of these lakes ensured a temperate climate in high latitudes that is in agreement with palaeobotanical data (see Section 2.5). In the Paraná basin (Brazil) [29] and Karoo basin (Malawi) [37] evidence of a lacustrine environment and a giant freshwater lake was found that did not desiccate, the 'Paraná-Karoo-Inland Sea'. Furthermore, an increasing sea level induced by the melting of the great southern ice cap lead to flooding of shallow coastal areas. For example, in the Late Permian, wide areas of Baltica were flooded. The 'Zechstein Sea', covering North-Central European Pangaea, connected the Uralian Epeiric Seaway with the Paleo-Tethys Ocean at some time [30].

The latitudinal orientation of Pangaea and the relative rotation of the different continents is based on palaeomagnetical data. For the Early Permian the agreement of the different palaeomagnetic poles is better than for the Late Permian [2, 31]. Especially the poles of the Chinese microcontinents do not superimpose with data of Laurasia [38]. Therefore, minor corrections on the basis of fossil floras [38] and sediments [31] are incorporated in the reconstructed topography. Yet, the latter still contains several uncertainties that have to be kept in mind for the evaluation of the simulation results in Chapter 5.

2.3. Atmosphere

The analysis of air trapped in glacial ice provides the most reliable information of the composition of the atmosphere of a past period. However, this method is only applicable

for the last 400,000 years since there is no ice left that is older than this [39]. That is why other methods have to be used for the Permian. One approach extracts information from proxies in geologic records that covary with the concentration of the respective gases. Moreover, it is possible to estimate the gas concentration via mass balance expressions that capture the major sources and sinks of the particular gas. In most cases these reconstructions suffer from great uncertainty that cannot be quantified in each case.

The following subsections summarise the proxies and model reconstructions for the most important gases in the atmosphere. The estimation for Permian concentrations is additionally emphasized.

2.3.1. Atmospheric Carbon dioxide

Carbon dioxide is the most important greenhouse gas in the atmosphere and it had a major impact on the regulation of global surface temperature in the past [40]. Due to its lifetime in the atmosphere (∼5-200 years [41]) and many sources and sinks, it can affect the climate on short as well as on very long time scales. Royer [5] and Royer et al. [6] have shown that the atmospheric carbon dioxide concentration is highly correlated to the occurence of widespread continental glaciation and to Phanærozoic sea surface temperatures derived from a marine carbonate δ^{18}O proxy[1] (see Chapter 2.5).

For Pre-Pleistocene periods information on the atmospheric carbondioxide content can either be obtained by geochemical carbon cycle models or by derivation from proxies. Other approaches estimate the carbondioxide content by total land area and latitudinal position of the continents [42, 43], but this only provides a relatively coarse guess of the actual values. The same is true for the approach of Hyde et al. [44], who infer the carbon dioxide concentration from glaciation level. The proxies are based on characteristics of the Earth system that are reliably measurable in the rock record and that covary with atmospheric carbon dioxide. The data is quantified for the present and then applied to past conditions. The most robust proxies for carbon dioxide palaeoconcentration are δ^{13}C of pedogenic minerals, stomatal densities and indices in plants, δ^{13}C of long-chained alkenones in haptophytic algae, δ^{11}B embedded in marine carbonate, and δ^{13}C of liverworts [39]. However, only the first two are applicable to the Permian period.

The carbonate in certain pedogenic minerals consits of carbon dioxide of atmospheric or biological origin. As these two components differ in their carbon isotopic compositions, the atmospheric carbon dioxide concentration can be estimated [6, 39, 45]. This method has only a small error range for high carbon dioxide concentrations (± 500-1000 ppm) but a relatively large error for small concentrations.

[1] The δ^{18}O denotes the relative deviation (%) of the ^{18}O/^{16}O isotope ratio of the proxy from the standard isotope ratio

Most higher land plants have pores to control the carbon dioxide uptake into their leaves. The proportion of these stomatal pores to all cells on the leaf epidermis is inversely related to the atmospheric carbondioxide concentration. This method allows records of high precision (± 10-40 ppm) and high time resolution. However, the relationship is not well examined for pre-Cretaceous plants [6, 39].

On a multimillion year time scale the predominant process of the carbon cycle is the exchange of carbon between rocks and the surficial reservoirs, i.e. atmosphere, biosphere, ocean, and soils [46]. Most carbon cycle models seek a parameterisation of the underlying geochemical processes that is as realistic and simple as possible. The best predictions [5] of the atmospheric carbon dioxide content in the course of the Phanærozoic are generated by the newest version of the GEOCARB model of Berner and Kothavala [4]. The uptake of carbon dioxide from the atmosphere during the weathering of calcium and magnesium silicates, that are found in rocks, is evaluated with a time step of 10 million years. Moreover, the model regards the burial of carbonates and organic matter in sediments, as well as the carbondioxide fluxes to the atmosphere and the ocean due to their weathering and their thermal decomposition at great depth by magmatic and metamorphic activities. The respective weathering rates depend on global temperatures, continental size, position and relief, river runoff, and land plant colonisation. An estimation of volcanic degassing is included additionally [4, 46–48].

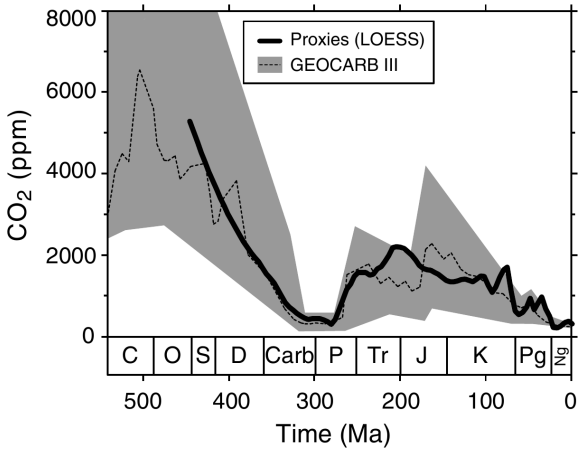

Figure 2.2.: Atmospheric carbon dioxide content in the course of the Phanærozoic from Royer [5]. The best-guess prediction of GEOCARB III [4] is compared to a weighted compilation of proxy records. Both methods predict a strong increase of carbon dioxide during the Permian period.

Royer [5] compiled data from about 500 proxies for the entire Phanærozoic and calculated a locally weighted regression (LOESS) to match the time step of the model. The resulting proxy-based curve as well as the best-guess predictions of GEOCARB III with the associated error range [4] are depicted in Figure 2.2. The comparison of both curves shows a high correlation for all periods and most proxy data are within the uncertainty range of the model [5, 6]. That is why the simulated atmospheric carbon dioxide content seems reasonable and the agreement with geological records yields a consistent picture.

Both, proxy data and GEOCARB simulation, predict rather low carbon dioxide concentrations for the Permo-Carboniferous (about 300 ppm, error range 80-450 ppm) that is slightly higher than the preindustrial concentration of the present. In the course of the Permian there was a significant increase to about 1250 ppm (error range: 200-2250 ppm) at the Permo-Triassic boundary that corresponds to approximately four times of the present-day concentration. As the assembly of the Pangaean supercontinent was essentially completed by the Late Permian, Crowell [16] and Kidder and Worsley [19] assume reduced orogenesis and, therefore, a decrease in silicate weathering and carbon burial to be the main cause of this increase. Furthermore, strong carbondioxide ejection by increased volcanic activity by the 'Siberian Traps' in Angara made a significant contribution to the overall increase [8, 49].

2.3.2. Atmospheric Oxygen

Oxygen is essential for biological life and by the distribution of the first land plants it started to accumulate in the atmosphere. On a short time scale the atmospheric oxygen concentration is controled by the production via photosynthesis and the consumption via respiration. However, on a long geological time scale different biological and geological processes are predominant. The oxygen production is mainly driven by the burial of organic matter and pyrite in sediments, whereas oxidative weathering of exposed old buried sedimentary organic matter and pyrite decreases the atmospheric oxygen concentration [50]. The presence of oxygen in the atmosphere is proved indirectly by the evidence of forest fires that cannot take place at sufficiently low oxygen concentration for all periods since the rise of woody plants about 450 mya. Berner [51] employs data from isotopic records of carbon and sulfur in sedimentary rocks for the entire Phanærozoic to determine the rates of processes that control the oxygen concentration. Including negative feedback processes, he additionally assumes that younger rocks are weathered preferentially and he also takes account of isotope discrimination by plant biomass in favour of ^{12}C during photosynthesis.

The model predicts a strong increase of atmospheric oxygen content to about 37% by the Permo-Carboniferous that is due to the rise of vascular land plants providing a new source of organic matter [51]. Subsequently, the oxygen content decreases significantly to about 15% at the Permo-Triassic boundary because of a change in climate to more arid conditions [52].

2.3.3. Atmospheric Methane

Atmospheric methane contributes significantly to the overall greenhouse effect because its greenhouse properties are about 20 times more effective than those of carbon dioxide on a molar basis [41, 53]. Further, methane effects troposheric ozone and stratospheric water vapour. Its net forcing is equivalent to about half that of carbon dioxide. [54, 55].

The main sources of atmospheric methane are continental wetlands, such as swamps, marshlands, bogs and lakes [56]. Anoxic conditions can develop in the underlying sediments and soils of these standing waters. These conditions are required for the anaerobic production of methane by methanogens. Further minor sources of atmospheric methane are the oceans, wildfires, termites, hydrates and volcanoes [53]. In order to estimate Phanærozoic methane concentrations, Beerling et al. [56] derive the abundance of wetlands from coal sediments and guess the methane emission flux by scaling an estimate of wetland methane fluxes during the Pliocene. The equilibrium atmospheric response is then determined by means of a chemistry-transport model.

At the beginning of the Permian tropical wetlands were most abundant and the model predicts methane concentrations of about 10,000 ppb. The concentration steadily decreases in the course of the Permian and has a significant dip (about 100 ppb) at the Permo-Triassic boundary when nearly all peat-forming plants were extinct [56].

2.4. Astronomical Constellation

2.4.1. Solar Radiation

The radiative forcing that determines the climate state of the earth system depends strongly on the intensity of the incoming solar radiation, i.e. the solar luminosity. As it is usual for a main-sequence star, our Sun generates energy in its core by nuclear fusion of hydrogen to helium. Thus, in the course of its lifetime the available hydrogen is reduced and the fraction of helium increases resulting in a growing mean molecular weight. Simple stellar models show that this leads to an increase in stellar luminosity [57, 58]. Since the emergence of the Earth the solar luminosity has increased by 25-40% [58, 59] in dependence on the initial composition of the Sun's core. Crowley and Baum [60] and Crowley, Baum, and Hyde [61] use these solar evolutionary models to predict the long-term evolution of the solar luminosity in the course of Earth's history. For the Middle Permian, their model estimates the solar luminosity to be reduced by about 2.6% in terms of the present-day luminosity [62].

2.4.2. Palaeorotation of the Earth

The rotation of the Earth around its own axis has a significant impact on the climate. The rotation not only generates the diurnal cycle of incoming radiation but also induces the Coriolis force. That way, the rotation rate controls the flow of air and water, and influences the strength of high and low pressure systems as well as the behaviour of ocean currents.

The analysis of sedimentary cyclic rhythmites of tidal origin in marine deposits in estuarine areas and tidal deltas [63] and the analysis of the growth layers of calcified

structures of fossil organisms, especially molluscan shells [64], indicates that the Earth's rotation rate has not been constant in the past. On the one hand the deceleration of rotation is due to lunar and solar tidal friction [63]. The attraction of the Moon on the Earth's tidal bulge generates a torque since the tidal bulge is delayed because of friction. The torque, however, decelerates the Earth's rotation and thus transfers rotational energy and angular momentum of the Earth to the Moon's orbital motion. Therefore, the length of a day is increased and the Moon recedes from Earth. The solar torque has a similar but minor effect. On the other hand further parts of the retardation energy are absorbed by the core, the generation of the geomagnetic field, as well as anomalously high seismicity, tectonics, and magmatism [65]. That is why the deceleration rate has not been constant but fluctuating. Palaeontological data provides information for the entire Phanærozoic and even prior but for some periods interpolation is necessary. The compilation of various data samples by Williams [63] indicates a day length of approximately 23 hours and about 380 solar days per year for the Permian. However, this aspect is not considered further in this work due to technical reasons (see Section 4.2.3).

2.4.3. Milankovitch Cycles

The gravitational interaction of Earth with the other planets of the solar system, primarily Jupiter and Saturn, as well as interactions with the Sun and the Moon cause quasi-periodic variations of Earth's spin around its axis and orbit around the Sun. These variations superimpose and cause cyclic longterm fluctuations of the intensity of incoming solar radiation, i.e. the solar constant. The solar radiation is not affeted on a global and annual mean, however, the regional consequences are significant, especially because of a non-symmetric distribution of land and sea. That way, the orbital variations affect the climate and the resulting sedimentary record that is used for analysis. Milanković [66] separated the most dominant contributions by variations of eccentricity, obliquity and precession, that are collectively denominated as 'Milankovitch cycle'.

Eccentricity. The Earth's orbit around the Sun is an ellipse and the eccentricity of the orbit is a measure of the elliptical shape. At present the eccentricity is $e = 0.0167$ corresponding to a near-circular orbit. The eccentricity varies between a minimum of $e = 0.005$ and $e = 0.07$ with a quasi-period of 100,000 years superimposed on a longer period of 400,000 years [67]. The more elliptical the orbit, the stronger is the difference of irradiation between perihelion (least distance to Sun) and aphelion (greatest distance to Sun). Furthermore, the season around the aphelion is prolonged due to Kepler's second law.

Obliquity. The angle between the rotational and orbital axis of the Earth is the obliquity. It varies from 22.1° to 24.5° with a quasi-period of 41,000 years [67]. At present the obliquity is 23.44° which is midway between the extreme constellations. The

larger the obliquity, the stronger is the seasonlity of the climate, especially in higher latitudes.

Precession. The gravitational interaction between the Sun as well as the Moon and the Earth's equatorial bulge, that is caused by its spin, induces a torque that in turn leads to a wobble of the Earth's rotation axis. This motion induces a motion of the position of the vernal equinox on the orbit, or in other terms, a variation of the angular position of the perihelion. The precession cycle has a period of 25,700 years [67]. However, primarily due to effects by Jupiter and Saturn the orbital ellipse precesses in space as well. Therefore, the resulting climatic precession, which describes the position of the perihelion with respect to the vernal equinox, varies with a quasi-period of 21,000 years. The present-day value of the perihelion's longitude is $\omega = 282.9°$ [67]. For $\omega \approx 90°$ the North Pole turns to the Sun in perihelion and the contrast between summer and winter is increased on the Northern Hemisphere and reduced on the Southern Hemisphere (opposite for $\omega \approx 270°$ like at present). For $\omega \approx 0°$ or $\omega \approx 180°$ the seasonality will be similar on both hemispheres.

The Milankovitch cycle has certainly influenced the climate on Earth in the past as it does at present, albeit evidence is scarce for the Palaeozoic. Anderson [68] presents a reconstruction of Milankovitch modes for precession and eccentricity based on a climate record for the equatorial Pangaea in the Late Permian compiled from evaporite varves. Several studies analysed the climatic consequences on the Pangaean supercontinent by Milankovitch variations. Kutzbach [69] observes an enhanced summer and winter monsoon circulation in their simulation for an idealised Pangaean continent. For the hemisphere where perihelion occurs in summer rainfall is increased by 25% in the tropics and subtropics. Further, Crowley, Baum, and Hyde [70] conclude from their simulations with an energy balance model for the Jurassic Pangaea that Milankovitch fluctuations can modulate the magnitude of summer warmings significantly, especially in high latitudes. They suggest to regard this bias when evaluating evidence of past high-latitude warmth.

2.5. Climate Indicators

The geological records that allow conclusions on the climate of the Permian period are rather sparse and not well distributed on the Earth. The ocean floor of the Pathalassic Ocean has subducted [31] and thus there are no sediments available to us any more that contain information about the climate of this part of the Permian Earth. Sediments of epeiric seas give some indication of the climate at the continental shores. But even for the Pangaean continent the coverage of data is not equally distributed. Several different methods have been developed to reconstruct past climates. The most important analyses for the Permian are presented in the following.

2.5.1. Phanærozoic δ^{18}O carbonate record

Veizer et al. [71] provide a dataset of δ^{18}O, δ^{13}C, and ^{87}S/^{86}S values from calcitic and phospatic shells collected in shallow tropical seas (30°S-30°N). The record covers the entire Phanærozoic. As carbonate with enriched ^{18}O values corresponds to warm water conditions and carbonate with depleted ^{18}O values corredponds to rather cold water, Veizer, Godderis, and François [72] derive the evolution of tropical sea surface temperature from the δ^{18}O record. However, the oxygen isotope incorporation in carbonate is additionally affected by the pH of seawater. Therefore, Royer et al. [6] correct the sea surface temperature reconstruction and find high correlation when they compare the latter with the temperature deviation based on GEOCARB predictions. The comparison is depicted in Figure 2.3.

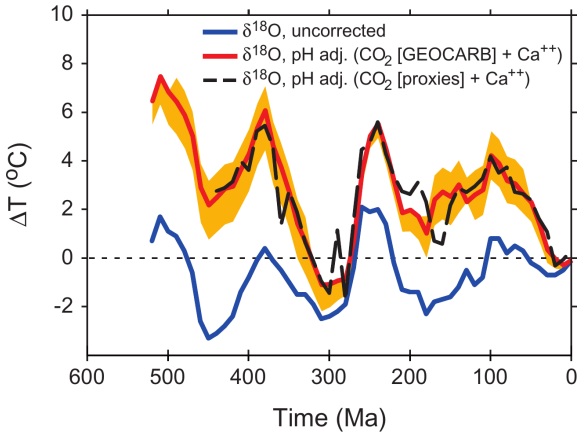

Figure 2.3.: Temperature deviations for Phanærozoic tropical sea surface temperature relative to the present day from Royer et al. [6]. The reconstruction is based on low-latitude, shallow marine δ^{18}O carbonate record. The blue curve corresponds to the detrended original data from Veizer et al. [71]. Royer et al. [6] corrected the proxy data for effects of temporal changes in the pH of seawater due to changes in Ca^{2+} concentration. The correction is based on predictions of atmospheric carbon dioxide concentration by GEOCARB III or proxies, respectively (see Section 2.3).

For the beginning of the Permian this proxy indicates a climate state with temperatures similar to the present-day climate or even slightly colder. In the course of the Permian, the temperature increases significantly. The climate transitions from icehouse to hothouse climate with tropical sea surface temperatures being about 6°C warmer than at present.

2.5.2. Climate-sensitive Sediments

The sediments in the geological record provide information about the net water balance of the corresponding regions. Generally, coal indicates a positive evapotranspiration balance, $P - E$, and sufficiently wet conditions with thriving vegetation like in the tropical rain forest belt or in temperate biomes. In contrast, evaporites and aeolian

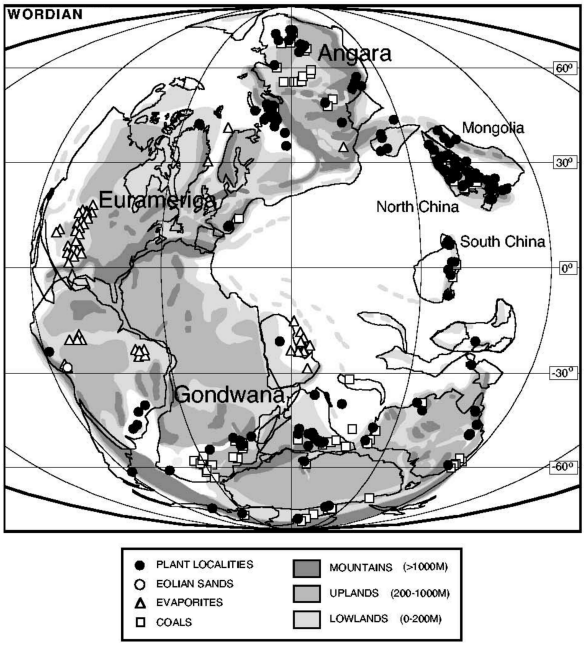

Figure 2.4.: Location of climate-sensitive sediments and Permian floral localities from Rees et al. [73]. Major geographical regions are highlighted.

sands suggest a negative $P - E$ balance and dry or seasonally dry conditions. Aeolian sands seem to be restricted to desert regions, as the formation of sand dunes requires an upper limit of annual precipitation of less than about 30 mm/yr and a wind speed of more than 6 m/s [74]. In this way the analysis of aeolian sand deposits and their foreset dip directions also gives some indication about the average wind speed and direction. However, the interpretation is sometimes difficult because only seasonal averages are recorded and the sand is not necessarily transported parallel to the wind. Subtropical trade winds can drive Ekman transport that induces upwelling zones in the ocean. In these areas organic-rich muds and phosphorites are deposited. Further, carbonate buildups and organic-rich shales can be found especially in tropical marine sediments indicating warm water conditions (see Section 2.5.1). Tundra and glacial environments are characterised by dropstones and tillites [3].

A compilation by Ziegler, Gibbs, and Hulver [3] is the most comprehensive data set of these climate-sensitve sediments for the Permian, including about 1,200 occurences for all nine Permian stages. By means of this data they work out a distribution of water masses for the different Permian stages corresponding to a distribution of 'marine climate zones' that are defined by temperature and salinity [3]. Moreover, they combine lithological with palaeobotanical data and construct a distribution of biomes for the Permian period [73, 74] (see also Section 2.5.3). The location of some of the sedimental occurences as well as the floral localities for the Wordian or Kazanian stage, respectively, are shown in Figure 2.4.

Summarising the finds for the Wordian or Kazanian stage, respectively, coal has been found in the northern part of Angara, the southern part of Gondwana, and on some of the microcontinents within the Tethys Ocean, in particular in North China, on the west coast of South China, and in parts of Cimmeria. Evaporites appear in the continental interior of Northern Gondwana and Euramerica, as well as on the west coast of Pangaea. Further evaporite finds have agglomerated in the Tethys Ocean close to the northeastern coast of Gondwana. The evidence of aeolian sands is very sparse. They merely exist in central Euramerica and on the west coast of Gondwana. Tillites and dropstones are not present in the data set. Phosphorites appear off the west coast of Euramerica at mid-latitudes. Organic buildups have been found in shallow marine environments off the tropical coast of the Tethys Ocean, Cimmeria, South China, Indochina, and off Pangaean west coast near the equator (not shown, see Ziegler, Gibbs, and Hulver [3]).

Hence, the lithological data suggests wet climate conditions in higher latitudes and tropical east-facing coast in the Tethys Ocean. In contrast, arid climate conditions seem to predominate in the continental interior as well as on the west coasts of Pangaea. Furthermore, no indication of glaciation exists for this period. Parrish [75] also points out extended evidence for red beds in central Pangaea. These sediments occur in alternating wet and dry conditions indicating monsoonal circulation.

2.5.3. Phytogeographical data

In addition to deposits in sediments, palaeobotanical finds can give information on the vegetation and thus on the climate conditions of a certain region. Rees et al. [73], Ziegler [76], and Rees et al. [77] compiled a comprehensive data set for the Early and Late Permian covering most parts of the Pangaean continent. They concentrated on finds of leaves, roots, and stems, since they assume these parts of the plant are the most affected by climate. The corresponding occurences (about 1,000 occurences from 150 localities) of plants for the Kazanian stage are also included in Figure 2.4. The finds were analysed for their botanical properties and categorised according to their genera. Considering the floral diversity and composition of the respective localities, Rees et al. [73, 77] determined floral patterns and climate signals. Especially the morphology of leaves can give information on the climate conditions [77]. However, the sample size at one location depends on the depositional environment and the preservertation potential is further affected by the climate and soil properties. Floodplains as well as riparian and lacustrine environments, for example, bias deciduous species [78] and improve the preservatation potential of plants at a certain location. Evergreen species are overrepresented in peat bog environments [79]. Hence, the palaeobotanical record is not necessarily representative of the surrounding region and predictions need to be evaluated carefully [77].

Including indications of lithological data [74] (see Section 2.5.2), Rees et al. [73] and Ziegler [76] assigned the phytogeographical units to a climate-based biome scheme that

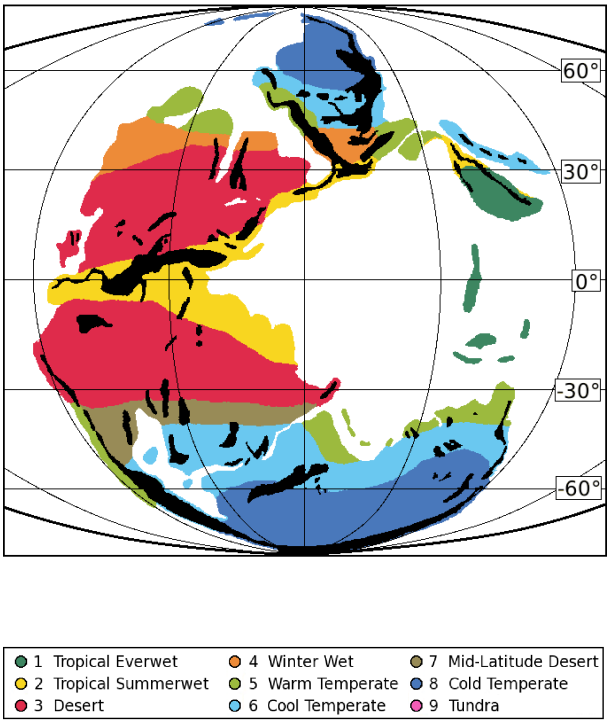

Figure 2.5.: Data-derived biomes for Kazanian stage from Rees et al. [73] following the biome classification scheme of Walter [80] (see Appendix B). The black areas denote elevated mountainous regions that are excluded as they are not representative for the global distribution.

has been originally developed for the present-day flora by Walter [80]. The biome scheme consists of ten different biomes from 'tropical everwet' to 'arctic and glacial' biome. Further details of the biomes are summarised in Appendix B. The reconstructed biomes for the Permian Earth are depicted in Figure 2.5. The boundaries between the different biomes are, however, rather gradual with smooth transitions and not sharp lines as depicted.

The tropical everwet realm (biome 1) seems restricted to the Tethysian microcontinents of Cathaysia and Cimmeria. Several palaeobotanical finds of North and South China, and Indochina indicate this biome. The summerwet biome (biome 2) is evidenced for the South of Euramerica and Northern Gondwana by some floral occurences, whereas the vast desert areas (biome 3) extending over Euramerica and Gondwana up to 40° of latitude are merely indicated by evaporite deposits. The warm temperate realm (biome 5) is supported for Northern Laurentia, the northern Uralian region, Tarim and the very south of Angara, as well as the southern Tethys margin by coal and a high floral diversity in the palaeobotanical finds. Ziegler [76] assumed the winterwet biome (biome 4) for a smooth transition to the desert region of the Northern Hemisphere. In contrast, there is evidence of a mid-latitude desert biome (biome 7) in terms of aeolian

sands for the South American part of Gondwana. This biome is not indicated for the Northern Hemisphere. Most of mid-latitude Angara and Gondwana is covered by the vast forests of the cool temperate biome (biome 6), proofed by coal deposists and various finds of deciduous tree fossils. The regions north and south of 60° of latitude have been assigned to the cold temperate biome (biome 8) because of the presence of coal deposits but low diversity in the floral data [73, 76, 77]. There is no indication for the arctic and glacial biome (biome 9 and 10) for the Kazanian stage. Yet, it is likely that glaciation occured in mountainous regions. Evidence for extended glaciation in Southern Gondwana exists, however, in the geological record for the Early Permian (see Section 2.1) [16, 17, 81].

Many climate simulations predict very cold climate conditions for the high-latitude regions of Angara and Gondwana (see Section 2.6). However, there is evidence of extended broadleaf forests at a palaeolatitude of 80-85°S in the geological record of Antarctica for the Late Permian. The analysis of the tree rings suggests a fast growing forest and gives no indication of long frost periods [82, 83].

2.6. Overview of Climate Simulations

There are various palaeoclimate simulations for the Permian period. The variety of models spans a wide spectrum of complexity, from rather simple energy balance models (EBM) to complex general circulation models (GCM). Most of the models confirm the general climate pattern that has been indicated by lithological and palaeobotanical data (see Section 2.5): strong seasonality and very dry conditions in the continental interior of Pangaea, very hot temperatures in the desert belt and very cold temperatures in high-latitude Gondwana, and monsoon circulation attended with high precipitation amounts along the margin of the Tethys Ocean [84]. Coarse resolution and insufficient heat transport from low to high latitudes seem to be the main difficulties for a number of studies [62]. Nonetheless, various issues have been studied that are briefly reviewed in the following. Subsequently, three studies are described in more detail as these will be used for evaluation of the simulation results presented in this work.

Very idealised geographic representations of the Permian topography are used in the studies of Kutzbach [69], Kutzbach and Gallimore [85], and Kutzbach and Guetter [86]. They assume the supercontinent of Pangaea to be symmetric about the equator and extended from about 75°N to 75°S. They do not consider any of the Tethysian microcontinents. Despite the coarse resolution of their atmospheric GCM (T10 [85] or T15 [69] grids[1] , respectively) and simplification due to the coupling to a mixed layer ocean (MLO), the main features of Permian climate are reproduced. Both, Kutzbach [69] and Kutzbach and Gallimore [85], observe arid conditions in the continental interior and a strong monsoon circulation with distinct precipitation in the summer season along the Tethys coast. The summer monsoon low is located at about 35° of latitude in

the summer hemisphere polewards of the Western Tethys Ocean, whereas the winter monsoon high, being more pronounced, is centered at about 40° of latitude on the opposite side of the Tethys [85]. The strength of the monsoon circulation is related to the precession of the Earth's orbit [69] (see Section 2.4.3). Kutzbach and Guetter [86] prescribe the surface forcing from the above simulation [86] and run a dynamical ocean model with eight levels. They find westward flowing equatorial ocean currents in the Panthalassic Ocean, poleward and eastward flowing currents along the Tethys coasts, and subpolar cyclonic as well as subtropical anticyclonic gyres in Panthalassa. Moreover, they regard the Tethys Ocean as important source for warm deep water.

Using an atmospheric GCM with prescribed sea surface temperatures, Fluteau et al. [87] investigate the climate for two different topographic configurations of Pangaea in the Late Permian and work out which configuration generates the more realistic climate state. Moreover, they study the effect of different elevations for the main Pangaean mountain ranges. They find significant effects on the precipitation pattern and a lower limit of the elevation of the Appalachian Mountains of at least 2,000 m for agreement with the indicated climate in Baltica. Kutzbach and Ziegler [36] can further show that the presence of equatorial highlands leads to an increase of tropical precipitation and intensification of the monsoon. In addition, they conclude that extensive lakes in central Gondwana have a moderating effect on the climate and the difference between summer and winter temperatures is significantly reduced in the vicinity of these lakes and over a large area to the north and east. The influence of vegetation also needs to be taken into account. By means of a coupled ocean-atmosphere-sea-ice GCM, Otto-Bliesner and Upchurch [88] show for the latest Cretaceous that extended forests in high latitudes induce a warmer climate in these regions. Montenegro et al. [23] investigate the influence of different ocean bathymetries for the Permian and conclude that the presence of ocean ridges leads to stronger meridional ocean circulation. For the Early Permian there is indication of extensive glaciation in Southern Gondwana (see Section 2.5). Using a Pleistocene icesheet model, Hyde et al. [81] study the conditions that are necessary for the generation of huge ice sheets in Southern Pangaea. Only if the solar luminosity is reduced by more than 2.75% in terms of the present-day value, they can generate glaciation. However, further decrease of luminosity has no effect on the extent of the icesheet. For a doubling of atmospheric carbon dioxide concentration from the present-day value, the size of the icesheet is reduced by a factor of two and there is no glaciation for a tripling of atmospheric carbon dioxide content. The influence of topography is negligible. Roscher, Stordal, and Svensen [89] examine the effect of rapid changes of radiative forcing on the climate at the Permo-Triassic Boundary. They suggest that the global cooling mechanism triggered by sulphur and ash particle ejection of the Siberian Traps has a stronger climatic effect than the warming induced by the release of greenhouse gases.

Gibbs et al. [74]: GENESIS. Gibbs et al. employ the climate model GENESIS II (Global Environmental and Ecological Simulation of Interactive Systems) [90] for their

[1] See Section 3.1.1.

studies. This comprises an atmospheric GCM that is coupled to a land-surface, sea-ice, and MLO model. The ocean component merely serves as heat storage and moisture source, as heat transport is solely included in terms of diffusion processes. Gibbs et al. use a horizontal T31 grid and 18 vertical levels within the atmosphere for their simulations. They assume the solar luminosity to be reduced by 2.1% and a circular orbit with an obliquity of 23.5°. The topography is based on Ziegler, Hulver, and Rowley [2] and they prescribe a uniform savannah vegetation, that consists of mixed trees and grassland, and uniform loamy soil. For the Wordian stage, they run two simulations with atmospheric carbon dioxide concentrations of 1380 ppm ($4\times CO_2$) and 2760 ppm ($8\times CO_2$), respectively. For both, the Sakmarian and Wordian stage, they can reproduce the main features of Permian climate, like extreme seasonality, high aridity in continental interiors and summer monsoons along the Tethysian margins, that are in good agreement with the lithological data. However, their simulations suggest very cold winters in high-latitude Gondwana contradicting the observations. Gibbs et al. assume the missing advective oceanic heat transport to be the reason of this disagreement. The simulation for the Wordian stage will be employed for the validation of our results in Section 5.4.

Winguth et al. [27]: LSG. Winguth et al. use a coupled system consisting of an atmospheric energy balance model and an ocean GCM for their simulations of the Permian oceans. The two-dimensional energy balance model (EBM) [91] determines the surface air temperature considering radiative, diffusive and advective processes. The EBM is coupled via surface heat flux to the Large-Scale Geostrophic ocean GCM (LSG) [92] that is, furthermore, forced by freshwater fluxes and wind stress (from GENESIS 2, Gibbs et al. [74]). Winguth et al. employ grid cells of $3.5°\times3.5°$ with 22 vertical levels within the ocean. They assume the same boundary conditions like Gibbs et al. [74] (see above) with a flat bottom bathymetry at a depth of 4,000 m and smoothed continental margins. Confirming the results of Kutzbach and Guetter [86], they find a strong westward equatorial current in the Panthalassic Ocean blocked by the Tethysian microcontinents, warm poleward currents along the Tethys coast and east of Gondwana, cold equatorwards currents along the east coast of Angara, and large meridional overturning circulation cells at both poles. There is deep water formation in these polar circulation cells and there is a warm deep ocean in eastern equatorial Panthalassa. They find best agreement with palaeoclimatic data for a $4\times CO_2$ scenario and open polar seaways. The latter encourage a moderate climate in high-latitude Gondwana. Oceanic heat transport to polar regions appears significantly larger compared to present-day conditions.

Kiehl and Shields [8]: CCSM. Kiehl and Shields employ the Community Climate System Model, version 3 (CCSM3) [93] for their climate studies of the Permo-Triassic Boundary. The model comprises coupled components for atmosphere, land, ocean, and sea-ice. They use a horizontal T31 grid for the atmosphere and a 3° grid with 25 levels for the ocean. The surface types setting vegetation and soil properties are prescribed on the basis of Rees et al. [77] . Kiehl and Shields assume a circular orbit with an obliquity

of 23.5° (present-day value) and a luminosity of 1338 Wm^{-2} (reduced by about 2%). The atmosphere contains 3550 ppm CO_2 ($10\times CO_2$), 0.7 ppm CH_4, and 0.275 ppm N_2O. The model has been run for 2,700 years to radiative equilibrium. In agreement with several other models and data for the latest Permian, Kiehl and Shields find hot climate conditions in wide parts of Pangaea. Moreover, they observe weak ocean overturning, especially in the Tethys Ocean. This indicates only weak transport of surface oxygen and nutrients favouring anoxic and euxinic conditions which are assumed to be one of the main causes for the great extinction.

3

The Earth System Model EMAC

3.1. Modular Earth Submodel System EMAC-MPIOM

The Modular Earth Submodel System (MESSy)[1] provides the infrastructure for a comprehensive Earth System Model (ESM). The general approach has been developed by Jöckel et al. [94]. Its modular structure facilitates the assembly of specific processes and diagnostic tools of different domains of the Earth system, i.e. land surface, ocean, atmosphere, and allows for feedback mechanisms via two-way coupling. The basic idea is that all process-specific calculations are swapped out to submodels and only the central prognostic quantities are evaluated by a base model.

The MESSy framework generally comprises four different layers: The base model layer (BML) contains the base model that manages the time integration and controls the execution of order of all involved processes. The communication between the base model and the single submodel is embedded in the base model interface layer (BMIL). Furthermore, data transfer between submodels and data import from boundary conditions is included here. The internal control of the individual submodels and the data import from the BMIL is implemented in the submodel interface layer (SMIL). Eventually, the self-consistent core routines of the submodels that perform the main calculations for the specific processes are part of the submodel core layer (SMCL). The calculations of the submodels are generally independent of the base model and every submodel can be included or excluded easily.

At the current development phase, the MESSy framework has been coupled to a number of regional and global models. The most common coupling employs a slightly modified version of the GCM ECHAM5 version 5.3.02 [95] as MESSy base model [96]. The resulting model system is denominated as ECHAM5/MESSy Atmospheric Chemistry

[1] `http://www.messy-interface.org/`

(EMAC). That way the base model determines the main meteorological quantities, as for instance temperature, specific humidity and wind speed, on a global scale and the latter are subsequently used for the process-specific calculations in the submodels. EMAC merely covers the atmosphere with prescribed land and ocean surface. By means of coupling the ocean GCM MPIOM [97] as submodel to EMAC, Pozzer et al. [98] assembled the oceanic domain and set up the atmosphere-ocean general circulation model EMAC-MPIOM. Coupling to the dynamic global vegetation model LPJ-GUESS [99] further allows for dynamic vegetation and eventually constitutes a fully comprehensive ESM.

The simulations of the Permian Earth in this work have been done with EMAC-MPIOM with MESSy version 2.50 [100] with prescribed vegetation (see Chapter 4). The effect of dynamic vegetation is studied separately and the corresponding submodel is merely included in certain simulations (see Section 5.2.3). The studies analysing the impact of nudging have applied stand-alone EMAC with MESSy version 2.42.

The base model ECHAM5 is briefly described in Section 3.1.1 and the ocean model MPIOM is surveyed in Section 3.1.2. Section 3.1.3 gives an overview of the MESSy submodels that have been applied in the simulations of this work. The underlying atmospheric convection schemes are discussed in Section 3.2.

3.1.1. ECHAM5

The climate model ECHAM5 is the fifth generation of the atmospheric GCM ECHAM of the Max Planck Institute of Meteorology (MPI-M, Hamburg, Germany). It originated from the operational weather forecast model of the European Centre for Medium-Range Weather Forecasts (ECMWF, Reading, United Kingdom) (hence 'EC') and a comprehensive parameterisation package developed at MPI-M (hence 'HAM'). A detailed model description is given in Roeckner et al. [95]. Coupled to the MESSy framework, ECHAM5 is modified such that processes contained in MESSy submodels are removed [96].

The dynamics of a moist atmosphere are fully described by the equation of motion of a compressible fluid on a rotating sphere, i.e. the Navier-Stokes equation, and additional boundary conditions in terms of conservation of mass (continuity equation), conservation of heat (first law of thermodynamics) and the ideal gas law. This gives a set of non-linear differential equations that is simplified by assuming hydrostatical equilibrium and further approximations [95]. The resulting set of primitive equations is solved numerically for the prognostic variables of the ECHAM5 model: vorticity, divergence, temperature, the natural logarithm of surface pressure, water vapour, cloud water, and cloud ice. The moisture variables are horizontally discretised in grid point space, whereas the other

prognostic variables are represented by truncated series of spherical harmonics:

$$X(\lambda, \mu, \eta, t) = \sum_{m=-M}^{M} \sum_{n=m}^{N(M)} X_n^m(\eta, t) P_n^m(\mu) e^{im\lambda}, \tag{3.1}$$

where X is any prognostic variable, m is the zonal wave number, n the meridional index, η the vertical level, t the time, and λ and μ are longitude and latitude, respectively. The P_n^m are the associated Legendre functions of the first kind:

$$P_n^m(\mu) = \sqrt{(2n+1)\frac{(n-m)!}{(n+m)!}} \frac{1}{2^n n!} (1-\mu^2)^{\frac{m}{2}} \frac{d^{(n+m)}}{d\mu^{(n+m)}} (\mu^2 - 1), \quad (m \geq 0). \tag{3.2}$$

The spectral coefficients X_n^m of the field X are given by

$$X_n^m(\eta, t) = \frac{1}{4\pi} \int_{-1}^{1} \int_{0}^{2\pi} d\lambda d\mu \; X(\lambda, \mu, \eta, t) P_n^m(\mu) e^{-im\lambda}. \tag{3.3}$$

The choice of $N(M)$ determines the truncation type and for a triangular truncation, like in ECHAM5, it is $N = M$. By means of this spherical representation, numerical dispersion and aliasing effects are avoided during the discretisation. As the spherical harmonics are the eigenfunctions of the Laplace operator, the equation system is further simplified and planetary waves are well represented. The transformation to the quadratic Gaussian grid of the grid point space applies a combination of Fourier and Legendre transformations. The standard truncations used in ECHAM5 are at wave numbers $M = \{21, 31, 42, 63, 85, 106, 159\}$ and the respective grids are summarised in Table 3.1. The vertical coordinate is given by a hybrid coordinate that is terrain-following in lower

Grid truncation and vertical levels	Number of boxes [lon × lat]	Box width [° × °]	Box width [km]	Time step [s]
T21 L19	64 × 32	5.6 × 5.6	621	2400
T31 L19	96 × 48	4.2 × 4.2	467	1800
T42 L31	128 × 64	2.8 × 2.8	311	1200
T63 L31	192 × 96	2.1 × 2.1	233	720
T85 L31	256 × 128	1.4 × 1.4	156	480
T106 L31	320 × 160	1.1 × 1.1	122	360
T159 L31	480 × 240	0.7 × 0.7	81	180

Table 3.1.: Standard horizontal grids and the respective resolution for ECHAM5 and EMAC.

levels and smoothly flattens to surfaces of constant pressure in upper levels. Most troposheric studies apply 19 or 31 levels up to a height of 10 hPa, but, also 87 or 90 levels are possible to resolve the middle atmosphere up to 0.1 hPa.

For numerical time integration ECHAM5 applies a semi-implicit leapfrog scheme [101–103] with a time Asselin filter [104] that dissipates and thereby prevents the growth

of numerical modes. The time step of Table 3.1 ensues the Courant-Friedrich-Levi criterion.

Passive tracer transport of water components (vapour, liquid, solid) and chemical substances is implemented according to a flux-form semi-Lagrangian scheme [105]. However, further advection algorithms are available. The cloud, convection, and radiation parameterisation is included in the MESSy submodels and the land surface parameterisation is discussed in Section 4.1.

3.1.2. MPIOM

The Max Planck Institute Ocean Model (MPIOM) is an oceanic GCM developed at MPI-M. It contributes the oceanic domain to numerous ESM and a detailed description is given in Marsland et al. [97] and Wetzel et al. [106]. MPIOM emerged from the last version of the Hamburg Ocean Primitive Equation (HOPE) model [107] and the coupled model system EMAC-MPIOM employs MPIOM version 1.3.0.

For the physical description of its dynamics, the ocean is approached as incompressible fluid on a rotating sphere. Assuming hydrostatical equilibrium and Boussinesq approximation (dynamic perturbations in density are small compared to mean background density) distinctly simplifies the Navier-Stokes equation. Conservation of mass, salinity, and heat, as well as the equation of state for the density of water complete the set of primitive equations that constitute the dynamical core of MPIOM. As further boundary condition a free surface is assumed that is lifted by convergence and lowered by divergence of the fluid throughout the underlying water column, respectively. Salinity and temperature are treated as tracers and determined via the advection-diffusion equations. By means of operator splitting techniques the primitive equations are decomposed into baroclinic and barotropic parts and, employing implicit methods, solved seperately for the prognostic variables, i.e. horizontal and vertical velocity, temperature, salinity, and surface elevation. The model is horizontally discretised on an Arakawa C-grid [108] and uses a bipolar orthogonal spherical coordinate system. The location and radius of the poles can be chosen *ad lib*. This offers the advantage of removing the numerical singularity associated with convergence of meridians at the geographical poles and allows the construction of regionally high-resolution models. The vertical discretisation applies a z-coordinate system with unevenly spaced levels. The horizontal grid for the Permian Earth model is presented in Section 4.2.

The coarse horizontal and vertical resolution requires subgrid-scale parameterisation of various processes. A bottom boundary layer slope convection scheme [97, 109] describes the flow of statically unstable dense water masses over sills and off-shelves. Convective overturning is adjusted using an enhanced vertical diffusion parameterisation [97]. Furthermore, the horizontal diffusion of tracers employs an isopycnal scheme [110, 111] and horizontal tracer mixing by advection with the unresolved mesoscale

eddies is implemented according to the parameterisation scheme of Gent et al. [112]. In contrast, vertical mixing and diffusion are considered by the Richardson number-dependent formalism of Pacanowski and Philander [113]. However, an additional wind mixing parameterisation is included, as the original scheme underestimates the turbulent mixing near the surface [97].

MPIOM comprises an embedded dynamic and thermodynamic sea ice model [97, 107] that is implemented on a subgrid scale. The external sea ice motion follows a momentum balance equation. The internal dynamics, i.e. the way in which ice flows, cracks, ridges, rafts, and deforms, are based on the viscous-plastic ice rheology of Hibler [114]. The local growth or melt rates at the base and surface of the sea ice are determined thermodynamically regarding net atmospheric heat flux, conductive heat flux within the sea ice/snow layer, and heat exchange at the ocean/sea ice interface. Snow accumulation on sea ice is included as well as snow-to-ice transformation. Sea ice is assumed to have constant salinity and, in general, salinity is conserved in the course of sea ice generation.

At each time step, the sea ice dynamics and thermodynamics are evaluated first. Considering the prescribed forcing at the surface (heat, momentum and freshwater input), the ocean momentum equation is *apriori* solved partially for the friction terms. Subsequently, the updated equation is solved for the advection terms employing a mixed central-difference and upstream integration scheme [97].

3.1.3. MESSy submodels

The MESSy framework comprises two different kinds of submodels. On the one hand there are generic submodels that are embedded in the BMIL. They undertake specific, superordinate tasks managing the MESSy infrastructure. The generic submodels that were used for the simulations of this work are summarised in Table 3.2.

On the other hand there are process-specific and diagnostic submodels. Table 3.3 surveys the submodels used for this work. Subsequently, the main tasks and principles of the individual submodels are briefly presented.

A2O. This submodel couples the ocean and atmosphere domain within the MESSy framework. EMAC is horizontally discretised on a quadratic Gaussian grid (see Section 3.1.1), whereas MPIOM operates on a curvilinear rotated grid (see Section 3.1.2). The grid interpolation is implemented by the generic submodel `GRIDTRAFO`. Scalar fields are interpolated via a bilinear remapping method and for flux fields a conservative remapping method is used. EMAC and MPIOM are fully coupled in such a way that boundary conditions, like sea surface temperature, wind speed and direction etc., are mutually exchanged in both directions. The variables required for the coupling are accumulated and averaged within each coupling period in order to deal with the different time steps.

Submodel name	Short description
CHANNEL	Memory and meta-data management and data export [100]
CONSTANTS	Constants shared between submodels [94]
GRIDTRAFO	Grid transformations [98, 100]
QTIMER	Optimal use of queue limits and run-time diagnostics [100]
SWITCH	Switch and call individual submodels [100]
TIMER	Time control [100]
TOOLS	Tools shared between submodels [94]
TRACER	Management of data and meta-data of constituents [115]
NCREGRID	Redriscretisation on different grids [96]

Table 3.2.: Overview of generic MESSy submodels that have been used for the simulations of this work.

CLOUD. The cloud scheme of this submodel deals with large-scale stratiform clouds that can be described directly by means of the prognostic model variables on the model grid. In contrast, subgrid scale convective clouds are treated by the CONVECT submodel. The submodel provides two different schemes: The cloud scheme of Sundqvist [121] is used for the simulations of the Permian Earth, whereas the simulations of the present-day Earth employ the scheme of Tompkins [122]. The latter is more sensitive to optimal tuning of free parameters and thus unsuitable for a palaeosetup.The Sundqvist scheme [121, 123] derives the fractional cloud cover directly from relative humidity by a non-linear function with a condensation threshold of 99% at the surface that decreases exponentially to 60% at the top level. Cloud formation is related to water vapour and total cloud water content. These prognostic variables are modified by budget equations that comprise the condensation of water within the cloud, evaporation of cloud water within the cloud and also after being transported to the cloud-free part of the grid cell, formation of precipitation by coalescence of cloud droplets and sedimentation of ice crystals, and evaporation of precipitation in the unsaturated part of a grid cell. The Tompkins scheme applies a statistical-dynamical approach that includes small variations of humidity and temperature within a grid cell. These fluctuations allow cloud formation before the grid cell mean values reach saturation. The grid cell mean values of total water content and cloud water content are taken from ECHAM5 due to consistency, whereas their internal distribution is described by a probability density function (PDF). The Tompkins scheme assumes general beta distributions as best choice for the PDF. The other shape parameters of the PDF, i.e. width and skewness, are determined according to prognostic equations that contain a convective, turbulent and microphysical contribution. Moreover, the effect of turbulences and large-scale condensation on water vapour and cloud water is included. The fractional cloud cover ensues directly from the PDF and microphysical in-cloud and cloud generation processes are eventually evaluated on the

Submodel name	Short description
A2O	Coupling of ocean and atmosphere; regridding, transformation of variables at surface layer [98]
CLOUD	Cloud model [116]
CONVECT	Convection model [117]
CVTRANS	Convective tracer transport [118]
DRADON	Diagnostics of ^{222}Rn tracer [100]
HD	Hydrological discharge model [119]
MPIOM	Ocean GCM [98]
RAD4ALL	Radiation incidence and interaction [96, 116]
TROPOP	Tropopause diagnostics [96]
VEG	Dynamic vegetation model LPJ-GUESS [120]

Table 3.3.: Overview of process and diagnostic MESSy submodels that have been used for the simulations of this work.

basis of the distribution of water content. Cloud generation is triggered by condensation, advection of water vapour in the presence of moisture convergence, and cooling.

CONVECT. Convective processes in the atmosphere occur on a scale that is far smaller than the usual grid size of a GCM and thus need to be parameterised as subgrid-scale processes. This submodel comprises several different convection parameterisations and the ones used in this work are discussed in Section 3.2.

CVTRANS. Vertical tracer transport in convective columns is treated by this submodel. Using a bulk approach [124], this submodel separates the tracer mass fluxes from convective mass fluxes and determines the tracer mixing ratio in the updraught and downdraught as well as the detrained tracer mass fluxes.

DRADON. The tracer ^{222}Rn is emitted from soil as radioactive decay product of ^{226}Ra and decays further with a half-life of 3.8 days. One of its decay products, ^{210}Pb, adheres well to aerosols and is eventually removed from the atmosphere by dry and wet deposition. This leads to a relatively short atmospheric life time of the order of days or weeks and that is why ^{222}Rn and ^{210}Pb are widely used tracers for transport studies. The submodel sets the emission rates and either simulates the decay of ^{222}Ra or, by means of an additional aerosol submodel, the decay chain up to the decay of ^{210}Pb.

HD. For closure of the hydrologic cycle the water that evaporated from the ocean and precipitated over land needs to be returned to the ocean, when it is not stored in either soil or plants. In the MESSy framework the hydrological discharge model by Hagemann and Dümenil [119, 125], that is contained in this submodel, treats the lateral waterflow from the continents into the ocean. In general, the model evaluates the translation and retention of the lateral discharge with respect to the spatially distributed land surface characteristics on a global scale [119, 125, 126]. Waterflow is decomposed into three

flow processes, i.e. overland, base, and river flow. Both overland flow and base flow are implemented as a single linear reservoir, whereas river flow is represented by a cascade of several equal linear reservoirs. Surface runoff is assumed to feed overland flow, base flow is fed by drainage from the soil, and river flow uses the inflow from the neighbouring grid cells as input. The flow generally depends on the topography gradient between grid cells, the slope within a cell, its length as well as the lake area, and the wetland fraction. The sum of all three flows eventually gives the total outflow from each grid cell that enters the neighbouring grid cell with the lowest topography. Due to the coarse grid, several additional mathematical methods are applied for more realistic river flow paths [119]. The hydrological discharge model operates on a $0.5° \times 0.5°$ grid and the discharge is computed with a daily time step.

MPIOM. This submodel includes the ocean GCM MPIOM that is described in Section 3.1.2.

RAD4ALL. The MESSy radiation scheme comprised in this submodel emerged from the radiation scheme of ECHAM5. For the short wave range the radiation scheme of Fouquart and Bonnel [127] is employed that considers Rayleigh scattering and absorption by water vapour and ozone for four spectral bands, one for visible and UV range, and three for the near IR. The scattering characteristics of the clouds are based on Mie calculations for idealised size distributions of cloud droplets and ice crystals. The scheme assumes an atmosphere consisting of uniformly mixed CO_2, N_2O, CO, CH_4, and O_2. It applies the Eddington approximation for the integration over the zenith and azimuth angles as well as the delta-Eddington approximation for the reflectivity while calculating the radiation flux. The long wave range is treated by the Rapid Radiation Transfer Model (RRTM) [128] that uses the correlated k-distribution method. For 16 different spectral bands the line absorption by H_2O, CO_2, O_3, CH_4, N_2O, CFC-11, CFC-12, and aerosols is included. Absorption by cloud droplets is assumed to depend on the effective droplet radius and to be independent of the wave number, whereas absorption by ice crystals varies with wave number and the inverse radius.

TROPOP. The diagnosis of the tropopause according to various definitions as well as the height of the planetary boundary layer is treated by this submodel.

VEG. Allowing for dynamic vegetation, this submodel couples EMAC with the dynamic global vegetation model LPJ-GUESS (Lund-Potsdam-Jena General Ecosystem Simulator) [99]. The vegetation is modelled in terms of eight woody and two herbaceous plant functional types (PFT). The PFT defines the plant's physiological and dynamical properties, as well as the bioclimatic limits that decide whether the plant can survive and/or regenerate under the prevailing climatic conditions. The limits are basically determined by soil moisture, temperature range, and the coldest monthly temperatures on the basis of a 20-year mean. If the bioclimatic limits are met, first herbaceous PFT and later also woody PFT establish in available non-vegetated areas. Several PFT can coexist within one grid cell and compete for resources. They are treated as a well-mixed mosaic of individuals or species cohorts and bare ground. Evapotranspiration, plant respiration,

photosynthesis, and soil hydrology processes are evaluated once per day, whereas general plant growth, maintenance, and reproduction are considered on an annual scale. For summergreen PFT budburst and leaf senescence are taken into account. Heat and water stress lead to reduced growth and higher mortality. Additionally, mortality due to light reduction or negative carbon balance is included as well as disturbance by fire. Biomass and heartwood of killed individuals is transferred into litter pools and gradually decomposed. The model's implementation ensures a closed carbon cycle.

3.2. Convection Scheme

Convective processes affect the atmospheric transport on a large as well as on a small scale and thus influence the distribution of energy within the atmosphere. Furthermore, convection increases the stability of the stratification and, to some extent, triggers precipitation. In this manner the simulated meteorology and climate, and hence the quality of an atmospheric GCM, is strongly affected by the description of convection. However, in most GCM the size of a grid cell is far larger than a single convective cloud. That is why a parameterisation that describes all the small-scale processes is employed. Several different parameterisations exist.

In the EMAC model the convective processes are computed by the `convect` submodel [118]. The convection schemes employed for this work are summarised in the following. Most of our simulations applied the scheme of Tiedtke [129] (see Section 3.2.1), whereas the scheme of Zhang and McFarlane [130] and Hack [131] (see Section 3.2.2) is merely applied to validate the influence of convection parameterisation (see Section 5.2.2).

3.2.1. Tiedtke convection scheme

Tiedtke [129] considers small-scale cumulus clouds to be embedded in the large-scale environment. The clouds are characterised by updraughts and downdraughts, i.e. by upward and downward mass fluxes. Moreover, the clouds are not individually resolved but regarded as cloud ensemble in terms of a bulk model with cumulative properties. The thermodynamic forcing of cumulus convection on the large-scale budget of the environmental dry static energy $\bar{s}$ ($s = c_p T + gz$) and specific humidity $\bar{q}$ is:

$$\begin{aligned} \frac{\partial \bar{s}}{\partial t} + \bar{\mathbf{v}} \cdot \nabla \bar{s} + \bar{w} \frac{\partial \bar{s}}{\partial z} = & -\frac{1}{\rho} \frac{\partial}{\partial z} \left[M_u s_u + M_d s_d - (M_u + M_d)\, \bar{s} \right] \\ & + L \left(c_u - e_d - \tilde{e}_l - \tilde{e}_p \right) - \frac{1}{\rho} \left(\bar{\rho} \overline{w' s'} \right)_{\mathrm{tu}} + \overline{Q_R} \end{aligned} \tag{3.4}$$

$$\begin{aligned}\frac{\partial \bar{q}}{\partial t} + \bar{\mathbf{v}} \cdot \nabla \bar{q} + \bar{w}\frac{\partial \bar{q}}{\partial z} = &-\frac{1}{\rho}\frac{\partial}{\partial z}\left[M_u q_u + M_d q_d - (M_u + M_d)\,\bar{q}\right] \\ &+ L\left(c_u - e_d - \tilde{e}_l - \tilde{e}_p\right) - \frac{1}{\rho}\left(\overline{\bar{\rho} w' q'}\right)_{\mathrm{tu}},\end{aligned} \tag{3.5}$$

where ρ is the density of air, $\mathbf{v}$ the horizontal wind velocity, w the vertical wind velocity, L the latent heat of condensation and Q_R the radiative heating. The overbar denotes the average over an area that is sufficiently large to contain several cumulus clouds. The net contributions from all clouds to the upward and downward mass flux, condensation in the updraught and evaporation in the downdraught are denoted by M_u, M_d, c_u and e_d, respectively. Further, $\tilde{e}_l$ represents the evaporation of detrained cloud air and $\tilde{e}_p$ the evaporation of precipitation. The term denoted by $()_{\mathrm{tu}}$ considers the contribution from boundary layer turbulence and the overbar labels quantities from the environmental atmosphere.

Tiedtke assumes the mass fluxes to be in a steady state. The bulk equations for the updraught of the cloud ensemble are given by:

$$\frac{\partial M_u}{\partial z} = E_u - D_u \tag{3.6}$$

$$\frac{\partial\left(M_u s_u\right)}{\partial z} = E_u \bar{s} - D_u s_u + L\bar{\rho} c_u \tag{3.7}$$

$$\frac{\partial\left(M_u q_u\right)}{\partial z} = E_u \bar{q} - D_u q_u - \bar{\rho} c_u \tag{3.8}$$

$$\frac{\partial\left(M_u l\right)}{\partial z} = -D_u l + \bar{\rho} c_u - \bar{\rho} G_p, \tag{3.9}$$

where E_u and D_u are the rates of mass entrainment and detrainment, respectively, and l is the cloud liquid water content. The corresponding bulk equations for the downdraught are:

$$\frac{\partial M_d}{\partial z} = E_d - D_d \tag{3.10}$$

$$\frac{\partial\left(M_d s_d\right)}{\partial z} = E_d \bar{s} - D_d s_d + L\bar{\rho} e_d \tag{3.11}$$

$$\frac{\partial\left(M_d q_d\right)}{\partial z} = E_d \bar{q} - D_d q_d - \bar{\rho} e_d. \tag{3.12}$$

The cloud air is assumed to be saturated, and freezing and melting processes are not considered. The precipitation formation G_p is simply parameterised as:

$$G_p = K(z) l, \tag{3.13}$$

where the empirical function $K(z)$ varies with height with respect to the cloud base Z_B:

$$K(z) = \begin{cases} 0, & \text{if } z \leq Z_B + 1500 \text{ m} \\ 2.10^{-3} \text{ s}^{-1}, & \text{if } z > Z_B + 1500 \text{ m}. \end{cases} \tag{3.14}$$

Thus, the rain water flux at height z is determined via integration:

$$P(z) = \int_{z}^{\text{cloud top}} (G_p - e_d - \tilde{e}_p)\,\bar{\rho} dz. \tag{3.15}$$

Tiedtke assumes entrainment of environmental air into the convective plume and detrainment in the opposite direction via turbulent eddies (1) at the cloud edges and organised flow (2) associated with large-scale convergence or outflow at cloud top, respectively:

$$E_u = E_u^{(1)} + E_u^{(2)}, \qquad D_u = D_u^{(1)} + D_u^{(2)}. \tag{3.16}$$

The turbulent entrainment and detrainment rates depend inversely on cloud radii, which leads to

$$E_u^{(1)} = \epsilon_u M_u, \qquad D_u^{(1)} = \delta_u M_u, \tag{3.17}$$

where

$$\epsilon_u = \delta_u = \begin{cases} 1 \times 10^{-4}\ \text{m}^{-1}, & \text{deep and mid-level convection} \\ 3 \times 10^{-4}\ \text{m}^{-1}, & \text{shallow convection.} \end{cases} \tag{3.18}$$

Entrainment and detrainment in the downdraught is parameterised similarly to Eq. 3.17 with $\epsilon_d = \delta_d = 2 \times 10^{-4}\ \text{m}^{-1}$.

Three different types of convection are considered in this scheme:

1. **Penetrative or deep convection.** Triggered by a deep layer of conditional instability and large-scale moisture convergence; convective plume can reach several kilometres in height.

2. **Shallow convection.** Controlled by subcloud layer turbulence; in undisturbed flow, e.g. tradewind cumuli, daytime convection over land, ridge regions of tropical easterlies.

3. **Mid-level convection.** Originated in levels above the boundary layer; rainbands at warm fronts and in the warm sector of extratropical cyclons.

The parameterisation of organised entrainment and detrainment depends on the convection type.

1. The entrainment results from large-scale moisture convergence via

$$E_u^{(2)} = -\frac{\bar{\rho}}{\bar{q}} \left(\bar{\mathbf{v}} \cdot \nabla \bar{q} + \bar{w} \frac{\partial \bar{q}}{\partial z} \right). \tag{3.19}$$

   Detrainment is assumed to occur only in the model layer corresponding to the zero-buoyancy level of the deepest clouds.

2. In order to include overshooting cumuli, the cloud air is assumed to detrain 70% of its mass into the cloud top layer and 30% into the layer above.

3. The cloud air is produced by large-scale moisture convergence above cloud base similarly to deep convection (Equation 3.19).

The Tiedtke convection scheme has been supplemented with some additions by Nordeng [132]. For penetrative convection the rates of organised entrainment and detrainment are parameterised with direct relation to cloud activiy, i.e. with respect to the buoyancy of the cloud air parcel. Organised entrainment corresponds to positive buoyancy of the cloud parcel and detrainment to negative buoyancy. This results in:

$$E^{(2)} = \left[\frac{b}{2\left({w_0}^2 + \int_0^z b dz \right)} + \frac{1}{\bar{\rho}} \frac{\partial \bar{\rho}}{\partial z} \right] \cdot M_u, \qquad b = \frac{g}{T} \left(T_v - \bar{T} \right) - gl, \tag{3.20}$$

with the vertical velocity at cloud base $w_0 = 1$ ms^{-1} and the buoyancy b. The detrainment is given by:

$$D^{(2)} = -\frac{M_d}{\sigma} \frac{\partial \sigma}{\partial z}, \qquad \sigma = \sigma_0 \cos\left(\frac{\pi}{2} \frac{z - z_d}{z_t - z_d} \right). \tag{3.21}$$

Here σ is the fractional cloud cover, z_t is the highest possible cloud top level, and z_d is the lowest level where clouds start to detrain.

Furthermore, the closure assumption has been replaced by an adjustment closure that relates the cloud base mass flux, M_B, to the degree of convective instability. The latter is determined via CAPE and the relaxation time τ for which the convective scheme should remove the instability. The closure assumption is:

$$M_\mathrm{B} = \frac{\mathrm{CAPE}}{\tau} \frac{M_\mathrm{B}^*}{\int_\mathrm{cloud} \left(\frac{1+\delta q}{c_p \overline{T_v}} \frac{\partial \bar{s}}{\partial z} + \delta \frac{\partial \bar{q}}{\partial z} \right) M^* \frac{g dz}{\bar{\rho}}}, \tag{3.22}$$

where M_B^* is an estimated starting value of M_B for the computation of CAPE. Unlike the previous definition, Nordeng includes the effect of liquid water:

$$\mathrm{CAPE} = \int_\mathrm{cloud} \left(\frac{T_v - \overline{T_v}}{\overline{T_v}} g - gl \right) dz. \tag{3.23}$$

In general, the convection scheme is triggered when the temperature difference between an air parcel and the environmental air in the level of free convection (LFC) exceeds 0.5 K.

3.2.2. Zhang-McFarlane-Hack scheme

The Zhang-McFarlane-Hack convection scheme combines the parameterisations for deep convection by Zhang and McFarlane [130] with the parameterisation for shallow and mid-level convection by Hack [131].

Like in the Tiedtke scheme, Zhang and McFarlane consider the convective clouds as an ensemble of updraughts and downdraughts that are embedded in the large-scale environment. The updraughts are described as entraining plume with a characteristic fractional entrainment rate. The fractional entrainment is assumed to be maximal in the lower troposphere and to decrease with height. Detrainment is constrained to the conditionally stable region near the plume top where the lifted mass is emitted to the environment. In contrast to the Tiedtke scheme, downdraughts are assumed to exist only in case of precipitation production in the updraught ensemble. They start at the detrainment level of the updraught and solely detrain to the subcloud layer. Evaporation of rain water ensures saturation of the downdraughts and, further, the downdraught massflux is restricted to 65% of the updraught mass flux at cloud base. For closure Zhang and McFarlane also assume the cumulus convection to consume CAPE at an exponential rate with characteristic time scale τ.

The shallow and mid-level convection processes are parameterised according to the moist convection scheme of Hack [131]. The general idea of this convection scheme is to stabilise moist instabilities by means of vertical water transport. In its core, the scheme consists of a three-level nonentraining cloud model. The upward flux is restricted to the inside of a convective element and the downflux to the outside. In the course of its ascent from the lowest level, the convective element is subsequently subjected to condenstation and rain out processes in the middle level, and to detrainment in the highest one. The relative alteration of buoyancy determines the detrainment rate. Eventually, the resulting convective mass flux is determined and the thermodynamic quantities are adjusted for all levels. This procedure is repeated for all model levels.

The validation of various convection schemes of Tost, Jöckel, and Lelieveld [117] shows that the Zhang-McFarlane-Hack scheme simulates the zonal average precipitation more realistically than the Tiedtke scheme but tends to overestimate precipitation in the tropics over the continents and to underestimate it over the ocean. The Zhang-McFarlane-Hack scheme shows a bias towards convective precipitation. Consequently, large-scale precipitation is suppressed and the integrated atmospheric water vapour content in the tropics is predicted too low. The simulation of surface temperature is similar for both schemes.

4

Simulation of Permian Palaeoclimate

For the simulation of the Permian palaeoclimate with EMAC, all domains of the ESM have to be adapted to the conditions and configurations of that time (see Chapter 2). This is one of the major tasks of this work. Section 4.1 surveys the land surface parameters that are requested as input for climate simulations with EMAC and shows how these parameters have been generated for the Permian Earth. The atmosphere and ocean grids as well as all other specific settings are summarised in Section 4.2. The initialisation setup is dealt with in Section 4.3 and Section 4.4 examines the transition of atmosphere and ocean to steady state.

4.1. Land Surface Parameters for Permian Earth

The transfer of heat, momentum and humidity at the Earth's surface significantly affects the flow in the atmospheric boundary layer. Therefore, adequate modelling of climate requires the proper description of surface properties. Simulations of the present-day climate with EMAC employ the same dataset of prescribed land surface parameters that is used by ECHAM5. The dataset comprises data of topography, orography, soil, and surface properties on a global scale on a latitude/longitude grid and, moreover, a monthly climatology of vegetation distribution is included. The elevation and shape of the surface is set by the orographic parameters. These are derived from the U.S. Navy 10'×10' elevation dataset [133] and smoothed by means of a Gaussian filter to the respective grid (see Table 3.1). Furthermore, type, texture, and cover of the surface is determined by means of remote sensing. The U.S. Geological Survey (USGS) uses data from a very high resolution radiometer (1 km resolution) [134] to derive a global distribution of major ecosystems [135] in accordance with the definitions of Olson [136, 137]. Hagemann et al. [138, 139] eventually allocate land surface parameters to all ecosystem types according to methods of Claussen et al. [140]. They aggregate

the data from the USGS global distribution to the respective model grid. Thermal soil properties are provided by an additional global dataset of soil type and texture [141]. Simulations with uncoupled EMAC use prescribed monthly climatological sea surface temperatures (SST) and sea ice concentrations. These are taken from the Center for Ocean-Land-Atmosphere Studies/Climate Analysis Center (COLA/CAC) dataset developed for the Atmospheric Model Intercomparison Project (AMIP) [142].

In contrast, the construction of a dataset of land surface parameters for the Permian Earth can only rely on sparse data and is more speculative on some points. The topography is based on reconstructions for the Kazanian stage by Scotese and McKerrow [1]; Ziegler, Hulver, and Rowley [2]; and Ziegler, Gibbs, and Hulver [3]. The elevation is given on a $0.5° \times 0.5°$ grid (see Figure 2.1) and the orographic parameters are determined as with the U.S. Navy data. Surface data defining type, texture, and cover are borrowed from the simulation of Kiehl and Shields [8] after personal communication with C. Shields. They assume an average composition of soil as well as vegetation cover according to palaeobotanical data of Rees et al. [77]. The procedure for the determination of all land surface parameters for the Permian Earth required by EMAC is elucidated in the following subsections 4.1.1-4.1.5 and the global distributions of the single parameters are depicted in Appendix C.

4.1.1. Topography

Sea-land mask (`SLM`). The sea-land mask describes the land fraction of every grid cell. Here, $\texttt{SLM} = 1$ corresponds to pure land coverage and $\texttt{SLM} = 0$ corresponds to pure ocean or lake coverage. Positive elevation of the original Permian elevation dataset is assigned as 'land', whereas zero or negative elevation is assigned as 'sea'. Subsequently, the sea-land mask is transformed to the respective model grid by means of area-weighted averaging over the involved grid cells of the original grid. The representation for the T63 grid is shown in Figure C.1.

Lake mask (`ALAKE`). The lake mask describes the lake fraction of every grid cell. Here, $\texttt{ALAKE} = 1$ corresponds to pure lake coverage and $\texttt{ALAKE} = 0$ corresponds to either pure land or ocean coverage. The grid cell of the original Permian elevation dataset is assigned as 'lake' in case of zero or negative elevation and if the grid cell or a small cluster of grid cells is surrounded by land grid cells. Again, the lake mask is transformed to the respective model grid via area-weighted averaging. The lake model of the EMAC framework is only called for $\texttt{ALAKE} > 0.5$, however, and the water fraction is otherwise set to zero [95]. The representation for the T63 grid is depicted in Figure C.2.

4.1.2. Orography

Orographic structures affect the atmospheric flow across the entire spectrum of length scales. Although the impact of large-scale formations predominates, small and mesoscale

variations can significantly influence the local climate. However, variations smaller than the extent of a grid cell cannot be resolved by the model and their effects, such as orographic turbulences and gravity waves, need to be parameterised.

EMAC and ECHAM5 employ the subgrid-scale orographic drag parameterisation scheme by Lott and Miller [143] and Lott [144] that is based on the description of subgrid-scale orography by Baines and Palmer [145]. Lott and Miller assume the mean orography, $\overline{h}$, to be the optimal representation regarding the large-scale flow. On a smaller scale, they consider the generation of gravity waves due to the lift exerted by mountains and the obstruction of the flow at low levels if the mountains are high enough. The scheme further includes subsequent propagation and dissipation of the gravity waves as well as wave breaking due to convective overturning or convective instability. Moreover, additions by Lott [144] allow for low-level trapped lee waves. In order to determine the momentum transfer, wave drag, and the drag exerted by mountains, information about the subgrid-scale orographic structure is required.

The mountains are parameterised as eliptically shaped obstacles defined by the half-axes a (cross-ridge direction) and b (along-ridge direction). Thus, the shape can be described by the mountain anisotropy γ,

$$\gamma = \frac{a}{b}, \quad \gamma \in [0, 1] \tag{4.1}$$

where $\gamma = 0$ represents a two-dimensional ridge and $\gamma = 1$ a circular hilltop. A grid cell is assumed to be filled with a sequence of several mountain chains. Hence, there are approximately $L^2/4ab$ mountains or ellipses, respectively, within one grid cell of length L. The orientation of the ellipses is given by the angle θ, that represents the angle between the x-axis of the grid and the a-axes of the ellipse. Furthermore, the terrain of a grid cell is characterised by the maximal and minimal elevation defining the topographic prominence of the mountains, and the inclination of the slope, σ. The standard deviation of orography, μ, indicates the variation of topographic heights within a grid cell. More precisely, μ describes the amplitude of the subgrid variations around the mean orography and 2μ is assumed as physical envelope of the peaks. According to the scheme of Baines and Palmer [145], the orography of each grid cell is represented by a parameter set $\{\overline{h}, h_{\min}, h_{\max}, \mu, \sigma, \theta, \gamma\}$.

Part of the parameters, i.e. $\overline{h}, h_{\min}, h_{\max}$, and μ, can be determined directly from the original dataset. The others are derived by means of the topographic gradient correlation tensor

$$H_{ij} = \overline{\frac{\partial h}{\partial x_i} \frac{\partial h}{\partial x_j}}, \tag{4.2}$$

where $x_1 = x$ represents the longitudinal axis and $x_2 = y$ the latitudinal axis. Diagonalisation provides information about the properties of the principal axis.

$$H_{11} = K + \sqrt{L^2 + M^2} \quad \text{and} \quad H_{22} = K - \sqrt{L^2 + M^2}, \tag{4.3}$$

where:

$$K = \frac{1}{2}\left\{\overline{\left(\frac{\partial h}{\partial x}\right)^2} + \overline{\left(\frac{\partial h}{\partial y}\right)^2}\right\}, \quad L = \frac{1}{2}\left\{\overline{\left(\frac{\partial h}{\partial x}\right)^2} - \overline{\left(\frac{\partial h}{\partial y}\right)^2}\right\}, \quad M = \overline{\frac{\partial h}{\partial x}\frac{\partial h}{\partial y}}. \tag{4.4}$$

Small-scale orographic structures on scales resolved by the model need to be removed because they can cause unrelated effects. Therefore, a smoothing filter is applied that computes the moving average for the mean orography and the orographic gradients. The value of the actual grid cell is weighted by a factor of 1/4, the direct neighbour cells in longitudinal and latitudinal direction are weighted by a factor 1/8, and the diagonal neighbour cells are weighted by a factor of 1/16. At the poles the value of the southern and northern neighbour cells, respectively, are taken. Owing to the spherical grid, the longitudinal size of the cells varies with the latitude. For compensation, the orography is additionally averaged over the next $\lfloor 1/\cos(\texttt{lat}) \rfloor$ longitudinal neighbour cells.

Mean orography (`OROMEA`). The mean elevation of the orography, $\overline{h}$, is derived from the original Permian elevation dataset via area-weighted averaging over the involved grid cells of the original grid. Subsequently, the smoothing filter (see above) is applied and oceanic grid cells are set to zero elevation. The representation for the T63 grid is shown in Figure C.3.

Orographic valleys elevation (`OROVAL`). The minimal elevation of the subgrid-scale orography, $h_{\min}$, is assigned to the lowest elevation of the original Permian elevation dataset that lies within the destination grid cell of the respective model grid. Again, the smoothing filter is applied and oceanic grid cells are set to zero elevation. The representation for the T63 grid is depicted in Figure C.5.

Orographic peaks elevation (`OROPIC`). Analogously, the maximal elevation of the subgrid-scale orography, $h_{\max}$, is assigned to the highest elevation of the original Permian elevation dataset that lies within the destination grid cell of the respective model grid. The smoothing filter is applied and oceanic grid cells are set to zero elevation. The representation for the T63 grid is illustrated in Figure C.6.

Standard deviation of orography (`OROSTD`). The standard deviation of subgrid-scale orography, μ, is determined according to the commonly-used definition

$$\mu = \sqrt{\overline{h^2} - \overline{h}^2}, \tag{4.5}$$

where, as before, the area-weighted average is used. Again the smoothing filter is applied subsequently and the oceanic grid cells are set to zero variance. The representation for the T63 grid is shown in Figure C.4.

Orographic orientation (`OROTHE`). The orientation of the subgrid-scale orography, θ, corresponds to the principal axis of the topographic gradients correlation tensor. The angle with respect to the x-axis is given by:

$$\theta = \frac{1}{2}\,\mathrm{atan2}\,(M, L), \quad \theta \in [-180^\circ, 180^\circ]. \tag{4.6}$$

Here, the smoothed orographic gradients are used. Oceanic grid cells are assigned as $\theta = 0°$. The representation for the T63 grid is depicted in Figure C.7.

As the principal axis constitutes a natural axis of the local orography, a local coordinate system is introduced where the axes are aligned along the principal axis:

$$x' = x\cos\theta + y\sin\theta, \quad y' = y\cos\theta - x\sin\theta. \tag{4.7}$$

With these coordinates, the tensor is diagonalised by

$$K' = K, \quad L' = \sqrt{L^2 + M^2}, \quad M' = 0. \tag{4.8}$$

Orograpic slope (`OROSIG`). The slope parameter, σ, is defined as the mean-square gradient along the principal axis where the topographic variations are largest:

$$\sigma^2 = \overline{\left(\frac{\partial h}{\partial x'}\right)^2} = K' + L' = K + \sqrt{L^2 + M^2}. \tag{4.9}$$

Here, the smoothed gradients are used as before and oceanic grid cells are assigned as $\sigma = 0°$. The representation for the T63 grid is illustrated in Figure C.8.

Orographic anisotropy (`OROGAM`). According to the definition in Equation 4.1, the anisotropy, γ, is determined from the aspect ratio of the subgrid-scale orography:

$$\gamma^2 = \overline{\left(\frac{\partial h}{\partial y'}\right)^2}\ \overline{\left(\frac{\partial h}{\partial x'}\right)^{-2}} = \frac{K' - L'}{K' + L'} = \frac{K - \sqrt{L^2 + M^2}}{K + \sqrt{L^2 + M^2}}. \tag{4.10}$$

Again, the smoothed gradients are used and oceanic grid cells are assigned as $\gamma = 0$. The representation for the T63 grid is shown in Figure C.9.

Surface geopotential (`GEOSP`). Approximating the Earth as a regular sphere, the surface geopotential, Φ_s, ensues directly from the mean orography via $\Phi_s = g\overline{h}$, where $g = 9.80665\ {}^{m}/_{s^2}$. The representation for the T63 grid is presented in Figure C.10.

4.1.3. Surface

Snow reservoir (`SN`). All simulations of the Permian Earth are initialised without any snow cover.

Glacier mask (`GLAC`). As discussed in Section 2.5, there is no evidence for extended glaciation in the record of the Kazanian stage. Hence, the glacier mask is set to zero everywhere.

Surface background albedo (`ALB`). The surface background albedo, α, sets the reflection properties of snow-free surface and thus determines the energy budget with respect

to incoming and outgoing radiation. The colour of soil as well as the vegetation cover are crucial for the reflectivity. The vegetation contribution is a weighted combination of the albedo of leaves and stems [146]:

$$\alpha_{\text{veg}} = \alpha_{\text{veg}}^{\text{leaf}} w_{\text{leaf}} + \alpha_{\text{veg}}^{\text{stem}} w_{\text{stem}}, \tag{4.11}$$

where the weighting factors $w_{\text{leaf}} = {}^{L}/_{L+S}$ and $w_{\text{stem}} = {}^{S}/_{L+S}$ depend on leaf and stem area index, L and S. The soil albedo generally varies with water content of the soil near the surface, θ [146]:

$$\alpha_{\text{soil}} = (\alpha_{\text{sat}} + \Delta) \leq \alpha_{\text{dry}}, \quad \Delta = 0.11 - 0.40\theta > 0. \tag{4.12}$$

Both components are blended considering the vegetation ratio, c_v [140, 147]:

$$\alpha = c_{\text{veg}} \alpha_{\text{veg}} + (1 - c_{\text{veg}})\, \alpha_{\text{soil}}. \tag{4.13}$$

Water surfaces are assigned as $\alpha = 0.07$. The surface background albedo of the Permian Earth is based on the soil and vegetation distribution from Kiehl and Shields [8]. The representation for the T63 grid is shown in Figure C.11.

Surface roughness length (`AZ0`). Orographic smallest-scale structures as well as the texture and cover of the surface affect the generation of atmospheric turbulences in the boundary layer as they control the turbulent exchange of momentum, energy and moisture. The surface structures are parameterised in terms of surface roughness length, z_0. This consists of contributions from orography, z_{oro}, vegetation, z_{veg}, and urban areas, z_{urb}. According to Tibaldi and Geleyn [148], the different parts are added pythagorically:

$$z_0 = \sqrt{z_{\text{oro}}^2 + z_{\text{veg}}^2 + z_{\text{urb}}^2} \tag{4.14}$$

Obviously, the urban contribution is irrelevant for the Permian Earth. The orographic contribution attempts to involve structures as small as possible. That is why the parameterisation of Tibaldi and Geleyn [148] also takes account of subgrid-scale variances of the higher-resolution source grid. Their parameterisation can be written conceptually as:

$$z_{\text{oro}} = \sqrt{n_{\text{ridge}}^{\text{primary}}} \cdot \mu + \sqrt{n_{\text{ridge}}^{\text{sub}}} \cdot \mu_{\text{sub}}. \tag{4.15}$$

The first term of Equation 4.15 describes the roughness due to subgrid-scale structures that are originally resolved by the source grid. It is given by the variance μ of Equation 4.5 weighted by the number of relative maxima (number of grid cells of the source grid whose elevation is higher than that of the neighbour cells) per surface area. This can be derived directly from the original Permian elevation dataset. The second term of Equation 4.15 indicates the roughness due to subgrid-scale mountain ridges with respect to the source grid. For the Permian orography there is no further information on orographic structures below the $0.5° \times 0.5°$ grid. However, this contribution cannot be neglected as comparisons with the present-day surface roughness have shown. Therefore,

the number of subgrid-scale mountain ridges is constructed randomly but biased by high mean orography and orographic variance:

$$n_{\text{ridge}}^{\text{sub}} = \frac{2|\aleph|}{A} \cdot h^{0.4} \cdot \sqrt{\left(\frac{\partial h}{\partial x}\right)^2 + \left(\frac{\partial h}{\partial y}\right)^2}, \tag{4.16}$$

where A is the surface area of the source grid cell and $\aleph$ is a normally distributed random number. The subgrid-scale variance of the source is derived from the mean elevation via

$$\mu_{\text{sub}} = \frac{1}{4}\sqrt{\left(\left(\frac{\partial h}{\partial x}\right)^2 x^2\right)^2 + \left(\left(\frac{\partial h}{\partial y}\right)^2 y^2\right)^2 + 2\frac{\partial h}{\partial x}\frac{\partial h}{\partial y}xy}, \tag{4.17}$$

where x and y denote the side length of the grid cell.

The parameterisation of Equation 4.16 and Equation 4.17 have been optimised on the basis of the present-day orography. Subsequently, z_{oro} is averaged to the respective model grid. The roughness length over the oceans is calculated on-line in dependence on the wind speed. For lakes it is set to 0.0002 m. Size and shape of plants basically determine the roughness of vegetation. For parameterisation, the aerodynamic properties are expressed in terms of canopy height, z_{top}, and ratio of momentum roughness length to canopy top height, R_{z0m} [146]:

$$z_{\text{veg},j} = z_{\text{top},j} R_{z0m,j}. \tag{4.18}$$

Both parameters are available for various plant functional types f_j [146, 149]. Thus, the vegetation roughness can be assigned using the distribution of Permian vegetation from Kiehl and Shields [8]. The aggregation of different plant types is not straightforward but requires averaging of the corresponding drag coefficients [138, 140]:

$$\frac{1}{\ln^2\left(\frac{z_b}{z_{\text{veg}}}\right)} = \sum_j \left(\frac{f_{ij}}{\ln^2\left(\frac{z_b}{z_{\text{veg},j}}\right)}\right), \tag{4.19}$$

where $z_b = 100$ m is chosen as blending height. The representation for the T63 grid is illustrated in Figure C.12.

4.1.4. Vegetation

Leaf area index (`VLTCLIM`). The evapotranspiration of plants basically depends on the size of the leaf area, as the flow is controlled by small variable openings in the leaves of plants, i.e. the stomata. Moreover, the leaf area also indicates the precipitation interception capacity of a plant. That is why the leaf area index (LAI) , which is defined as the ratio of the leaf area to its projection at the ground, is an important parameter to determine the water budget at the surface. For our setup of the Permian vegetation,

the monthly climatology of LAI is directly borrowed from the setup of Kiehl and Shields [8]. An excerpt for the T63 grid is depicted in Figure C.17.

Vegetation ratio (`VGRATCLIM`). The vegetation ratio, c_{veg}, indicates the fractional area covered by plants within a grid cell. Here, only plants which are able to modify evapotranspiration by their stomata are considered. The monthly climatology is derived from the vegetation distribution of the Permian setup from Kiehl and Shields [8]. The contributions of all plant functional types (PFT) of the dataset are aggregated and the vegetated area fraction of the grid cell is subsequently determined. Furthermore, seasonal variations between growing and dormacy season are included [138, 139]. The corresponding modulation factor is tuned according to the seasonal variation of the LAI. An excerpt of the climatology of the vegetation ratio for the T63 grid is presented in Figure C.18.

Forest ratio (`FOREST`). The forest ratio, c_{forest}, indicates the fractional cover of trees, regardless of whether they actively perform photosynthesis or not. Thus, this parameter allows to consider the different behaviour of the snow albedo in forested and non-forested regions. The forest ratio for the Permian Earth is determined similarly to the vegetation ratio. However, the seasonal variation is omitted and all non-arborescent PFT are excluded. The representation for the T63 grid is shown in Figure C.13.

4.1.5. Soil

Soil water holding capacity (`WSMX`). The absorption of water by the ground is an important aspect of the hydrological cyle. In general, the amount of water that can be stored in the ground depends on the porosity but also on the composition of the soil. The rainfall-drainage scheme by Dümenil and Todini [150], that is employed by the EMAC framework and ECHAM5, assumes the storage capacity to be parameterised in terms of probability densities in order to take account of the heterogeneous distribution of soil capacity within a grid cell. The soil water holding capacity defines the maximal amount of water the ground can store. This parameter is given by the field capacity W_{cap} that indicates the amount of water retained in an originally saturated soil by capillary forces after several days of drainage [138]. The global distribution of soil capacity is relatively uncertain for the present-day Earth and is even more obscure for the Permian. Therefore, a generic mean field capacity of $W_{\text{cap}} = -10$ kPa is assumed [151] all over Pangaea. Given a mean sand content of about 43% (soil composition data of Kiehl and Shields [8]), this corresponds to a water column of 1.109 m. The representation for the T63 grid is illustrated in Figure C.16.

Plant available water capacity (`WS`). As plants cannot access the entire amount of water stored in the ground, the soil water holding capacity is pointless estimating the water flow from plants to the outside air. For this reason, the plant available water capacity, W_{ava}, is additionally required by the model. This hydrological parameter is

defined as the maximum amount of water that plants can extract from the soil before they start to wilt. Again, there is no information for the Permian Earth. That is why W_{ava} is estimated according to the total water content from the monthly climatology of soil moisture by Kiehl and Shields [8]. The representation for the T63 grid is presented in Figure C.15.

Soil type (`FAO`). The energy budget at the Earth's surface is also affected by the thermal properties of the soil. Both, the heat capacity and heat concuctivity of the soil, depend on the composition of the soil with respect to sand, clay, and silt content. The parameterisation of EMAC and ECHAM5 distinguishes between five soil classes with different mixing ratios of sand and clay. According to the Canadian system of soil classification [152], 'Sand' (`FAO` = 1) is assigned for soil that contains 85% or more sand, whereas 'sandy loam' (`FAO` = 2) corresponds to soil that contains 7-20% clay and more than 52% sand. 'Loam' (`FAO` = 3) consists of 7-27% clay and less than 52% sand, and 'clay loam' (`FAO` = 4) is assigned when the soil contains 27-40% clay and 20-45% sand. 'Clay' (`FAO` = 5) corresponds to soil with more than 40% clay and less than 45% sand. Each class is assigned to specific values of the thermal parameters [153]. The dataset of Kiehl and Shields [8] contains soil data of sand and clay content which can be transformed directly to the five soil classes. However, they simply assume moderate mixing ratios all over Pangaea that corresponds to 'Loam'. The representation for the T63 grid is depicted in Figure C.14.

4.1.6. Waterflow

The HD submodel requires some additional information that characterises the retention properties and the main direction of riverflow. Based on the orography and the distribution of lakes and glaciers, Stefan Hagemann kindly constructed a dataset comprising the retention parameters, k, for all three types of waterflow, the number of linear reservoirs within a cascade of riverflow, n, and the river direction for the Permian Earth. The parameters are given on a $0.5^\circ \times 0.5^\circ$ grid. The grid cell area as well as the sea-land mask are additionally included in the HD input data.

4.2. Grid and Model settings

4.2.1. Model grids

For the simulation of Permian climate, a horizontal grid with T63 truncation and 31 vertical levels within the atmosphere is used for EMAC. The model time step has been chosen as $\tau = 600$ s. However, a coarser grid has been applied for multi-millenial 'spin-up' in order to reduce the computation time. Here, a T31 and T21 grid have been used with a time step of $\tau = 1800$ s and $\tau = 2400$ s, respectively (see Table 3.1).

The curvilinear Arakawa C-grid for the ocean domain is generated by means of MPIOM grid tools. It consists of 122×101 horizontal grid cells (GR30 Standard) and 20 vertical levels. The vertical levels are not uniformly distributed, but the layer thickness increases with depth. More precisely, the shallow regions up to a depth of 600 m are covered by 10 levels and the remaining levels cover the deep sea up to 6,000 m. The two grid poles are placed at Central Angara and Southern Gondwana. Consequently, the Tethys Ocean is resolved more finely than the extensive Panthalassic Ocean. The grid is illustrated in Figure 4.1. The ocean time step is $\tau = 2$ hours.

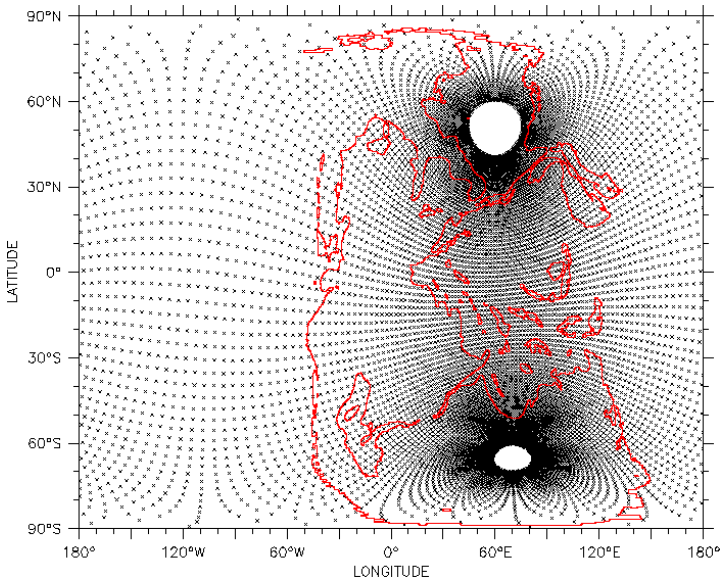

Figure 4.1.: Arakawa C-grid for ocean discretisation used by MPIOM submodel for Permian topography. The poles are located at 50° N 60° E in central Angara and at 65° S 70° E in Southern Gondwana. The grid has a horizontal resolution of 122×101 grid cells (GR30 Standard) and consists of 20 vertical levels. Apart from the continental margins a flat bathymetry at 4,000 m depth is assumed. The sea-land mask is revised in order to allow for water flow in narrow straits despite the coarse resolution of the ocean model.

Due to subduction there is no information available on the Permian ocean floor. That is why a flat bottom bathymetry at a depth of 4,000 m with smoothed continental margins is chosen in accordance with Winguth et al. [27]. Although the presence of ocean ridges significantly affects the ocean circulation [23], their location would only be speculative. Hence, they are not considered for all simulations of this work.

Narrow straits are not resolved and have to be exaggerated manually after grid generation to ensure water flow. Furthermore, the coupling of ocean, surface, and lake domain within the `A2O` submodel has been adapted. Originally, lakes within coastal grid cells have not been considered as water surfaces. This caused a constant temperature rise of the ocean at this point because the relation of water and land has not been correct. By

means of a proper weighting of land, lake, and ocean fraction, the overheating has been fixed.

4.2.2. Atmospheric composition

As it is discussed in Section 2.3, the composition of the Permian atmosphere is not well known and reconstructions by models and proxies contain rather large margins of error. Nevertheless, the simulation with EMAC requires specific values for the concentrations of various gases.

As the increase of atmospheric carbon dioxide is one of the most prominent changes affecting the Permian climate, several scenarios of carbon dioxide concentrations are considered in the simulations of Permian climate (see Table 4.1). The concentrations

Scenario	$1\times CO_2$	$2\times CO_2$	$4\times CO_2$	$6\times CO_2$	$8\times CO_2$	$10\times CO_2$
CO_2 content [ppm]	355	710	1420	2130	2840	3550

Table 4.1.: Atmospheric carbondioxide content for different scenarios of Permian atmosphere. The concentration is varied covering the range of the reconstructed increase in the course of the Permian (see Section 2.3.1) and the assumptions of Kiehl and Shields [8]. The denomination is related to the present concentration.

of all other gases in the atmosphere are set as constant. The oxygen concentration (O_2) is a fixed value in EMAC since all submodels dealing with atmospheric chemistry are excluded. The concentration corresponds to the present-day atmosphere. The meridional distribution of atmospheric ozone is approximated to the idealised symmetric distribution of an aqua-planet setup which better reflects the north-south symmetry of Permian topography compared to the present-day asymmetric distribution. More precise information about Permian ozone concentrations has not been available. The assumptions for greenhouse gases basically follow Kiehl and Shields [8]. The assumed methane concentration is also confirmed by the simulation results of Beerling et al. [56] for the Kazanian stage (see Section 2.3.3). The greenhouse gas concentrations for our simulation are assumed as follows: methane (CH_4): 0.7 ppm, and nitrous oxide (N_2O): 0.275 ppm. Hence, the assumed methane content approximately corresponds to the half of its present-day value and the nitrous oxide content is only slightly smaller. The Permian atmosphere is assumed as free of chlorofluorocarbons and aerosols.

4.2.3. Earth's orbit and solar luminosity

Earth's orbit. Section 2.4.3 points out that variations of the eccentricity, obliquity, and the precession of the Earth's orbit in the course of the Milankovitch cycle have a significant impact on the climate. However, with respect to geological time scales the Milankovitch fluctuations merely appear as small fluctuations around a mean climate.

The compilation of geological records that are used as climate indicators for evaluation also covers a long period and, therefore, most likely reflects the mean climate state of that epoch and no specific orbital configuration. In general, this work is aimed at simulating the climate of Permian epochs as realistic as possible. The simulations rather correspond to a time slice experiment and are not supposed to represent the temporal development of climate over a certain period. That is why the orbital parameters are fixed to a specific orbit. For the sake of simplicity, the orbital parameters of the present day are chosen.

In order to estimate the impact of Milankovitch fluctuations, different scenarios with extreme values for eccentricity, obliquitiy, and precession are considered, too. The scenarios are summarised in Table 4.2.

Scenario	standard	$e_{\min}$	$e_{\max,90}$	$e_{\max,270}$	$\theta_{\min}$	$\theta_{\max}$	ave
Eccentricity e	0.0167	0.0050	0.0700	0.0700	0.0167	0.0167	0.0280
Obliquitiy θ	23.44°	23.44°	24.50°	24.50°	22.10°	24.50°	23.30°
Perihilion ω	282.9°	282.0°	90.0°	270.0°	282.9°	282.9°	0.0°

Table 4.2.: Orbit parameters for simulation of Permian climate. The first column shows the standard setup which corresponds to the present-day orbit. For some simulations, eccentricity, obliquitiy, and the longitude of perihilion are also modified in order to estimate their impact. For each parameter a minimum, average, and maximum scenario is considered.

The $\theta_{\min}$ and $\theta_{\max}$ scenario describe the case of minimal and maximal axis tilt, respectively, but with present-day orbit around the sun. In contrast, the $e_{\min}$ scenario considers the present-day axis tilt and a minimal eccentricity. Both the $e_{\max,90}$ and $e_{\max,270}$ scenario represent the case with maximal axis tilt and maximal eccentricity. Here, the $e_{\max,90}$ scenario considers a perihilion during northern summer season, whereas $e_{\max,270}$ corresponds to a perihilion in southern summer. The latter is the most extreme scenario for the Permian topography where most of the land is located on the Southern hemisphere. Furthermore, medium conditions are assumed for the 'ave' scenario.

Palaeorotation. Although the rotation of the Earth around its axis has been faster in the Permian than at present (see Section 2.4.2), this aspect is not considered in this work. On the one hand the change is only small and on the other hand the Earth's rotation is deeply hard-coded in EMAC. That is why it cannot be changed without extensive modifications of `TIMER` and numerous process and diagnostic submodels. The present rotation rate is therefore also assumed for the Permian Earth.

Solar luminosity. As discussed in Section 2.4.1, the solar luminosity was weaker in the Permian than at present. Therefore, the luminosity parameter in EMAC is set to $S_0^{\mathrm{P}} = 1329.5\ {}^{W}/_{m^2}$ which corresponds to a reduction of 2.6% [62]. The control run and all present-day simulations assume $S_0 = 1365\ {}^{W}/_{m^2}$.

4.3. Initialisation

In addition to the land surface and bathymetry parameters defining the boundary conditions, the EMAC framework requires global data of all prognostic variables that set the initial state of atmosphere and ocean. In contrast to a simulation of the present-day climate, this data is mostly unknown for palaeoclimate simulations. Thus, the ESM is initialised with an arbitrary general state and subsequently balanced in a 'spin-up' period until the coupled system of atmosphere and ocean has reached radiative equilibrium (see Section 4.4).

For initialisation of our Permian climate simulation, surface and soil water reservoirs are assumed as empty, and the prognostic variables of the atmosphere, i.e. vorticity, divergence, temperature, humidity, and surface pressure, are set to the initial state of the aqua-planet setup. However, this choice of initial state has no effects in the long run since the atmosphere quickly adapts to the new circumstances. The far slower ocean circulation prevents a fast adaption of the ocean and the initial state is conserved especially in the deep ocean for several centuries. In order to shorten the spin-up period of the Permian setup, the ocean variables, temperature and salinity, are not initialised with a constant value throughout the entire ocean but depending on depth. For each ocean level both parameters are assigned to the global mean of the present-day ocean as approximation. That way the state of the deep ocean is already closer to the equilibrium state, although horizontal differences are not included yet. The initial state of atmosphere and ocean is the same for all CO_2 scenarios.

4.4. Spin-up: From Initialisation to Equilibrium

At the first phase of spin-up a T21L19 grid is chosen for the atmosphere. The resolution of this grid is sufficiently coarse to reduce the computation time significantly, but also sufficiently fine to resolve the main processes that drive the global climate. As the MPIOM submodel is merely called once a day, it negligibly affects computation time and the GR30L20 ocean grid is always employed.

In the course of the spin-up, the coupled system of atmosphere and ocean adapts to the new boundary conditions of the Permian Earth and approaches the radiative equilibrium state. In a balanced model the energy of incoming radiation equals the energy of outgoing radiation on a global average over a longer period. Moreover, the mean annual global temperature remains stable for all atmosphere and ocean layers over a period of several years and only small fluctuations occur. However, the balance is not perfectly realised in EMAC. That is why the radiation budget at the top of the atmosphere is not completely equalised in the equilibrium state and a net radiation balance between 0 and 2 $^{W}/_{m^2}$ is rated as sufficient [154, 155].

The adaption of the ocean to the new circumstances is the bottleneck of the spin-up as ocean circulation is relatively slow. Starting from the uniform temperature in all layers, an equator-to-pole gradient quickly arises in near-surface ocean layers and the cooling in high latitudes causes vertical destratification, i.e. the circulation gets started. Depending on the CO_2 scenario, the deep ocean gradually warms up or cools down compared to the present-day initial value. Whereas near-surface layers adapt to changed temperature conditions within a few years, transitions in the deep ocean proceed very slowly and continue for several centuries of simulation. Thus, the spin-up period is subdivided into three phases: the atmospheric response stage (1-2 months), the surface ocean-atmosphere coupling stage (about 3 years), and the deep ocean response stage (about 1,000 years and longer) [156].

The spin-up on the T21L19 grid has been continued for 2,500 years. At this stage the mean annual ocean temperature is predominantly stable in all layers. For the colder scenarios the sea surface is extensively covered by ice (up to 40°N and S for the $1\times CO_2$ scenario) and there is still persistent ice coverage at the North Pole for the warmest scenario. Near the equator the temperature maximum is between 16°C and 30°C, respectively. The temperature of the deep ocean varies between -1.7°C for the $1\times CO_2$ scenario and 5.0°C for the $10\times CO_2$ scenario. The warming of the deep ocean for both the $8\times CO_2$ and $10\times CO_2$ scenario is still ongoing whereas the deep ocean has stabilised in a cold state for the others cases.

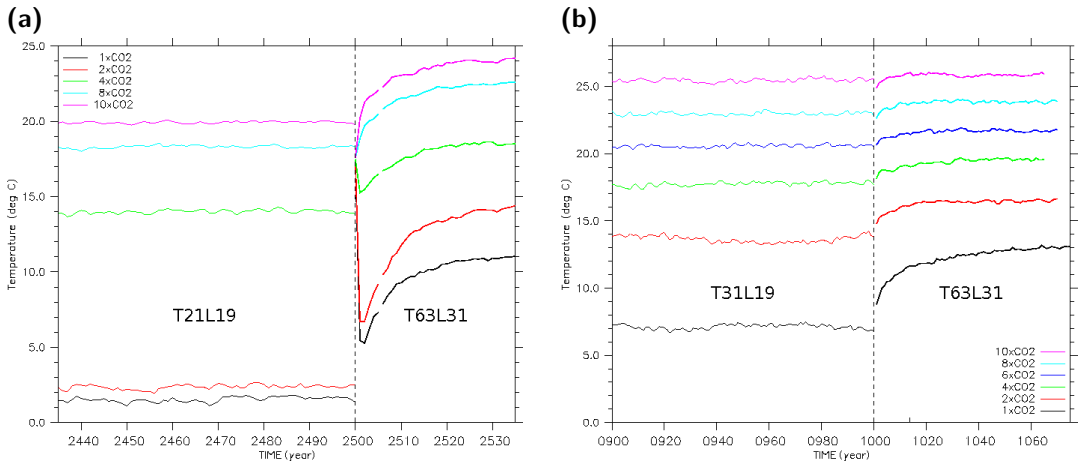

Figure 4.2.: Grid transition from (a) T21L19 and (b) T31L19 to T63L31 at the end of spin-up after 2,500 and 1,000 years of simuation, respectively, when the equilibrium state has been reached. The temporal development of mean annual global surface air temperature is shown for the $1\times CO_2$, $2\times CO_2$, $4\times CO_2$, ($6\times CO_2$), $8\times CO_2$, and $10\times CO_2$ scenario. The
For grid transition, the state of the ocean is retained and the atmosphere domain is restarted again.

For grid transition from T21L19 to T63L31, the ocean state at the end of spin-up is retained and a new simulation with EMAC-MPIOM is initialised on the new atmospheric

grid. This procedure is necessary because direct interpolation of the restart information to the new atmospheric grid is not possible. The general idea is to continue with another short spin-up period to make the atmosphere adapt to the ocean of the previous equilibrium state. Subsequently, the simulation is continued for another 30 years for analysis. Figure 4.2(a) shows the temporal development of mean annual global surface air temperature before and after the grid transition for all CO_2 scenarios.

All temperature curves show only very small fluctuations within the last 60 years of spin-up on the T21L19 grid. At the grid transition the atmosphere has to be reinitialised again, since the model variables can not be interpolated directly to the T63L31 grid. The coupled system of atmosphere and ocean is stabilised after another 20 years of simulation. However, this equilibrium state is totally different to the previous. The grid transistion caused a tremendous impact on the physical stability of the coupled system. This gets particularly obvious by the significant increase in temperature as shown in Fig. 4.2(a): about +12°C for the colder scenarios ($1\times CO_2$ and $2\times CO_2$), and about +4°C for the warmer scenarios ($4\times CO_2$, $8\times CO_2$, and $10\times CO_2$). The mean global temperature generally depends on the radiative equilibrium. The inconsistency is caused by the implementation of the radiative forcing related to parameterised subgrid-scale processes and the insufficient optimisation of free parameters with respect to the grid resolution. Most of the processes that determine the density and thickness of clouds, but also the cloud cover in general, depend on subgrid-scale parameterisation. However, especially the cloud radiative forcing has a significant impact on the position of the equilibrium. Sea ice cover in high latitudes further amplifies the climate variability due to the ice-albedo feedback [157, 158]. That is why the cold $1\times CO_2$ and $2\times CO_2$ scenarios are affected most.

The optimal tuning of all free parameters is generally less important for an uncoupled GCM with prescribed SST because of the strong additional forcing. In contrast, a free-running coupled atmosphere-ocean GCM is relatively sensitive to the parameter tuning, especially for a long simulation period. Kern [155] performed a parameter optimisation for EMAC-MPIOM on a T42L47MA grid. In the course of the described procedure, he varied the correction factor for asymmetric radiation scattering, cloud homogeneity factors, the fraction of convective mass flux above the level of non-buoyancy, the conversion rate from cloud water to rain, the entrainment rate for shallow convection, and the accretion of cloud droplets by precipitation. He attempts to achieve minimal net radiation flux at the top of the atmosphere, realistic global surface temperatures, and reasonable results for cloud cover and water paths. However, the optimal tuning for all parameters within the parameter's uncertainty range is, to some extent, arbitrary. Moreover, the optimal tuning eventually depends on the grid size, general model settings, and the climate state of the Earth. Proceeding analogously for a palaeosetup is virtually impossible. In default of suitable data the ESM needs to be tuned for present-day conditions. A test simulation with EMAC-MPIOM on a T21L19 grid for a present-day setup shows that the ESM is far from being optimised: almost the entire Earth is frozen after 50 years of simulation (not shown). However, the optimisation is a

lengthy procedure and not part of this work. Therefore, the next finer atmospheric grid, i.e. T31L19 (see Tab. 3.1), is chosen that has been proven in the studies of Pozzer et al. [98]. A simulation with EMAC-MPIOM testing the transition from T31L19 to T63L31 grid after 200 years of simulation for present-day conditions shows a satisfying behaviour. Here the mean annual global temperature is merely reduced by 0.35 K, which is within the range of interannual variability.

The model spin-up is subsequently continued on a T31L19 grid for another 1,000 years of simulation. The ocean state is retained from the previous spin-up period, as this is presumably closer to the equilibrium state than the initial state, and the atmosphere model is reinitialised as before. The three response stages of spin-up are undergone again as described before. At the end of this 1,000-year spin-up simulation the deep ocean response is still active for ocean layers deeper than 1,000 m, but only a very slight warming of the deep ocean is observed for the $4\times CO_2$, $6\times CO_2$, $8\times CO_2$, and $10\times CO_2$ scenario. Studying the atmosphere-ocean coupling, Liu et al. [156] have shown that the SST and air temperature are virtually not affected by this evolution. Except for small interannual fluctuations there are no further temperature evolutions within all atmospheric layers as well as near-surface and intermediate ocean layers, i.e. from this point of view the equilibrium is reached. The same is true considering the net radiation flux at the top of the atmosphere (TOA). As described above energy conservation is not perfectly implemented in EMAC and the balance of incoming and outgoing radiation thus deviates from zero in equilibrium. Table 4.3 lists the average radiation imbalance for each scenario. For all cases the imbalance lays within the sufficient range. For comparison Jöckel et al. [159] observed a noticeably larger radiation imbalance of 1.375 W/m^2 for their simulation with EMAC-MPIOM using a present-day setup and optimised parameters.

$1\times CO_2$	$2\times CO_2$	$4\times CO_2$	$6\times CO_2$	$8\times CO_2$	$10\times CO_2$
0.55 ± 0.05	1.02 ± 0.06	1.17 ± 0.06	1.37 ± 0.06	1.28 ± 0.06	1.38 ± 0.06

Table 4.3.: Net radiation imbalance at TOA [W/m^2] for radiative equilibrium state at end of spin-up for various CO_2 scenarios. The radiation flux is averaged globally and annually. The last 50 years of spin-up are considered and additionally the respective standard error is given.

In addition the climate state at the end of the spin-up process needs to be checked for its uniqueness. Due to the complex structure of an ESM, the simulated climate state does not converge necessarily to a unique climate state in the course of spin-up, but depending on the initial state several attractors are possible [156]. Furthermore, the convergence can be non-monotonic and hysteresis-like behaviour can appear. The test is performed exemplarily for the $2\times CO_2$ scenario. Two different initial ocean states are chosen where one is the ocean state after 2,500 years of simulation on a T21L19 grid (see above) and the other is the original uniform initial state that has been described in Sect. 4.3. The comparison of the respective final state after 1,000 years of spin-up simulation is shown in Fig. 4.3.

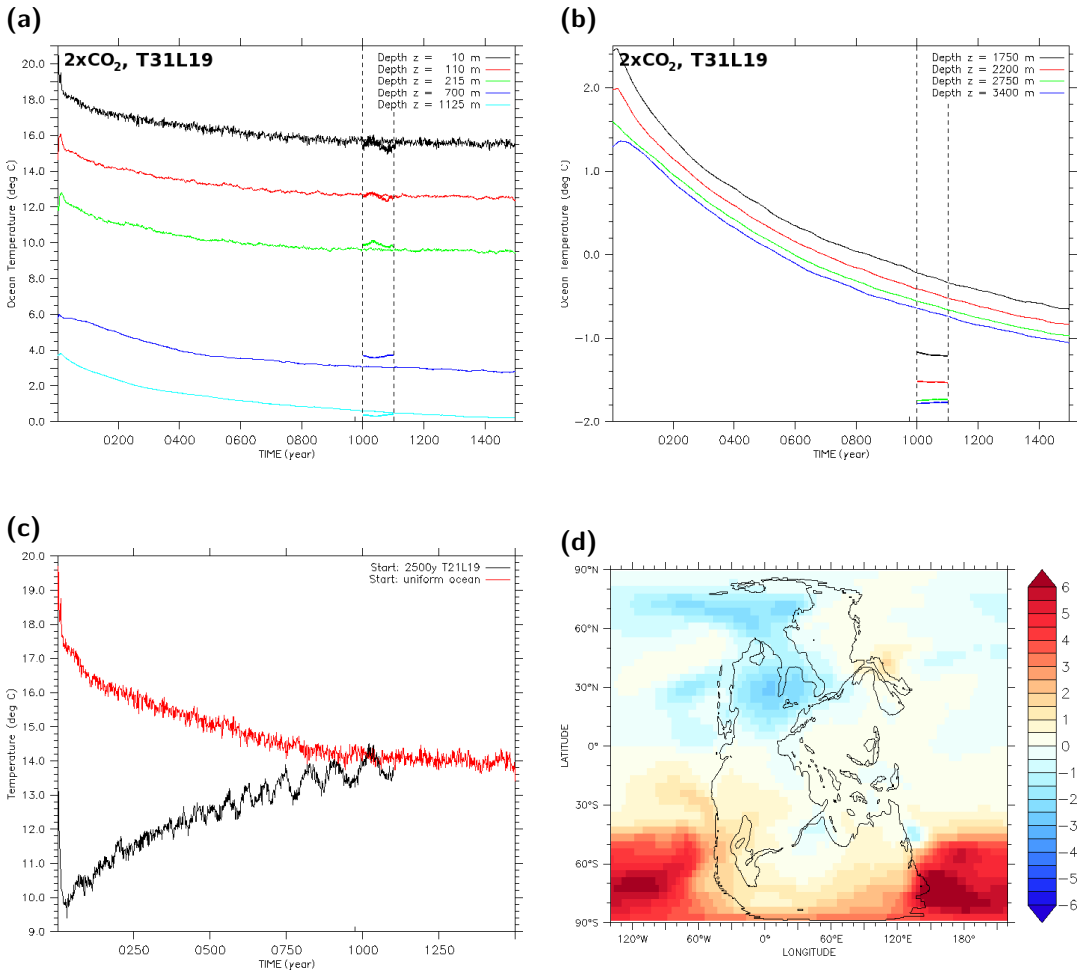

Figure 4.3.: (a) Temporal development of mean annual ocean temperature for several depth levels up to 1,125 m for $2\times CO_2$ scenario. The ocean has been initialised with uniform temperature layers and the simulation has been continued for 1,500 years. For comparison, the ocean temperature of the simulation that has been started after 2,500 years of simulation on a T21L19 grid and continued for further 1,000 years on a T31L19 grid is overlaid. (b) The same as before but for deep ocean levels. (c) Temporal development of mean annual surface air temperature for both scenarios. The black line corresponds to the simulation that continues the 2,500-year spin-up on a T21L19 grid and the red line corresponds to the simulation initialised with uniform ocean layers. (d) Mean difference of mean annual surface temperature [K] of both scenarios for time intervall between 1,000 and 1,100 years of spin-up.

The two upper panels, Fig. 4.3(a) and (b), show the temporal evolution of mean global ocean temperature for several ocean layers. The temperature curves of the uniformly-initialised ocean are depicted for the entire spin-up period. The corresponding curves of the combined T21/T31-spin-up are overlaid for one century at year 1000. In near-surface and intermediate ocean layers (Fig. 4.3(a)) the mean global temperature of both simulations match well. In contrast, the temperature clearly mismatches in the deep ocean (Fig. 4.3(b)). The deep ocean response is still ongoing at this stage, but the extrapolated curves seem to converge. That is why the match of both equilibrium ocean states is still satisfying. The temporal evolution of the mean annual surface air temperature of both simulations is plotted in Fig. 4.3(c). The convergence of both simulations to a similar atmosphere state can be observed clearly after 1,000 years of spin-up simulation. Thus, the simulated Permian climate seems to be unique for the EMAC-MPIOM model and the prolonged spin-up simulation has proved essential for a balanced climate state. Whereas the discussion has focussed so far on the global mean, regional differences are considered in Fig. 4.3(d). Here the local difference of surface air temperature is shown for the last phase of spin-up simulation. Although the global mean temperature of both simulations agree, there are significant disparities especially over the ocean in high southern latitudes. East of Southern Gondwana the discrepancy is more than 6 K and over Southern Panthalassa it is still about 4 K. At this stage the hysteresis-like response of the climate system to the forcing of palaeoenvironment is the critical factor. For the uniformly initialised ocean (red curve in Fig. 4.3(c)) there is no sea-ice at the beginning and nearly no sea-ice in Southern Panthalassa at the end. In contrast, the other simulation (black curve) has been started with extended sea-ice in both hemispheres and there is still ice coverage in most parts of Southern Panthalassa at the end of spin-up. Due to the ice-albedo feedback, ice buildup or melting has been suppressed and the temperature discrepancy is significantly amplified. This effect is minimal in the Northern Hemisphere as there is ice coverage in both cases. The difference in low latitudes is negligible.

The grid transition from T31L19 to T63L31 has far less impact on the simulated climate. The behaviour of mean annual global temperature is illustrated in Fig. 4.2(b) for each sceanario. The offset is significantly reduced: for the $10\times CO_2$ scenario there is virtually no difference. The $8\times CO_2$ and $6\times CO_2$ scenario exhibit a warming of 1 K, the $4\times CO_2$ and $6\times CO_2$ scenario warm about 2 and 3 K, respectively, whereas in the $1\times CO_2$ scenario the temperature is still increased by about 5 K. Again, the ice-albedo feedback induces the pronounced warming of the colder scenarios. Apart from the $1\times CO_2$ scenario the model behaviour during grid transistion is satisfying and the offset is mainly insignifacant compared to other uncertainties of palaeoclimate modelling.

The simulations are subsequently proceeded for another 40 years (45 for the $1\times CO_2$ scenario) on the T63L31 grid in order to adapt to the new grid and, eventually, for another 30 years for diagnostics. All scenarios with different orbital configurations are treated analogously to the $4\times CO_2$ scenario during spin-up. The scenario employing the Zhang-McFarlane-Hack convection scheme is first started with the Tiedtke convection

scheme. The convection scheme has been merely changed for the last 300 years of spin-up. Similarly, the dynamic vegetation submodel is coupled after 500 years of spin-up simulation with prescribed default vegetation. The spin-up is then proceeded for another 200 years. For each CO_2 scenario the resulting vegetation is used as prescribed vegetation in an additional diagnostic simulation.

5

Permian Climate

The essential features of Permian climate are strong seasonality, strong monsoon circulation, very dry conditions in the continental interior, very hot temperatures in the desert belt, and very cold temperatures in high-latitude Gondwana. They are indicated by sedimental and palaeobotanical data (see Section 2.5) and generally confirmed by numerous simulations (see Section 2.6). The Permian climate as simulated by EMAC-MPIOM is analysed in this Chapter. In accordance with the modelling results of Berner and Kothavala [4] and proxy reconstructions of Royer [5] (see Section 2.3.1) the $4\times CO_2$ scenario is chosen as reference scenario. At first the mean global climate as well as regional characteristics are described in Section 5.1. Subsequently, the climate sensitivity to atmospheric carbon dioxide content, convection parameterisation, dynamic vegetation, and the impact of astronomical variations in the course of the Milankovitch cycle are estimated in Section 5.2. Potential error sources and uncertainties are discussed in Section 5.3. For evaluation, the simulated climate is eventually compared with simulations of other models and the reconstructed data-based biome distribution of Rees et al. [73] and Ziegler [76] in Section 5.4.

5.1. Mean Permian Climate

This section surveys the mean climate state of the Permian Earth for the $4\times CO_2$ scenario as simulated with EMAC-MPIOM. On the one hand the global distributions of annual mean temperature and precipitation are described. On the other hand the seasonal behaviour of temperature, precipitation, surface pressure, and the mean horizontal wind field are analysed. For a comprehensive description, the ocean surface is characterised with respect to mean SST and surface circulation at the end of this Section.

5.1.1. Temperature

The globally averaged annual mean temperature of the Permian Earth for the $4\times CO_2$ scenario is 18.4°C. Its global distribution is illustrated in Figure 5.1.

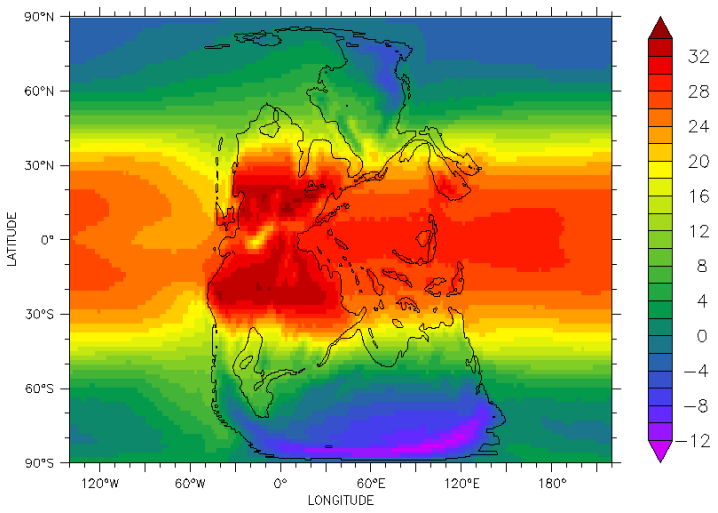

Figure 5.1.: Annual mean surface air temperature [°C] for $4\times CO_2$ scenario.

Due to its extensive landmass, Gondwana exhibits the most extreme temperatures. In polar latitudes, south of the polar circle, the mean annual temperature is below 0°C in most regions of Gondwana. The South Gondwanan Mountains in the very southeast are the coldest region on the Permian Earth for the $4\times CO_2$ scenario on annual average. There the higher altitude lowers the temperature by some degrees compared to the adjacent plains and thus it is the only region where the mean annual temperature is below −10°C. The giant lake in central Western Gondwana, the Paraná-Karoo-Inland Sea, leads to more moderate temperatures. In mid-latitudes the mean annual temperature gradually increases from 0°C at 60°S to about 10°C at the Tethys coast or even 20°C in the continental interior of central Gondwana. The low-latitude regions of Gondwana are characterised by severe heat with maximum annual mean temperatures of about 34°C near the Tropic of Capricorn in the continental interior. The temperature decreases slightly to about 30°C towards the equator. Near the equator the Appalachian Mountains are a cooler than the adjacent plains. In Cimmeria the mean annual temperature is about 26°C and in South- and Indochina it is a little warmer with 28°C on average. The temperature distribution in Laurasia is generally similar to Gondwana but less extreme. The low-latitude regions of Euramerica exhibit mean annual temperatures between 28 and 32°C in most areas. However, at some places the annual mean temperature also reaches 34°C. In Cathaysia and Laurentia the mean annual temperature varies between 26°C in the south and 10°C in the north, whereas Baltica still has a mean temperature of 16°C at its northern coast. In the southern part of Angara the annual mean temperature is about 20°C. It decreases

gradually to about 4°C at the polar circle and −2°C at the island arc at the northern margin. The mountains in the northeast are the coldest area of Angara with annual mean temperatures of about −4°C.

The distribution of annual mean temperature provides a first approximation to the climatic conditions. However, for a more comprehensive description, variations throughout the year have to be analysed as well. Figure 5.2 shows the seasonal mean temperatures for all four seasons.

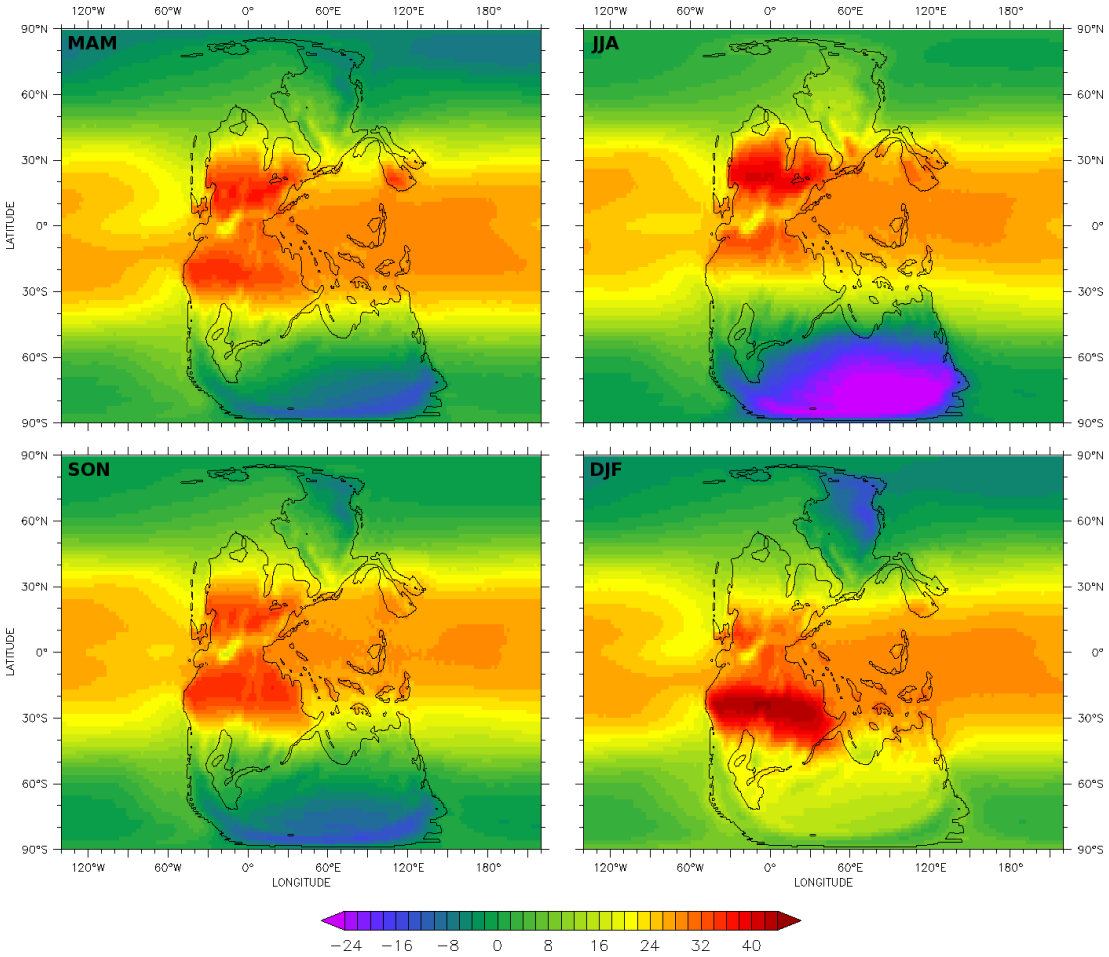

Figure 5.2.: Seasonal mean surface air temperatures [°C] for 4×CO_2 scenario for all four seasons: March-May (MAM), June-August (JJA), September-November (SON), and December-February (DJF).

As expected seasonal temperature variations are small in the equatorial regions of Pangaea and the South- and Indochinese microcontinents. The temperature fluctuation is mostly smaller than 2 K. In the adjacent northern and southern low-latitude regions of Euramerica and Gondwana the seasonal mean temperature varies between 40°C in summer and 24°C in winter, or 44°C and 24°C, respectively. Due to its location in the

Tethys Ocean, Cimmeria exhibits smaller seasonal temperature differences with 32°C in summer and 20°C in winter. In northern mid-latitude regions the mean summer temperature stretches from 12°C in Northern Laurentia and Cathaysia to about 30°C in Northern Baltica and Southern Angara. In contrast, mean winter temperatures are between 6 and 10°C. Seasonal temperature differences are similar for mid-latitude Gondwana. There the temperature fluctuation is about 20 K, with 24°C in southern summer for both, the Tethys coast and the continental interior, and 4°C in winter. The seasonal temperature difference is huge for high-latitude Gondwana: the mean winter temperature is merely −26°C in most of Southern Gondwana and in summer the temperature reaches 10 to 12°C on seasonal average. The Paraná-Karoo-Inland Sea moderates this difference significantly and induces higher winter temperatures. As Angara is far smaller, seasonal temperature differences are not as distinct in northern polar regions. There the average temperature varies between 4°C in summer and −12°C in winter. Thus, the continental interior of Southern Gondwana shows the largest seasonal temperature difference of about 40 K. The spring and autumn season represent a transitional state between summer and winter and are not discussed seperately at this point.

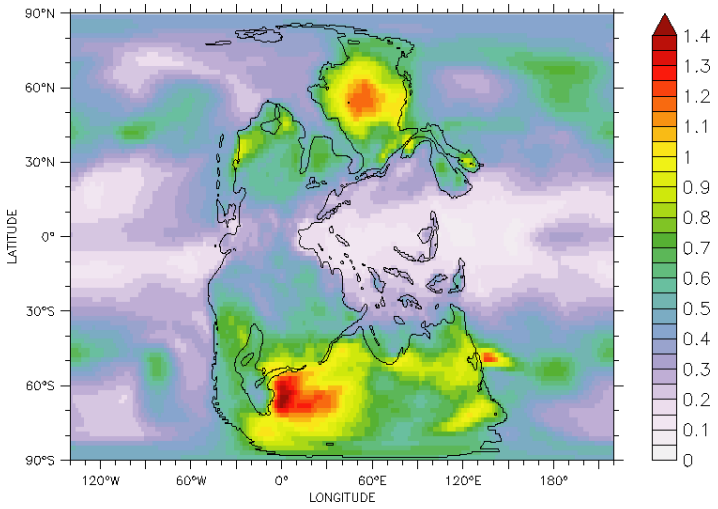

Figure 5.3.: Interannual variability of annual mean surface air temperature in terms of standard deviation [°C] for 4×CO_2 scenario.

In addition to the examination of seasonal temperature fluctuations, analysing the interannual variability reveals whether there are strong fluctuations within the diagnostic period and how well the mean climate represents the actual annual mean of the respective years. Figure 5.3 shows the standard deviation of the annual mean surface temperatures with respect to the 30-year diagnostic period. The interannual variability of the surface temperature is smaller than 1 K in most regions and thus significantly smaller than seasonal variations. It is especially small (< 0.4 K) in near-equatorial regions of Pangaea and on the Tethysian microcontinents which corresponds to about 20% of the seasonal

variation of about 2 K. It increases slightly further to the North and South and lies between 0.6 and 0.8 K in most regions of Northern Gondwana, Southern Euramerica, and Cathaysia up to 40° of latitude. The strongest interannual variability occurs between 40 and 70° of latitude in the continental interior in both hemispheres. Central Gondwana exhibits a variability of 1.4 K east of the Paraná-Karoo-Inland Sea and the variability is slightly smaller in Central Angara (1.2 K). However, the internannual variability is very small compared to the seasonal variability of about 18 K in Angara and 40 K in Gondwana in the same regions. The monthly breakdown (not shown) reveals that the variability of these areas is significantly larger for winter months and that is why small differences of temperature and snow coverage are most likely amplified by the ice-albedo feedback.

5.1.2. Precipitation

The climate is further characterised by the total annual precipitation amount and its seasonal distribution. Figure 5.4 shows the global distribution of integrated annual precipitation flux (Figure 5.4(a)) as well as the balance of precipitation and evaporation (Figure 5.4(b)).

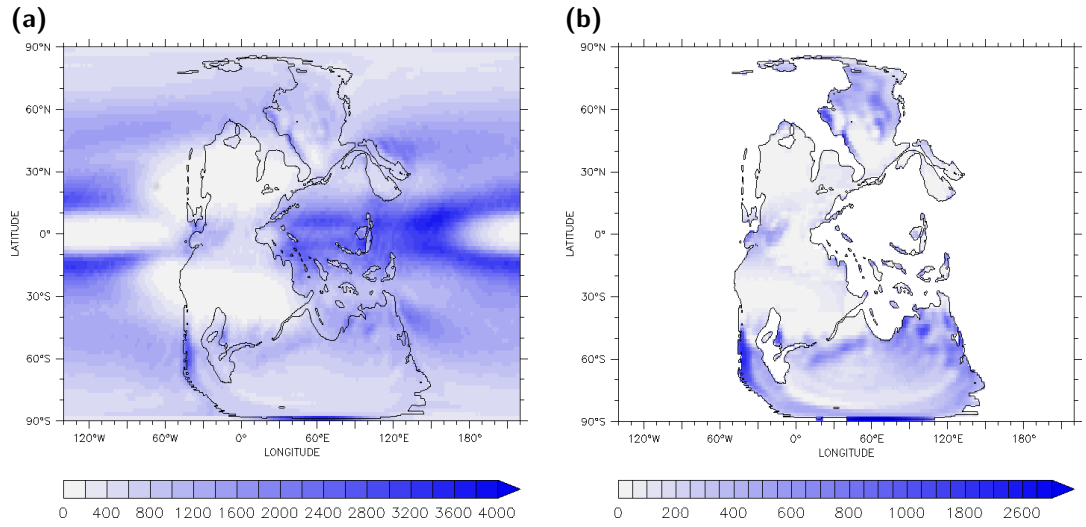

Figure 5.4.: (a) Integrated annual precipitation [mm] and (b) annual precipitation and evaporation balance, $P - E$, [mm] for $4\times CO_2$ scenario.

The global precipitation distribution clearly agrees with the expectations that the precipitation is not distributed equally on the Permian Earth, but concentrated in a wide band close to the equator around the Inter-tropical Convergence Zone (ITCZ). In the west of the Panthalassic Ocean, east of South- and Indochina, there is the region with the highest annual precipitation amount of about 3,600 mm. Beyond this region of

maximum precipitation the band is split into a northern and a southern part over the rest of the Panthalassic. Thus, the precipitation pattern seems to represent a double ITCZ that is a known bias in coupled GCM [160]. The southern part exhibits slightly more precipitation throughout the year, about 3,000 mm, whereas there is merely 2,600 mm in the northern part. The two parts are seperated by about 20° of latitude and there seems to be virtually no precipitation in between. This phenomenon also occurs over the Tethys Ocean, however less distinct with about 2,400 mm of annual precipitation in the splitted band and still about 1,800 mm in between. In South- and Indochina annual precipitation ranges from 1,200 to 1,800 mm. Over the Pangaean continent there is considerably less precipitation near the equator. More precisely, the precipitation sums up to 1,000 mm in the western Appalachian Mountais, whereas it is only about 400 mm in the eastern part. In the hot regions adjacent to the north and south there is virtually no precipitation (less than 200 mm per year). These dry areas of Hadley cell downwelling extend over most of Euramerica and Northern Gondwana as far as 45°N and S. Due to their location within the Tethys Ocean and their relatively small landmasses, Cathaysia and Cimmeria are not as dry and still exhibit 600 mm of annual precipitation. Further south, in Central and Southern Gondwana, there is a belt between 45° and 60°S with annual precipitation from 800 to 1,200 mm. Evaporation over the Paraná-Karoo-Inland Sea and the Southern Tethys Ocean increases annual precipitation to about 1,600 mm in adjacent regions. The southern high-latitude Gondwana exhibits a moderate annual precipitation between 400 to 800 mm in most regions. At the sharp southern edge of the South Gondwanan Mountains, where the mountain range plunges down into the sea over several hundreds of meters, precipitation formation is considerably enhanced. The annual precipitation can reach 3,400 mm in some areas. However, this is most likely a model artefact of the reconstructed Permian orography that exaggerates the actual slope and the total precipitation amount seems not reasonable. The very south of Angara is also part of the very dry zone, whereas there is an annual precipitation from 600 to 800 mm in most of Angara. The north of Angara is less humid and exhibits 200 to 400 mm of precipitation throughout the year. The Andean-like South Gondwanan Mountains as well as the Ural Mountains both provide a barrier for atmospheric water transport into the continental interior in the westerlies. Hence, the coastal regions west of the mountains are considerably more humid than the continental interior to the east.

The annual precipitation and evaporation balance is presented in Figure 5.4(b). In most parts of Pangaea most of the precipitation is compensated by evaporation in the course of the year and aridity is prevalent. An annual surplus of precipitation of more than 200 mm can only be found in Angara north of 50°N, some of the Tethysian microcontinents, and in Southern Gondwana close to the Paraná-Karoo-Inland Sea, ocean inlets, and coastal areas. Moreover, the precipitation surplus is particularly high in mountainous areas: about 500 mm in the Appalachian Mountains, 1,000 to 1,200 mm in the Ural Mountains and western South Gondwanan Mountains, and even 2,400 mm in the southern part of this mountain range. However, the latter is most likely exaggerated as discussed above.

In addition to the annual sum, the distribution of precipitation throughout the year further characterises the climate of a certain region. In order to analyse the seasonal variation of precipitation, the seasonally integrated precipitation is discussed in the following. The global precipitation distribution for each season is shown in Figure 5.5.

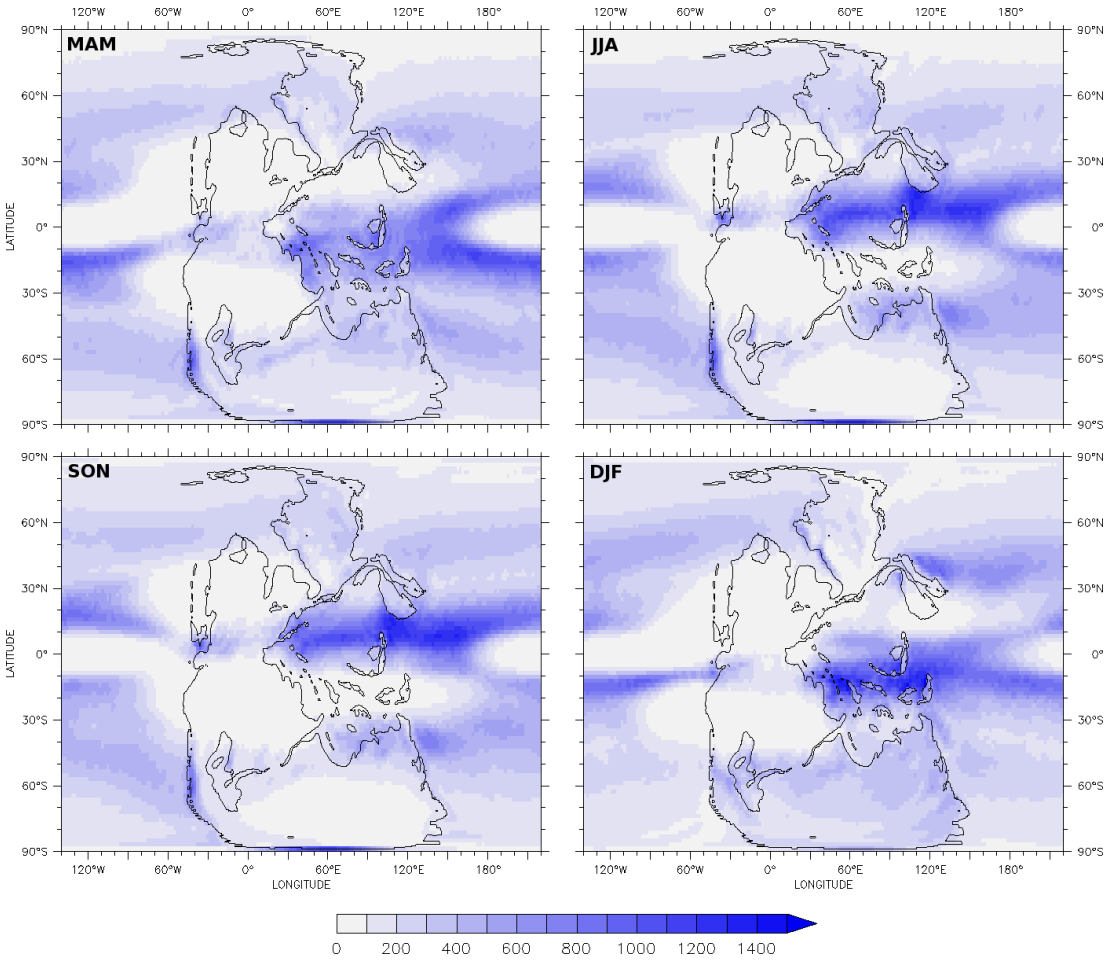

Figure 5.5.: Integrated seasonal precipitation [mm] for $4\times CO_2$ scenario.

Driven by the seasonal cycle of solar radiation, the ITCZ and the corresponding zone of high precipitation follow the Sun's zenith point with an offset of some weeks. This behaviour is also present in the seasonal precipitation distribution.

From March to May, i.e. in northern spring or southern autumn, the ITCZ, coming from the south, crosses the equator and moves further north. The zone of high precipitation lies slightly south of the equator at the beginning and slightly north at the end of the season. Hence, precipitation is distributed throughout an area close to the equator in Central Pangaea, the Central and Southern Tethys Ocean including Cimmeria and South- and Indochina, as well as the Central Panthalassic Ocean. However, lower

SSTs in eastern Panthalassa around the equator (see Section 5.1.4) suppress convective precipitation formation in this area in late spring and force the zone of high precipitation to a more northern position where higher SSTs are present. Thus, the observed ITCZ splitting corresponds to a nortward shift of ITCZ rather than a double ITCZ. The resulting arid area over the Panthalassic Ocean is connected in the East to the arid area of northern Hadley downwelling that spreads across entire Euramerica, Baltica, Southern Angara, Cathaysia, and the Northern Tethys Ocean. Northern Gondwana is an arid area due to southern Hadley downwelling. The mid- and high latitudes of Angara and Gondwana exhibit moderate to minor precipitation.

In northern summer or southern winter, i.e. from June to August, the ITCZ reaches its northern maximum position and the zone of high precipitation spreads across Southern Euramerica, the Northern Tethys Ocean, Southern Cathaysia, and the Northern Panthalassic Ocean at about 15 to 20°N. The arid area of northern Hadley downwelling is located in Euramerica and Baltica. In this season the arid area over the east equatorial Panthalassa is connected to the arid area of southern Hadley downwelling spreading across Northern Gondwana, the Southern Tethys Ocean, and Cimmeria. There is moderate precipitation all over Angara and within a small belt in mid-latitude Gondwana from the Paraná-Karoo-Inland Sea to the southern Tethys coast. The vast continental interior of Southern Gondwana exhibits virtually no precipitation.

From September to November, i.e. in autumn on the northern and spring on the Southern Hemisphere, the ITCZ crosses the equator on its way to the south. At the beginning of the season the precipitation distribution is basically equivalent to the distribution of northern summer. However, the distribution pattern gradually transitions to the spring/autumn pattern outlined at the beginning. In short, the dry season in the Southern Tethys Ocean and Cimmeria ends, whereas it starts in Cathaysia and Southern Euramerica. The continental interior of Southern Gondwana gets more humid again

In southern summer or northern winter, i.e. from December to February, the ITCZ reaches its southern maximum position and the zone of high precipitation spreads across the very north of Gondwana, the Central Tethys Ocean, Cimmeria, and the Southern Panthalassic Ocean at about 15 to 20°S. The rest of Northern Gondwana is arid because it remains in the area of southern Hadley downwelling. The equatorial arid area over Eastern Panthalassa is connected with the arid area of northern Hadley downwelling that stretches over Euramerica, the Northern Tethys Ocean, Southern Angara and Cathaysia. Southern Gondwana exhibits moderate precipitation. In contrast, Angara is less humid as there is low precipitation in the west and virtually no precipitation in the east close to the frozen Northern Panthalassic Ocean.

In summary, the Tethysian microcontinents and coastal areas are subjected to a monsoonal climate comprising dry and humid seasons. Most of Euramerica and Northern Gondwana are dry throughout the year. Angara exhibits moderate precipitation all year round, albeit slightly less during winter. There is an everwet zone of moderate precipitation in mid-latitude Gondwana from the Paraná-Karoo-Inland Sea to the southern

Tethys coast, whereas most of Southern Gondwana is arid during winter and moderately humid during summer.

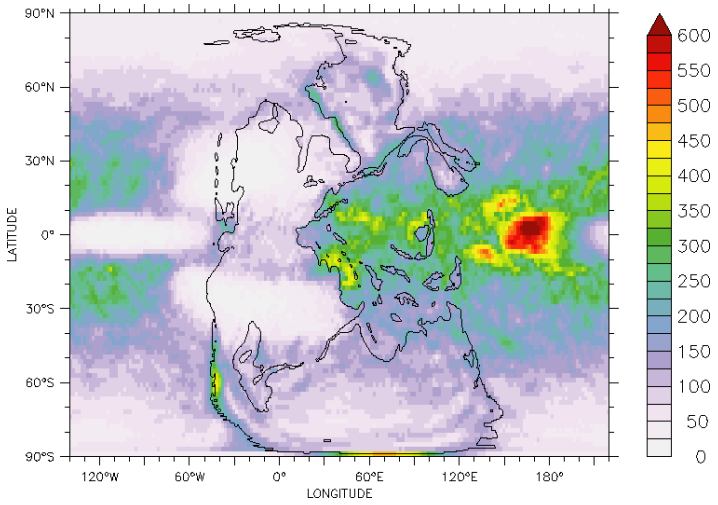

Figure 5.6.: Interannual variability of annual mean precipitation in terms of standard variation [mm] for 4×CO_2 scenario.

Figure 5.6 shows the interannual variability of the integrated annual precipitation within the 30-year diagnostic period in terms of the standard variation. The variability is generally small compared to the annual mean in all regions of Pangaea and the Permian oceans. It is about 50-150 mm in humid areas near the equator (Southern Laurentia, Northern Gondwana, and the Tethysian microcontinents) in mid-latitudes (Gondwana and Angara), and in high latitudes (Angara). Arid regions in Laurentia, Baltica, and Northern Gondwana exhibit an interannual variability of less then 50 mm and the variability lies between 50 and 100 mm in the arid areas of Southern Gondwana in high latitudes. The pattern is similar over the oceans. The variability is higher (300-600 mm) over the Tethys and the Western Panthalassic Ocean in low latitudes where the annual precipitation amount is rather high as well. The highest variability occurs over Western Panthalassa in the area of the precipitation maximum. In contrast, precipitation is very low over the Central and Eastern Panthalassic Ocean and the same applies for the variability ($<$ 50 mm). The variability is moderate (100-250 mm) over the Panthalassic Ocean in mid-latitudes and low ($<$ 100 mm) in high latitudes. Hence, the interannual variability of the precipitation is less than 25% of the annual mean precipitation in all areas except for very dry regions.

5.1.3. Surface Pressure and Wind

On a global scale the distribution of mean surface pressure is closely linked to the surface temperature and follows its seasonal variation with low pressure over the continents in summer and high pressure over the continents in winter. Due to the larger landmass

of Gondwana, this effect is more pronounced on the Southern Hemisphere. The mean wind pattern basically corresponds to cyclonic and anti-cyclonic flow around the main low and high pressure systems. The seasonal mean surface pressure and wind of the Permian Earth are presented in Figure 5.7.

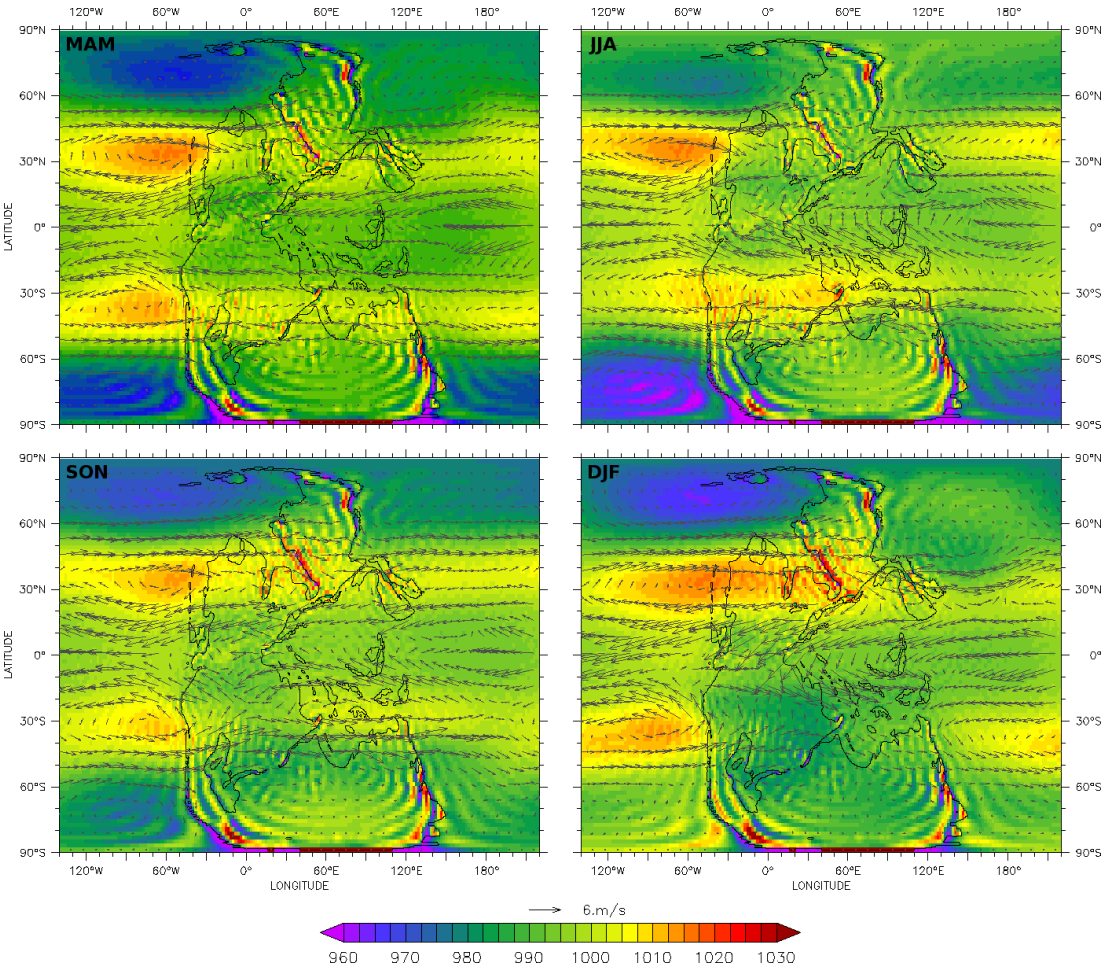

Figure 5.7.: Mean seasonal sea level pressure [hPa] and horizontal wind $[m/s]$ at 850 hPa for 4×CO_2 scenario.

The most pronounced pressure formations of the boreal winter season are the summer monsoon low over Northern Gondwana ($\sim 50°$S) and the winter monsoon high over Euramerica and the adjacent part of the Eastern Panthalassa ($\sim 35°$N). They affect the northern and southern trade winds in such a way that a system of winter monsoon northeasterlies and summer monsoon northwesterlies arise over eastern equatorial Pangaea and the Western Tethys Ocean. This leads to cross-equatorial flow and the linked system contains the strongest mean winds at 850 hPa on the Permian Earth for this season. The air is enriched with water on its way over the warm Tethys Ocean and provides moisture to Cimmeria and the Southern Tethys Ocean. The southern

subtropical high is retracted to the mid-latitude Panthalassic Ocean. The westerlies on its southern side provide humidity to western mid-latitude Gondwana. A less pronounced low pressure system over summery Southern Gondwana distributes moisture of the southern Tethys coast over the continent. Westerlies prevail in mid-latitudes on the Northern Hemisphere. They are significantly influenced by the extended subtropical high over Euramerica and subpolar lows in Northern Panthalassa south of the northern island arc as well as off the east coast of Angara.

The summer monsoon low on the Northern Hemisphere is less pronounced. This non-symmetrical behaviour is caused by the smaller landmass of Laurasia. Furthermore, the Uralian Epeiric Seaway divides the continent and splits the summer monsoon low pressure centre into two centres. These summer monsoon lows are located further south at about 20°N, one over Central Euramerica and the other one over Cathaysia (North China). The winter monsoon high over Northern Gondwana is centered at about 30°S and less pronounced as well. Consequently, the winter monsoon southeasterlies and especially the summer monsoon southwesterlies are weaker. A strong subtropical high over the Northern Panthalassa and a subpolar low drive westerly winds that are split at the Angaran west coast. One branch bends to the north following the coastline, whereas the other one crosses the Ural Mountains and continues over Central Angara. In the Southern Hemisphere there is a strong subpolar low over the southeast Panthalassic Ocean. Strong westerlies prevail in mid-latitude Gondwana and provide moisture supply. Most of the carried moisture is rained out on the west side of the South Gondwanan Mountains but the Paraná-Karoo-Inland Sea provides another water source for the continental interior to the east.

The spring and autumn seasons represent a transition state. There is no cross-equatorial air flow in the Tethys region and both northern and southern trade winds proceed westwards over the Pangaean continent in low latitudes. Westerlies are prevailing in mid-latitudes on both hemispheres and the subtropical highs are located mainly over the ocean. There are subpolar lows over the Panthalassic Ocean in high latitudes that drive poleward winds at the western coasts of Angara and Gondwana and equatorwards winds at the eastern coast.

5.1.4. Ocean Surface

The ocean circulation is essentially affected by temperature and salinity gradients, the Coriolis effect, and the wind at the surface. The mean circulation pattern of near-surface ocean layers is illustrated in Figure 5.8.

The general features of the circulation pattern of the Panthalassic Ocean are comparable to the present-day Pacific Ocean. There are an equatorial current flowing westwards as well as strong subtropical and polar gyres in both hemispheres. The equatorial current is predominantly controlled by the trade winds and proceeds from the west coast of Pangaea

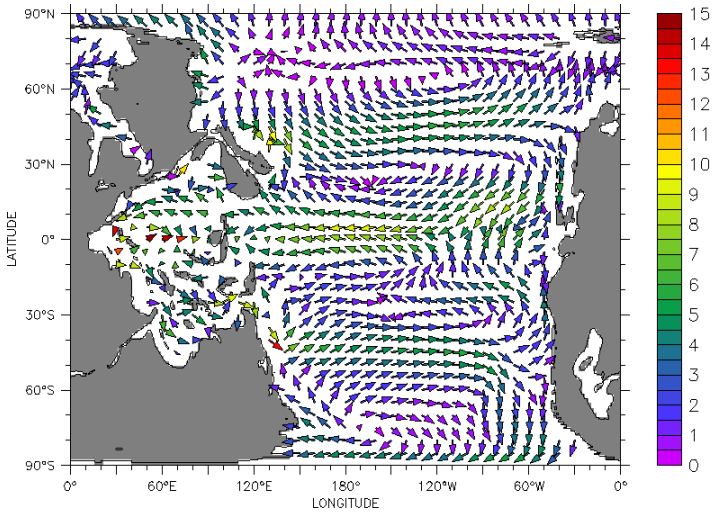

Figure 5.8.: Mean annual ocean circulation $[^{cm}/_{s}]$ for 4×CO_2 scenario at 50 m depth.

into the Tethys Ocean. In the present-day Pacific Ocean a narrow eastward flowing equatorial counter current separates the north and south equatorial current. Most likely, this counter current also existed in the Panthalassic Ocean but is not resolved by the coarse grid of the ocean model. The equatorial current is basically continued in the Tethys Ocean and eventually follows the coastline to the north and south. However, the current is partly blocked or deflected by the Tethysian microcontinents or even amplified due to the funnel effect. The landmasses of Cathaysia and Eastern Cimmeria prevent a simple backflow into the Panthalassic Ocean. The seasonal shift of the trade winds (see Figure 5.7) has an impact on the strength and location of the current, especially directly at the surface (not shown). In northern winter the strengthened northeasterly trades force the equatorial current predominantly into the Northern Tethys Ocean towards the Laurasian coast. In contrast, in southern winter the predominant southeasterly trades force the current across Cimmeria towards the coast of Northern Gondwana. The equatorial current is part of the subtropic gyres of both hemispheres. These are centered at about 25°N and 30°S, respectively. They affect equatorwards flow off the west coast of Pangaea in low and mid-latitudes, westward flow in mid-latitudes, and poleward flow off the eastern coast of Cathaysia, Cimmeria, and Gondwana in low and mid-latitudes. The southern gyre contains two distinct smaller gyres centered at about 10°S and 30°S. Furthermore, there is another strong gyre in high latitudes in each hemisphere. The southern polar gyre is located at about 80°S, whereas the northern one is centered at about 65°N because of the presence of sea ice. They cause poleward flow off the western coasts of high-latitude Angara along the northern island arc and Gondwana, as well as equatorward flow off the high-latitude eastern coasts of Angara and Gondwana, westward flow in mid-latitudes, and eastward flow in very high latitudes. In general, the location of both subtropical and polar gyres underlies seasonal change as they are located closer to the equator in winter. There is a circumpolar current in both

hemispheres (clock-wise in the Northern Hemisphere, anti-clock-wise in the Southern Hemisphere). However, the southern circumpolar current is restricted to an area very close to the South Pole.

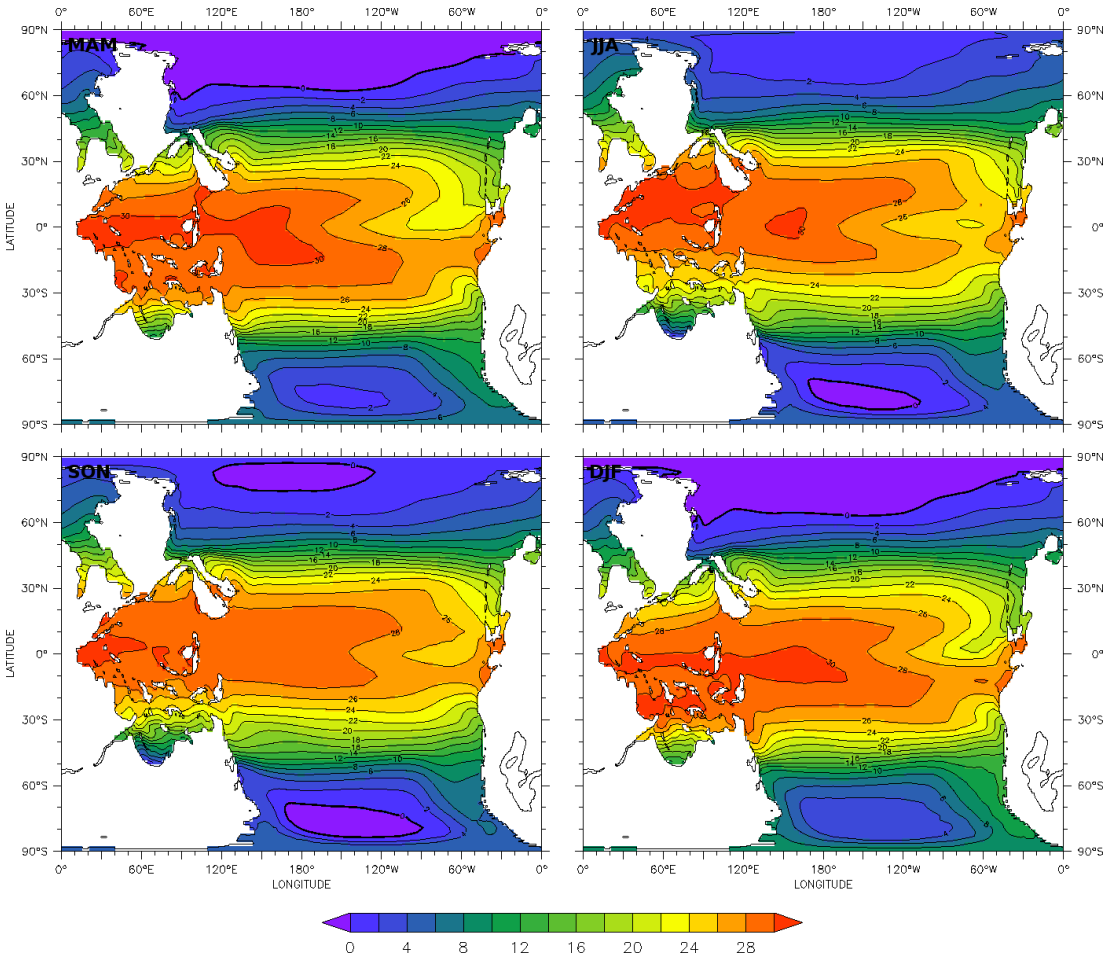

Figure 5.9.: Mean seasonal sea surface temperate [°C] for 4×CO_2 scenario.

The ocean circulation has a signicant impact on the SST, but also warming or cooling due to heat exchange with the atmosphere and radiative transfer is essential. Figure 5.9 shows the mean seasonal SST of the Permian Earth. The zero-degree level defines the area where sea ice is common. The seasonal sea ice extent is presented in the Appendix in Figure D.1.

The highest SST of the Permian oceans, about 30°C, can be found in some regions of the Tethys Ocean and the Western Panthalassic Ocean in low latitudes. The Tethys Ocean is generally rather warm with SSTs of more than 26°C in most areas throughout the year. Colder regions occur solely in the very north (Tarim bay, from 18°C in winter to 24°C in summer) and the very south (south of Cimmeria, from 2-12°C in winter to

12-22°C in summer). The seasonal shift of equatorial current and ITCZ is consistent with the SST distribution. From June to August the warmest area is in the Northern Tethys between Baltica, North China and South China, whereas from December to February the Tethys Ocean is warmest in the South around the microcontinents of South- and Indochina, and Cimmeria. In spring and autumn the warmest region is near the equator.

In the Panthalassic Ocean the subtropical gyres bring cooler sea water from higher latitudes along the Pangaean west coast close to the equator. On its way along the equator to the West the water is gradually warmed before it flows into the Tethys Ocean or polewards again along the eastern coasts of Cathaysia and Gondwana. That is why in low latitudes the ocean surface is cooler in the Eastern Panthalassic than in its western part. However, in mid- and high latitudes the polar gyres provide warm water to the polar west coasts of Angara and Gondwana as well as cold water to the east coasts of both continents. This pattern holds throughout the year, although the absolute temperature changes with season. Along the Pangaean west coast the SST is about 26-28°C near the equator, about 16-18°C at 20°N, and between 6-14°C (winter) and 8-16°C (summer) at mid-latitudes. The Ural Epeiric Seaway exhibits SST from 6°C minimum in the North to 26°C maximum in the South. In polar latitudes the SST further decreases to 0-4°C at the northern island arc. The SST decreases along the west coast of Gondwana is basically similar, however, the Southern Panthalassic Ocean is slightly warmer. The SST varies from 12-16°C in mid-latitudes to 4-10°C in high latitudes. Along the east coast, Amuria exhibits a SST from 8-22°C in winter to 14-26°C in summer, whereas in Angara the SST varies from 0°C in winter to 10°C in the south in summer. The Panthalassic Ocean along the east coast of Gondwana has a SST between 2 and 8°C in high latitudes.

There is no permanent sea ice coverage on both hemispheres of the Permian Earth (compare mean seasonal sea ice extent in Figure D.1). In the North the maximum ice extent is 60°N off the coast of Angara and the west Panthalassic Ocean, whereas the ice does not extend further south as the northern island arc at about 80°N in the East. The sea ice has melted completely by July and starts to re-form by November. Sea ice is considerably less common in the Southern Hemisphere. It occurs in the very South of the Tethys Ocean and in an area in the southwest Panthalassic Ocean far-off the Gondwanan coast. It starts growing by July and is melted again by November. The southern icesheets reach a thickness of only a few centimetres, whereas the northern icesheets grow to a thickness of about 60 cm.

The interannual variability of the SST is small in most areas (see Figure 5.3). It is between 0.1 and 0.2 K in most parts of the tropical Tethys and Panthalassic Ocean. Larger variability merely occurs off the west coast of Laurentia. In mid- and high latitudes the variability is in the range between 0.4 and 0.7 K, although, it is generally smaller in most of the cold regions of the polar Panthalassic Ocean. Hence, the interannual variability of the SST is small compared to seasonal, like the variability of the surface temperature over land.

5.2. Climate Sensitivity

The modelling of the Permian Earth entails several uncertainties, such as atmospheric carbon dioxide content, astronomical constellation, and land cover, that have been discussed in Chapter 4. The inevitable parameterisation of subgrid-scale processes within the model framework provides further uncertainties. The following section examines the sensitivity of the simulated climate to the choice of various parameters, surface characteristics, and convection scheme.

5.2.1. Climate sensitivity to atmospheric CO_2 content

The setting of the atmospheric carbon dioxide concentration is a very crucial point for palaeoclimate simulations because its radiative forcing has a strong impact on the mean temperature. Reconstructions on the basis of geological records and carbon cycle modelling predict a rather low carbondioxide concentration for the Permo-Carboniferous (about 300 ppm, error range 80-450 ppm, $\sim 1\times CO_2$) that increased to about 1250 ppm (error range: 200-2250 ppm) at the Permo-Triassic boundary ($\sim$4-8$\times CO_2$) (see Section 2.3.1). Although the mean temperature is affected primarily, this pertains to the entire global and regional climate and ocean circulation .

	$1\times CO_2$	$2\times CO_2$	$4\times CO_2$	$6\times CO_2$	$8\times CO_2$	$10\times CO_2$
global [°C]	11.56	15.20	18.40	20.62	22.85	24.93
land [°C]	10.27	14.12	18.03	20.87	23.68	26.28
ocean [°C]	12.03	15.59	18.56	20.53	22.56	24.44

Table 5.1.: Mean annual surface temperature for all CO_2 scenarios of Permian climate.

The globally averaged mean annual temperatures for all CO_2 scenarios are summarised in Table 5.1. As expected, the $1\times CO_2$ scenario generates the coldest climate state. The global average temperature is slightly lower than the present-day reference value as simulated with EMAC-MPIOM for the present climate (12.2°C). For rising carbon dioxide concentrations the temperature increases rather exponentially for the cooler $1\times CO_2$, $2\times CO_2$, and $4\times CO_2$ scenarios and rather linearly for the warmer $4\times CO_2$, $6\times CO_2$, $8\times CO_2$, and $10\times CO_2$ scenarios. The mean global temperature of the warmest $10\times CO_2$ scenario is about 12 K warmer than the present-day reference value. The temperature increase is generally stronger over land than over the ocean.

The global distribution of mean annual surface temperature for all scenarios is shown in Figure 5.10. Except for the global temperature increase, all scenarios show a similar relative temperature pattern in general. As with the $4\times CO_2$ reference climate the coldest temperatures can be found in the south of Gondwana, whereas mean annual temperatures of Northern Angara are significantly milder. The warmest regions are Southern Euramerica and Northern Gondwana. The near-equatorial region of Pangaea

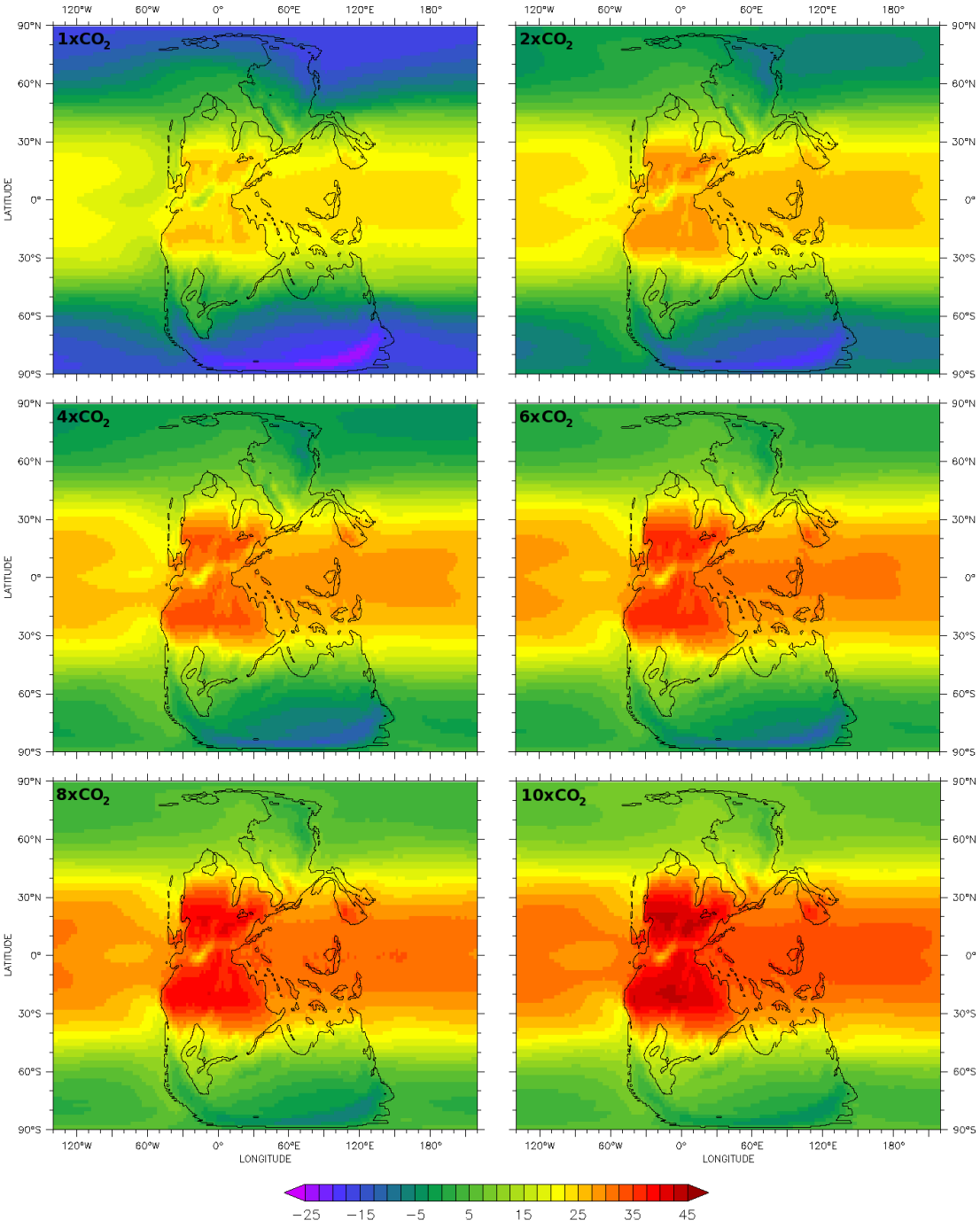

Figure 5.10.: Mean annual surface air temperature [°C] for all CO_2 scenarios.

as well as the Tethysian microcontinents are slightly cooler. The warmest SSTs occur in the low-latitude Tethys Ocean and Western Panthalassa, whereas the eastern part of the Panthalassic Ocean exhibits considerably cooler temperatures in low and mid-latitudes. In polar latitudes, the ocean is slightly warmer in the east than in the west.

The mean annual temperature of the $1\times CO_2$ scenario spreads from $-25°C$ in the South Gondwanan Mountains and $-15°C$ in the adjacent plains as well as in Northern Angara to 25°C in low-latitude Euramerica and Gondwana. There is permanent sea ice coverage in both hemispheres (see Figure D.2 in the Appendix). The sea ice extents approximately to 45° of latitude on annual average. It stretches along the entire east coast of Angara and most of the east coast of Southern Gondwana all year round, whereas the adjacent seas of Laurentia and Baltica remain ice-free. The Southern Tethys Ocean is covered by sea ice during winter. The $2\times CO_2$ scenario exhibits warmer climate conditions in every region, but still most of Southern Gondwana as well as Northern and Central Angara have mean annual temperatures below 0°C. The annual mean of the coldest regions is about $-20°C$ (Gondwana) or $-10°C$ (Angara). The warmest region, Central Euramerica, has a mean annual temperature of 30°C. The sea icesheet is generally thinner. The sea ice extents to 55° of latitude on yearly average with the exception of the areas of warm ocean currents off the western coasts. The southern icesheet vanishes in summer, whereas the northern icesheet shrinks but outlives the warmer season. The $4\times CO_2$ scenario exhibits a spectrum of mean annual temperature from $-15°C$ to 33°C and merely seasonal sea ice coverage in both hemispheres (see more detailed discussion in Section 5.1). The $6\times CO_2$ scenario is again slightly warmer: $-12.5°C$ in Southern Gondwana, $-2.5°C$ in Northern Angara, and 35°C in the continental interior of Pangaea in low latitudes. The polar ocean regions are sufficiently warm to prevent sea ice formation all year round, i.e. the Permian Earth is virtually ice-free for this carbon dioxide content. For the $8\times CO_2$ scenario there is no area on the Northern Hemisphere where the mean annual temperature is below 0°C. Such low mean temperatures merely occur in the very south of Gondwana ($-7.5°C$). Some areas in the hot continental interior of Pangaea in low latitudes even reach a mean annual temperature of 40°C. The $10\times CO_2$ scenario generates the most extreme Permian climate state in line with expectations. Mean annual temperatures below 0°C can only be found in higher elevations of the South Gondwanan Mountains. The adjacent plains have an annual mean temperature of 2.5-7.5°C. Northern Angara exhibits similar temperatures. Polar oceans have a mean annual SST between 3-5°C. On the continent the 30°C-isotherm reaches 40° of latitude in several areas of Euramerica or Northern Gondwana. Extensive regions of low-latitude Pangaea have a mean annual temperature of more than 40°C, or even 42.5°C at some places. The central Tethys Ocean as well as the Tethysian microcontinents exhibit a mean annual temperature of 34°C. Hence, the tenfold increase of atmospheric carbon dioxide concentration leads to an increase of mean annual temperature of about 15-20 K for most parts of Pangaea. The increase is more pronounced in colder regions, however.

For all CO_2 scenarios the regional pattern of seasonal temperature variations is basically similar to the pattern of the $4\times CO_2$ reference scenario. However, the amplitude of the

seasonal temperature fluctuations is affected considerably, especially over the Pangaean continent. Rising the atmospheric carbon dioxide content leads to decreased seasonal temperature differences in high-latitude regions of Angara and Gondwana, poleward of approximately 50° of latitude. In contrast, the seasonal temperature difference is increased in mid-latitudes, i.e. between 20 and 50° of latitude. This behaviour can be observed for all CO_2 scenarios. For example, the seasonal temperature difference of central Southern Gondwana is 50 K for the $1\times CO_2$ scenario and 38 K for the $10\times CO_2$ scenario, whereas in Central Gondwana, east of the Paraná-Karoo-Inland Sea, it is 24 K for the $1\times CO_2$ scenario and 31 K for the $10\times CO_2$ scenario. Low-latitude regions generally exhibit a rather small temperature seasonality in all scenarios. Seasonal temperature fluctuations over the oceans are also generally small and hardly affected. However, the permanent sea icesheets of the colder scenarios suppress the moderating effect of the ocean. That is why the seasonal temperature difference over the polar oceans is far larger for the $1\times CO_2$ and $2\times CO_2$ scenario than for the other ones.

The rising temperatures cause an intensification of the hydrological cycle. The warmer atmosphere can hold more water, but also more water evaporates at the surface. In total, an increase of the total precipitation amount can be observed for rising atmospheric carbon dioxide concentrations. The global mean precipitation is summarised in Table 5.2.

	$1\times CO_2$	$2\times CO_2$	$4\times CO_2$	$6\times CO_2$	$8\times CO_2$	$10\times CO_2$
global [mm/day]	2.60	2.81	3.00	3.11	3.23	3.33
land [mm/day]	1.32	1.42	1.54	1.60	1.68	1.74
ocean [mm/day]	3.06	3.31	3.52	3.66	3.79	3.90

Table 5.2.: Mean integrated daily precipitation for all CO_2 scenarios of Permian climate.

The relative increase is approximately the same over the continent or the ocean. In both cases the tenfold increase of carbon dioxide content leads to a mean global precipitation increase of about 28%. The global precipitation distribution as well as its seasonal variation are hardly affected and conform with the $4\times CO_2$ reference climate for all scenarios. Thus, the essential effect is merely the increase of the total precipitation amount in all regions.

The rising temperatures also have an impact on the mean pressure distributions and wind fields. The mean locations of monsoon high and low pressure systems as well as subtropical high and polar low are basically similar for all CO_2 scenarios. However, the pressure gradients rise in low latitudes for higher atmospheric carbon dioxide content and the strength of the pressure systems increases. This leads to a slight increase of the mean wind velocity in most regions, especially the trade winds on the winter hemisphere are strengthened. The warming of the polar regions generally reduces the temperature gradient between the tropics and the polar regions. This affects the horizontal pressure gradient and weakens the thermal wind. As a consequence the strength of the westerlies is decreased in mid-latitudes of both hemispheres.

The major effect of higher atmospheric carbon dioxide concentrations on the ocean is the comprehensive warming and the consequential melting of the polar sea icesheets (see above). The warming is not only observed at the surface but also at the deep sea. For the colder $1\times CO_2$ and $2\times CO_2$ scenarios the deep ocean has a mean temperature of -1.7-2°C at a depth of 1,100 m in most regions. The induced warming at the surface increases the deep ocean temperature to 2-6°C ($4\times CO_2$ and $6\times CO_2$ scenario) or even to 8-12°C for the warmer $8\times CO_2$ and $10\times CO_2$ scenarios. Moreover, the ocean circulation is affected since there are changes in horizontal and vertical temperature gradients, wind speed at the surface, and salinity due to increased precipitation. The comparison of the simulated Permian oceans reveals that the basic circulation pattern remains unchanged for all CO_2 scenarios, but the circulation velocity slows down for warmer ocean temperatures. This behaviour can be observed especially for the long ocean-traversal currents in the Panthalassic and Tethys Ocean and for the northward and southward currents along the Tethys coasts of Laurasia and Gondwana. In polar seas, however, the melted icesheets enabled accelerated ocean circulation. The vertical up- and downwelling is also slowed down for warmer Permian oceans in low- and mid-latitudes. The subpolar large-scale upwelling zone is shifted further polewards and the vertical circulation is accelerated in polar seas.

In summary, the carbon dioxide concentration of the Permian atmosphere considerably impacts on the mean temperature. Within a range of concentration from 355 to mbox3550 ppm ($1\times CO_2$ to $10\times CO_2$) the mean annual global temperature varies by about 13 K. This corresponds to local temperature variations up to 15-20 K in most parts of Pangaea. The overall effects are manifold and tremendous for the Permian climate. Depending on the region, the local temperature seasonality can be altered by up to 10 K. For rising atmospheric carbon dioxide concentrations the total annual precipitation amount increases, in total by about 30% on global average for a tenfold increase. The strength of the seasonally dominant pressure systems increases as well. As a consequence, the low-latitude trade winds are strengthened and the mid-latitude westerlies are weakened. The warming of the atmosphere also induces warming of the ocean, in near-surface layers as well as in deep layers. Hence, permanent polar sea ice coverage on both hemispheres only exists for the coldest scenario, whereas the warmer scenarios exhibit merely seasonal or even no sea icesheets. The ocean circulation generally slows down for higher ocean temperatures except for polar latitudes where the absence of icesheets enables accelerated circulation.

5.2.2. Climate sensitivity to convection parameterisation

As discussed in Section 5.1.2, the global distribution of mean annual precipitation exhibits a splitted ITCZ over the tropical Panthalassic Ocean with two branches of wet areas separated by an arid region at the equator (see Figure 5.4(a)). This pattern seems to resemble a double ITCZ that is a known bias in simulations with coupled GCM [160]. However, the splitted ITCZ does not appear in the distributions of mean

seasonal precipitation. The seasonal breakdown shows that the precipitation pattern corresponds to a northward and southward shift of the ITCZ over the eastern Panthalassic Ocean rather than a persistent ITCZ splitting (see Figure 5.5). Still, there is virtually no precipitation over the eastern equatorial Panthalassa throughout the year. As precipitation in tropical regions is predominantly triggered by convective processes, the observed precipitation distribution over the tropical oceans is possibly a model artefact because of the convection parameterisation. A widespread convection parameterisation scheme in global atmospheric models, that is also used for the simulation of the reference climate, is the Tiedtke convection scheme [129] (see Section 3.2.1). In order to estimate the sensitivity of the simulated precipitation distribution to the choice of convection parameterisation scheme, the reference climate is compared to the climate simulated by use of the Zhang-McFarlane-Hack convection scheme [130, 131] (see Section 3.2.2) in the following.

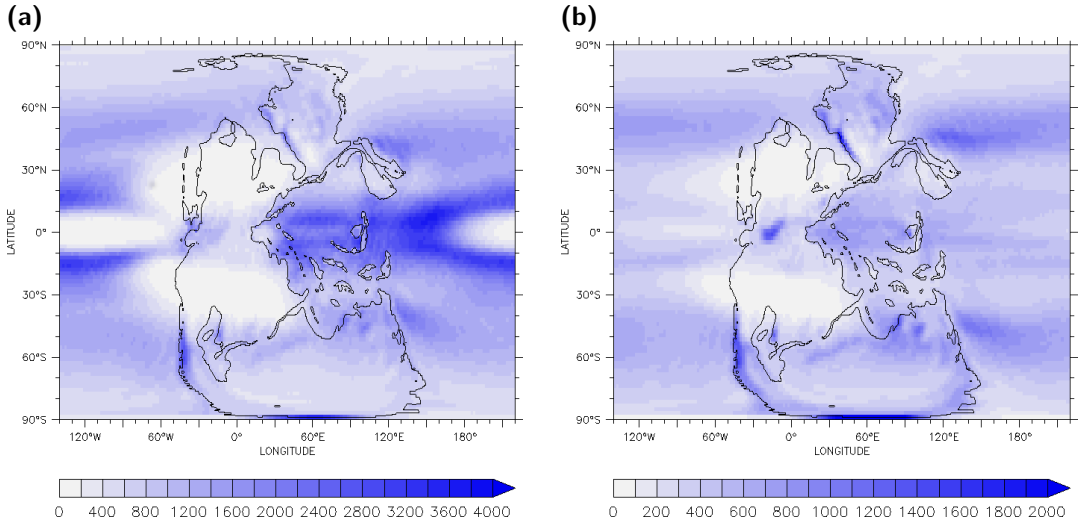

Figure 5.11.: Global distribution of integrated annual precipitation [mm] dependent on convection parameterisation: (a) Tiedtke convection scheme (same as Figure 5.4(a)) and (b) Zhang, McFarlane, and Hack convection scheme. Note the different scale for precipitation amount.

The mean annual precipitation for both convection parameterisation schemes is shown in Figure 5.11. The global precipitation distribution based on the Zhang-McFarlane-Hack convection scheme in Figure 5.11(b) differs significantly from the precipitation distribution of the reference climate in Figure 5.11(a). Over land the highest annual precipitation is found over the Ural (∼1600 mm), Appalachian (∼1400 mm), and South Gondwanan Mountains (∼2000 mm). The near-equatorial region of Pangaea and the Tethysian microcontinents exhibit an annual precipitation of about 200-400 mm. In the area of Hadley downwelling, in most parts of Euramerica, Southern Angara, and Northern Gondwana between 20 and 45°N and S, there is virtually no precipitation throughout the year. The mid-latitude westerlies in Angara and Gondwana, between

45 and 65°N and S, have the most precipitation apart from the mountainous regions with 400-700 mm. The regions adjacent to the Paraná-Karoo-Inland Sea and the Southern Tethys Ocean are even slightly more humid. The high-latitude regions of Angara and Gondwana exhibit an annual precipitation amount of 200-400 mm. The interior of Southern Gondwana is the driest region apart from the low-latitude deserts with about 200 mm. Over the ocean the precipitation is moderate in most areas in low latitudes (300-400 mm). There is merely a small area in the east Panthalassa near the equator that is drier with about 100 mm of annual precipitation. The tropical Tethys Ocean and the Western Panthalassa are slightly more humid (600-700 mm). The highest annual precipitation over the ocean is found in the westerlies off the east coasts of Angara and Gondwana. There the precipitation aggregates to more than 1,000 mm throughout the year which is more than in most parts of the mid-latitude Panthalassic ocean (600-700 mm).

The comparison of both global precipitation distributions reveals two essential differences. First, the Zhang-McFarlane-Hack scheme reduces the total precipitation amount considerably almost everywhere with reference to the Tiedte convection scheme. First, the global annual mean (Tiedtke: 1,095 mm; Zhang, McFarlane, Hack: 420 mm) is reduced to nearly one third of the reference simulation. Second, the main impact can be found over the tropical oceans where the conspicuous belt of very high precipitation does not exist as well as its splitting.

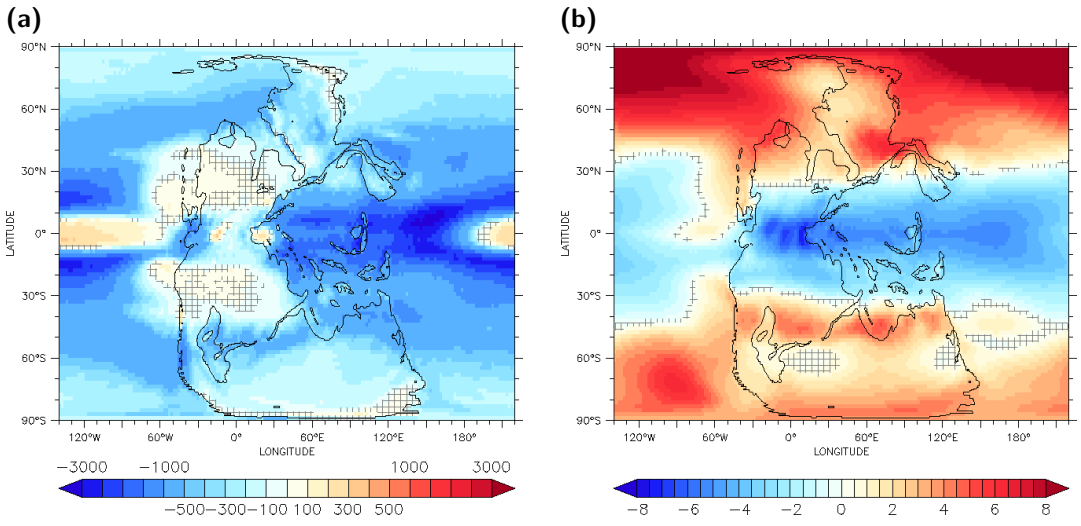

Figure 5.12.: Impact of convection parameterisation scheme on the mean annual Permian climate: The simulated mean climate state employing the Zhang, McFarlane, and Hack convection scheme is compared to the reference simulation that employs the Tiedtke convection scheme. (a) Difference of integrated annual precipitation [mm]. (b) Difference of mean annual temperature [K]. In hatched areas the difference is not highly significant based on an unpaired Student's t test and on a significance level of 1%.

The more quantitative comparison is presented in Figure 5.12(a). In most areas the difference is highly significant based on an unpaired Student's t test on a significance level of 1%. As the Zhang-McFarlane-Hack scheme does not induce very high precipitation in the area of the ITCZ, the reduction is obviously largest in this area, especially over the tropical Panthalassa with more than 3,300 mm. In contrast, the dry area in the eastern equatorial Panthalassa between both ITCZ locations is not induced either and thus the annual precipitation amount in this region is increased by about 200 mm. The precipitation reduction in the low-latitude Tethys Ocean is smaller but still high between 1,000 and 2,000 mm per year. Over near-equatorial Pangaea the precipitation is also decreased considerably except for the central Appalachian Mountains and directly off the Tethys coast where it is increased by up to 300 mm. The very arid areas of Hadley cell's descends exhibit a slight increase of precipitation, whereas Southern Gondwana and Angara are generally less humid (decrease of 100-300 mm). A narrow belt between the Paraná-Karoo-Inland Sea and the Tethys Ocean is affected even stronger. Both Northern Angara as well as Central and Southern Gondwana exhibit increased precipitation during the winter season, although the general effect diminishes in higher latitudes where the contribution of convective precipitation is relatively negligible.

Due to its impact on the atmospheric water content, both convective as well as large-scale precipitation formation are affected by the convection parameterisation scheme. A breakdown of the total precipitation amount reveals that the Zhang-McFarlane-Hack scheme amplifies large-scale precipitation along the equator, especially over near-equatorial Pangaea and the Western Tethys Ocean, as well as convective precipitation formation over the eastern equatorial Panthalassa. In contrast, the scheme suppresses considerably convective precipitation over the low-latitude Tethys Ocean and both belts of heavy precipitation over the Panthalassic Ocean. Furthermore, large-scale precipitation is suppressed in the mid-latitude westerlies, especially over the ocean and Southeastern Gondwana adjacent to the Tethys Ocean.

The mean annual global temperature at the surface is slightly increased due to the change of convection parameterisation scheme: from 18.4°C (Tiedtke) to 18.5°C (Zhang-McFarlane-Hack). However, the increase seems restricted to the land surface since the mean global ocean surface temperature is virtually not affected. This slight increase disagrees with the results of Tost, Jöckel, and Lelieveld [117] who observed a slight decrease of mean annual global surface temperature for the Zhang-McFarlane-Hack scheme. Still, the difference is only small in both cases. Figure 5.12(b) illustrates the local effect on the mean annual temperature at the surface. In short, the mean surface temperature is decreased in lower latitudes and increased in higher latitudes. The sign of the temperature variation seems to be related basically to the mean annual surface temperature of the Tiedtke scenario and follows approximately the 20°C-line. The absolute local variation, however, is further affected by radiation effects as well as the hydrological cycle. That is why considerable regional variations arise. The strongest temperature decrease due to the Zhang-McFarlane-Hack convection scheme is found in near-equatorial Pangaea (7 K) and the strongest temperature increase occurs over

the northern polar Panthalassa (8 K) or Southeastern Angara (6 K), respectively. The temperature variation is highly significant based on a significance level of 1% in most regions. Hence, the Zhang-McFarlane-Hack scheme generally leads to a more balanced climate state since it reduces the temperature gradient between the equator and the poles.

In summary, the simulated Permian climate is highly sensitive to the choice of the convection parameterisation scheme. The simulated precipitation distribution and amount is considerably affected. The belt of heavy precipitation along the near-equatorial ocean and its splitting seems to be an artefact of the Tiedtke scheme. The Zhang, McFarlane, and Hack scheme generates a more balanced distribution of precipitation across the Permian oceans and merely shows a bias towards high orography. Furthermore, the total precipitation amount is strongly decreased in most areas. Although the mean annual global temperature is virtually not affected, the local mean annual temperature is changed up to 8 K in some areas and the temperature gradient from equator to pole is smaller by use of the Zhang-McFarlane-Hack scheme than by use of the Tiedtke scheme.

5.2.3. Climate sensitivity to dynamic vegetation establishment

The general impact of vegetation on the climate is manifold: Trees and other tall-growing plants increase the surface roughness, vegetation cover alters the albedo, and moreover, plants are involved in the hydrological cycle via evapotranspiration. Therefore, a meticuluous description of the vegetation cover is essential for the simulation of a realistic climate. As comprehensive vegetation data is not available in most cases, palaeoclimate simulations have to rely on reconstructions based on extrapolations of the scarce palaeobotanical records. The reconstruction of Permian vegetation by Rees et al. [77] (see Figure C.18) is applied in the simulation of the reference climate as well as related simulations in this work. It assumes regionally uniform vegetation for all parts of Pangaea that approximates the average of the respective records. The employment of dynamical vegetation models offers an alternative approach to overcome this dilemma. Depending on the long-term climatic circumstances of the environment, the model considers the establishment, flourishing, or dieback of plants of various types. That way the artificial forcing by a possibly speculative vegetation prescription can be eliminated and the vegetation-climate feedback eventually generates a more balanced state of the Earth system. The application of the comprehensive ESM consisting of EMAC-MPIOM coupled with LPJ-GUESS for palaeoclimate simulations entails two intrinsic limitations, however, that possibly slightly bias the results. First, the feedback from the vegetation on the carbon cycle is not considered in this study and the atmospheric carbon dioxide concentration is assumed to be constant. Second, the vegetation model is tuned for present-day plants and does not consider specific properties of the Permian flora.

The prescribed vegetation cover and the vegetation cover that established after 200 years of spin-up simulation by means of a coupled dynamic vegetation model exhibit several

differences. For direct comparison, the vegetation ratio of both approaches is contrasted in Figure 5.13 for January and July. The comprehensive climatologies are shown in the Appendix C in Figure C.17-C.20.

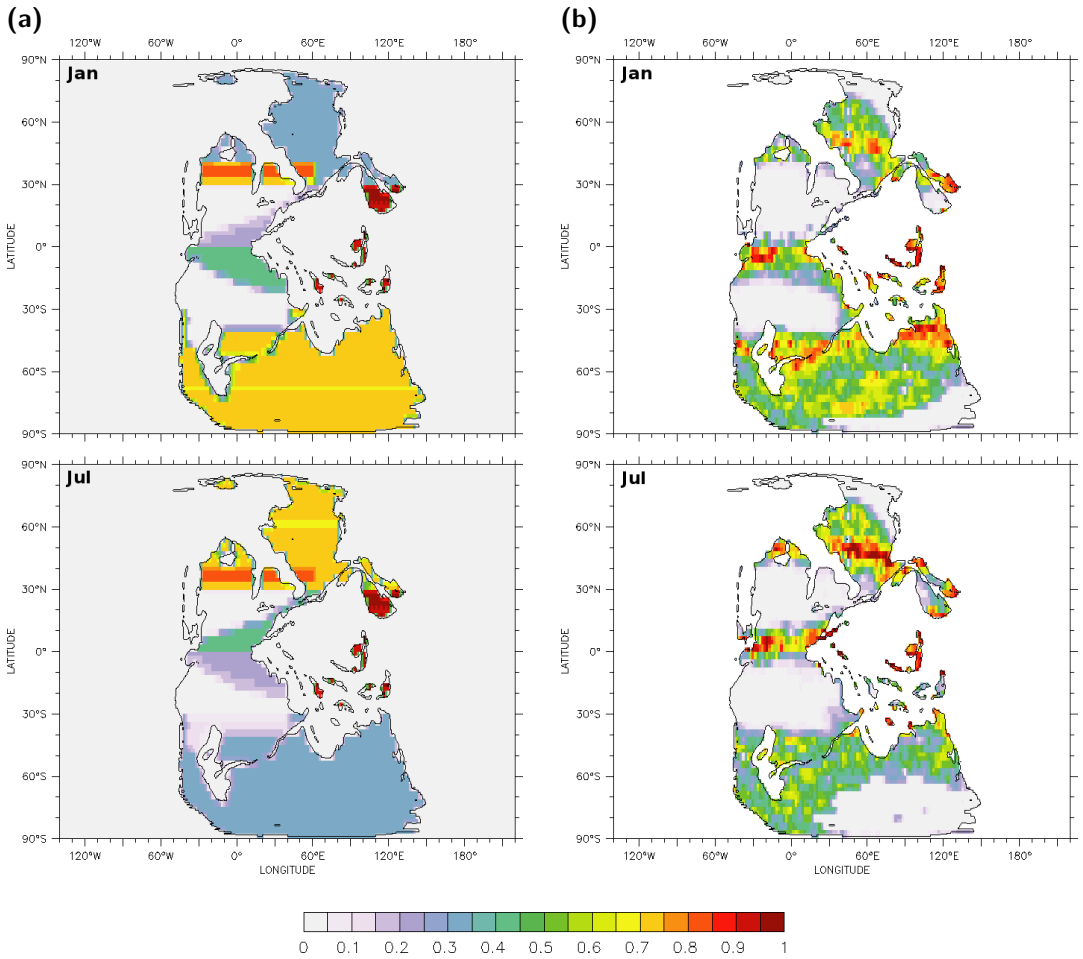

Figure 5.13.: Comparison of vegetation ratio in terms of land surface for Permian Earth for $4\times CO_2$ scenario: (a) Prescribed vegetation by Kiehl and Shields [8] based on palaeobotanical data of Rees et al. [77] as employed for reference climate. (b) Dynamically grown vegetation after 200 years of spin-up simulation. The complete climatologies of LAI and vegetation ratio are shown in the Appendix C in Figure C.17-C.20.

In Laurasia the prescribed vegetation following Rees et al. [77] assumes vast non-vegetated areas in Southern and Central Euramerica, that extends from the west to the east coast. Only directly at the Tethys coast and near the equator there is a belt of tropical flora with sparse density in winter and moderate vegetation density in summer during the wet season. In mid-latitudes, directly north of the desert area, there is a belt of dense evergreen shrub vegetation stretching across Laurentia, Northern Baltica, and Southern Angara. Northern Laurentia and the rest of Angara, up north to the

polar island arc, exhibit moderate deciduous vegetation that is sparse in winter and moderately dense in summer. The general distribution of the self-establihed vegetation is similar. However, the desert area extends slightly further to the South, up to the Tethys coast in the East, and considerably further to the North, replacing the mid-latitude shrub belt. According to the simulated PFTs (not shown), near-equatorial Pangaea exhibits moderate to dense vegetation of tropical trees in the West and grasslands in the East which means higher vegetation density than assumed by Rees et al. [77]. Northern Laurentia, Baltica, and Southern Angara are vegetated by broadleaved ever- and summergreen forests and Central Angara is predominated by boreal needleleaved evergreen forests. Within a belt between 40 and 60°N the vegetation density is high, or in summer even very high, even though the leaf area is mostly smaller than in the prescribed setup. Further to the north the established vegetation is less dense in summer but denser in winter which indicates a higher fraction of evergreen plants. The north and northeast of Angara are non-vegetated in contrast to the prescribed assumptions.

For Cathaysia the prescribed vegetation distribution assumes two different sectors: the northern part exhibits moderate deciduous vegetation like in adjacent Angara, whereas the south is very densely vegetated all year round. The model establishes dense temperate grassland vegetation in the north and tropical grasslands in southern North China with occasional tropical forest areas that flourish during the wet summer season. Only Southern Amuria is densely vegetated all year round. The microcontinents of South- and Indochina have high vegetation density according to Rees et al. [77] which is consistent with the dense model-established tropical ever- and raingreen forests. Cimmeria is assigned to dense vegetation all year round as well, whereas the model-established tropical grasslands are merely dense in summer and moderately dense during the dry winter season.

The vegetation distribution assumed for Gondwana is similar to Laurasia: There is a small belt from the equator to the Tethys coast with sparsely to moderately dense tropical vegetation. A vast desert area spreads across most parts of Northern Gondwana, whereas Southern Gondwana is assigned to moderate deciduous vegetation that is sparse in winter and moderately dense in summer. As in the Northern Hemisphere the non-vegetated desert area is more extensive. The near-equatorial vegetation density and leaf area is higher, but the vegetated area reaches the Tethys coast only during the wet summer season. Tropical forest established in the west, whereas the eastern region is vegetated by tropical grasslands. Like in Angara the model has predicted a higher fraction of evergreen vegetation in most parts of Southern Gondwana, i.e. the vegetation ratio is higher in winter but lower in summer. In mid-latitudes there is a belt from the Paraná-Karoo-Inland Sea, along the Tethys inlet to the southern Tethys coast with prevalent temperate broadleaved ever- and summergreen forests of very high vegetation density during summer and still moderate density during winter. Central Southern Gondwana exhibits dense temperate grassland vegetation in summer and virtually no vegetation during winter. The south-west of Gondwana is predominantly vegetated by boreal needleleaved evergreen forests and the south-east is non-vegetated all year round.

The model-generated forest fraction of the vegetation (not shown) resembles the assumptions of Rees et al. [77] (see Figure C.13) in most parts of Pangaea. Considerable differences can be found in eastern near-equatorial Pangaea and Cathaysia where the forest fraction is scarce. In addition, the mid-latitude temperate forest belts in Angara and Gondwana are denser. The leaf area, that is crucial for the albedo, is larger in near-equatorial Pangaea but considerably smaller in mid- and high latitude Angara and Gondwana (see Figure C.19 in the Appendix). The difference is larger during the summer season.

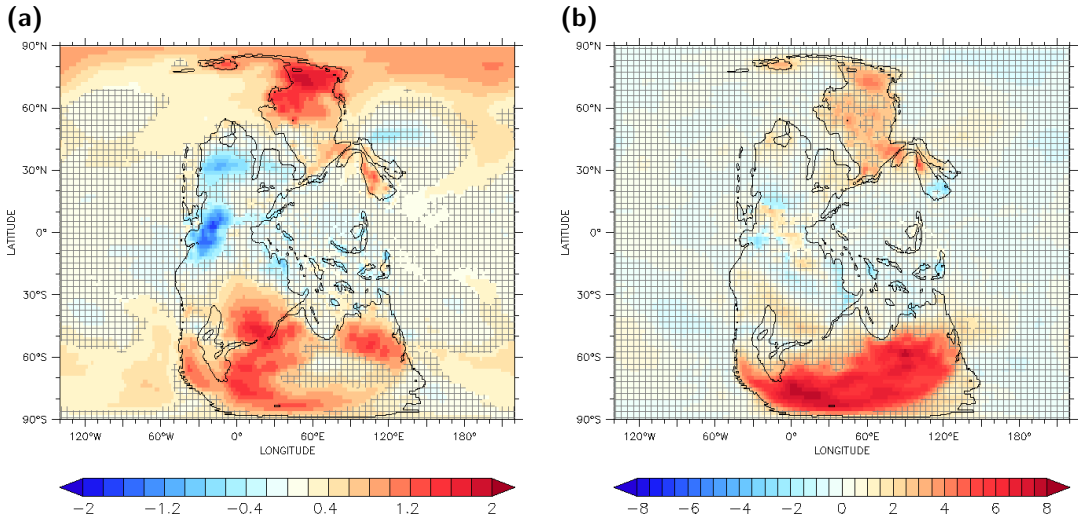

Figure 5.14.: Impact of coupled dynamic vegetation on simulated Permian climate for $4\times CO_2$ scenario: The simulated mean climate state based on dynamically established vegetation is compared to the mean climate based on prescribed vegetation. (a) Difference of mean annual temperature [K]. (b) Difference of temperature seasonality with respect to July- and January-temperature [K]. In hatched areas the difference is not highly significant based on an unpaired Student's t test and on a significance level of 1%.

The altered vegetation distribution has consequences for the mean Permian climate. The effect on the mean annual temperature is represented in Figure 5.14(a), whereas Figure 5.14(b) illustrates the regional change of temperature seasonality. The area where the difference is highly significant on a significance level of 1% is marked as before. However, the temperature is merely affected significantly in some parts of Pangaea or the Permian oceans. Thus, the global mean annual temperature is only slightly altered (prescribed vegetation distribution: 18.40°C, dynamical vegetation distribution: 18.79°C) and the effect arises rather regionally.

In general, the vegetation-climate feedback has positive and negative contributions. On the one hand larger LAI and vegetation height reduce the albedo of the surface and have a warming effect as bare soil or even snow have a higher albedo than vegetation. The effect is most pronounced in high latitudes in winter, but it also occurs in low

latitudes when the LAI is reduced due to higher temperatures and the feedback induces cooling. On the other hand larger leaf area reinforces evaporative cooling which is the predominating effect in warmer environments [161].

This impact is basically confirmed by the simulated changes of the Permian climate. The annual mean temperature is decreased by up to 1.75 K in near-equatorial Pangaea west of the Appalachian Mountains where the LAI of the tropical forests has been increased. Similar behaviour is found along the low-latitude Tethys coasts of Gondwana and Euramerica as well as on the Tethysian microcontinents (-0.875 K). In Central Laurentia and Baltica the shrub belt is replaced by desert. In this dry environment evaporative processes do not affect the temperature, but the higher albedo induces cooling by about 1 K. The LAI of most temperate and boreal forests in Angara and Gondwana is reduced or the surface is even unvegetated in high latitudes. This causes higher temperatures in summer and autumn, whereas in winter and spring the snow-covered unvegetated area exhibits cooler temperatures due to higher albedo, especially in Southern Gondwana. However, in sum these regions exhibit warmer temperatures on yearly average. The temperature increase is moderate in Southern and Central Angara (+0.75 K) and Cathaysia (+1.25 K), but reaches up to 2 K in Northern Angara, as well as Central and Eastern Gondwana. As a consequence of the higher summer temperatures, the sea ice formation is retarded in winter and the icesheet is less extended. The temperature-albedo feedback further amplifies the temperature difference and thus the mean annual temperature is increased by up to 1 K over the Northern Panthalassa.

The seasonal breakdown reveals that the mean summer temperatures are affected most in high-latitudes of Angara and Gondwana, whereas the mean winter temperature is merely slightly altered. The difference can reach up to 6 K (Angara) and 7 K (Gondwana) in July/January. Consequently, the seasonal temperature difference is strongly increased in these areas (see Figure 5.14(b)).

The behaviour is basically similar also for the simulation of scenarios with other atmospheric carbon dioxide concentrations and the respective model-established vegetation distributions. For the cold $1\times CO_2$ scenario the northern polar ocean is even warmed by up to 4 K. As most of Southern Gondwana is virtually unvegetated all year round, the mean annual temperature is decreased by about 1 K. This effect is also observed for the $2\times CO_2$ scenario. However, warmer temperatures in Northern Gondwana warm the polar ocean current which in turn causes retarded sea ice formation in the Southern Panthalassa and higher temperates by about 2.5 K. The $6\times CO_2$ and $8\times CO_2$ scenarios are permanently free of sea ice and thus the warming in mid- and high latitudes is restricted to the continent. For the $10\times CO_2$ scenario Angara and Southern Gondwana are both densely vegetated, but as they exhibit lower LAI as well the mean annual temperature of Southern Gondwana is increased by up to 4.5 K.

The altered vegetation distribution also affects the precipitation. The impact on the integrated annual precipitation is represented in Figure 5.15. However, the changes are only significant in few areas. Near the equator the denser vegetation increases

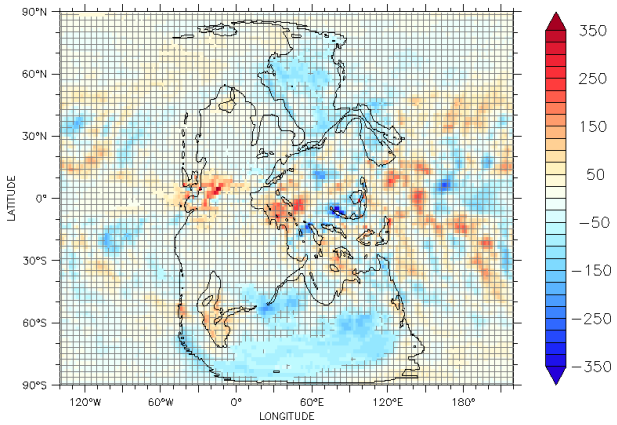

Figure 5.15.: Impact of coupled dynamic vegetation on simulated Permian climate for $4\times CO_2$ scenario: The simulated annual precipitation [mm] of the mean climate state based on dynamically grown vegetation is compared to the mean climate based on prescribed vegetation. In hatched areas the difference is not highly significant based on an unpaired Student's t test and on a significance level of 1%.

moisture via evapotranspiration and causes an increase of precipitation up to 350 mm. Furthermore, higher temperatures in Southern Gondwana enhance the evaporation over the Paraná-Karoo-Inland Sea whereby the annual precipitation is increased by 150 mm. In the continental interior of Gondwana and Angara the reduced vegetation density provides less moisture and thus the yearly precipitation amount is reduced as well. The effect is largest in Central Gondwana (200 mm) and Angara (125 mm). In Southern Gondwana the precipitation is still reduced by 150 mm which is about 30% of the total yearly amount. The behaviour is similar for altered atmospheric carbon dioxide content.

In summary, the self-establihed vegetation increases the vegetation density in near-equatorial Pangaea and mid-latitude forests on the one hand. On the other hand, the leaf area of temperate and boreal forests is reduced. The subtropical deserts are extended further to the North and South, and the eastern polar regions are virtually unvegetated. Reduced evaporative cooling increases the mean temperature in most parts of Gondwana and Angara, especially during summer, whereas cooling is observed near the equator. The difference can reach up to 2 K on annual average. The altered vegetation distribution also affects the available moisture and causes differences of the mean annual precipitation of up to 350 mm.

5.2.4. Climate sensitivity to orbital forcing

The gravitational interactions of the Earth with the other planets of the solar system and tidal forces exerted by the Sun and the Moon influence the Earth's orbit as well as the axial tilt and direction (see Section 2.4.3). This causes longterm fluctuations of the intensity of incoming solar radiation and its seasonal variation in the course

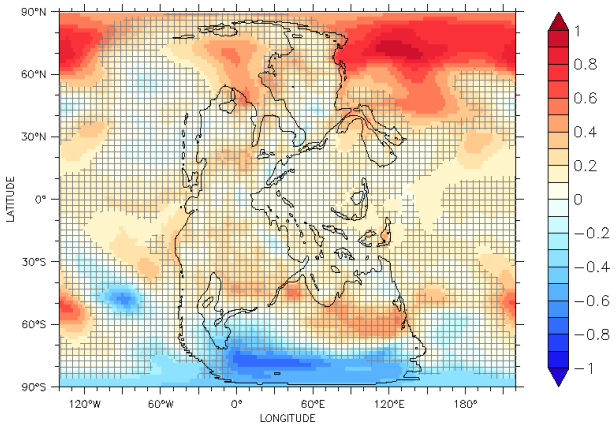

Figure 5.16.: Impact of obliquity change on simulated Permian climate for $4\times CO_2$ scenario: In the course of the Milankovitch cycle the obliquity changes between $24.5°$ and $22.1°$. The mean annual temperature [K] of both extreme scenarios is compared ($\theta_{\text{max}} - \theta_{\text{min}}$ scenario). In hatched areas the difference is not highly significant based on an unpaired Student's t test and on a significance level of 1%.

of the year. The resulting quasi-periodic alteration of the radiative forcing depends on the superposition of the single movements that are all independent and have a different periodicity. The effects on the climate are regionally different, however, due to a non-symmetric distribution of land and sea and the elliptical shape of the orbit.

For the simulation of the Permian reference climate the present-day orbit and axis tilt are used, i.e. a virtually circular orbit with perihelion in southern summer and medium axis tilt. In order to estimate the magnitude of the impact of the orbital fluctuations on the Permian climate, special arrangements within the Milankovitch cycles are considered (see Section 4.2.3 and Table 4.2). The extrema of obliquity and eccentricity are assumed as they occured in the Milankovitch cycles of the Quaternary. Since there is no evidence for a heavy meteoritic impact during the Phanærozoic that could have warped the Earth's motion significantly, these assumptions seem reasonable also for the Permian.

The climate impact of the obliquity fluctuation is represented in Figure 5.16. The diagram shows the difference of mean annual temperature for maximal and minimal axial tilt ($\theta_{\text{max}} - \theta_{\text{min}}$ scenarios, see Table 4.2). The global mean annual temperature is virtually not affected and merely warmer by 0.15 K for higher obliquity. In contrast, significant changes can be observed mainly in polar regions where it alters the length of polar night and the solar altitude. The effect is different in both hemispheres, however. In the north polar region the mean annual temperature is primarily increased over the ocean: up to 1 K in Western and Central Panthalassa and about 0.5 K in the east. The temperature of Angara is not affected significantly. The seasonal breakdown shows that the polar ocean is warmer for higher obliquity all year long. In summer the SST is about 0.5-1 K warmer due to stronger solar irradiation. The high heat capacity of water suppresses a fast cooling down in autumn and ice formation is retarded. The ice-albedo

feedback further amplifies the difference and the icesheet grows considerably slower. Hence, the icesheet of the high-obliquity scenario is about 40% smaller by March. That is why the maximal temperature difference occurs in late winter and spring (up to 3 K), although the solar altitude is actually less at that time. In the southern polar region the higher obliquity leads to cooler temperatures on annual mean, however, over the ocean (0.4 K) as well as in the far south of Gondwana (0.7 K). The difference occurs primarily in summer and autumn, from January to April, in spite of the stronger solar irradiation. The reason for this discrepancy can be found in the ocean circulation of the Southern Panthalassa. First, the low-obliquity scenario generally exhibits slightly weaker poleward heat transport by the ocean. Second, in the southeast Panthalassa the ocean water feeding the southern circumpolar current is warmed up less in low- and mid-latitudes. Consequently, the SST of the ocean current is cooler at most times of the year, up to 2 K in January, and the far south of Gondwana is cooled down as well. The stronger solar irradiation merely leads to warmer temperatures in Gondwana between 50 and 70°S, but the difference is not significant on a level of 1%. Further tiny differences can be found over the low- and mid-latitude Panthalassic Ocean. Thus, the expected warmer summer and cooler winter seasons due to higher obliquity cannot be observed. The precipitation distribution is not altered significantly on a large scale.

Figure 5.17(a) illustrates the climate impact of the axial precession, i.e. the longitudinal shift of the perihelion. As before the diagram shows the impact on the mean annual temperature and compares the scenarios when the perihelion coincides with southern and northern summer ($e_{\mathrm{max},270} - e_{\mathrm{max},90}$ scenarios, see Table 4.2). Maximal eccentricity and obliquity are assumed. The more elliptically-shaped orbit leads to a luminosity difference between perihelion and aphelion of about 28% (present: 6.7%). As with obliquity change, the global mean annual temperature is virtually unaffected. The major changes can be found in Southern Gondwana as well as in the polar ocean regions on both hemispheres. In the north polar region lower SSTs are observed all year round for perihelion in winter and aphelion in summer since the sun of the polar day is considerably weaker to warm the ocean. Moreover, sea ice formation is enhanced. The icesheet is about 25% larger and thus the difference is largest in March with 2.5 K and still about 1 K on annual mean. Analoguously, the southern polar ocean and the far south of Gondwana are warmer by about 0.5 K for perihelion in summer and aphelion in winter. The impact is less pronounced due to the absence of sea ice. Sea ice exists during winter in the very south of the Tethys Ocean. The size of the icesheet is doubled when the summer coincides with the aphelion. The winter temperature at the adjacent region is consequently lowered by about 3 K between June and August. Hence, the perihelion during summer seems to induce higher temperatures in mid- and high latitudes and to overcompensate the weaker irradiation during the winter season and aphelion on both hemispheres. The precipitation distribution is again not altered significantly.

The difference of solar luminosity between perihelion and aphelion depends on the eccentricity of the Earth's orbit. The above comparison considers the maximal effect in the course of the Milankovitch cycle. For minimal eccentricity (e_{min} scenario, see

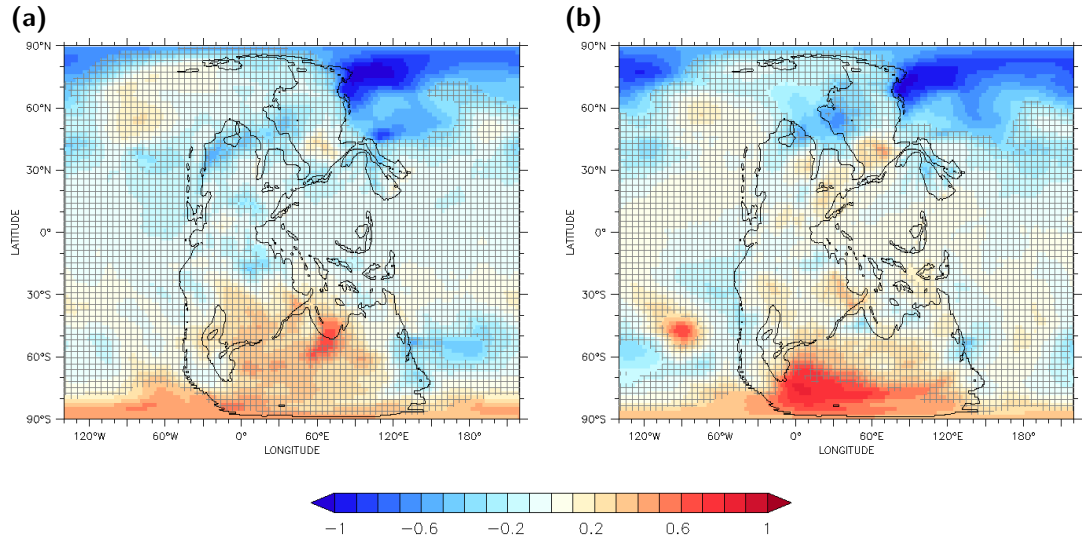

Figure 5.17.: Impact of orbit change on simulated Permian climate for 4×CO_2 scenario: In the course of the Milankovitch cycle the eccentricity of the Earth's orbit varies between $e = 0.005$ and $e = 0.07$. Furthermore, the axial precession shifts the longitude of the perihelion. (a) Difference of mean annual temperature [K] for perihelion in summer on Southern and Northern Hemisphere and maximal eccentricity and obliquity ($e_{\text{max,270}} - e_{\text{max,90}}$ scenario. (b) Difference of mean annual temperature [K] for maximal and present-day eccentricity in case of maximal obliquity and perihelion in southern summer ($e_{\text{max,270}} - \theta_{\text{max}}$ scenario). In hatched areas the difference is not highly significant based on an unpaired Student's t test and on a significance level of 1%.

Table 4.2) the orbit is almost circular and the luminosity of the perihelion equals the luminosity of the aphelion. The climate impact for fixed perihelion longitude but varying eccentricity is presented in Figure 5.17(b). The diagram shows the difference of mean annual temperature between the scenario with maximal eccentricity and present-day eccentricity ($e_{\text{max,270}} - \theta_{\text{max}}$ scenario, see Table 4.2). The perihelion is set to the summer of the Southern Hemisphere and the obliquity is maximal. Again, the significant differences arise primarily in the polar regions of both hemispheres. As the northern summer coincides with the aphelion, the high eccentricity causes reduced solar irradiation for that season. Consequently, the polar ocean is warmed up less during the polar day and sea ice formation during winter further enhances the difference. The temperature impact is again about 1 K on annual average. The south polar region is warmed considerably stronger in summer for high eccentricity. The polar ocean as well as the south of Gondwana are about 0.5-1 K warmer on annual mean and the temperature increase is most pronounced at the end of the summer season (2-2.5 K). The winter temperatures do not differ much and in June, at the time of aphelion, the scenario with high eccentricity is even about 1 K cooler. Again, the precipitation distribution is not altered significantly as precipitation is already scarce in polar latitudes. The minimal eccentricity of the Milankovitch cycle is even slightly lower than the present-day orbit. However, the impact on the mean Permian climate state is not significant (not shown).

The arrangements considered so far are special scenarios to separate the climate impact of single fluctuations in the course of the Milankovitch cycle. The superposition of all effects can possibly further enhance or weaken the resulting temperature change in some regions, but the single fluctuations provide a good first-order approximation to estimate the impact. Furthermore, the scenario representing average and maximum conditions are examined in the following and compared to the reference scenario with present-day orbit and axial orientation.

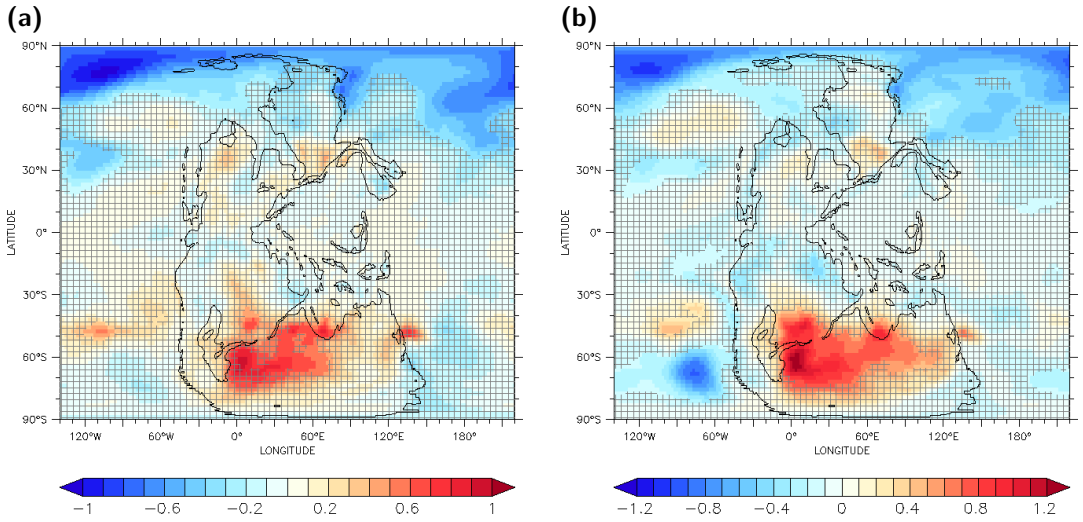

Figure 5.18.: Impact of orbital forcing in the course of Milankovitch cycles on simulated Permian climate for $4\times CO_2$ scenario: The simulated mean climate state for medium and extreme orbit configurations is compared to the mean climate of the reference simulation with present-day orbit. (a) Difference of mean annual temperature [K] for medium obliquity and eccentricity with perihelion in spring/autumn (ave-scenario in Table 4.2). (b) Difference of mean annual temperature [K] for maximal obliquity and eccentricity, enhanced by perihelion in southern summer ($e_{\mathrm{max},270}$ scenario in Table 4.2). In hatched areas the difference is not highly significant based on an unpaired Student's t test and on a significance level of 1%.

The climate impact for medium positions of the Milankovitch oscillations is represented in Figure 5.18(a). The obliquity is slightly lower by 0.14°, the eccentricity is approximately doubled and the perihelion is set to the spring/autumn season (ave scenario of Table 4.2), i.e. the irradiation is equal for both hemispheres despite the more elliptical orbit. Due to the change to a more elliptical orbit, the difference of solar luminosity between the perihelion and aphelion is increased from 6.7% to 12%. The diagram shows the impact on the mean annual temperature. However, the temperature change is only significant in some regions of the Permian Earth and the global mean annual temperature remains constant. The most prominent changes arise in the northern polar region over the polar ocean and in Central Gondwana east of the Paraná-Karoo-Inland Sea. Over the northern polar ocean the temperature is decreased by 0.6-1.0 K on annual mean and

the change is strongest over the Central Panthalassa. The seasonal breakdown reveals that the effect mainly occurs during the winter season. It is maximal in Februay and March when the mean monthly temperature is even decreased by 3.0 K. In this region, the solar irradiation is reduced during winter since the perihelion is shifted to the end of March and the distance from the Sun is enlarged. The slight change of obliquity is negligible. As a consequence the formation of sea ice is enhanced and the area covered by sea ice is increased by about 30% in March. The ice-albedo feedback further amplifies the temperature difference. The sea ice still melts completely by July and that is why the impact on the mean annual temperature is only moderate. In Southern Gondwana the mean annual temperature is increased by 0.8 K. As in the North the warming is not permanent but can be observed mainly in winter, in July and August. At that time the mean monthly temperature rises by about 3.8 K. As the southern winter season coincides no longer with the aphelion the distance from the Sun is reduced. Thus, solar luminosity is increased as well as the temperature. Furthermore, the warming is enhanced by the ice-albedo feedback since the ice coverage of the Paraná-Karoo-Inland Sea is reduced by 15%. The westerly winds further advect the warmer air into the continental interior. Precipitation does not change significantly.

The maximal impact is supposed to be induced for maximal eccentricity, maximal obliquity, and perihelion during southern summer ($e_{\max,270}$ scenario). As with the other cases the mean annual temperature is virtually not affected globally. The local effects are shown in Figure 5.18(b). Significant temperature changes can be found in the northern and southern polar oceans and Southern Gondwana. The Northern Panthalassa is about 0.5-1 K cooler on annual average. The impact is strongest far away from the continents. The higher obliquity reduces the solar irradiation in polar latitudes during the winter season but this is partly compensated by higher luminosity as the northern winter coincides with the perihelion passage. Similarly, the reduced luminosity during the aphelion passage in summer is compensated by higher irradiation because of the higher obliquity. As a result the temperature difference is smaller in summer and larger in winter. Due to enhanced sea ice formation, it is maximal in March in the Central Panthalassa (3.5 K). The southern polar Panthalassic Ocean receives higher solar irradiation during the perihelion passage in summer, but also considerably less during the prolonged polar night that coincides with the aphelion passage. The latter effect prevails on annual average and as a consequence the ocean temperature is reduced about 0.4-1 K at the surface. In contrast, the faster warming of the continent prevails in Southern Gondwana. Furthermore, sea ice formation in the Southern Tethys Ocean is suppressed because the nearshore ocean is warmed slightly so that the ocean temperature does not fall below the freezing point. The sea ice of the Paraná-Karoo-Inland Sea is also extended less. The ice-albedo feedback enhances the difference and causes considerably higher winter temperatures in the continental interior of Southern Gondwana. The temperature difference is up to 1.2 K on annual average and reaches 4.5 K in August. The precipitation barely varies on a large scale.

The above discussion focusses on changes of the Earth's motion and the resulting

consequences for the solar irradiation. Another possible mechanism for changing the radiative forcing is changing the stellar luminosity of the Sun itself (see Section 2.4.1). Stellar models predict that the luminosity of the Middle Permian was reduced by 2.6% compared to the present-day luminosity. The reduced luminosity has been used for the simulation of the reference climate. In order to estimate the magnitude of the impact, the reference climate is compared to a scenario that assumes present-day solar luminosity.

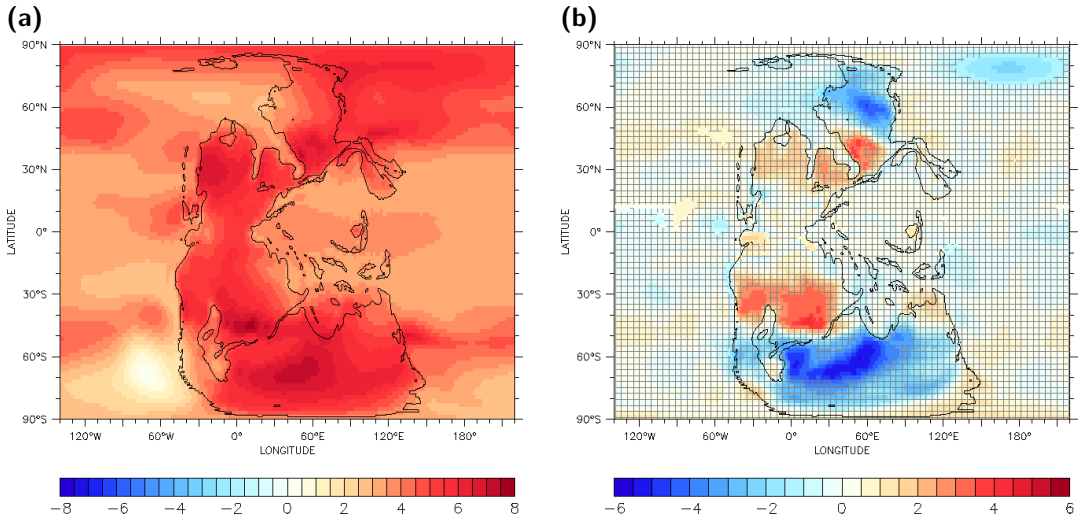

Figure 5.19.: Impact of solar luminosity change on simulated Permian climate for $4\times CO_2$ scenario: The simulated mean climate state that results for present-day solar luminosity is compared to the mean reference climate that is based on a luminosity reduced by 2.6%. (a) Difference of mean annual temperature [K]. (b) Difference of temperature seasonality with respect to July- and January-temperature [K]. In hatched areas the difference is not highly significant based on an unpaired Student's t test and on a significance level of 1%.

The global mean annual temperature increases to 22.51°C (+4.11 K). In general, the land is affected more (land: +5.28 K, sea: +3.67 K). The local effect on mean annual temperature and temperature seasonality is presented in Figure 5.19. With regard to the annual average temperature the strongest warming occurs in the continental interior (+7 K on annual average) of Gondwana in both mid- and high latitudes. Most of Pangaea is at least 5 K warmer, except for Eastern Angara (2 K). As there is no sea ice at any time of the year, the mean temperature of the northern polar Panthalassa is also increased considerably (5-6 K). The rest of the ocean is merely warmed by about 3 K. The simulated mean climate for present-day luminosity corresponds approximately to the climate of the $8\times CO_2$ scenario with deviations of less than 1 K. In Northern Angara and Southern Gondwana the winter temperatures are increased particularly. That way the seasonal difference is reduced (see Figure 5.19) by 4 K (Angara) or 6 K (Gondwana), respectively. In mid-latitudes, between 20 and 50° of latitude, the winter temperature

of both scenarios is similar, whereas the higher luminosity causes considerably higher summer temperatures. The impact is similar in Northern Gondwana, Southern Angara, and Baltica (+4 K) and less pronounced in Laurentia (+2 K) because of cooler ocean currents. The temperature seasonality of the near-equatorial area of Pangaea, the Tethysian microcontinents as well as the oceans is not altered significantly.

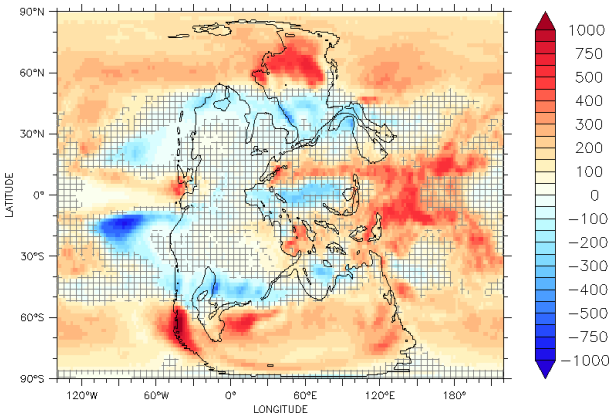

Figure 5.20.: Impact of solar luminosity change on simulated Permian climate for $4\times CO_2$ scenario: The simulated annual precipitation [mm] of the mean climate state that results for present-day solar luminosity is compared to the mean reference climate based on reduced luminosity. In hatched areas the difference is not highly significant based on an unpaired Student's t test and on a significance level of 1%.

The elevated temperature causes higher precipitation as evaporation and the water holding capacity of the air are both enhanced. The impact on the total annual precipitation amount is shown in Figure 5.20. On the one hand the precipitation is considerably increased due to stronger evaporation over the polar oceans (∼100 mm), also during the polar night, the near-equatorial Tethys Ocean (∼300 mm) and the low-latitude Western Panthalassa (∼450 mm). The westerlies carry more humid air into the interior of Angara and Gondwana or cause enhanced precipitation along the western sides of the Ural and South Gondwanan Mountains (up to 1,200 mm). On the other hand the dry areas in mid-latitudes are extended further to higher latitudes and over the Western Panthalassic Ocean.

In summary, the fluctuation of solar irradiation in the course of the Milankovitch cycles primarily affects the temperature in polar latitudes. The effect on the mean annual temperature is in the range of ±1 K in most cases, but the effect on the mean monthly temperature can also reach up to ±4 K. Due to the ice-albedo feedback, the impact is especially high when the sea ice formation is affected. Although there is no icesheet in the Southern Panthalassic Ocean, the small icesheets within the Paraná-Karoo-Inland Sea or the Southern Tethys Ocean significantly influence the climate of Southern Gondwana. The difference of solar irradiation is more crucial during summer than winter. The precipitation formation is not altered significantly and thus the observations of stronger monsoon circulation on an idealised Pangaean continent by Kutzbach [69]

cannot be confirmed. Higher solar luminosity causes considerably higher temperatures and increases the annual precipitation amount in most regions.

5.3. Uncertainties of Palaeoclimate modelling

In the previous section the sensitivity of the simulated Permian climate to several external and model-intrinsic factors has been examined. Figure 5.21 and 5.22 summarise the resulting variations around the mean reference climate and estimate the uncertainty range for the simulated Permian climate. In the diagrams the mean annual temperature and integrated annual precipitation are considered along two different meridians: across Gondwana, Euramerica, and the Northeastern Panthalassic Ocean (0°E); and across the Panthalassic Ocean (140°W).

As the previous analysis has shown the variation of atmospheric carbon dioxide content, solar luminosity, but also the choice of convection parameterisation have a distinct impact on the simulated climate. The altered radiative forcing impacts evenly on the mean annual temperature and only the sea ice in polar latitudes might amplify the deviations for colder scenarios due to the albedo-temperature feedback. Over land the precipitation amount basically increases with higher radiative forcing near the equator and in mid- and high latitudes. Furthermore, the poleward extent of the subtropical arid areas grows. Over the ocean the precipitation amount increases evenly except for the arid belt at the equator. As a consequence of the relatively large uncertainty range of the Permian carbon dioxide content (200-2250 ppm) the uncertainties of annual mean temperature are 5-7 K (smaller over the ocean, even larger near the poles) and about 250 mm for the precipitation amount, which is rather large as well. The uncertainty due to solar luminosity is approximately similar, since the maximal effect of an increase to the present-day intensity resembles the effect of doubling the atmospheric carbondioxide to $8\times CO_2$, for both temperature and precipitation. The temperature impact due the Zhang-McFarlane-Hack convection scheme is negative in lower latitudes and positive in higher latitudes, but mostly within this range. In contrast, the annual precipitation amount is decreased considerably and zonal differences are reduced. Compared to the above uncertainties, the influence of vegetation distribution and fluctuations of solar irradiation in the course of the Milankovitch cycles is weaker, even though marked seasonal and local alterations can arise.

The sensitivity studies have examined the separate climate impact of the specific factors. However, coinciding impacts can amplify or compensate each other. That is why the separate analyses shall be treated as first-order estimations. Moreover, the scarce data of the Permian Earth on the one hand and model constraints on the other hand provide further uncertainties. These are summarised in the following and the magnitude of the respective impact is estimated.

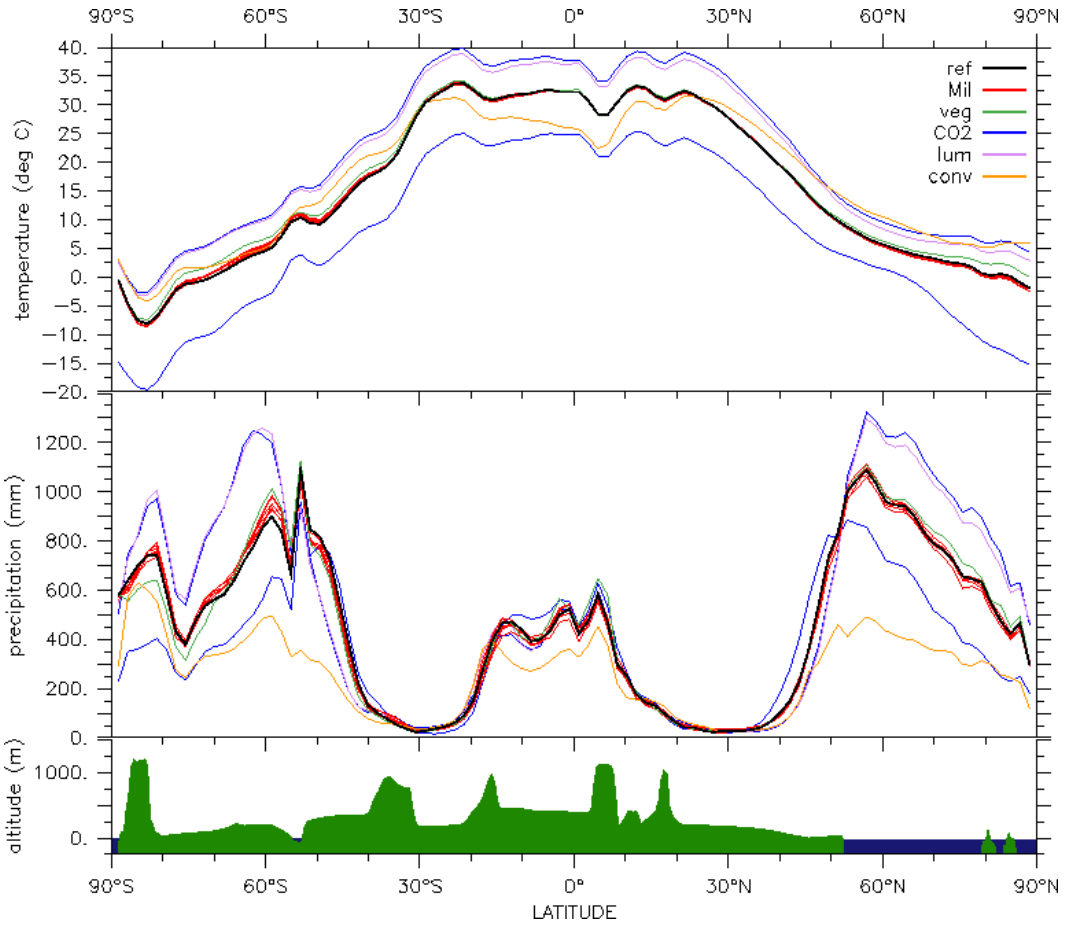

Figure 5.21.: Uncertainty range of simulated Permian climate: Mean annual temperature [°C] (top panel), integrated annual precipitation [mm] (middle panel), and orography [m] (bottom panel) along the 0°E meridian (across Gondwana, Euramerica, and the northeastern Panthalassic Ocean). The plot summarises the climate impact of radiation fluctuations in the course of the Milankovitch cycles, vegetation distribution, low and high atmospheric carbon dioxide concentrations within the uncertainty range for the Permian (200-2250 ppm, $\sim$1-8$\times CO_2$), higher solar luminosity, and the choice of different convection parameterisation schemes.

Topography. The reconstructed Permian topography is based on a comprehensive geological record [1–3] and it is one of the best known topographies within the Palaeozoic and Mesozoic. However, small uncertainties exist about the exact merging of the subcontinents that form Laurasia and Gondwana. The potential displacements are rather small compared to the size of the grid cell of the T31 and T63 grids. Thus the impact on the simulated climate is negligible. In contrast, the exact amalgamation of Laurasia and Gondwana is less certain because palaeomagnetic data of Gondwana is scarce. The Permian topography used in this work harks back to the reconstruction by Wegener [162]. A second attempt places Gondwana further northwest [163]. Fluteau et al. [87], however, have shown that the first configuration better reproduces the indicated

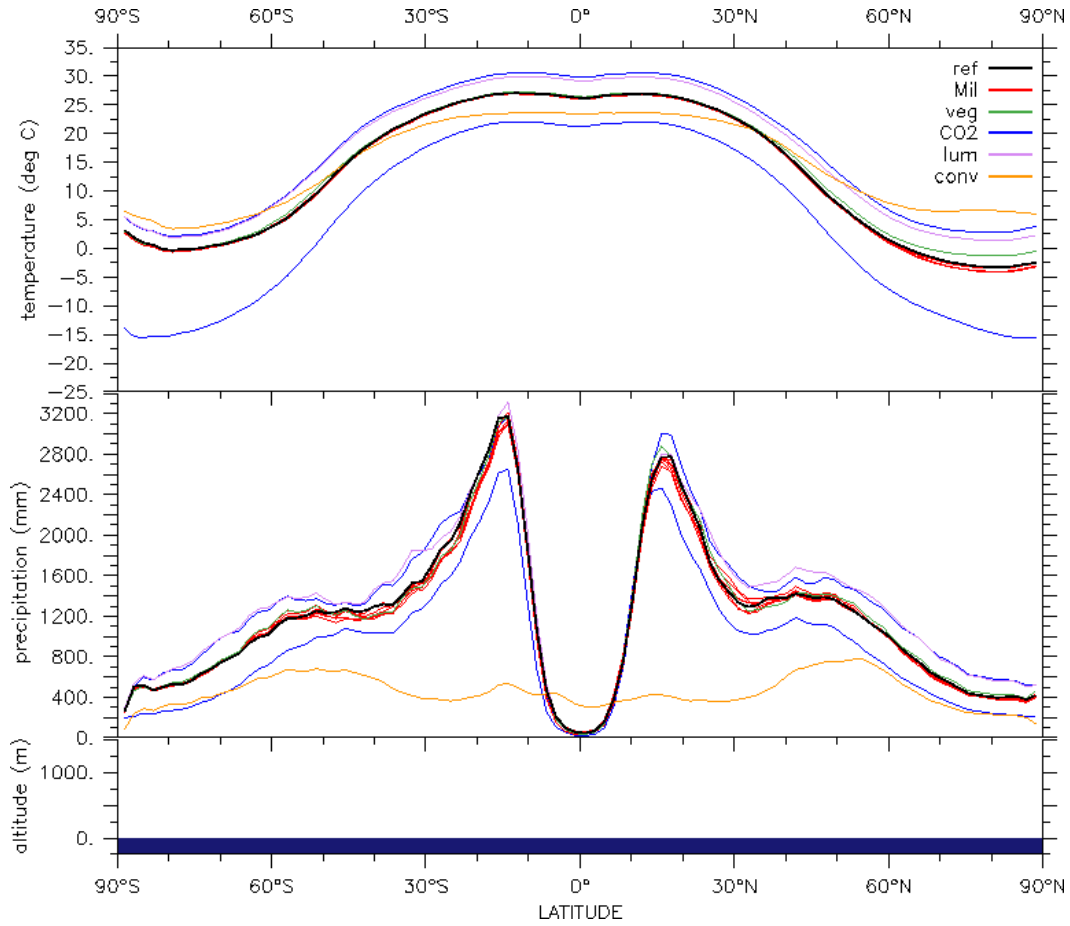

Figure 5.22.: Uncertainty range of simulated Permian climate: Mean annual temperature [°C] (top panel), integrated annual precipitation [mm] (middle panel), and orography [m] (bottom panel) along the 140°W meridian (across the Panthalassic Ocean). The climate impact of radiation fluctuations in the course of the Milankovitch cycles, vegetation distribution, low and high atmospheric carbondioxide concentration within the uncertainty range for the Permian (200-2250 ppm, ∼1-8×CO_2), higher solar luminosity, and the choice of different convection parameterisation schemes is summarised.

climate. A different amalgamation would probably change the local climate considerably when the latitude or the distance to the ocean is altered, but global changes are supposed to be rather small. In addition the time of the merging is not clearly determined as well. Roscher and Schneider [164] assume the Rheic Ocean between Laurasia and Gondwana is only closed by the end of the Permian and that the Appalachian Mountains merely consist of a sequence of smaller mountains. They observe a less pronounced monsoon for an open Rheic Ocean since more moisture reaches the continental interior. Once the ocean is closed a cold ocean current along the Laurasian west coast blocks moisture coming with the westerly winds. This leads to aridification in the continental interior and a stronger monsoon system. The exact position of the Tethysian microcontinents is more uncertain as well. A shift to the North or South can implicate a shift into a different

climate zone. This solely affects the local climate of the respective microcontinent. As discussed in Section 2.2 Pangaea shifted northwards in the course of Permian. First this entails a shift of climate zones, and second circumpolar ocean currents arise and possibly cause warmer surface temperatures at the adjascent coasts when the South Pole is within the ocean [27].

Sea level. In contrast to the arrangement and location of the subcontinents, the height of the sea level remains rather uncertain. Sediments and fossils of flora and fauna indicate marine or terrestrial environment only in very few areas. In flat coastal areas small changes of sea level can shift the coastline considerably or even flood entire regions. The Zechstein Sea covered wide areas of Baltica for several times in the Late Permian, for example, and connected the Uralian Epeiric Seaway with the Tethys Ocean. The advance of the sea reduces seasonal temperature differences and provides moisture in the adjacent regions.

Orography. The exact altitude of the main mountain system is controversial (see Section 2.2). However, a moderate elevation of the Appalachian and Uralian Mountains like it is assumed for the simulations of this work seems more plausible. Higher elevation would affect the atmospheric circulation in the boundary layer considerably and provide stronger rain barriers that would alter the global precipitation pattern [87]. The southern edge of the South Gondwanan Mountains is most likely exaggerated and the induced precipitation overestimated. The overestimation of precipitation at very strong ascents is a common issue of several global and also regional models at the ascents of the Andes along the west coast of South America [165, 166]. There were most likely some additional small mountains within the widespread plains, but the climate impact is supposed to be rather small. The available orographic data is too coarse to resolve small-scale orographic structures. That is why the generation of the surface roughness dataset required the inclusion of randomly generated subgrid-scale mountain ridges (see Section 4.1.3) that affect the generation of atmospheric turbulences in the boundary layer. Hence, the depending processes should be regarded with care.

Lakes. The geological record contains evidence of lacustrine environments in Gondwana (see Section 2.2). The employed orography includes the Paraná-Karoo-Inland Sea and further lakes where the orographic dataset exhibits negative elevation within the continent. On the one hand further lakes could exist that provide additional moisture sources in the continental interior and cause a more humid and moderate climate in the adjacent region [36]. On the other hand the assumed lakes can be drained and less moisture is available. The lake model is limited to extensive lakes. That is why a bias towards a more arid climate is likely.

Hydrological discharge. The hydrological retention properties and main directions of riverflow for the Permian Earth are merely generated by means of the relatively coarse $0.5° \times 0.5°$ grid. Small-scale structures that influence the river course are not considered. As a consequence the waterflow into the ocean can be underestimated, exaggerated, or the outfall is placed wrong. In the ocean the salinity near the coast is

affected primarily, but additional effects on the ocean circulation and the sea level are possible. The impact on the climate is supposed to be relatively small compared to other uncertainties.

Bathymetry. As most parts of the Tethysian and Panthalassic ocean floor have subducted by present, the bathymetry is unknown for most parts of the ocean apart from the continental shelves. For the simulations of this work a constant ocean depth of 4,000 m is simply assumed. However, ocean ridges and trenches certainly existed in the Permian oceans. Simulations with estimated locations of ocean ridges have shown that the meridional ocean circulation is strengthened [23]. By this means the general ocean circulation is stimulated and the poleward heat transfer enhanced, especially in the Tethys Ocean [167].

Vegetation. The difference in vegetation distribution for prescribed and dynamical establishment as well as the climate impact has been examined in Section 5.2.3. The comparison has shown that the vegetation density has been overestimated in high latitudes and in the mid-latitude desert regions. The strength of the simulated vegetation-climate feedback within the model is reduced, however, since the dynamical vegetation model is not coupled online and only the first iteration step is considered. Moreover, the dynamical vegetation model is tuned for a present-day flora. The Permian flora differs significantly, as this flora is predominated by lycopods (Early Permian) and gymnosperms (Late Permian). Angiosperms, that predominate the present-day flora, merely established by the Cretaceous. It is more likely that the Permian flora is better adapted to Permian climate conditions. That is why the dynamically established vegetation probably underestimates the vegetation distribution and LAI and the best guess lies in between both reconstructions.

Soil. The soil type determines several properties of the land surface, like e.g. heat capacity and conduction, water capacity, and albedo. As there was no data on Permian soils available, a medium soil type ('Loam', see Section 4.1.5) is chosen for all regions. However, a larger variety of soil types with different thermal and hydrological properties probably also existed on the Permian Earth. As a result the heat and moisture exchange at the surface as well as the plant growth of the dynamical vegetation model can be affected. Furthermore, moist soil is darker and reduces the surface albedo. The impact of the changes is supposed to be of the same magnitude as the impact of the dynamical vegetation establishment.

Albedo. The generated albedo of bare soil and vegetated areas depends on the albedo coefficients of the different plant and soil types as they are used in the CCSM3/CLM [146]. The comparison with the allocated albedo as used in ECHAM5 [138–140] reveals that the albedo assigned for the Permian Earth is slightly lower for similar land surface types. This reduces the reflected radiation and leads to slightly warmer surface temperatures. The effect differs from region to region and is probably in the magnitude of less than 1 K.

Permian atmosphere. As summarised in Section 2.3 the composition of the Permian atmosphere was different than compared with the present day. For the simulations of this work fixed concentrations of methane, nitrous oxide, and ozone are prescribed and only the carbon dioxide content is varied. However, methane, nitrous oxide, and ozone also contribute to the greenhouse effect and control the climate via radiative forcing. The methane concentration is assumed on the basis of mass balance models and these predictions have relatively large errors as well. The ozone and nitrous oxide concentrations are even just set to preindustrial (aqua-planet) conditions. Thus, there is considerable uncertainty about the concentration of the greenhouse gases. Due to the smaller concentrations, the possible effect on the climate is supposed to be less strong than for carbon dioxide in spite of the larger greenhouse properties. The oxygen concentration, that was slightly higher in the Middle Permian, does not affect the climate. Aerosols are not considered, but they certainly existed in the Permian atmosphere. The mean lifetimes of aerosols in the troposphere are relatively short and some of the main sources like forest fires and volcanic eruptions are also only active for a relatively short time. However, strong eruptions and convection can transport aerosols into the lower stratosphere. Moreover, aerosols from oceanic sources like e.g. carbonyl sulphides (COS) contribute continuously to the stratospheric aerosol layer. Brühl et al. [168] have shown that carbonyl suphides exist about 1-2 years in the stratosphere and strongly affect the radiative forcing. At the Permo-Triassic boundary the volcanic fields of the Siberian Traps were active for a long time and that is why the geological record can be biased.

Carbon cycle. The carbon cycle is not implemented in the EMAC framework and the carbon dioxide concentration is prescribed and fixed. Hence, the interaction of the established vegetation with the atmospheric carbon dioxide cannot change the concentration. On the one hand this influences the equilibrium of the Earth system, but on the other hand this would require a lengthy spin-up simulation to find the equilibrium and even several attractor states are possible. In order to mitigate this issue, a spectrum of different concentrations is considered.

Palaeorotation. The rotation of the Earth around its own axis was faster in the Permian than compared to the present day (see Section 2.4.2). Reconstructions based on geological records predict a day length of approximately 23 hours and 380 solar days per year. On the one hand the diurnal cycle of incoming radiation is accelerated, but on the other hand the Coriolis force is strengthened (Coriolis parameter is increased by about 4%). The latter influences the flow of air and water. Hence, effects on the mean pressure distribution and ocean circulation are expected and as a consequence on temperature and precipitation. The magnitude of the impact has not been examined since the Earth's rotation is deeply hard-coded in EMAC and hardly alterable.

Earth's orbit. The Milankovitch cycles include variations of the orbital eccentricity and axial tilt as well as the climatic precession due to precession of the Earth's axis and orbit (see Section 2.4.3). The impact of the single variations on the Permian climate has been studied in Section 5.2.4 and also the maximum impact has been estimated.

However, the study assumed the extrema of eccentricity and obliquity as they occured during the Quaternary. Different extrema are principally imaginable and would certainly alter the magnitude of the impact. As there is no evidence for a heavy meteoritic impact during the Phanærozoic that could have warped the Earth's motion significantly, a totally different orbit and axial tilt seem rather unlikely. The Milankovitch theory does not consider the precession of the ecliptic, i.e. the drift of the inclination of the orbital plane. The inclination drift with respect to the invariable plane of the solar system has a cycle of 100,000 years which is similar to the eccentricity cycle. This variation has no efffects on the incoming solar radiation at the Earth if taken by itself. Yet, it is possible that the orbit sometimes crosses or lies totally within areas with interplanetary dust accreting on the Sun through the destruction of a large comet, for example. Similar to volcanic dust emissions the accretion of the interplanetary dust in the atmosphere can induce cooling in the long-term, as it attenuates the incoming solar radiation and sinks only very slowly to the surface. Hence, the precession of the ecliptic can influence the global climate via this link [169]. The existence of the interplanetary dust for the Permian is rather speculative, but Farley [170] has shown that dust accretion occured about 1.5 mya, for example. Most likely the dust accretion would decrease the global mean annual temperature by 1-2 K and this impact might have biased parts of the geological record used as climate indicators.

Grid size. The GCM can only resolve processes on a length scale that is larger than the width of a grid cell and all remaining processes need to be parameterised. Consequently, the smaller the grid size the better the processes are resolved. The choice of the grid is always a compromise between computing time and resolution. The T63L31 grid employed for the atmosphere is commonly used for global climate simulations. The main features of the global climate are reproduced and the 31 vertical levels satisfyingly resolve the atmospheric circulation and transport processes in the troposphere and lower stratosphere. This applies for the present-day as well as for the Permian Earth. Higher resolutions would probably not provide considerably more information. The impact due to the grid transition from T31L19 to T63L31 after spin-up is discussed below. The GR30 horizontal ocean grid has a similar size of the grid cells on average. The vertical resolution L20 of the ocean is rather coarse, however and an ocean model consisting of 40 levels can presumably resolve the vertical ocean circulation better.

Parameter tuning. The spin-up procedure has shown that for a free-running coupled atmosphere-ocean GCM wrongly tuned free parameters controlling radiative forcing of subgrid-scale processes lead to an aberrant climate state (see Section 4.4). However, the optimisation is virtually impossible for a palaeosetup. The testing for a present-day setup showed satisfying behaviour for both T31 and T63 grids. The grid transition from T31 to T63 after the spin-up procedure caused an increase of mean global temperature by 0.35 K for the present-day setup and by 2 K for the $4\times CO_2$ Permian setup (see Figure 4.2(b)) which indicates the uncertainty range.

Cloud formation parameterisation. The more simple cloud scheme by Sundqvist [121] is employed for the simulation of the Permian climate, whereas the more complex

cloud scheme by Tompkins [122] is employed for the present-day setup (see Section 3.1.3). The Tompkins scheme is more sensitive to optimal tuning of free parameters and thus unsuitable for a palaeosetup. Sundqvist's scheme derrives the formation of clouds directly by the average water vapour and total cloud water content of the entire grid cell. It does not consider intrinsic fluctuations related to microphysical processes that could cause cloud formation before the grid cell mean reaches saturation. The global average precipitation amount is only slightly altered as testings for the present-day setup have shown. However, the Sundqvist scheme seems to promote the formation of large-scale clouds and in turn convective cloud formation and precipitation is considerably suppressed in the respective regions.

Conservation of energy, momentum, and water. The conservation of energy is not perfectly realised in EMAC-MPIOM as discussed in Section 4.4. The net radiation imbalance between incoming and outgoing radiation at the top of the atmosphere (model lid) is 1.17 $^{W}/_{m^2}$ for the T31L19 grid at the end of the spin-up period (see Table 4.3) which lays perfectly within the acceptable range. The imbalance for simulations with the T63L31 grid during the diagnostic period is relatively high but still acceptable, with 2.93 $^{W}/_{m^2}$ for the $4\times CO_2$ scenario. This difference results from the slight warming after the grid transition (see above) and indicates that the response of mid-level and deep ocean layers is still active. The impact has been smaller for the $10\times CO_2$ scenario, for example. Here the imbalance is also smaller (2.05 $^{W}/_{m^2}$). The conservation of momentum is not perfectly ensured at the atmosphere-ocean boundary where bilinear interpolation methods are employed for grid transformation of scalar fields such as wind stress or surface water velocity [98]. The closure of the hydrological cycle is satisfying as the sea level of the Permian oceans has virtually not changed in the course of 1,000 years of spin-up period.

Deep ocean. The temperature analysis of the ocean at the end of the spin-up period has revealed that the deep ocean response is still active for ocean layers deeper than 1,000 m (see Section 4.4). However, only a very slight warming of the deep ocean has been observed for the $4\times CO_2$ scenario. Furthermore Liu et al. [156] have shown that the SST and the air temperature are virtually not affected. The vertical ocean circulation is expected to be slightly decelerated since the vertical gradient is reduced. In general, a higher vertical resolution would describe the vertical exchange and the vertical circulation more precisely as discussed above.

Oceanic heat transport. The meridional heat transport from the equator to the poles is a crucial issue for the simulation of realistic palaeoclimates. Simulations with coupled mixed layer ocean models have revealed that diffusive heat transport is not sufficient to reproduce the climate indicated by the geological record [73, 74]. The oceanic heat transport by EMAC/MPIOM is evaluated in Section 5.4 (see Figure 5.29). In comparison with results from other models it is satisfying in lower latitudes but rather weak in mid- and high latitudes, particularly in the Northern Hemisphere. A higher vertical resolution of the ocean grid and a better representation of the bathymetry

would describe the vertical branches of the ocean circulation more precisely and, most likely, improve the poleward heat transport by the ocean even further.

Sea ice. Since the albedo of sea ice is considerable higher than of the unfrozen ocean, the formation of sea ice has a great impact on the local climate because of the temperature-albedo feedback on the one hand. On the other hand the icesheet disables the coupling of atmosphere and ocean. That is why the distribution of sea ice has a strong impact on the climate in polar latitudes, the ocean circulation, and the poleward heat transport in general. Originally small temperature differences are strongly amplified and lead to totally different climate states in the end. For the simulated Permian climate this is particularly crucial in northern polar regions as it has been observed in Section 5.2.4. The formation of sea ice is triggered by the sea ice model (see Section 3.1.2) and unfortunately the uncertainties in sea ice modeling are relatively large [158, 171]. Goosse et al. [157] ascertain that the behaviour of sea ice models is generally similar for palaeoenvironments and the present-day arrangement unless different feedback processes or boundary conditions predominate. The validation of MPIOM coupled to ECHAM5 for Arctic sea ice reveals that the ice extent in winter conforms well with observations, but the predicted extent in summer depends strongly on the atmospheric forcing and the interannual variability is underestimated considerably [172]. In contrast, Hübner [173] observed good agreement in area and variability for the Arctic for ECHAM6/MPIOM, whereas the minimal extent is underestimated by a factor of 3.7 for the Antarctic sea ice and only the saisonal cycle is well reproduced. Evaluating EMAC-MPIOM Pozzer et al. [98] have shown that the simulated sea ice coverage slightly overestimates observations and exhibits much larger interannual variability. The Permian topography in the northern polar region neither corresponds to Arctic conditions with an enclosed basin nor to Antarctic conditions with a central continent. The open Panthalassic ocean rather resembles Antarctic conditions, presumably, and the area north of Angara is rather similar to Arctic conditions. That is why the ice extent in the open ocean is probably slightly underestimated and the sea ice could possibly persist during the summer in some areas. In contrast, the sea ice along the east coast of Angara is probably slightly overestimated.

5.4. Evaluation: Comparison with Data and other Simulations

The availability of data indicating the climatic conditions on the Permian Earth is rather scarce within the geological record and spatially not well distributed. The different methods and results have been summarised in Section 2.5. The second option to evaluate the simulated climate is the comparison with simulation results from other models. In general, the evaluation has to be done with caution. On the one hand the geological data is potentially biased or not available for all regions. The climate models further employ rather coarse resolution or simple models for the ocean domain. On the other

hand the uncertainties discussed in Section 5.3 have to be considered. In the folllowing, the agreement of the simulated Permian climate with the data from the geological record is examined first and second, the simulated climate is compared with the climate simulated by other models.

Royer et al. [6] have reconstructed tropical sea surface temperature deviations relative to the present day for the entire Phanærozoic on the basis of $\delta^{18}O$ carbonate record from shells in shallow tropical seas (see Section 2.5.1). They predict an increase of tropical SST from 1 K lower than at present for the Permocarboniferous to about 6 K warmer than at present for the Permo-Triassic boundary. Hence, the prediction for the Kazanian stage and the Middle Permian lays in between at 3-4 K warmer than at present. The deviation of tropical SST for the simulated Permian climate of the $4\times CO_2$ scenario to a present-day reference climate is +2.7 K, which is in good agreement with the prediction of the carbonate record. Furthermore, the agreement is best for $4\times CO_2$ content in the atmosphere ($2\times CO_2$: +0.4 K, $6\times CO_2$: +4.5 K).

The type of sediment in the geological record can provide information about the net water balance and indicate either wet or arid conditions (see Section 2.5.2). The compilation of climate-sensitive sediments by Ziegler, Gibbs, and Hulver [3] predicts wet conditions for Angara and Gondwana in mid-latitudes and also coastal regions in high latitudes, as well as North China, the east coasts of South China and some Cimmerian microcontinents. The wet climate is reproduced by the simulation for Angara, Gondwana, and the tropical microcontinents (see Figure 5.4(b)). Disagreement merely arises for North China where the simulated climate predicts arid conditions instead. The sediment data exhibits evaporite finds indicating arid conditions for western near-equatorial Pangaea, the continental interior of Northern Gondwana, the north-eastern Tethys coast of Gondwana, and Southern Angara. This agrees with the simulation results along the Tethys coast and in the continental interior of Gondwana. However, the simulation predicts rather wet or at least seasonally wet conditions for the west coast region of near-equatorial Pangaea. As the evaporite sediments found in this region appear near the coast, they more likely indicate temporarily flooded area. Aeolian sands, that indicate desert areas, exist for Central Gondwana and Southern Baltica. Again, this confirms the simulation results as both regions exhibit virtually no precipitation. The sedimental record contains no evidence of glacial environments which is in agreement with the simulated climate as well. Warm-water conditions are indicated by organic buildups for the Euramerican Tethys coast, shallow areas around the Tethysian microcontinents, and the Pangaean west coast near the equator. The simulated SST is between 28-30°C in most of these regions and only off the Euramerican coast the SST falls to 24°C in winter. There is extensive evidence for red beds in Central Pangaea [75]. These occur in alternating wet and dry conditions, which agrees well with the seasonal shift of the precipitation area related to the ITCZ (see Figure 5.5). Consequently, the simulated climate of the $4\times CO_2$ scenario reproduces well the indicated climate conditions in most regions. Discrepancies appear in western equatorial Pangaea and North China where the simulated climate is too wet or too arid, respectively. The agreement of the simulated

climate with the sedimental data is also good for the $6\times CO_2$, $8\times CO_2$, and $10\times CO_2$ scenarios. However, the climate sensitivity of sediments is generally weak for warmer climate scenarios [89].

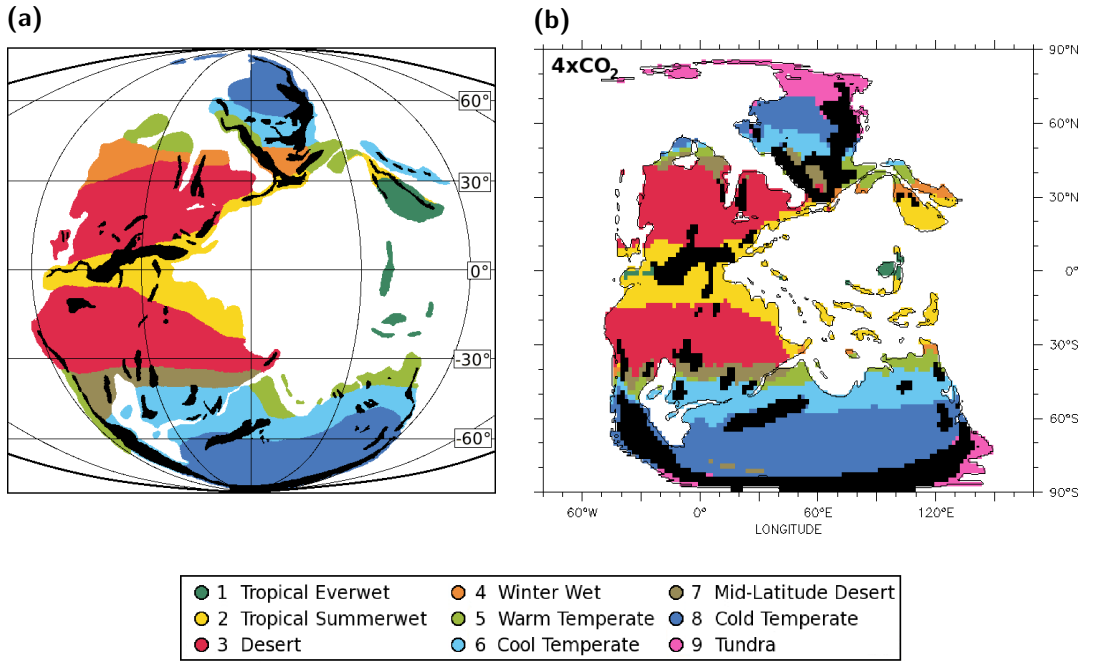

Figure 5.23.: Comparison of biomes with reconstructed biome distribution for Permian Earth based on sedimental and palaeobotanical data. (a) Data-derived biomes for Kazanian stage (see Section 2.5.3) from Rees et al. [73]. (b) Simulation with EMAC-MPIOM, $4\times CO_2$ reference scenario. Mean elevations of more than 600 m are shaded black to neglect elevation effects on the biome distribution.

In addition to the climate-sensitive sediments, palaeobotanical finds provide information on the vegetation and thus on the climate conditions of certain regions (see Section 2.5.3). Rees et al. [73] and Ziegler [76] combined both lithological and palaeobotanical data and assigned the phytogeographical units to the climate-based biome scheme by Walter [80]. The reconstructed biome distribution for the Kazanian stage is presented in Figure 5.23(a) (same as Figure 2.5). The biome scheme consists of ten different biomes. The details are summarised in Appendix B. The assignment of the biomes merely depends on monthly mean temperatures and precipitation amounts (see Table B.1). Therefore, the transformation of the simulation results into the biome system is straightforward. The simulated biome distribution of the $4\times CO_2$ scenario is shown in Figure 5.23(b).

Tropical everwet climate is indicated by the lithological and palaeobotanical data for South- and Indochina, Cimmeria, and the southern part of North China. This is, however, only reproduced to some extent by the simulation. Tropical everwet climate is simulated for South- and Indochina, whereas Cimmeria and southern North China

exhibit a shorter wet season and are assigned to tropical summer wet climate. The data predicts tropical summer wet climate for equatorial Pangaea and along the Tethys coast of Euramerica, Baltica, Southern Angara, and Northern Gondwana. This agrees very well with the simulated climate. Small discrepancies merely occur directly at the equator, where tropical everwet climate is simulated, as well as in the near-equatorial region and at the Tethys coast of Gondwana, where the biome is distributed even further. Both data and simulation predict tropical desert climate for the most part of Northern Gondwana that transitions into mid-latitude desert climate at 40°S. Along the southern Tethys coast warm temperate climate is indicated. This is well reproduced by the simulation except for the north-eastern tip where winter wet or tropical summer wet climate is assigned. However, this is more likely an artefact of the strict assignment. The cool temperate biome is evidenced for most of mid-latitude Gondwana and the high latitude region seems predominated by cold temperate climate. The simulation basically agrees with these predictions. The tundra biome is simulated along the southern coast, but there is no data available for this area. For the most part of Euramerica the tropical desert biome is predicted by data. Northern Baltica and Laurentia are assigned to winter wet or warm temperate climate. The model simulation reproduces the extensive tropical desert realm, but discrepancies occur for Northern Baltica and Laurentia. The simulated climate of these regions corresponds to tropical or mid-latitude desert biomes. The warm temperate biome only matches for Northern Laurentia, although even cool and cold temperate biomes are simulated further north. Hence, the simulated climate of mid-latitude Euramerica seems too dry and partly too cold. Similarly, in Southern Angara the mid-latitude desert biome is simulated by the model instead of the predicted winter wet biome. For Southeastern Angara and Northern Cathaysia there is evidence of warm temperate climate (Angara, Tarim), cool temperate climate (Amuria), and even tropical summer wet (North China). The warm temperate biome is well reproduced. Differences arise in North China, where the simulated climate is too cold in winter and rather corresponds to the winter wet biome, and Amuria, where the simulated climate is too warm and thus assigned to warm temperate and winter wet biomes. The data indicates cool temperate climate for Central Angara, warm temperate climate along the west coast, and cold temperate climate in high latitudes. The transition from cool to cold temperate biome is reproduced well, but the simulated climate seems generally biased to colder temperatures in Northern Angara. The cool temperate biome extends to the west coast and the area north of 70°N is assigned to the tundra biome instead. In summary, the simulated climate of the $4\times CO_2$ scenario agrees well with the lithological and palaeobotanical data, especially in the Southern hemisphere. The simulated climate seems too dry in northern mid-latitudes and most of the Tethysian microcontinents. Furthermore, the temperatures of Northern Angara seem too cold. The data coverage of both areas is relatively high.

The winter cooling in continental interiors is a relatively widespread disagreement between palaeoclimate model predictions and observations [62]. Higher mean temperatures in high northern latitudes are generated for higher atmospheric carbon dioxide concentrations. The biome distributions for the $8\times CO_2$ and $10\times CO_2$ scenarios exhibit cold

temperate climate also for Northern Angara, but the precipitation amount in northern mid-latitudes is still too low and the most parts of Euramerica and Southern Angara are even assigned to the tropical desert biome. Moreover, Cathaysia and Cimmeria are still too dry as well. Hence, higher atmospheric carbon dioxide concentrations are no remedy to overcome the issue as they, in turn, also entail significant summer warming, especially in lower latitudes [62]. The Zhang-McFarlane-Hack convection scheme as well as the altered vegetation distribution generate a warmer climate in Northern Angara (see Section 5.2.2 and 5.2.3). However, the biome distribution resulting for the Zhang-McFarlane-Hack convection scheme (not shown) exhibits tropical and mid-latitude desert climate in most parts of Pangaea and thus disagrees considerably with the data-derived biome distribution. The biome distribution that corresponds to the self-established vegetation distribution (not shown) is generally similar to the distribution for prescribed vegetation. The tropical summer wet biome is extended slightly further to the north and south, the transition from cool to cold temperate climate in Gondwana is shifted slightly further to the south, and the cold temperate climate in Angara is extended to 80°N. This restricts the tundra biome basically to the northern island arc. Hence, the simulated climate for self-established vegetation attains the best agreement with the lithological and palaeobotanical data, even though the mid-latitude belt is still too dry. The established vegetation reflects the discrepancies. C3-grasses constitute the predominating PFT in the dry mid-latitude belt across Northern Laurentia, Baltica, Southern Angara, and North China and Amuria. Similarly, Cimmeria and Indochina are mostly covered by C4-grasses instead of tropical evergreen trees. There is no vegetation cover on the northern island arc and in norther Angara where the simulated climate is too cold.

In contrast to the rather qualitative comparison with geological data, the simulated climate can be compared with other simulations of the Permian climate more quantitatively. Gibbs et al. [74] have employed the climate model GENESIS II to simulate the Permian climate for the Sakmarian and Wordian stage (see Section 2.6). They used a coarser atmospheric grid (T31L18) and a MLO model for the oceanic domain that only allows diffusive heat transport. The solar luminosity is assumed slightly higher. Their results for the Wordian stage are compared with the simulated climate of EMAC-MPIOM for the $4\times CO_2$ and $8\times CO_2$ scenario in the following. The global mean annual temperature of the $4\times CO_2$ scenario is similar for both models (EMAC-MPIOM: 18.4°C, GENESIS II: 18.8°C), whereas the climate simulated by EMAC-MPIOM is warmer for the $8\times CO_2$ scenario (EMAC-MPIOM: 22.9°C, GENESIS II: 21.4°C). For both scenarios EMAC-MPIOM simulates considerably warmer temperatures on land, whereas the ocean surface temperatures are slightly cooler. The mean global precipitation is approximately similar for both scenarios as well ($4\times CO_2$: EMAC-MPIOM: 3.0 $^{mm}/_{d}$, GENESIS II: 3.2 $^{mm}/_{d}$; $8\times CO_2$: EMAC-MPIOM: 3.2 $^{mm}/_{d}$, GENESIS II: 3.4 $^{mm}/_{d}$). This applies to precipitation simulated over both, land and ocean.

Figure 5.24 contrasts the zonal average surface temperature for the summer and winter season over land, whereas Figure 5.25 considers the temperature over the ocean. The

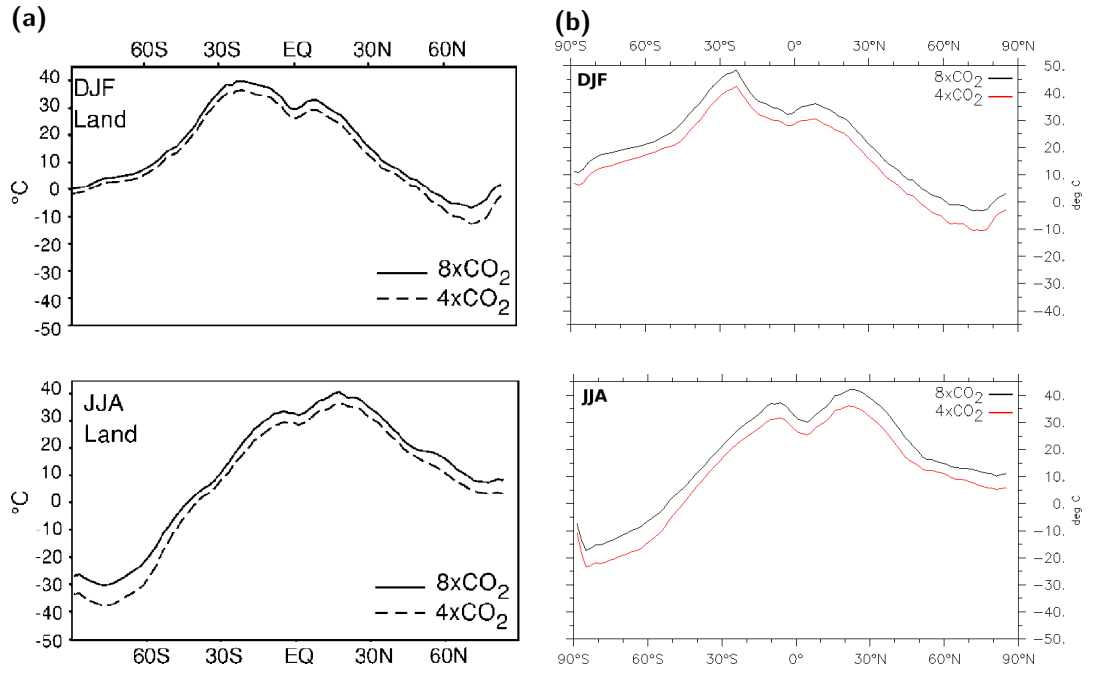

Figure 5.24.: Comparison of zonal average land surface temperature [°C] for $4\times CO_2$ and $8\times CO_2$ scenario. (a) Simulation from Gibbs et al. [74]. (b) Simulation with EMAC-MPIOM, $4\times CO_2$ reference scenario. Note the different scale of the temperature axis.

meridional profile of mean temperatures over land is generally similar for both models, but discrepancies occur for the extrema in the tropical deserts and polar regions. Near the equator the difference is relatively small with about 2 K. The zonal mean temperature simulated by EMAC-MPIOM is slightly warmer than the GENESIS II simulation for both scenarios for southern summer (27.9°C and 32.1°C at 3°S), whereas it is slightly warmer during the northern summer season (25.3°C; 30.0°C at 5°N). The warmest temperatures are generated for the tropical desert regions. They reach 42.5°C or 48.5°C, respectively, on the Southern Hemisphere during the summer season for EMAC-MPIOM, which is about 8-10 K warmer than for the GENESIS II simulation. The difference is considerably smaller during winter (about 4 K), however. In the Northern Hemisphere the temperatures are approximately equal in summer for both scenarios. In winter the $8\times CO_2$ temperature is slightly warmer for EMAC-MPIOM. The latitudes of the temperature maxima match well on both hemispheres. In the northern polar region the temperature minima in winter are −10.6°C or −3.3°C, respectively, as simulated by EMAC-MPIOM. This agrees well with the GENESIS II simulation and the difference is relatively small with 2 K. The same applies for the summer temperatures. However, the temperature difference is more distinctive in southern polar regions. There the summer temperatures differ by 8-10 K and in winter the difference reaches even 15 K. Thus, the zonal average surface land temperatures are similar in the Northern Hemisphere,

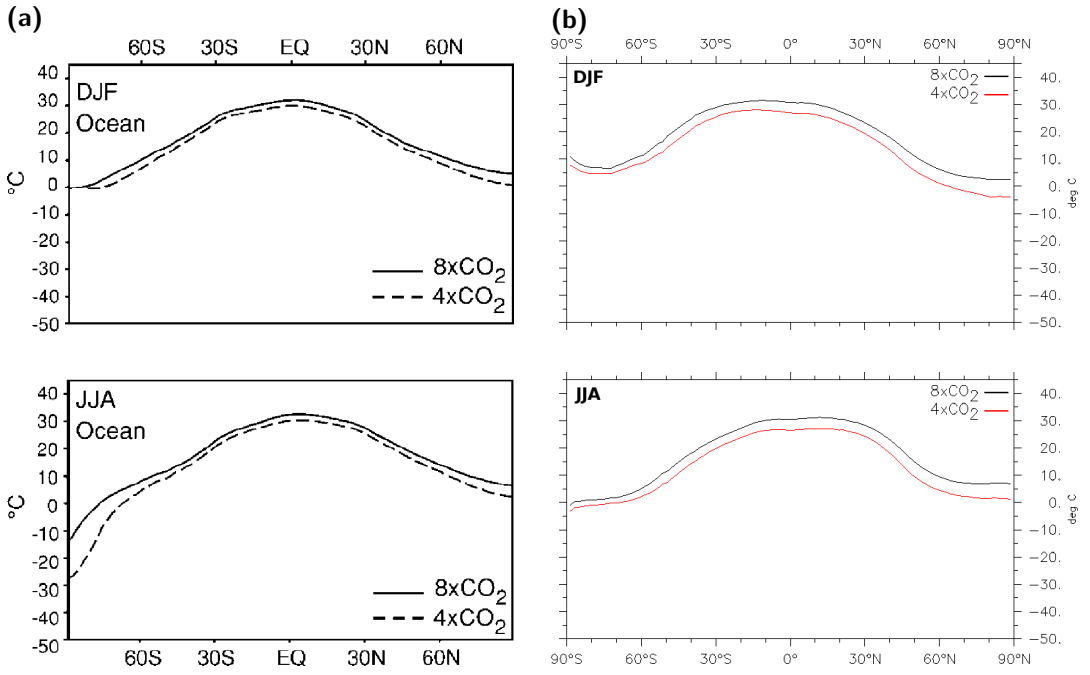

Figure 5.25.: Comparison of zonal average ocean surface temperature [°C] for $4\times CO_2$ and $8\times CO_2$ scenario. (a) Simulation from Gibbs et al. [74]. (b) Simulation with EMAC-MPIOM, $4\times CO_2$ reference scenario.

whereas the simulation by EMAC-MPIOM is considerably warmer in the Southern Hemisphere.

The zonal average SST also exhibits similar meridional profiles for both climate models. The SST of the tropical oceans merely differs by 1-2 K. This applies for both seasons. In the northern polar oceans the summer SSTs are approximately equal for both models and CO_2 scenarios (1.0°C and 6.7°C). The winter SSTs simulated by EMAC-MPIOM are −4.0°C or 2.4°C, respectively, which is about 4 K cooler than simulated by GENESIS II. In contrast, EMAC-MPIOM simulates considerably warmer SSTs in the southern polar ocean. The summer SSTs differ by 4-6 K for both scenarios and in winter the difference is even 24 K for the $4\times CO_2$ scenario and 14 K for the $8\times CO_2$ scenario. Hence, the meridional heat transport by the ocean is similar in the Northern Hemisphere, whereas the southward heat transport is significantly stronger for EMAC-MPIOM.

The zonal average precipitation over land of both climate models is contrasted in Figure 5.26. As before the winter and summer season are considered separately. In the tropics the precipitation maximum related to the ITCZ is about 3.5 $^{mm}/_{d}$ in southern summer for both models. However, the maximum is shifted to the South by more than 10° of latitude for EMAC-MPIOM. The location of the maximum in northern summer is equal for both models, but the mean daily amount is increased by about 1.5 mm.

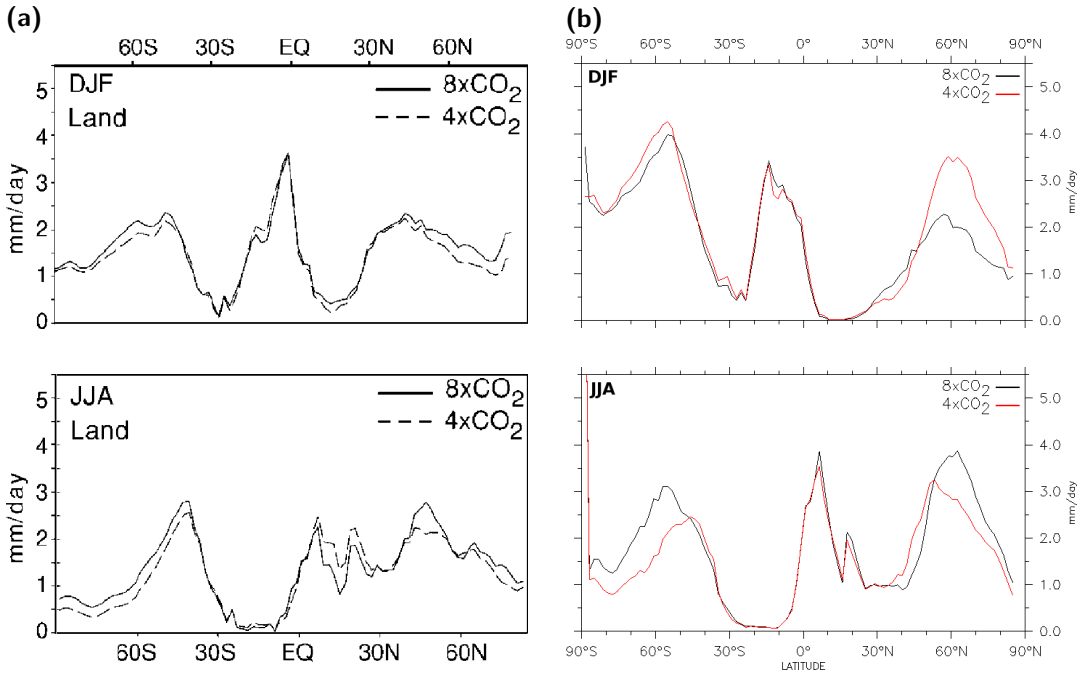

Figure 5.26.: Comparison of zonal average precipitation over land [mm] for $4\times CO_2$ and $8\times CO_2$ scenario. (a) Simulation from Gibbs et al. [74]. (b) Simulation with EMAC-MPIOM, $4\times CO_2$ reference scenario.

The second maximum is similar again for both models. In mid- and high latitudes the winter maximum is shifted further north or south, especially for the $8\times CO_2$ scenario (about 15° of latitude). The mean precipitation amount during winter is similar for both scenarios in the south, but increased by 1.5 mm in the north for the $4\times CO_2$ scenario. In summer the difference is 1-1.5 $^{mm}/_{d}$ for both CO_2 scenarios.

In summary, both zonal land and ocean temperatures are similar in the Northern Hemisphere, whereas EMAC-MPIOM generates higher temperatures in the Southern Hemisphere. The difference is especially high during southern winter, most likely because of the temperature-albedo feedback. Precipitation is enhanced in mid- and high latitudes.

Kiehl and Shields [8] employ the CCSM3 for their simulation of the climate at the Permo-Triassic boundary (see Section 2.6). In contrast to Gibbs et al. [74], they use a GCM for the oceanic domain and thus advective heat transport in the ocean is included. The ocean grid size is similar to the grid used for MPIOM in this work. The atmospheric grid is still rather coarse, however, since they also employ a T31 grid. The solar luminosity is assumed slightly higher. The atmospheric carbon dioxide content is adapted to the more extreme circumstances of the latest Permian and set to 3550 ppm

($10\times CO_2$ scenario). The comparison with EMAC-MPIOM is especially interesting because the prescribed vegetation and soil distributions are identical as well as the composition of the atmosphere.

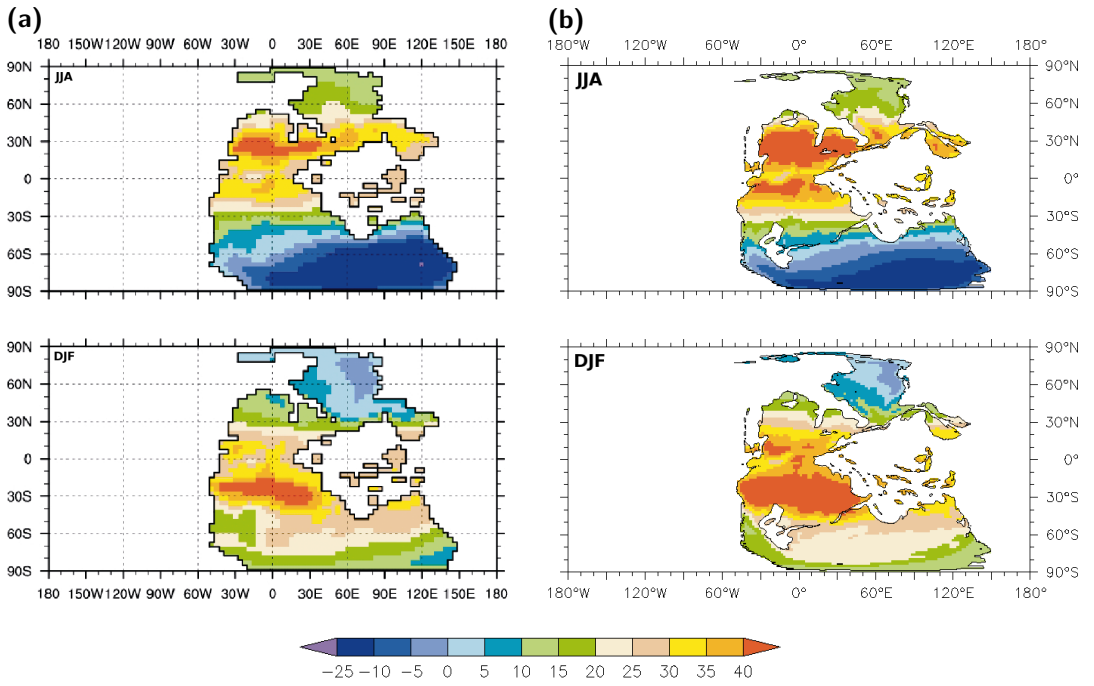

Figure 5.27.: Comparison of mean seasonal surface air temperature [°C] for summer and winter with Kiehl and Shields [8]. Both simulations assume $10\times CO_2$ for the atmosphere of the Permian Earth. (a) Simulation from Kiehl and Shields [8]. (b) Simulation with EMAC-MPIOM.

The mean seasonal surface temperature over land for summer and winter are contrasted in Figure 5.27. In spite of the slightly lower solar luminosity, the simulated climate of EMAC-MPIOM exhibits higher temperatures in several regions. This applies for summer and winter temperatures. The warming is observed across most parts of Gondwana, Euramerica, and Southern Angara, as well as on the Tethysian microcontinents. The difference is between 5-10 K in most regions. The hot desert area with mean summer temperatures over 40°C in Euramerica and Northern Gondwana extends about 10° of latitude further to the North and South in EMAC-MPIOM, but both regions are considerably warmer during winter as well. Similarly, the coldest region in Gondwana with mean winter temperatures below −10°C is restricted to the area south of 60°S, which is about 15° degrees further to the south than simulated by CCSM3. The continental interior of Southern Gondwana is also warmer during the summer season. The warming is not observed in Northern and Central Angara, however. The area north of about 45°N exhibits similar summer and winter temperatures as simulated by CCSM3 in contrast to the rest of Pangaea. The same behaviour is observed for the mean annual SSTs (not shown). The Tethys Ocean and the Panthalassic Ocean are 2-5 K

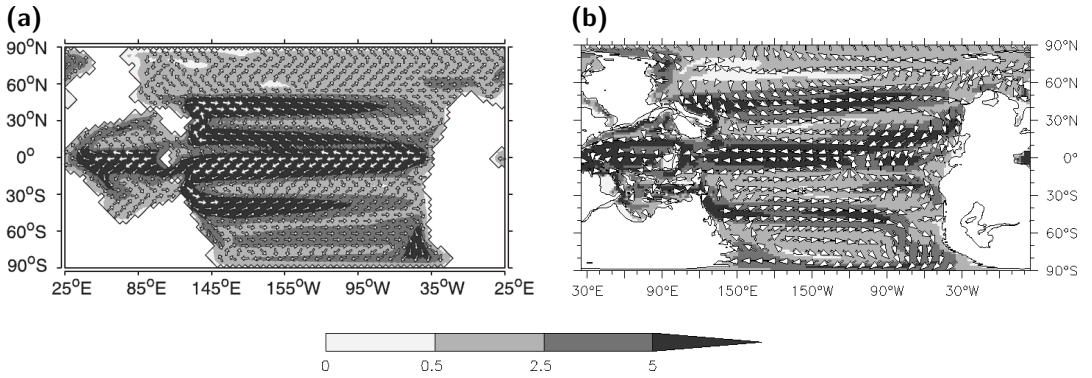

Figure 5.28.: Comparison of horizontal ocean circulation [$^{cm}/_{s}$] in near-surface ocean layers. Both simulations assume $4\times CO_2$ for the atmosphere and employ ocean GCM. (a) Simulation from Winguth et al. [27]. (b) Simulation with EMAC-MPIOM, $4\times CO_2$ reference scenario.

warmer in low and southern mid- and high latitudes, whereas the northern polar ocean is even slightly colder. Hence, the northward heat transport of EMAC-MPIOM seems to be weaker, which in turn further heats up the low-latitude regions. This confirms the results of the previous comparison with GENESIS II. The warmer conditions in Gondwana and Southern Laurasia most likely result from the finer grid and the better representation of small-scale processes.

The ocean circulation makes an important contribution to the heat transport from the equator to the poles. That is why the examination of the ocean circulation potentially reveals the reason for the asymmetric heat transport. Winguth et al. [27] performed a simulation of the Permian oceans for a $4\times CO_2$ scenario that was driven by the climate simulated by Gibbs et al. [74] (see Section 2.6). They employed the ocean GCM LSG on a grid comparable to the GR30L20 grid used in this work. Furthermore, they also assumed a flat bottom bathymetry at 4,000 m depth with smoothed continental margins. The deep-sea basin of the Tethys Ocean is assumed to be separated from the Panthalassic Ocean, however, and Pangaea is extended to the North and South Pole.

The resulting global SST distribution is similar to the distribution simulated by EMAC-MPIOM (not shown). For EMAC-MPIOM the tropical Tethys and Western Panthalassic Ocean are slightly warmer ($\sim$ 2 K), but the cold tongues off the Pangaean west coast are pronounced stronger and extended closer to the equator. Cooler SSTs are observed in the central Southern Panthalassic Ocean ($\sim$4-6 K) and in the entire Northern Panthalassic Ocean ($\sim$2-6 K).

The ocean circulation at the surface is contrasted in Figure 5.28. Both ocean models generate marked equatorial eastward currents, although they are less distinct in the Eastern Panthalassic Ocean for the MPIOM simulation due to the more rugged coastline. In the Tethys Ocean the ocean circulation generated by MPIOM is even stronger. The mid-latitude westward currents are slower in both hemispheres and the circulation

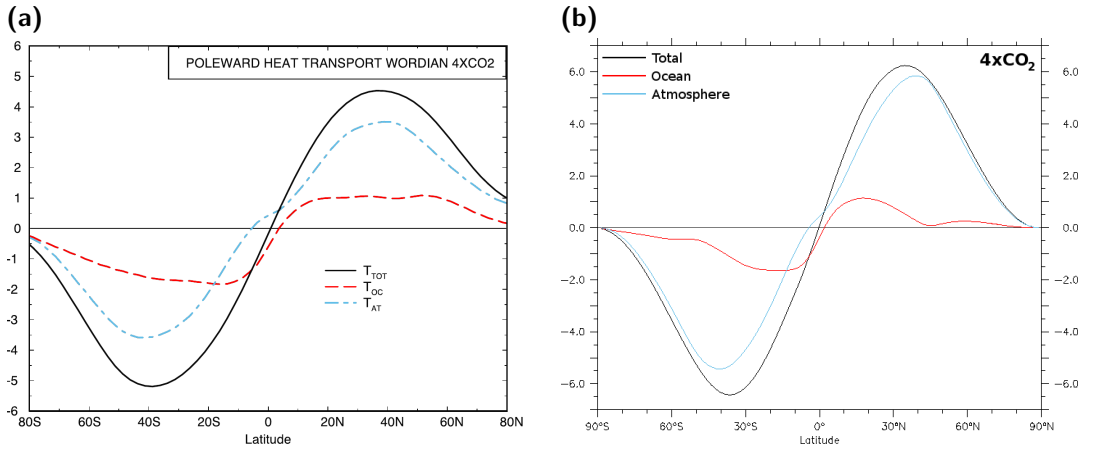

Figure 5.29.: Comparison of total, oceanic, atmospheric poleward heat transport [PW]. Both simulations assume $4\times CO_2$ for the atmosphere and employ ocean GCM. (a) Simulation from Winguth et al. [27]. (b) Simulation with EMAC-MPIOM, $4\times CO_2$ reference scenario. Note the slightly different ordinate scale.

in higher latitudes rather forms a large gyre that is connected to the circumpolar currents. The gyres are more distinct in the simulation by EMAC-MPIOM, especially in the Southern Panthalassa, as the circumpolar currents are suppressed in the LSG setup from Winguth et al. Consequently, the surface velocity is smaller near the centre of the gyres. The weaker heat transport to higher northern latitudes in the EMAC-MPIOM simulations can be explained by two aspects: First, the circulation in lower latitudes is stronger because the equatorward currents along the Pangaean west coast are significantly stronger. Second, the fraction of the warm equatorial current that is branched off to the north along the coasts of North China and Amuria (Cathaysia) is small and the most part continues into the Tethys Ocean. This is different for the LSG simulation by Winguth et al. where the major part is branched off to the north. The ocean ridge between the Tethys and Panthalassic Ocean, that is not assumed for the bathymetry in this work, is most likely the reason for this different behaviour. In the Southern Hemisphere the warm current along the Southern Tethys coast is not blocked by a landmass like along the northern coast. Thus, it continues into the Panthalassic Ocean where it is connected to the southern circulation. This compensates the missing warm water current branched off the equatorial current to the south. The behaviour is suppressed by the ocean ridge of the bathymetry of the LSG simulation, however. The effects on the poleward heat transport are illustrated in Figure 5.29.

Even though the maximal heat that is transported by the ocean (red curve) is similar for both models (north: 1.2 PW (ECHAM-MPIOM), 1.1 PW (LSG); south: 1.6 PW (ECHAM-MPIOM), 1.8 PW (LSG)), the total heat that is transported by the ocean is considerably less for EMAC-MPIOM. The oceanic heat transport seems restricted

to low latitudes presumably due to the relatively closed circulation. EMAC-MPIOM simulates merely very weak oceanic heat transport north of 40°N and south of 50°S compared to the LSG simulation that exhibits a rather constant heat transport up to polar latitudes. In contrast, EMAC-MPIOM generates considerably stronger heat transport by the atmosphere. In sum this compensates the weak oceanic transport so that the total poleward heat transport is stronger for EMAC-MPIOM (maximum: north: 6.3 PW (EMAC-MPIOM), 4.5 PW (LSG); south: 6.5 PW (EMAC-MPIOM), 5.3 PW (LSG)). Both models exhibit stronger heat transport in the Southern Hemisphere.

Thus, the weakness of the northward heat transport is revealed as decisive factor to understand the simulation of too low mean temperatures in Angara and too high mean temperatures in the tropical deserts of Laurentia and Baltica by EMAC-MPIOM. Heat transport by the ocean is basically determined by the ocean circulation. The circulation pattern is not only influenced by the bathymetry and topography but also by winds and density gradients due to temperature and salinity. Near-surface winds exert stress on the water surface and affect the motion of the near-surface water layers. More saline or colder sea water is denser and sinks starting convection currents. The strength of the ocean circulation and the resulting heat transport are expected to vary strongly for different temperature distributions. In the following the simulated heat transport by MPIOM is evaluated for different Permian scenarios. Figure 5.30 compares the meridional heat transport for all CO_2 scenarios supplemented by a present-day reference scenario.

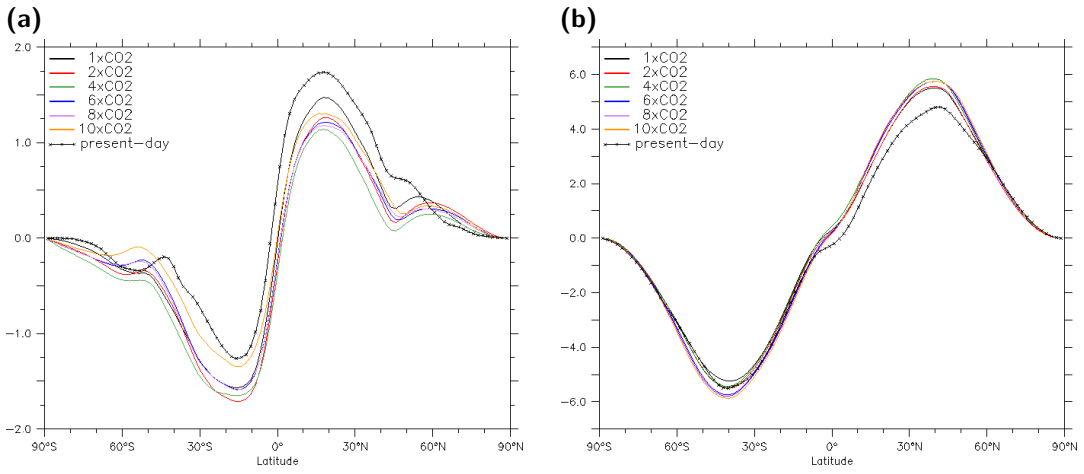

Figure 5.30.: Mean zonal meridional heat transport on yearly average [PW] for Permian Earth and various CO_2 scenarios and the present-day Earth as reference: (a) Heat transport by ocean. (b) Heat transport by atmosphere.

The general meridional distribution is similar for all Permian CO_2 scenarios and the present-day reference as shown in Figure 5.30(a). Poleward heat transport by the ocean is strong in low latitudes and exhibits a maximum around 15° of latitude. It declines

rapidly between 30° and 50° of latitude and then relatively slowly further poleward in high latitudes. In the Northern Hemisphere the heat transport is strongest for the $1\times CO_2$ scenario, except for the polar region, and it is weakest throughout the entire range for the $4\times CO_2$ scenario. The warm and ice-free $6\times CO_2$, $8\times CO_2$, and $10\times CO_2$ scenario are intermediate as well as the cold $2\times CO_2$ scenario. Hence, the strength generally decreases with increasing mean global temperatures for the colder scenarios but varies hardly for the warmer scenarios. The maximum is 1.48 PW for the $1\times CO_2$ scenario and 1.14 PW for the $4\times CO_2$ scenario. Moreover, all Permian scenarios exhibit a distinct minimum at about 45°N and a slight increase in higher latitudes. The heat transport on the Northern Hemisphere is pronounced significantly stronger for the present-day scenario. On the one hand the power of the heat transport by the ocean is higher in low latitudes (1.74 PW at maximum). On the other hand it does not decline that strong in mid-latitudes and there is a tableau at about 0.6 PW instead of the minimum. The behaviour is different in the Southern Hemisphere. The southward heat transport from the equator is strongest for the $2\times CO_2$ and the $4\times CO_2$ scenario (1.65 PW at maximum) and weakest for the $10\times CO_2$ scenario (1.35 PW at maximum). The power of the ocean heat transport simulated for the $1\times CO_2$ scenario is less strong in low latitudes but relatively strong in mid-latitudes. The meridional distributions of the colder $1\times CO_2$, $2\times CO_2$, and $4\times CO_2$ scenarios all exhibit a plateau in mid-latitudes at about 0.38 and 0.36 PW, respectively, while the warmer scenarios have a minimum in this range. In contrast to the North, the heat transport of the present-day reference is significantly weaker than for the Permian scenarios in the Southern Hemisphere (1.26 PW at maximum), except for the range of the present-day southern storm track in mid-latitudes.

The meridional distribution of the heat transport by the atmosphere is similar for all Permian scenarios and the present-day reference scenario as well (see Figure 5.30(b)). Both hemispheres exhibit a pronounced maximum at about 40° of latitude. The power of the heat transport increases strongly in low latitudes north and south of the equator and declines relatively slowly in high latitudes. The warm $6\times CO_2$, $8\times CO_2$, and $10\times CO_2$ scenarios are characterised by strong atmospheric heat transport in both hemispheres (N: 5.75 PW at maximum, S: 5.75-5.85 PW at maximum) and the heat transport is generally weaker for the colder $1\times CO_2$ and $2\times CO_2$ scenarios (N: 5.50-5.56 PW at maximum, S: 5.25 PW and 5.50 PW, respectively). The $4\times CO_2$ scenario deviates from this pattern. The simulated heat transport by the atmosphere in the Northern Hemisphere is even stronger than for the warm scenarios (5.85 PW at maximum), whereas it is weaker than the simulated transport power of the $2\times CO_2$ scenario in the Southern Hemisphere (5.44 PW at maximum). The present-day reference scenario exhibits very weak atmospheric heat transport in the North (4.80 PW at maximum) and the transport power is in the range of the $2\times CO_2$ scenario in the South. Hence, the weaker northward ocean heat transport is compensated by the atmosphere for all Permian scenarios.

The comparison confirms the weakness of the simulated northward heat transport by the ocean to mid- and high latitudes for the Permian setup. This applies for all Permian

scenarios, although the heat transport is especially weak for the $4\times CO_2$ scenario. Large temperature gradients, like for the $1\times CO_2$ scenario, correlate with stronger transport in low and mid-latitudes, although the $10\times CO_2$ scenario, that has the smallest pole-to-equator SST gradient, exhibits stronger northward heat transport than the cooler scenarios. However, altered winds as well as altered salinity of near-surface layers due to enhanced evaporation over the warmer tropical oceans and the total absence of sea ice have an impact as well. The polar oceans of the $4\times CO_2$ scenario are completely ice-free during summer, but covered by icesheets during winter and thus the impact by the formation and melting of sea ice on the salinity is expected to be relatively strong.

The northward heat transport differs by up to 0.34 PW for the different Permian scenarios. This provides a rough estimation of how strong the climate can affect the simulated poleward heat transport. Since the simulated transport for the present-day scenario is even stronger by about the same amount and all meridional distributions of Permian scenarios show the minimum in mid-latitudes, the weakness of northward oceanic heat transport is most likely caused by the prescribed Permian topography. On the one hand the shape of the Permian topography itself can be the cause of this weakness (see above). On the other hand simplifying assumptions for the modelling of the topography like the prescription of flat bathymetry within the deep oceans [27] and the discretisation onto the curvilinear grid can also be responsible. The latter potentially leads to more narrow or even closed seaways such as the shallow seaway between Angara and Tarim or Amuria that blocks the continuos circulation from the Tethys into the Panthalassic Ocean.

The southward heat transport from the equator is significantly stronger than the present-day reference for all Permian scenarios, especially for the colder scenarios. This agrees well with the meridional temperature distributions observed for the Permian simulations and indicates that the chosen model setup is able to simulate adequate heat transport. The comparison of the heat transport of the present-day scenario with simulation results of other ESMs employing MPIOM further allows to evaluate the general performance of the ocean heat transport by this particular model configuration. The meridional distribution is generally confirmed by a setup of MPIOM on a GR30L40 grid coupled to ECHAM6 using a T63L31 grid for the atmosphere [174]. This setup also exhibits maxima at about 18°N and 10°S, a plateau in northern mid-latitudes and a minimum in southern mid-latitudes, a smooth decline in high latitudes, as well as the general imbalance in favour of heat transport towards the North. However, the power of the transport is higher by about 0.2-0.3 PW on zonal average in low and mid-latitudes on both hemispheres for this setup. Small discrepancies can arise due to the different coupling of atmosphere and ocean model, but this systematic difference by about 15-20% suggests that a higher vertical resolution of the ocean increases the strength of the ocean circulation and the power of the ocean heat transport due to a higher resolution of the ocean overturning circulation.

The comparison with observed data and simulation results of other climate models reveals the climate of the $4\times CO_2$ scenario simulated by EMAC-MPIOM reproduces well

the indicated climate conditions in Euramerica and Gondwana, but tends towards cooler temperatures in Angara. Furthermore, the simulated climate seems too dry in northern mid-latitudes and on the Tethysian microcontinents. The simulated temperatures of the $4\times CO_2$ and $8\times CO_2$ scenarios agree well with the simulation results of Gibbs et al. [74] on the Northern Hemisphere, whereas the Southern Hemisphere is considerably warmer. The precipitation amount is increased in mid- and high latitudes. Based on similar boundary conditions, the simulated climate for a $10\times CO_2$ scenario by Kiehl and Shields [8] is about 5-10 K cooler on annual mean in Gondwana and Euramerica, but as warm as the simulation by EMAC-MPIOM in Angara and even warmer over the Northern Panthalassic Ocean. The ocean circulation simulated by EMAC-MPIOM restricts poleward oceanic heat transport basically to lower latitudes, especially in the Northern Hemisphere where the Cathaysian landmass blocks warm inflow from the Tethys ocean. This causes enhanced warming of low-latitude regions, in particular in the tropical desert regions, and explains the lower temperatures in Angara. Assuming an ocean ridge between the Tethys and Panthalassic Ocean, Winguth et al. [27] observed stronger meridional heat transport which confirms the results of Montenegro et al. [23]. The effect is compensated in the Southern Hemisphere where the warm Tethysian current continues into the Panthalassic Ocean. Hence, the Tethys Ocean is an important warm water source like observed by Kutzbach and Guetter [86]. Compared to the simulation with idealised topography by Kutzbach [69] and Kutzbach and Gallimore [85] the summer monsoon low of the EMAC-MPIOM simuation that employs a more realistic asymmetric topography is centered about 15° of latitude further to the south in Gondwana but 15° of latitude closer to the equator in Euramerica. The winter monsoon high is centered about 5-10° of latitude closer to the equator on both hemispheres. The strengthening of the monsoon circulation for higher orbital precession has not been observed as well as the warming effect of extended forests in high latitudes that was found by Otto-Bliesner and Upchurch [88]. However, the extent of the sea icesheets is in good agreement with the results of Hyde et al. [81] who have predicted a significant decrease for the transition from the $1\times CO_2$ to $2\times CO_2$ scenario and no glacation for a tripling of atmospheric carbon dioxide dioxide.

All in all the agreement of the simulated Permian climate with observations and results of other models is satisfying. The palaeoclimate simulation by EMAC-MPIOM matches the distribution of data-derived distribution of biomes better than other models in the Southern Hemisphere and in the low-latitude range of the Northern Hemisphere, especially for the setup considering self-established vegetation.

6

Comparison of atmospheric Transport in Permian and Present-Day Climate

Due to altered topography and composition of the atmosphere, the simulated Permian climate exhibits several differences compared to the present-day climate. The Permian climate is warmer on global average and there is merely a small and rather thin ice coverage in the northern polar region while the southern hemisphere is virtually free of permanent ice coverage. The extensive landmasses, especially in Gondwana, induce very strong seasonality of temperature and very arid conditions. The Tethysian microcontinents and coastal areas along the very warm Tethys Ocean are subjected to a monsoonal climate with dry and humid seasons. Everwet conditions merely appear in most of Angara and mid-latitude Gondwana.

The climatic conditions heavily influence transport processes within the troposphere and affect the atmospheric mixing. Since the buoancy of an air parcel depends on temperature and moisture content of the air parcel itself and of the surrounding environment, the prevailing temperatures and the balance of precipitation and evaporation determine the static stability of the atmosphere as well as the triggering and intensity of convection. That way the specific set-up with the supercontinent of Pangaea that stretches almost from pole to pole and constitutes a very extensive landmass implicitly affects the atmospheric transport pattern distinctly. The previous analysis of poleward heat transport (see Section 5.4) has revealed the simulated oceanic heat transport to the North to be significantly weaker for the Permian than for the present-day reference while the atmospheric heat transport is considerably enhanced. The heat transport to the South is enhanced for both, atmosphere and ocean.

The resulting pattern of atmospheric mixing will be analysed in the following. The analysis will primarily concentrate on convectional activities since these provide strong impact on the vertical exchange. The processes will be characterised by means of their

propensity to vertical motion, their intensity, and the tropopause height constituting the uppermost boundary for most of the convective motion in the troposphere.

The equivalent potential temperature is conservative with respect to moist and dry adiabatic processes during the parcel's ascent. It is related to the buoancy of the respective air parcel (see Section 1.3). Therefore, the vertical gradient of the equivalent potential temperature is an appropriate measure to estimate the static stability of the atmosphere. The degree of stability does not necessarily indicate whether a convection event has been triggered, however. That is why the frequency of triggered convection events as well as their intensity are considered separately. CAPE indicates the amount of energy available for convection and is directly related to the maximum potential vertical speed within an updraught (see Section 1.3). Both CAPE and the convective upward mass flux will be employed to estimate the intensity of the convection activities.

The large-scale circulation pattern has been considered during the analysis of the Permian climate in Section 5.1.3. The modelling of small-scale orographic structures and especially the determination of the surface roughness length are rather uncertain because of the available orographic data. The simulation of turbulent processes in the boundary layer heavily depends on the roughness of the surface, however. That is why the significance of the simulated turbulent transport is difficult to estimate and the latter will not be considered within this study.

During the following analysis the simulated characteristic quantities of the Permian climate are compared with their present-day reference to separate the impact of the Permian set-up. The comparison will primarily focus on zonal mean quantities since the direct regional comparison is not reasonable due to different topography. The respective regional distributions are collected in the Appendix E. Section 6.1 deals with atmospheric stability. The frequency and intensity of triggered convection is enlightened in Section 6.2 and Section 6.3 considers the tropopause height.

The Permian atmosphere is represented by the simulation of the $4\times CO_2$ reference scenario. This scenario assumes present-day eccentricity and obliquity, and 97% of the present-day luminosity. The diagnostic simulation of 5 years with 5-hourly output prolongs the diagnostic 30-year run. The integration time step is again 600 s. The corresponding reference simulation for the present-day set-up is also based on a coupled atmosphere-ocean simulation by EMAC-MPIOM. The simulation has been initialised by means of monthly climatologies of the prognostic model variables. After a spin-up simulation of 200 years on a T31L19 grid the simulation has been continued for 45 years on a T63L31 grid for spin-up to the finer grid and by another 5 years with 5-hourly output for diagnostics. The ocean model also employs a bipolar Arakawa C-Grid of GR30 Standard with 20 vertical levels. The poles are located at 72°N 40°W in Greenland and 84°S 60°E in Antarctica. The size of both grids as well as the integration time steps of 600 s for the atmosphere and 2 hours for the ocean are chosen consistently with the Permian set-up. The luminosity, obliquity and eccentricity are set to their present value. Thus, the luminosity is slightly higher in the present day simulation

while the other orbital parameters are identical for both scenarios. The greenhouse gas concentrations are assumed as: 348 ppm CO_2 ($\sim 1\times CO_2$), 1.65 ppm CH_4, and 0.306 ppm N_2O. The carbon dioxide concentration corresponds to a quarter of the Permian set-up, the concentration of methane is about twice as much, and the concentration of nitrous oxide is slightly increased. Both models employ the Tiedtke convection scheme and the cloud scheme by Sundqvist.

6.1. Static Stability

The buoancy of an air parcel depends on the difference of its temperature and moisture content with the surrounding air. These are affected by condensation and expansion during the ascent. In contrast, the equivalent potential temperature of the air parcel considers the release of latent heat and adiabatic temperature changes by definition and is generally conserved at moist-adiabatic ascents and descents. That is why a monotonically increasing equivalent temperature with height denotes suppression of buoancy, i.e. stably stratified conditions. Monotonically decreasing equivalent potential temperature indicates unstable conditions (see Section 1.3). On the discretised atmospheric grid of the GCM the vertical gradient of the equivalent potential temperature is determined by the centered derivative between the levels. Since the horizontal planes of the grid essentially follow the isobars in higher levels, the gradient of the equivalent potential temperature is determined in terms of pressure coordinates. The stability condition can be rewritten by means of the hydrostatic equation as:

$$\frac{\partial \theta_e}{\partial z} = \frac{\partial \theta_e}{\partial p}\frac{\partial p}{\partial z} = -\frac{\partial \theta_e}{\partial p}\,\rho g > 0. \tag{6.1}$$

This implies $\frac{\partial \theta_e}{\partial p} < 0$ to indicate stable conditions and $\frac{\partial \theta_e}{\partial p} > 0$ for unstable conditions.

The proportion of unstable conditions in the Permian atmosphere on annual and zonal average is presented in Figure 6.1(a). This evaluation does not consider the degree of stability but simply concentrates on whether the gradient is positive or negative. Unstable conditions are generally most frequent in lower latitudes in the lower part of the troposphere. The meridional distribution is symmetrical around the equator for the most part, although a slight bias towards the Southern Hemisphere can be observed. The predominance of unstable conditions reaches the highest altitude at about 10°S. High relative frequencies of more than 75% of the simulated period can be found approximately between 45°S and 45°N and up to 650 hPa at maximum near the equator. Moderate relative frequencies of more than 50% occur between 70°S and 70°N. In high latitudes they are restricted to the planetary boundary layer (PBL), while they reach an altitude of 700 hPa at 30° of latitude and 550 hPa near the equator. Unstable conditions are rare (< 20%) at altitudes higher than 800 hPa in high latitudes and 500 hPa in low latitudes.

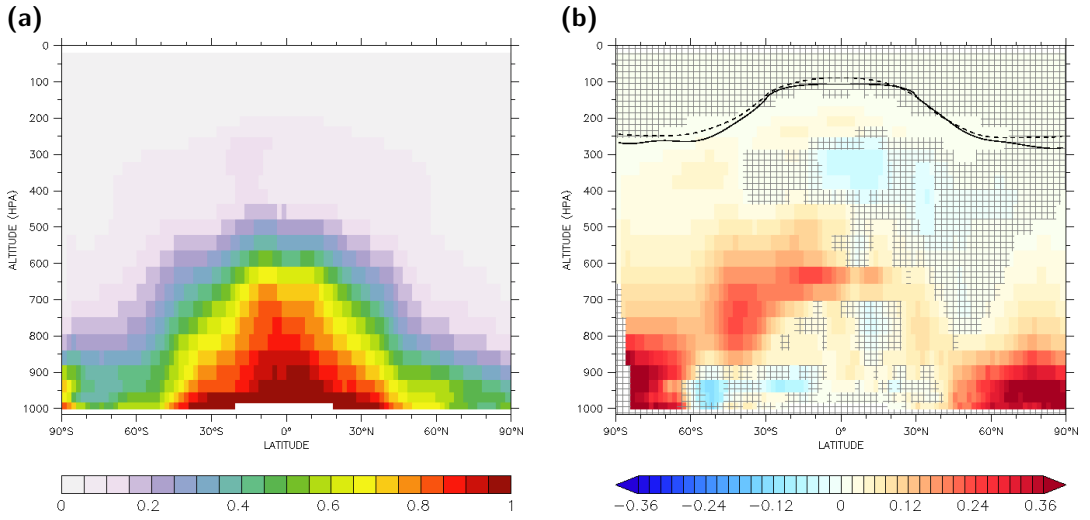

Figure 6.1.: Proportion of unstable conditions on zonal average: (a) The profile shows the annual average with respect to the simulated period of 5 years for the Permian 4×CO_2scenario. (b) Comparison between the mean proportion of unstable conditions for the Permian and the present-day reference scenario. Bluish colours mark areas where the frequency of unstable conditions is decreased, whereas reddish colours mark areas where the frequency is increased. In hatched areas the difference is not highly significant based on an unpaired Student's t test and on a significance level of 95%. In addition the mean altitude of the tropopause is marked for both scenarios (solid: Present scenario, dashed: Permian scenario).

Figure 6.1(b) compares the proportion of simulated unstable conditions in the Permian atmosphere with the present-day atmosphere. Again, the zonal and annual mean is considered and the statistical significance of the difference is evaluated by means of an unpaired Student's t test. Due to the relatively short simulation length of 5 years the test is performed for a significance level of 5%. In the Permian scenario most ranges of the troposphere exhibit destabilisation. This effect is especially pronounced in high latitudes in the lower troposphere up to 800 hPa (∼40 pp[1]). The lower troposphere is also affected significantly in mid-latitude areas in the Southern Hemisphere (22 pp). Although the effect is less strong there, the increase of instabilities reaches higher altitudes and is even stronger in higher layers. The PBL exhibits slight stabilisation in these areas (12 pp). In northern mid-latitudes and in low latitudes of both hemispheres the proportion of stability in the lower troposphere is only weakly increased or there are even no significant changes. The frequency of instabilities in the middle troposphere is most strongly increased in low and mid-latitudes of the Southern Hemisphere by up to 22 or 18 pp, respectively. Weak increases (4-10 pp) can be observed in northern low latitudes as well as in high latitudes of both hemispheres. In contrast to the strong increase in the Southern Hemisphere, the frequency of instabilities is not affected significantly in northern mid-latitudes. In the upper troposphere there are generally

only small effects on the frequency of unstable conditions. Slight increases occur in southern mid- and high latitudes as well as in the range directly below the tropopause in the entire Southern Hemisphere and in northern low and mid-latitudes. The only area of significant stabilisation besides the boundary layer can be observed in northern low latitudes between 250 and 450 hPa (4-6 pp).

Due to warmer temperatures the Permian atmosphere has a higher water capacity than the present-day atmosphere. This is presumably the main trigger for the observed increase of instabilities. The analysis of the Permian climate has revealed relatively high surface temperatures (see Section 5.1.1) with respect to the present-day reference. Near the surface the annual mean temperatures range between -12°C in the South Gondwanan Mountains and 34°C in the tropical deserts of Northern Gondwana and Southern Euramerica. Over the Permian oceans the mean surface temperature exceeds 28°C in most areas of the Tethys and Western Panthalassic Ocean between 10° of latitude, while it is coldest by -6°C in the Northern Panthalassic Ocean (see Figure 5.1). This corresponds to an increase of the zonal mean temperature by about 5 K with respect to the present-day reference in low and mid-latitudes and up to 15 K and 40 K in northern and southern high latitudes, respectively (not shown). The temperature increase is not only restricted to near-surface layers, but can be observed within the entire troposphere (see Figure E.4 in the Appendix). Again, the effect is strongest in high latitudes and more pronounced in the Southern Hemisphere in agreement with the previously observed weaker heat transport to the North: the mean zonal temperature of the middle troposphere at 500 hPa shows an increase by 14-16 K in the South and 4-6 K in the North. The upper troposphere at 300 hPa is warmer by 8-10 K in the South and 2-4 K in the North. The zonal mean temperature is increased by 4-8 K in the Southern Hemisphere and by 2-4 K in the Northern Hemisphere in most layers in low and mid-latitudes. On the one hand the higher temperatures of the Permian climate increase the water capacity of the atmosphere, but on the other hand the extensive continental areas of the Pangaean supercontinent decrease the availibility of water. That is why the specific humidity is high especially over the warm Tethys and Western Panthalassic Ocean as well as over near-equatorial Pangaea in the range of the Appalachian Mountains where the distance between the Panthalassic and Tethys coast is shortest. The Permian atmosphere exhibits increased specific humidity with respect to the present-day scenario in the entire troposphere (see Figure E.5 in the Appendix). The difference is again more pronounced in the Southern Hemisphere, about 2-4 $^{g}/_{kg}$ in the lower troposphere for all latitudes and still about 1 $^{g}/_{kg}$ in the middle troposphere. Considerable effects appear in the Northern Hemisphere only in the lower troposphere in high latitudes (1-2 $^{g}/_{kg}$) and close to the equator (2-3 $^{g}/_{kg}$). Hence, the increased atmospheric water content can explain the increased frequency of instabilities in high latitudes in the lower troposphere and in southern mid- and low latitudes in the middle troposphere. In low latitudes of the lower troposphere the frequency of instabilities is already so high in the present-day scenario that it is nearly not affected by the increase

[1] percentage points

of water content. The specific humidity is generally low in the upper troposphere and has only minor effects on the buoancy of the air parcel. Although the absolute increase is small on average in these areas and is related to some specific events, it corresponds to an increase of more than 100% and contributes to the observed slight destabilisation in the range below the tropopause.

The increased humidity, however, is not the only factor that affects the stability in the Permian atmosphere. The stability of dry air is generally specified by the vertical gradient of the potential temperature. The corresponding profiles reveal that the frequency of instabilities in dry air differs less strongly (see Appendix, Figure E.6) and significant effects can be observed in the PBL and lower troposphere as well as in the upper troposphere. Instabilities in dry air appear relatively frequently over the warm tropical oceans off the equator close to the surface. This behaviour can be found in both scenarios, however, it reaches higher altitudes over the Tethys Ocean. Due to the dry Permian climate, dry-air instabilities occur in the PBL as well as in the lower troposphere over the arid continents of Northern Gondwana, Euramerica, and Southern Angara. They are relatively common in these areas by frequencies of up to 20% which corresponds approximately to the half of the frequency of all instabilities. In the present-day scenario they exist to some extent over Australia and the African desert areas, but distinctly less frequent. The zonal mean frequency is not affected strongly (4 pp). There are basically two distinct differences with regard to dry-air instabilities in the upper troposphere between the Permian and present-day scenario. First, the present-day atmosphere exhibits a belt of dry-air instabilities close to the equator between 200 and 300 hPa that does not exist in the Permian atmosphere. Second, the dry-air instabilities reach higher altitudes on average in the Permian scenario, especially over the warm Tethys and Western Panthalassic Ocean. The effect on the zonal mean frequency is small in both cases (2-3 pp). Moreover, the instabilities generally appear less frequently between 300 and 400 hPa in mid- and low latitudes, but significantly more frequently in the range below the tropopause.

In addition to humidity and temperature the altered topography and other local effects also influence the zonal mean frequency of instabilities. The scarcity of landmasses in southern mid-latitudes in the present-day topography allows strong winds in the southern west wind drift. In these areas large-scale lifting in the range of the warm and cold sectors of the low pressure systems along the storm track as well as updraughts at the fronts generally induce a relatively high frequency of instabilities. Since the Pangaean supercontinent nearly stretches from pole to pole, it prevents the formation of such distinct storm tracks. That is why the zonal mean frequency of instabilities is decreased in the PBL and lower troposphere between 60° and 40°S by up to 12 pp. Moreover, both northern South America and Central Africa exhibit higher orography and denser vegetation coverage than the flat and sparsely-vegetated Northern Gondwana. The forced lifting as well as the increased atmospheric water content due to evaporation of the vegetation increase the frequency of instabilities in the PBL in the respective areas for the present-day reference scenario. The effect appears locally, but it decreases

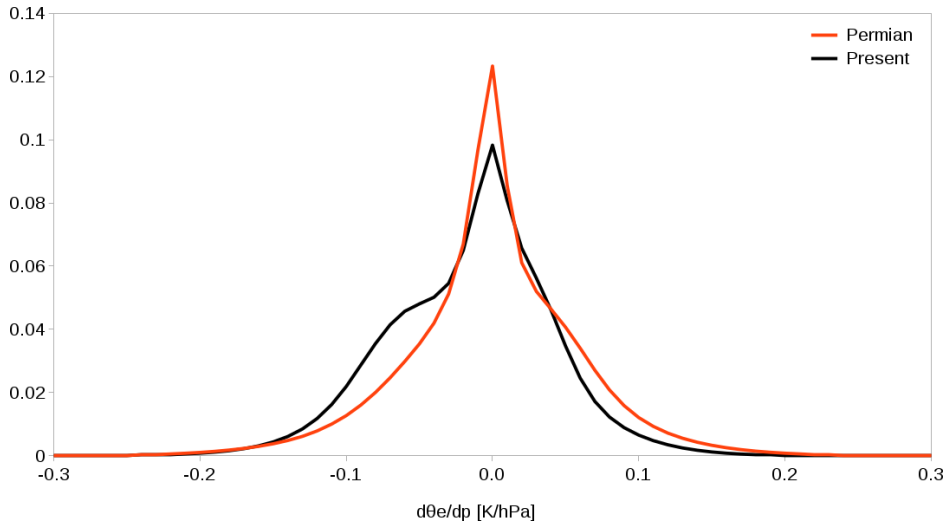

Figure 6.2.: Frequency distribution of the degree of static stability in the lower troposphere at 850 hPa: The curves show the frequency distribution of the vertical gradient of the equivalent potential temperature in terms of pressure from the entire Earth with respect to the simulated period of 5 years. The negative gradient indicates stable conditions, whereas the positive gradient indicates instabilities. The red line represents the Permian $4\times CO_2$ scenario and the black line represents the present-day reference scenario.

the zonal mean frequency by up to 8 pp. The high temperature and high atmospheric water content in the Indo-Pacific Warm Pool area triggers unstable conditions that reach up to the upper troposphere very frequently. Although the temperature and specific humidity are even higher in the upper troposphere at 300 hPa over the Tethys Ocean, instabilities occur less frequently than in the Warm Pool region. This behaviour can be observed only locally. Still, the zonal mean frequency is decreased by 6 pp.

In the following the magnitude of destabilisation is estimated at different levels to analyse the increase of unstable conditions in the Permian atmosphere in more detail. The degree of static stability is represented by the vertical gradient of the equivalent potential temperature. Figure 6.2 shows the frequency distributions of both scenarios for the lower troposphere at 850 hPa from the entire Earth for the 5 year-period. Both distributions have a strong peak at the neutral metastable case ($\frac{\partial \theta_e}{\partial p} = 0$) and decline moderately fast towards stable and unstable conditions. The frequency distribution for the present-day reference has a distinct shoulder at about -0.5 $^{\mathrm{K}}/_{\mathrm{hPa}}$ and thus shows a significant bias towards moderately stable conditions. The mean is at -0.015 $^{\mathrm{K}}/_{\mathrm{hPa}}$ and the proportion of instabilities is 46.8%. For the Permian scenario stable and unstable conditions are nearly balanced. Weakly stable and unstable conditions are strongly pronounced. In addition there is a slight bias towards moderately unstable conditions. The mean is close to the neutral case (-0.0003 $^{\mathrm{K}}/_{\mathrm{hPa}}$) and the proportion of instabilities is 55.6%. Hence, the frequency of moderately stable conditions is significantly reduced in favour of weakly stable and unstable, as well as moderately unstable conditions.

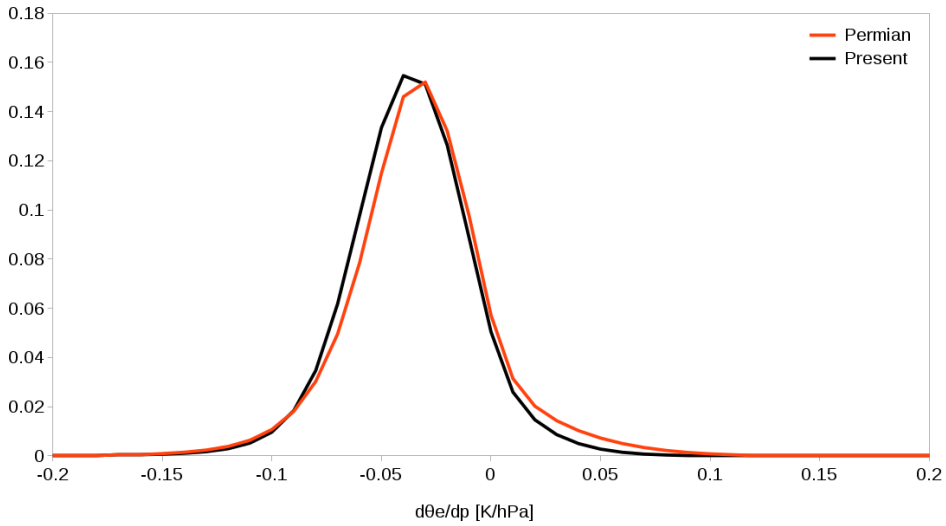

Figure 6.3.: Frequency distribution of the degree of static stability in the middle troposphere at 550 hPa: The curves show the frequency distribution of the vertical gradient of the equivalent potential temperature in terms of pressure from the entire Earth with respect to the simulated period of 5 years. The negative gradient indicates stable conditions, whereas the positive gradient indicates instabilities. The red line represents the Permian $4\times CO_2$ scenario and the black line represents the present-day reference scenario.

In the middle troposphere at 550 hPa the frequency of moderately stable conditions is decreased, while weakly and moderately unstable conditions occur more frequently. Weakly stable conditions are similarly frequent for both scenarios. The corresponding frequency distributions are presented in Figure 6.3. The degree of stability seems normally distributed around weakly stable conditions for both scenarios and the distribution for the Permian appears slightly shifted towards instability by about 0.01 $^{\mathrm{K}}/_{\mathrm{hPa}}$. However, the latter declines significantly faster for stable conditions and more slowly for weakly and moderately unstable conditions. The mean of the Permian distribution is consequently closer to the neutral case (Permian: $-0,032$ $^{\mathrm{K}}/_{\mathrm{hPa}}$, present: $-0,037$ $^{\mathrm{K}}/_{\mathrm{hPa}}$) and the proportion of unstable conditions is higher by about 5 pp (Permian: 15.4%, present: 11.0%). Strongly stable and unstable conditions are generally very rare in both scenarios.

The frequency distributions corresponding to the upper troposphere at 300 hPa are shown in Figure 6.4. Stable conditions predominate clearly for both scenarios in this range. The frequency distributions both exhibit a significant peak for moderately stable conditions and decline slowly towards stability, but fast towards instability. The Permian distribution peaks at slightly more stable conditions (∼-0.5 $^{\mathrm{K}}/_{\mathrm{hPa}}$) than the present-day reference (∼-0.4 $^{\mathrm{K}}/_{\mathrm{hPa}}$), whereas the latter exhibits a pronounced shoulder for strongly stable conditions. Weakly unstable conditions are slightly more frequent for the Permian scenario. Moderately and strongly unstable conditions are very rare in both scenarios. Thus, strongly stable conditions are significantly suppressed for the Permian scenario

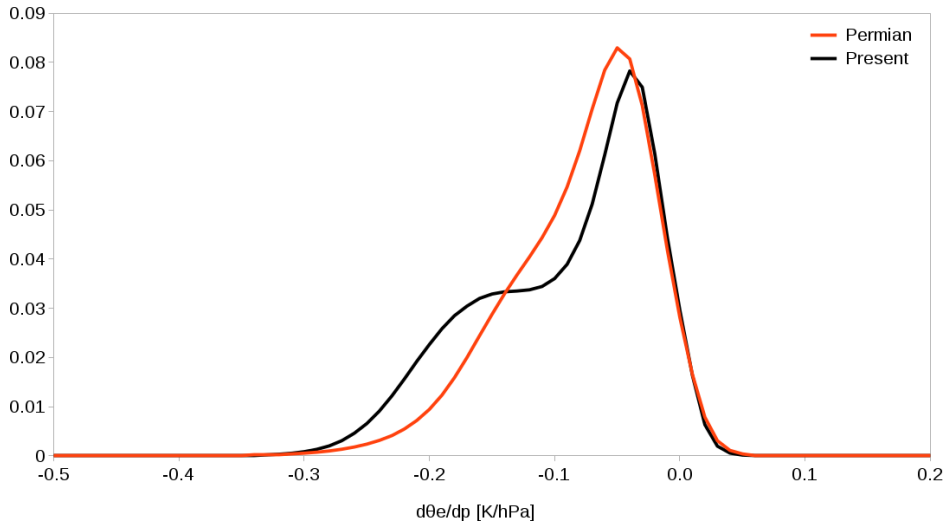

Figure 6.4.: Frequency distribution of the degree of static stability in the upper troposphere at 300 hPa: The curves show the frequency distribution of the vertical gradient of the equivalent potential temperature in terms of pressure from the entire Earth with respect to the simulated period of 5 years. The negative gradient indicates stable conditions, whereas the positive gradient indicates instabilities. The red line represents the Permian $4\times CO_2$ scenario and the black line represents the present-day reference scenario.

in favour of moderately stable conditions and weakly stable. Unstable conditions are similarly frequent. The mean of the present-day reference is consequently significantly further in the stable range (Permian: $-0,080$ $^{\mathrm{K}}/_{\mathrm{hPa}}$, present: $-0,093$ $^{\mathrm{K}}/_{\mathrm{hPa}}$), while the proportion of unstable conditions is only slightly higher for the Permian scenario (Permian: 5.7%, present: 5.5%).

6.2. Convection

The previous section has evaluated the frequency of unstable conditions and the degree of static stability in different layers of the Permian troposphere with respect to the present-day reference. The indication of unstable conditions, however, does not necessarily imply the triggering of convection events as well as their intensity, however (see Section 3.2). Both aspects will be examined in this section.

Figure 6.5 shows a summary of all triggered convection events within the simulated period of 5 years for the Permian and present-day scenario. While the left panel considers the relative frequency with respect to the entire simulation period, the right panels presents the fraction of the different convections types. The frequency of triggered convection events is significantly higher for the Permian scenario which agrees well with the observed increase of unstable conditions. Convection is triggered on average

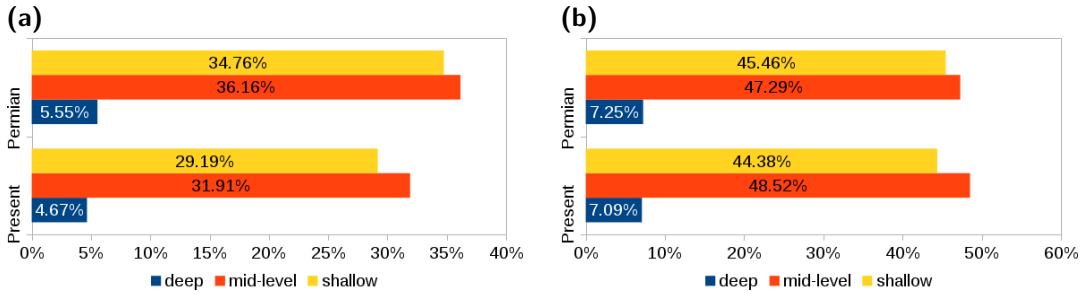

Figure 6.5.: Frequency of triggered convection events for the different types of convection: (a) The relative frequency with respect to the simulated period of 5 years is shown for both the Permian 4×$CO_2$and the present-day reference scenario. (b) The proportion of each type with respect to all triggered convection events is shown for both the Permian and the present-day scenario.

in 76.47% of the simulated period for the Permian scenario and in 65.77% for the present-day scenario. This corresponds to an increase by about 16%. Mid-level and shallow convection are more frequent by about 5 pp, while deep convection is increased by about 1 pp. Thus, the different convection types are affected virtually equally and their composition is nearly preserved for both scenarios: Mid-level convection is most frequent ($\sim$ 48%), shallow convection slightly less frequent ($\sim$ 45%), and deep convection occurs relatively rare ($\sim$ 7%).

Regional differences in the frequency of triggered convection events as well as the breakdown for different convection types are considered in Figure 6.6. The comparison is confined again to the zonal mean frequency of convection events due to the different topography of both scenarios. The corresponding global distributions are collected in the Appendix (see Figure E.8 -E.10).

Figure 6.6(a) shows the zonal mean fraction of triggered convection events of any type with respect to the entire simulation period for both scenarios. In low latitudes convection is triggered similarly frequently for the Permian scenario as well as for the present-day reference, especially close to the equator. The fraction varies between 90% near the equator and about 70% near the tropical circles. Significant differences appear in mid- and high latitudes in agreement with the observed increase of unstable conditions in lower layers of the troposphere. In the Northern Hemisphere convection is distinctly more frequent for the Permian scenario in this range. The difference is merely small at 30°N, but increases to 20 pp at 60°N and even to 50 pp near the North Pole. In contrast, convection is reduced in southern mid-latitudes by about 10 pp, although it is also increased in high latitudes by more than 50 pp. Thus, both hemispheres exhibit a very high fraction of triggered convection events by about 80% of the simulated period in high latitudes.

Shallow convection is generally distributed over the entire Earth. It is triggered in the PBL, but its buoyant energy is not sufficient to form cumulus clouds of large cloud depth

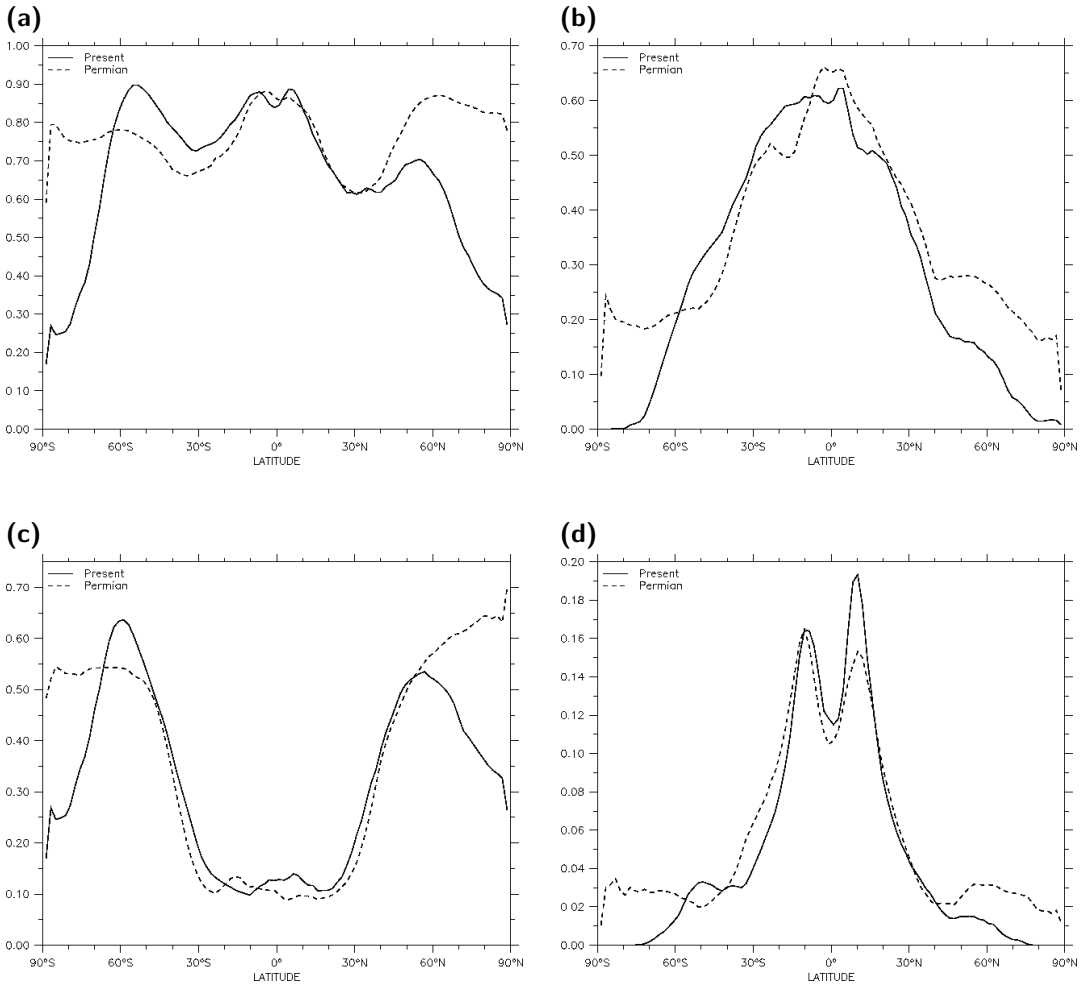

Figure 6.6.: Zonal profile of mean proportion of triggered convection events on annual average for the different types of convection: (a) All types, (b) shallow convection, (c) mid-level convection, and (d) deep convection.

and high cloud top heights. Prominent examples are trade-wind cumuli under subsidence inversions or daytime convection over land. The zonal mean fraction of triggered shallow convection events with respect to the entire simulation period is plotted in Figure 6.6(b). For both scenarios the fraction is largest near the equator and decreases towards the poles. The fraction of the Permian scenario is about 65% around the equator, that is about 5 pp more than the fraction of the present-day reference. Shallow convection is triggered more frequently on zonal average in the Permian scenario in the entire Northern Hemisphere. In low latitudes the relative frequency declines to 50% towards the Tropic of Cancer and the difference is mostly between 5-10 pp. There is virtually no difference around the Tropic of Cancer and the difference remains smaller than 5 pp

further poleward up to 40°N. The fraction of triggered shallow convection then stays at a level of about 30% up to 60°N and merely drops to 15% at 80°N. The reference fraction of the present-day scenario already falls below 15% at 50°N and is less than 5% in most of the high-latitude range. Thus, shallow convection is triggered more frequently by 15-20 pp in northern mid- and high latitudes in the Permian scenario. In contrast, shallow convection is less frequent in southern low and mid-latitudes for the Permian scenario. The difference is especially large around 20°S and 50°S (10 pp) and smallest around 30°S (2 pp). In high latitudes the frequency of the Permian scenario is about 20%, whereas it is vanishingly small for the present-day reference. On the one hand the increased frequency of unstable conditions in the PBL and lower troposphere leads to an increased frequency of triggered shallow convection. This is especially true for the high-latitude range where the fraction of convection is generally increased. On the other hand stabilisation in the upper troposphere can also increase the frequency of shallow convection when the buoyant energy is not sufficient for deep convection. This behaviour can be observed close to the equator where the high degree of instability in the range of the Indo-Pacific Warm Pool suppresses shallow convection in favour of deep convection. Furthermore, the decrease of shallow convection events in the Southern Hemisphere agrees well with the observed stabilisation in the PBL due to reduced intensity of the southern west wind drift and lower orography as well as lower vegetation fraction in low latitudes. Shallow convection is very scarce over Pangaea and Cathaysia. Cimmeria as well as South- and Indochina exhibit a mean frequency of about 30-40%. Similar frequencies can be found in northern South America, Central Africa, and South-East Asia. The mean convection top height is similar for both scenarios in low and mid-latitudes and increased by about 50 hPa in high latitudes for the Permian scenario (not shown).

Mid-level convection is rooted in levels above the PBL. It is basically triggered by static instability in the respective levels and moisture supply due to large-scale lifting of moist low-level air from close to the surface to the level of free convection. This is common in the range of rainbands at warm fronts and in the warm sector of extratropical cyclons and that is why mid-level convection occurs very frequently in the range of the west wind drift in mid-latitudes. Figure 6.6(c) shows the zonal mean fraction of triggered mid-level convection events with respect to the simulated period for the Permian and the present-day reference scenario. Mid-level convection events are rarely triggered in low latitudes for both scenarios (10-15%), but their frequency rises rapidly to 50-60% in mid-latitudes at about 30° of latitude. Although the strong increase in frequency is shifted further poleward by about 5° of latitude for the Permian scenario in both hemispheres, the difference is generally small in the range between 50°S and 50°N. This is again different in high latitudes. The frequency of mid-level convection of the Permian scenario increases further to up to 70% near the pole in the Northern Hemisphere and remains at about 55% in southern high latitudes. In contrast, it reaches 50% in the North and even 65% in the South at about 60° of latitude for the present-day reference, but it drops rapidly below 30% near the pole in both hemispheres. The previous analysis has revealed a slight increase in frequency of unstable conditions in

the lower troposphere in low latitudes. The different occurences of higher orographic structures that provoke the lifting of moist air from near the surface seems to be more decisive for the different triggering of mid-level convection in low latitudes, however, since the frequency is largest in the range of the Appalachians Mountains as well as in northern South America and Central Africa. The poleward shift of the rapid increase in mid-latitudes indicates a slight poleward shift of the west-wind drift in the Permian scenario. The weaker intensity of the southern storm track with respect to the present-day reference leads to less frequently triggered mid-level convection events in agreement with the generally decreased frequency of unstable conditions in this range. Similarly, the distinctly increased frequency of mid-level convection events in higher latitudes agrees well with the increased occurence of instabilities. Mid-level convection occurs very frequently in most of Angara and the northern island arc in particular, the northern polar Panthalassic Ocean, the South Gondwanan Mountains, as well as parts of the southern polar Panthalassic Ocean. Its mean convection height is increased by 50-100 hPa in southern mid- and low latitudes in agreement with the observed destabilisation in the middle troposphere in this range.

Deep convection is also triggered in the PBL, but its buoyant energy is sufficient to reach the upper troposphere up to the tropopause. It generally occurs very frequently in low latitudes in a broad belt along the ITCZ. However, deep convection can also be found in mid- and high latitudes in the range of cold fronts of extratropical cyclons, for example. Deep convection is triggered scarcely compared to the other convection types, but it is responsible for the bulk of the vertical mass transport in the troposphere. The zonal mean fractions of triggered deep convection events with respect to the simulated period are shown in Figure 6.6(d) for both scenarios. Deep convection events are most frequent at about 10°N and 10°S and slightly less frequent in the vicinity of the equator. This applies for the Permian as well as for the present-day reference scenario. The southern branch is more pronounced for the Permian scenario (south: 16%, north: 14%), whereas the northern branch is significantly more distinct for the present-day reference (south: 16%, north: 19%). Hence, the fraction of triggered deep convection is smaller for the Permian scenario in the range of the northern branch and the equator, but similar in the range of the southern branch. It drops rapidly to about 3% further poleward of 20° of latitude. This decline can be observed in the same latitude range in the Northern Hemisphere for both scenarios. In the Southern Hemisphere it is shifted further south by about 7° for the Permian scenario. The fraction of deep convection events in high latitudes is vanishingly small for the present-day reference, but remains at 3% up to the pole for the Permian scenario. The previous analysis has revealed that the frequency of deep convection events has been increased on global average by about 1 pp to 5.55%. This corresponds to a relative increase of 18.8% (see Figure 6.5(a)). However, the comparison of the zonal mean frequencies shows that the increase seems confined to mid- and high latitudes, whereas the fraction of deep convection is even decreased in low latitudes. This agrees well with the observed stabilisation in the upper troposphere between 10°S and 20°N and 400-250 hPa (see Figure 6.1(b)). The increase of stable conditions in the middle and upper troposphere suppresses deep convection in the

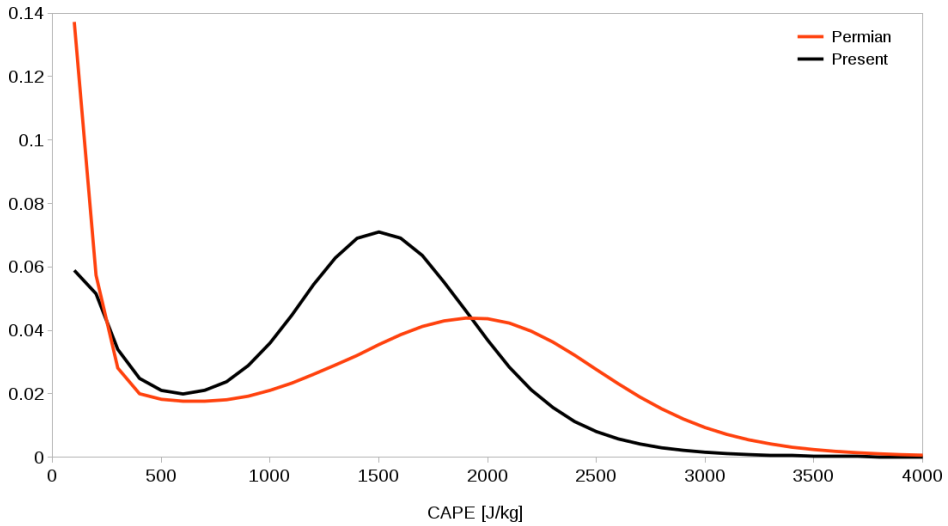

Figure 6.7.: Frequency distribution of CAPE at deep convection events: The curves show the global frequency distribution with respect to the simulated period of 5 years. The red line represents the Permian 4×CO_2 scenario and the black line represents the present-day reference scenario.

respective areas despite of the increase of unstable conditions in the upper troposphere between 250-150 hPa. Breaking through the more stable layers and reaching the unstable regions requires very high buoyant energies, however. That is why the frequency of deep convection is decreased in favour of shallow convection in low latitudes, although the frequency of unstable conditions in the lower troposphere, the degree of stability, and even CAPE (see below) are increased. The global distribution shows that deep convection is most frequently triggered in the range of the Indo-Pacific Warm Pool for the present-day reference. This region exhibits a high frequency of unstable conditions in the upper troposphere. However, it is not possible by means of this analysis to break down whether the triggered deep convection events lead to instability in the upper troposphere or whether the occurence of instabilities enhance the frequencey of deep convection events in this range. For the Permian scenario deep convection is most frequent over the western Panthalassic Ocean near the equator and along two bands at about 15° of latitude in the Central Panthalassic Ocean. The increase of instabilities in the lower troposphere in southern mid- and high latitudes as well as northern high latitudes agrees well with the increased frequency of deep convection in these ranges and increases the mean convection height by up to 100 hPa.

In addition to the frequency of triggered convection events, their intensity is also important to characterise the vertical transport in the atmosphere. The intensity of convective processes can be measured by the amount of available energy, i.e. CAPE that is directly related to the maximum potential vertical speed within an updraught. The following analysis considers the maximum CAPE within an air column. That way, the respective value of CAPE does not necessarily correspond to the air parcel at the surface or at the level where the convection has eventually been triggered. Figure 6.7 shows

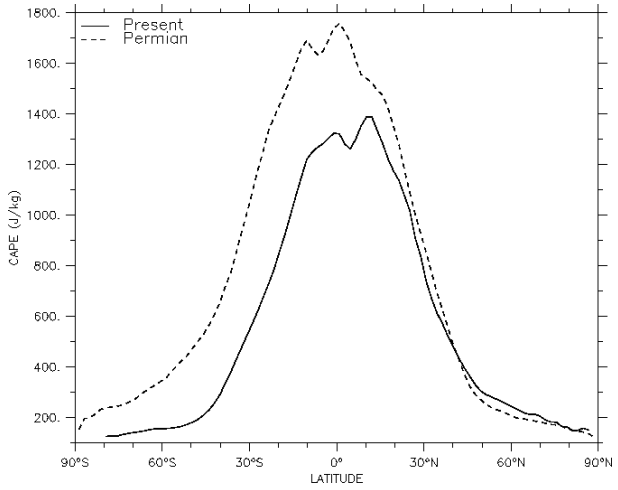

Figure 6.8.: Zonal distribution of mean CAPE [J/kg] on zonal and annual average. The annual mean is prefiltered with a minimum of 100 J/kg to exclude non-convective events.The dashed line represents the Permian 4×CO_2 scenario and the solid line represents the present-day reference scenario.

the global frequency distributions of CAPE in the case of deep convection events. The general shape of the distribution is similar for both scenarios. The distributions indicate high frequencies for low values of CAPE of less than 250 J/kg. Deep convection events with moderate CAPE are relatively rare, whereas events with high values of CAPE occur distinctly more frequently. The distributions decline rapidly for very high CAPE and events with CAPE of more than 3500 J/kg are very rare. The distribution of the Permian scenario shows a significantly higher fraction of convection events with CAPE in the very low-energy range. This increase is most likely related to the increased frequency of deep convection in mid- and especially in high latitudes. Moreover, the frequency maximum in the high-energy range is shifted to higher energies and comprises a larger energy range. The minimum in the medium-energy range consequently stretches further up to 1250 J/kg (present-day: 750 J/kg), the maximum peak is shifted to 2000 J/kg (present-day: 1500 J/kg), and its FWHM is increased to 1600 J/kg (present-day: 1000 J/kg). Hence, the higher temperatures and atmospheric moisture content of the Permian scenario increase the frequency of deep convection events with very high CAPE on the one hand, while events in the range of medium-high energies are most likely suppressed by the previously observed stabilisation in the upper troposphere in low latitudes on the other hand. The mean of the Permian distribution is 1431.61 J/kg, which is about 11% higher than the mean of the distribution of the present-day reference scenario (1287.23 J/kg).

The intensity of convective processes is affected differently according to the latitudinal range. The zonal mean CAPE in case of convection events is plotted in Figure 6.8. All types of convection are considered for this analysis, but events with CAPE of less than 100 J/kg are excluded to focus on distinct convective activities. In general, CAPE is high on zonal average in low latitudes, declines rapidly in mid-latitudes in both hemispheres, and decreases slowly towards the poles in high latitudes. This applies for the Permian as

well as for the present-day reference scenario. The analysis of the frequency distributions has indicated a significant increase of CAPE on global average for the Permian scenario. However, the meridional break-down reveals that this increase can only be found in the Southern Hemisphere and in northern low latitudes. For the Permian scenario CAPE is largest on zonal average directly around the equator (1758.3 J/kg) and around 10°S (1691.3 J/kg). These maxima are mainly affected by areas of high CAPE over the Tethys Ocean along the equator and along the southern ITCZ branch over the Panthalassic Ocean (see Figure E.7(a) in the Appendix). The largest annual mean values of CAPE can be found above the western edge of the Tethys Ocean (about 3600 J/kg) where the SST is highest. However, the frequency of unstable conditions in the middle and upper troposphere is low in this area and mainly shallow convection events are triggered. The difference between the Permian and the present-day reference scenario is generally largest in southern low latitudes and varies between 400 and 600 J/kg. This corresponds to an increase of about 30% near the equator and 90% at 30°S. It is less pronounced in northern low latitudes. On the one hand the zonal mean CAPE of the present-day reference is increased due to high CAPE in the range of the Indo-Pacific Warm Pool, and on the other hand CAPE is generally weaker along the northern branch of the ITCZ over the Panthalassic Ocean. The difference merely ranges between 100 and 200 J/kg northward of 10°N (10-15%). In southern mid-latitudes CAPE decreases from 1010.8 J/kg on zonal average at 30°S to 342.01 J/kg at 60°S. The absolute difference decreases within this range from 400 to 200 J/kg, while the relative difference is increased from about 90% to 150%. The global distribution basically shows high CAPE in the area from the Paraná-Karoo-Inland Sea, along the inlet from the Tethys Ocean to the Tethys coast. Hence, convection events with high intensity basically occur over land. In this region the frequency of deep convection events is generally low and mid-level convection predominates. In southern high latitudes CAPE ranges from 150 to 350 J/kg for the Permian scenario, which is about 100-200 J/kg more than in the equivalent range for the present-day scenario. Convection events with relatively high CAPE occur again over Gondwana. CAPE is only slightly affected in northern mid-and high latitudes. This agrees well with the observed weakness of poleward heat transport in the Northern Hemisphere for the Permian scenario. CAPE is even lower on zonal average northward of 40°N, but the difference is smaller than 30 J/kg. Hence, the frequency of instabilities and triggered convection events is significantly increased in this range, whereas the intensity of the convection events is virtually not altered. CAPE is reduced from 852.5 J/kg to 203.2 J/kg in mid-latitudes and further poleward to about 120 J/kg.

The analysis of CAPE at convection events provides information about the intensity of convective activity within the entire air column. It does not allow any assertions about the intensity of vertical tranport at different layers of the atmosphere, however. That is why the upward mass flux at different altitudes will be used as additional measurement to characterise the intensity in the follwing. Figure 6.9(a) shows the profile of the convective upward mass flux on zonal average for the Permian scenario. The upward mass transport is generally strongest in the PBL and lower troposphere between 950 and 850 hPa. There are four zones of relatively strong upward mass flux in

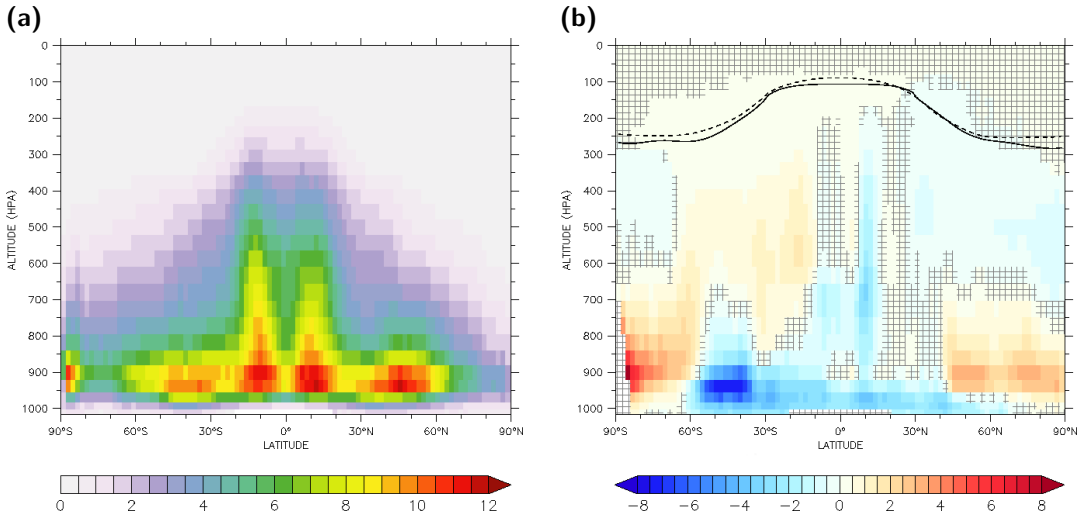

Figure 6.9.: Convective upward mass flux [g/m²] on zonal average: (a) The profile shows the annual average with respect to the simulated period of 5 years for the Permian 4×CO_2 scenario. (b) Comparison between the mean upward mass flux averaged over all convection events for the Permian and the present-day reference scenario. In hatched areas the difference is not highly significant based on an unpaired Student's t test and on a significance level of 95%. In addition the mean altitude of the tropopause is marked for both scenarios (solid: Present scenario, dashed: Permian scenario).

low and mid-latitudes, respectively, that reflect the mean global circulation pattern. In low latitudes the upward mass transport is strongest between 5° and 15° of latitude (∼11 g/m² in the lower troposphere), and furthermore, it reaches the highest altitudes in these zones. The upward mass transport is slightly more pronounced in the southern zone and the mass flux is about 6 g/m² in the middle troposphere at 550 hPa and still about 2 g/m² in the upper troposphere at 300 hPa. It is generally slighty weaker close to the equator (∼8 g/m² in the lower troposphere and ∼4 g/m² in the middle troposphere). In the range of the Hadley downwelling the downward motion generally predominates and that is why the upward mass flux is significantly lower in the latitudes around the tropical circles. The resulting zonal mean mass flux is about 8.5 g/m² at maximum in the lower troposphere and about 3 g/m² at 550 hPa. The upward mass flux is stronger again in mid-latitudes in the range of the westerlies and fronts of the low pressure systems. This is pronounced more strongly in the Northern Hemisphere. There the mass flux reaches 11 g/m² in the lower troposphere, while it is 9-10 g/m² at maximum in the Southern Hemisphere. The northern zone is located about 10° of latitutde further poleward than the southern and extends from 40°N to 55°N. However, the upward mass flux in the middle troposphere is slightly stronger in the Southern Hemisphere in this range (∼2 g/m²). There is another maximum of very high upward mass flux (∼10 g/m²) close to the South Pole in the lower troposphere that is most likely caused by the exaggeratedly sharp southern edge of the South Gondwanan Mountains.

The convective upward mass flux within the Permian atmosphere is compared to the mean mass flux of the present-day scenario in Figure 6.9(b). The observed behaviour generally agrees well with the previously found alterations of CAPE and the frequency of triggered convection events (see Figures. 6.6 and 6.8). The lower frequency of convection events reduces the average upward mass flux in low latitudes despite of higher CAPE. In the Northern Hemisphere deep convection is significantly less frequent for the Permian scenario, especially in the range of the northern ITCZ branch. The upward mass flux is consequently decreased by up to 4 g/m² (20-30%) and the effect can be found up to an altitude of 200 hPa. Deep convection occurs similarly frequently for both scenarios in the range of the southern ITCZ branch and thus there are no significant effects on the mass flux. The mass flux is additionally reduced in the lower and middle troposphere up to an altitude of 650 hPa by 2 g/m² (10-20%) in a range between 15° of latitude. Lower frequencies of shallow convection in the Southern Hemisphere as well as of mid-level convection in the Northern Hemisphere most likely cause this weakening. The mass flux is merely enhanced directly over the equator where CAPE is strongly increased. The resulting mass flux is slightly increased by 1 g/m² (20-30%) in the middle and upper troposphere higher than 600 hPa. Shallow convection is generally triggered less frequently in most of southern mid- and low latitudes, partly in favor of deep convection. This reduces the upward mass flux in the PBL and lower troposphere significantly by 3-4 g/m² (30-40%), although the mass flux is increased in the middle and upper troposphere by about 1 g/m². Since the mass flux is generally weak in these layers, this corresponds to a strong increase of about 60% in the middle troposphere and even more than 100% in the upper troposphere. In contrast, both CAPE and the frequency of deep convection are even slightly lower than the present-day reference in the Northern Hemisphere and that is why such behaviour can not be observed there and the mass flux is reduced in higher altitudes by 1 g/m² (50-70%). Shallow and mid-level convection occur more frequently in high latitudes of both hemispheres for the Permian scenario and shallow convection is also more frequent in mid-latitudes northward of 40°N. This enhances the upward mass flux in the lower troposphere significantly by 3-4 g/m² (30-50% in northern mid-latitudes and >100% in high latitudes). The increase is even stronger close to the southern edge of the South Gondwanan Mountains, but most likely exaggerated due to the presecribed orography. Moreover, the southern storm track is less intense for the Permian scenario. The observed decrease of triggered convection events of all types leads to strongly reduced mass flux in the PBL and lower troposphere (7 g/m²).

6.3. Tropopause

The tropopause constitutes the uppermost boundary for most of the convective motion in the troposphere. The dry and very stable conditions as well as the positive temperature lapse rate in the lower stratosphere prevent any further ascent. By that means the height of the tropopause determines the maximal level of vertical exchange and thus

has a significant impact on the atmospheric mixing. Shallow and mid-level convection processes generally do not reach such high altitudes and in many cases the energy of the updraughts of deep convection is not sufficient either, especially in higher latitudes. Only very energy-rich convection is able to overshoot into the lower stratosphere.

EMAC determines the tropopause height according to the WMO definition depending to the temperature lapse rate in low latitudes between 30°S and 30°N, and by the potential vorticity iso-surface of 3.5 PVU at latitudes poleward of 30° of latitude [96]. There is no smoothing applied at the transition and therefore inconsistencies can appear at 30° of latitude.

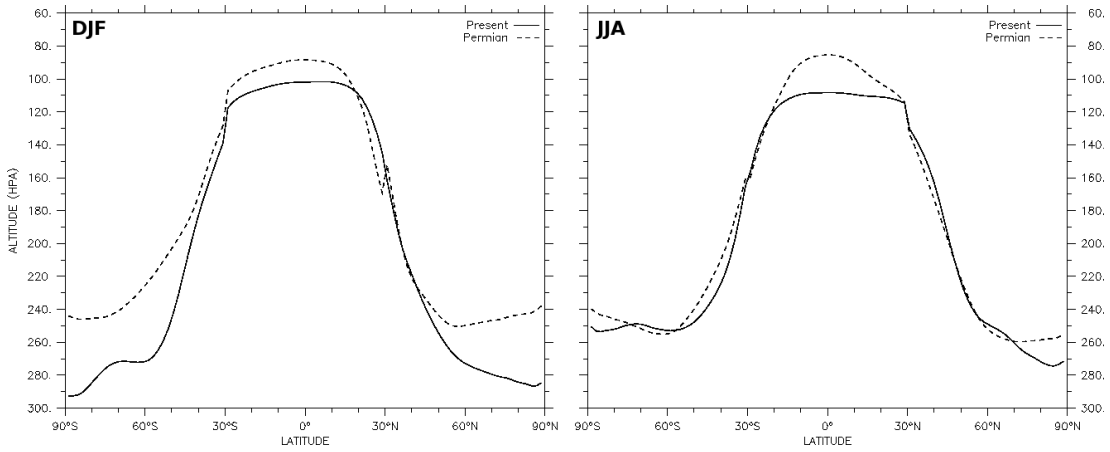

Figure 6.10.: Zonal mean tropopause height [hPa] for for winter and summer. The left panel depicts the seasonal mean for northern winter or southern summer, the right panel shows the mean for northern summer or southern winter. The dashed line represents the Permian $4\times CO_2$ scenario while the solid line represents the present-day reference scenario.

Figure 6.10 presents the zonal and seasonal mean tropopause height for winter and summer for both scenarios. The left panel corresponds to northern winter while the right panel considers the mean tropopause height for the northern summer. Significant differences of the tropopause height occur for both seasons. The Permian scenario generally exhibits a higher altitude of the tropopause than the present-day reference and the effect is more pronounced in low and high latitudes. In low latitudes the tropopause is lifted in the range between 30° of latitude in the summer hemisphere and 20° of latitude in the winter hemisphere. The tropopause height is increased in summer by about 10 hPa in the Southern Hemisphere and in the North by about 20 hPa near the equator but only 5 hPa at 20°N. In winter the Northern Hemisphere exhibits an increase of about 10 hPa, whereas it is increased by about 20 hPa in the South. Hence, the tropopause is lifted stronger during winter in low latitudes of both hemispheres. The behaviour is contrasting in higher latitudes. The troposphere height is increased distinctly by 30-50 hPa in the Southern Hemisphere poleward of 45°S during summer. However, it is approximately equal up to 70°N during summer and only further poleward an increase of 10-15 hPa can be observed. The tropopause is

lifted strongly by up to 40 hPa in the Northern Hemisphere poleward of 45°N in winter by contrast, while there are only small changes of less than 10 hPa in the South during winter. Inconsistencies occur in the range of the transition of the tropopause definition in both winter hemispheres.

6.4. Conclusions

The previous analysis has revealed that the characteristics of the Permian climate significantly affect the static stability and the vertical transport within the atmosphere. The higher temperatures throughout the troposphere, especially in high latitudes, and the increased moisture content destabilise the atmosperic stratification in the lower troposphere in high latitudes and in the lower and middle troposphere in southern mid-latitudes. The effect is generally stronger in the Southern Hemisphere due to the weaker poleward oceanic heat transport in the Northern Hemisphere. Stabilisation occurs in the upper troposphere in low latitudes between 300 and 400 hPa. The degree of static stability is generally decreased on global average in all ranges of the troposphere, but there are no exceptionally unstable areas like the Indo-Pacific Warm Pool in the present-day reference scenario. Deep convection is triggered less frequently in northern low latitudes in favour of shallow convection, whereas it is similarly frequent in southern low latitudes and even more frequent in southern mid-latitudes. Shallow convection occurs more frequently in northern mid-latitudes and high-latitude areas exhibit significantly increased frequency of all types of convection events. The intensity of convective processes is enhanced in the entire Southern Hemisphere and in northern low latitudes in agreement with the observed weakness of northward heat transport. The mean convection top height as well as CAPE are significantly increased in this range. On the one hand convection events involving high energies occur more frequently, but on the other hand the stabilisation in the upper troposphere in low latitudes suppresses deep convection events in the medium-energy range. That is why the resulting upward mass transport is lower in low latitudes. In the Southern Hemisphere the increased intensity as well as the increased frequency of deep convection lead to stronger upward mass transport in the middle and upper troposphere in mid-latitudes and both also enhance the upward mass flux in the lower troposphere in high latitudes. In contrast, the upward mass flux in northern mid- and high latitudes is solely increased by the higher frequency of convection events. The Permian topography prevents the formation of a strong storm track in the range of the westerlies. Thus instabilities and convective activity are reduced in the PBL and lower troposphere in comparison with the southern storm track of the present-day reference. The tropopause is lifted mainly by 10-20 hPa in low and even by up to 50 hPa in high latitudes.

7

Transport in Present-Day Atmosphere: Impact of Data Assimilation

The simulation of an ESM heavily depends on the initial conditions. This is especially true for simulations on synoptic scales but also during the spin-up period before the equilibrium state has been reached (see Section 4.4). Insufficient resolution, inaccurate parameterisations of small-scale processes as well as deficient boundary conditions like orographic or other external forcings are error sources of the model predictions. In other words the simulated state of the Earth system represents one possible solution related to the initial and boundary conditions which is not necessarily the state that has been observed in reality. Weather forecasts, validation studies of particular model parameterisations as well as diagnostic analyses of dynamical or chemical processes in the atmosphere require the simulation to represent the observed situation as good as possible, however. That is why the assimilation towards observed or reanalysed data of a particular synoptic situation is common practise for simulations with atmospheric and oceanic GCMs [175–177].

There are a number of different approaches for data assimilation in GCMs. Most of them apply an additional forcing towards the observational data. One of the simplest methods is the *nudging* method that is employed in EMAC. The additional forcing generally constitutes a non-physical impact on the model dynamics, although several different techniques are applied to dampen the perturbation. The model responses by rebalancing to return to its equilibrium state again. In the following the previously established methods will be applied to examine the impact of nudging on atmospheric stability and atmospheric transport processes. Section 7.1 gives an overview of the different approaches of data assimilation in GCMs and describes the nudging algorithm, that is employed in EMAC, in more detail. The implementation of the nudging procedure in EMAC is described in Section 7.2. Section 7.3 summarises the model setup for the nudged and free scenarios used in this study and Section 7.4 surveys a method by Stein and Alpert [178] to separate the influence of single factors and their interactions that is

employed in the analyses. The impact of nudging on atmospheric stability and vertical transport is discussed in Section 7.5.

7.1. Approaches of Data Assimilation in GCM

A number of different approaches for data assimilation has been established that each have certain advantages and disadvantages. The simplest approach is to replace the model prediction of the respective grid cell with the observation at the nearest location [179]. However, this direct insertion can have a shock-like impact on the system when the inserted mass fields and the model-computed wind fields are mismatched, for example. Gravity waves with high amplitudes are generated as the model attempts to restore the dynamical equilibrium [180, 181]. This behaviour seems inappropriate for a satisfying simulation of realistic conditions. Other approaches focus more on a relatively small perturbation.

On the one hand there are variational approaches that try to optimise the initial forcing by means of the minimisation of some cost function, i.e. the difference between model and observations [182, 183]. Although the underlying physics of the model are retained, the solution of the corresponding Euler-Lagrange equations is complex and very expensive. On the other hand there are stochastic approaches that employ Kalman filtering [184] to include the observations. They consider the prognostic fields as realisation of stochastic processes, more particularly first-order Markov processes. The next state is initially estimated solely by the estimate of the current state without any regard to the observation. Subsequently, the estimate of the next state is refined as weighted average of the system's prediction and the observation information. The weight depends on the covariances of both the process and the statistical noise of the observation. The second step is not necessarily executed depending on the availability of observations. The original Kalman filter is only applicable to linear equations, but Kalman and Bucy [185] extended the framework for non-linear equations. Still, the computation of the covariance matrices is computationally very expensive for high-dimensional systems as they usually occur for meteorological data assimilation. Simplifications either prescribe the covariances or employ a Monte Carlo approximation that uses an ensemble of forecasts to estimate the covariances [186–188]. Unbalanced dynamical states can appear due to the discontinuity of the data assimilation procedure as well as the covariance localisation, that is employed to remove long-range correlations of the observations [189]. They trigger the generation of gravity waves and unphysical readjustment processes. There are several strategies to avoid this impact, like rebalancing directly after the assimilation step, balancing the reanalysed observations, or augmenting specific observation informations [190, 191].

The Newtonian relaxation, or *nudging*, represents a relatively simple implementation of the stochastic approach [192, 193]. Both, model prediction and observation, are

assumed as noise-free and the weight is just prescribed as relaxation coefficient. The forcing due to the assimilation consequently depends directly on the difference between the model prediction and the observation. The differential equation of any arbitrary prognostic model variable X can be written as [177]:

$$\frac{\partial X}{\partial t} = F_{\mathrm{m}}(X) + G\left(X_{\mathrm{obs}} - X\right). \tag{7.1}$$

The first term F_m describes the model forcing resulting from the dynamical and physical processes. The forcing of the prognostic variable towards its observed value is contained in the second term, the relaxation term. The relaxation coefficient G controls the strength of this non-physical forcing and is related to the characteristic relaxation time τ by $\tau = G^{-1}$. In contrast to the direct insertion procedure, the model prediction is not just replaced by the observation, but it is nudged exponentially with time constant τ towards it. Large relaxation coefficients or small relaxation times, respectively, imply strong nudging, whereas weak nudging is realised by small coefficients or long relaxation times. The relaxation coefficients can vary with time and place and the application with spectral models allows to exclude specific scales. Generally, the implementation of the nudging procedure can be realised without a lot of effort and the computation costs are relatively low. Therefore, this technique of data assimilation is employed in several studies and a number of different methods and algorithms have been developed [194–196]. The determination of the optimal relaxation coefficients constitutes the major difficulty, however, since they do not follow directly from the algorithm. In most cases the value of the coefficient is assumed constant and is estimated empirically from a broad range of coefficients in the magnitude of the smallest time scale of the phenomena captured by the model. Other approaches try to determine the coefficient by means of a minimisation procedure [196, 197]. Although the non-physical impact of each assimilation is damped exponentially, the continuous assimilation causes a continuous spin-up of the model [177].

7.2. Nudging in EMAC

Data assimilation in EMAC is completely covered by its base model ECHAM5 since the latter executes the time integration of the prognostic model variables. Jeuken et al. [177] integrated the first implementation of the Newtonian relaxation formalism as written in Equation 7.1 into ECHAM3 [198] on a rather coarse T21L19 grid. The following generations, i.e. ECHAM4 [123] and ECHAM5 [95], provided minor revisions and extensions to finer grids [199, 200].

As reported in Section 3.1.1 the prognostic variables of ECHAM5 are vorticity, divergence, temperature, the natural logarithm of surface pressure, and moisture variables. Moisture variables include water vapour, cloud water, and cloud ice. They are treated horizontally

discretised in grid point space and advection is implemented according to a semi-Lagrangian flux scheme. That is why Jeuken et al. [177] do not apply the nuding procedure to these variables but solely consider the nudging of vorticity, divergence, temperature, and the natural logarithm of surface pressure, that are all integrated in spectral space. They regard the nudging of the vorticity as more important than the nudging of the divergence to represent a particular synoptic situation. That is because the rotational part of the wind is related to quasi-geostrophic motion and the evolution of Rossby wave type flow, whereas the divergent part is associated with gravity waves. The nudging of the surface pressure is included to avoid errors at the surface.

The nudging is performed at an additional step during the time integration. The model forcing F_m is determined and applied to the prognostic variable X_t at first:

$$X^\mathrm{m}_{t+\Delta t} = F_\mathrm{m}\left(X_t\right). \tag{7.2}$$

Subsequently, the resulting model prediction for the following time step $X^\mathrm{m}_{t+\Delta t}$ is nudged towards the assumed real value $X^\mathrm{an}_{t+\Delta t}$. The relaxation term is determined by the discretisation of Equation 7.1:

$$\frac{X_{t+\Delta t} - X^\mathrm{m}_{t+\Delta t}}{2\Delta t} = G(X)\left[X^\mathrm{an}_{t+\Delta t} - X_{t+\Delta t}\right]. \tag{7.3}$$

Hence, the final nudged result for the following time step is:

$$X_{t+\Delta t} = \frac{2\Delta t\ G(X)}{1 + 2\Delta t\ G(X)}\ X^\mathrm{an}_{t+\Delta t} + \frac{1}{1 + 2\Delta t\ G(X)}\ X^\mathrm{m}_{t+\Delta t}. \tag{7.4}$$

Both limiting cases, very strong as well as very weak nudging, show the desired behaviour:

$$\lim_{G\to\infty} X_{t+\Delta t} = X^\mathrm{m}_{t+\Delta t} \quad \text{and} \quad \lim_{G\to 0} X_{t+\Delta t} = X^\mathrm{an}_{t+\Delta t}. \tag{7.5}$$

The implementation of the nudging procedure in spectral space offers the opportunity to employ a different forcing depending on the scale by using different relaxation coefficients for each spectral coefficient in Equation 3.3. Despite that Jeuken et al. [177] employ constant nudging and equal relaxation coefficients on all scales. The only exception is the first spectral component that represents the global average. This component is not assimilated to ensure mass and momentum conservation. However, Jöckel et al. [201] observe significant implications on temperature biases of the model when the first component is included.

There is no implemented procedure to determine the values of the relaxation coefficients. The choice of coefficients has been optimised empirically to yield the best match with observational data. Jeuken et al. [177] examine a wide range of values. They conclude that strong nudging reduces the global averaged precipitation, evaporation as well as the vertical transport of tracers, whereas weak nudging leads to bad agreement with the observations. Moreover, they find the precipitation and vertical transport in convective

clouds to be sensitive to the magnitude of the temperature relaxation coefficient and suggest relatively small coefficients. The relaxation times typically assumed in studies with ECHAM are 12 h for temperature, 6 h for vorticity, 48 h for divergence, and 12 h for surface pressure [202, 203].

7.3. Model Setup for nudged and free Scenarios

The reanalysed observation information used within this studies is ERA-Interim [204]. This is a comprehensive global atmospheric reanalysis of the ECMWF covering the time span between 1979 and the present day. It is updated regularly with a delay of two month for reanalysis. The data set includes a 4-dimensional variational analysis on a 12 h time interval and on a T255 spectral grid with 60 vertical levels from the surface up to 0.1 hPa. Since data assimilation in EMAC is executed at every integration time step, i.e. about every 450 s, the data is interpolated by the model within the 12 h interval. Similarly, the data needs to be averaged to the coarser spatial grid of the model. Both mappings provide possible error sources and can generate additional non-physical forcings. Atmospheric processes on short time scales are not captured in the ERA-Interim data set and thus excluded from data assimilation. Large-scale processes that originated on smaller scales appear more abrupt in that way. In addition the data set includes processes on small length scales that trigger proccesses in the assimilated model without any physical base on the coarser grid.

This study employs the EMAC model as presented in Chapter 3 with some adjustments. A slightly earlier version of EMAC, i.e. EMAC 2.42, is used, but without any major changes in the involved submodels. The coupled ocean model has been replaced by a monthly climatology of prescribed SST. On the one hand this represents an additional unphysical forcing and also triggers some kind of nudging towards a particular state. On the other hand this includes wide-ranging phenomena like the El Niño-Southern Oscillation and allows the comparison of the nudged and free scenario with the overlay of such variations. The simulations are performed for present-day orography on a T63L31 grid with a time step of 450 s. The study considers the time span between 1st January 1996 and 31st December 2004.

Two scenarios are compared in the following: For the *free scenario* EMAC is used without any nudging but with prescribed SST. The *fully-nudged scenario* is affected by nudging of vorticity, divergence, temperature, and surface pressure at every simulation time step. However, the relaxation coefficients are chosen differently depending on the vertical level. There is no nudging applied in the three lowermost and uppermost levels to reduce the unphysical impact in the boundary layer and a smooth transition with respect to the levels with full nudging strength. This corresponds to a frequently used assumption of relaxation coefficients. The coefficients are summarised in Table. 7.1. The analysis of the impact due to the nudging requires additional simulations with

Level	G_{temp} [10^{-5} s^{-1}]	G_{vort} [10^{-5} s^{-1}]	G_{div} [10^{-5} s^{-1}]	G_{press} [10^{-5} s^{-1}]
1 - 3	0	0	0	
4	0.1447	0.5787	0.0723	
5	0.2894	1.1574	0.1447	
6	0.5787	2.3148	0.2894	
7 - 25	1.1574	4.6296	0.5787	
26	0.5787	2.3148	0.2894	
27	0.2894	1.1574	0.1447	
28	0.1447	0.5787	0.0723	
29 - 31	0	0	0	<31>: 1.1574

Table 7.1.: Relaxation coefficients typically used in EMAC. The corresponding relaxation times of the non-reduced coefficients are 12 h for temperature, 6 h for vorticity, 48 h for divergence, and 12 h for surface pressure.

arbitrary combinations of one, two, or three of the prognostic variables being nudged. The assimilated variables are nudged with the same coefficients as in the fully-nudged scenario, whereas $G = 0$ is chosen for the others.

7.4. Factor Separation Method

In sensitivity studies the impact of a particular factor on a certain environment, e.g. atmospheric fields, is typically examined and separated by means of two simulations or two records, one under the influence of this factor and the other one without. The difference of both eventually allows to isolate the impact. The situation is more complicated when the impact of two or even more factors is to be analysed. The comparison of two simulations or records, merely reveals the combined effect, which actually represents the superposition of the single and joint impacts. Considering the single impacts separately neglects the interaction between these factors, however.

Stein and Alpert [178] have developed a numerical method that allows to isolate both the single and interactive impacts of various factors. This approach will be employed to analyse the impact of nudging the prognostic model variables and to break down the respective contributions. The derivation is presented in Appendix F and the general formula to determine the isolated contributions is given in Equation F.9. According to the number of combinations of wether the nudging is applied to one or more of the four prognostic variables the comprehensive analysis requires $2^4 = 16$ simulations. For any arbitrary predicted atmospheric field f the separated impacts $\hat{f}$ due to the nudging of temperature (t), vorticity (v), divergence (d), and the surface pressure (p) are:

$$\hat{f}_{\text{free}} = f_{\text{free}} \tag{7.6}$$

$$\hat{f}_{\text{d}} = f_{\text{d}} - f_{\text{free}} \tag{7.7}$$

$$\hat{f}_{\mathrm{v}} = f_{\mathrm{v}} - f_{\mathrm{free}} \tag{7.8}$$
$$\hat{f}_{\mathrm{t}} = f_{\mathrm{t}} - f_{\mathrm{free}} \tag{7.9}$$
$$\hat{f}_{\mathrm{p}} = f_{\mathrm{p}} - f_{\mathrm{free}} \tag{7.10}$$
$$\hat{f}_{\mathrm{dv}} = f_{\mathrm{dv}} - (f_{\mathrm{d}} + f_{\mathrm{v}}) + f_{\mathrm{free}} \tag{7.11}$$
$$\hat{f}_{\mathrm{dp}} = f_{\mathrm{dp}} - (f_{\mathrm{d}} + f_{\mathrm{p}}) + f_{\mathrm{free}} \tag{7.12}$$
$$\hat{f}_{\mathrm{dt}} = f_{\mathrm{dt}} - (f_{\mathrm{d}} + f_{\mathrm{t}}) + f_{\mathrm{free}} \tag{7.13}$$
$$\hat{f}_{\mathrm{tv}} = f_{\mathrm{tv}} - (f_{\mathrm{t}} + f_{\mathrm{v}}) + f_{\mathrm{free}} \tag{7.14}$$
$$\hat{f}_{\mathrm{pv}} = f_{\mathrm{pv}} - (f_{\mathrm{p}} + f_{\mathrm{v}}) + f_{\mathrm{free}} \tag{7.15}$$
$$\hat{f}_{\mathrm{pt}} = f_{\mathrm{pt}} - (f_{\mathrm{p}} + f_{\mathrm{t}}) + f_{\mathrm{free}} \tag{7.16}$$
$$\hat{f}_{\mathrm{dtv}} = f_{\mathrm{dtv}} - (f_{\mathrm{dt}} + f_{\mathrm{dv}} + f_{\mathrm{tv}}) + (f_{\mathrm{d}} + f_{\mathrm{t}} + f_{\mathrm{v}}) - f_{\mathrm{free}} \tag{7.17}$$
$$\hat{f}_{\mathrm{dtp}} = f_{\mathrm{dtp}} - (f_{\mathrm{dt}} + f_{\mathrm{dp}} + f_{\mathrm{pt}}) + (f_{\mathrm{d}} + f_{\mathrm{t}} + f_{\mathrm{p}}) - f_{\mathrm{free}} \tag{7.18}$$
$$\hat{f}_{\mathrm{dpv}} = f_{\mathrm{dpv}} - (f_{\mathrm{dp}} + f_{\mathrm{dv}} + f_{\mathrm{pv}}) + (f_{\mathrm{d}} + f_{\mathrm{p}} + f_{\mathrm{v}}) - f_{\mathrm{free}} \tag{7.19}$$
$$\hat{f}_{\mathrm{ptv}} = f_{\mathrm{ptv}} - (f_{\mathrm{pt}} + f_{\mathrm{pv}} + f_{\mathrm{tv}}) + (f_{\mathrm{p}} + f_{\mathrm{t}} + f_{\mathrm{v}}) - f_{\mathrm{free}} \tag{7.20}$$
$$\begin{aligned}\hat{f}_{\mathrm{dtpv}} = {} & f_{\mathrm{ptv}} - (f_{\mathrm{dtv}} + f_{\mathrm{dtp}} + f_{\mathrm{dpv}} + f_{\mathrm{ptv}}) + \\ & (f_{\mathrm{dt}} + f_{\mathrm{dp}} + f_{\mathrm{dv}} + f_{\mathrm{tv}} + f_{\mathrm{pt}} + f_{\mathrm{pv}}) - (f_{\mathrm{d}} + f_{\mathrm{t}} + f_{\mathrm{p}} + f_{\mathrm{v}}) + f_{\mathrm{free}}\end{aligned} \tag{7.21}$$

The notation is defined such that f_{dv} correponds to the simulation where the divergence and vorticity are nudged whereas the temperature and surface pressure are not assimilated.

7.5. Impact on atmospheric vertical Transport

Data assimilation in GCM by means of nudging not only makes the model prediction approach a particular observed or predefined situation but also provides a continuous non-physical impact on the dynamics of the model (see Section 7.1). Although the nudging takes account of mass and momentum conservation, its forcing implies a perturbation to the dynamic and thermodynamic equilibrium. The model reacts by rebalancing to return to an equilibrium state again. This rebalancing is particularly realised in the form of atmospheric motion to overcome altered vorticity and divergence as well as altered temperature and pressure gradients. Hence, nudging may potentially induce atmospheric motion and consequently affect the atmospheric flow. The impact is further enhanced due to the continual nudging at each time step during integration and the consequential consistent triggering of the rebalancing processes.

This study analyses the impact of nudging on atmospheric transport and mixing processes. It focusses on relatively short-range processes on a time scale in the magnitude of the relaxation times of the nudging since these processes reflect the direct response of the model to the nudging on the one hand. On the other hand short-range processes also

contribute to processes on a larger scale. Particular emphasis is given to vertical motions because of their strong contributions to the atmospheric mixing. The impact of nudging on large-scale circulations is not part of this study, however. The nudging is not applied in the lowermost and uppermost levels as mentioned in Section 7.3. That is why the impact on processes within the planetary boundary layer is not considered in detail. Furthermore, turbulent processes, that predominate in these layers, are disregarded since no significant effects apart from statistical noise have been observed. At first, the impact on static stability and the frequency of triggered convection is considered in Section 7.5.1 to estimate the effect on the propensity of vertical motions. Section 7.5.2 examines the impact on the intensity of convection and enlightens differences of available energy and shifted mass. Induced displacements of the tropopause constituting a major upper barrier to vertical transport are dealt with in Section 7.5.3. Most of the following analyses consider the difference between the fully-nudged scenario and the free scenario to isolate the impact of nudging. For a proper assessment it is essential to take into account that this difference results from both aspects, the altered synoptic situation on the one hand as well as the rebalancing due to the non-physical perturbation on the other hand.

7.5.1. Impact of Nudging on Static Stability and the Frequency of Convection

The potential of a particular air parcel to vertical motion within an air column is generally indicated by the degree of its static stability depending on temperature and moisture of the surrounding environment. The vertical gradient of the equivalent potential temperature has revealed to be a good measure of the degree of stability as it has been reviewed in Section 1.3. Again, the gradient is determined as centered derivative between the vertical levels in terms of pressure coordinates. This implies $\frac{\partial \theta_e}{\partial p} < 0$ to indicate stable conditions and $\frac{\partial \theta_e}{\partial p} > 0$ for unstable conditions (see Section 6.1).

The first issue to be examined is whether nudging affects the frequency of unstable conditions and where these changes can be found. Figure 7.1(a) shows the mean proportion of unstable conditions on annual average for the free scenario by means of a zonally averaged profile of the troposphere and lower stratosphere. This evaluation does not consider the degree of stability but simply concentrates on whether the gradient is positive or negative. As expected unstable conditions are most frequent in lower latitudes in the lower part of the troposphere. Near the equator the predominance of unstable conditions generally reaches the highest altitude. High relative frequencies of more than 75% of the simulated period can be found between 20°S and 20°N up to 700 hPa. Moreover, there is another very unstable belt within the planetary boundary layer between 40°S and 20°S (The mean planetary boundary layer height is depicted in the Appendix in Figure G.1). Moderate relative frequencies of more than 50% occur between 55°S and 40°N up to an altitude of 800 hPa at 30° of latitude and 600 hPa near

to the equator. Unstable conditions are rare (< 20%) in polar latitudes and in altitudes higher than 500 hPa also in mid- and low latitudes. The meridional distribution is not symmetrical since the higher sea fraction on the Southern Hemisphere extends the zone of high instability further to the south.

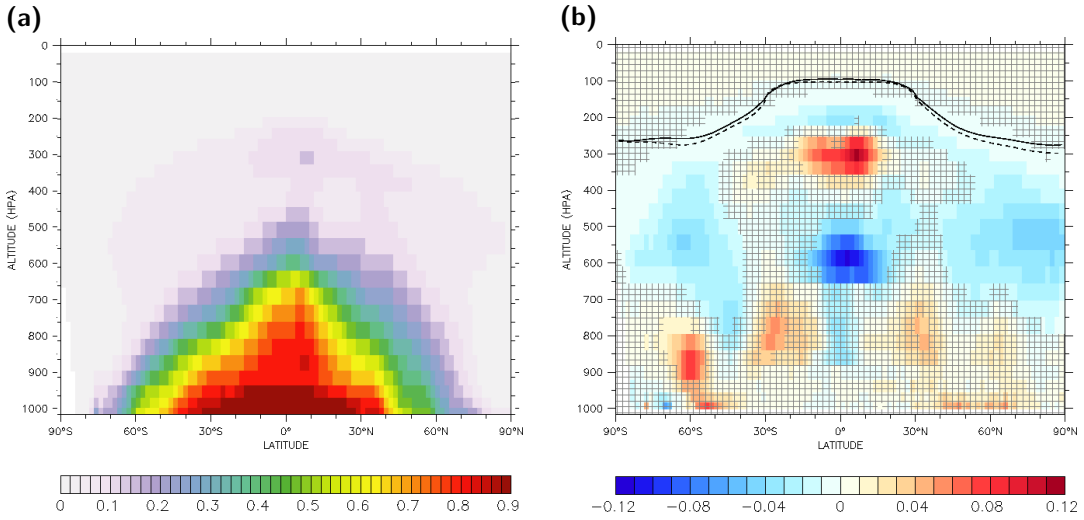

Figure 7.1.: Impact of nudging on the proportion of unstable conditions on zonal average: (a) Proportion of unstable conditions with respect to the simulated period of 9 years. The profile shows the annual average for the free scenario. (b) Impact by nudging: The simulated annual and zonal mean proportion of unstable conditions that results for the fully-nudged scenario is compared to the free model scenario. In hatched areas the difference is not highly significant based on an unpaired Student's t test and on a significance level of 95%. The black lines indicate the altitude of the cross sections where the distribution of conditional instabilities and their changes due to nudging are examined in more detail in the following. In addition the mean altitude of the tropopause is marked for both scenarios (solid: free scenario, dashed: fully-nudged scenario).

The comparison of the proportion of statically unstable conditions between both scenarios is presented in Figure 7.1(b). The free scenario serves as reference. There bluish colours mark areas where the frequency of unstable conditions is decreased due to nudging, whereas reddish colours mark areas where the frequency is increased. The statistical significance of the difference is again evaluated by means of an unpaired Student's t test. Due to the simulation length of 9 years the test is performed for a significance level of 5%. In the lower troposphere the nudging leads to significantly more frequent unstable conditions in southern mid-latitudes. There is an increase of about 8 percentage points (pp) of relative frequency at the southern edge of the southern westerlies between 920 and 850 hPa from 65°S to 55°S. This increase can be observed up to 750 hPa, but it is less pronounced in higher altitudes. The most distinct decrease of unstable conditions occurs over the equator between 10°S and 10°N in the middle troposphere between 500 and 650 hPa. The relative frequency of unstable conditions is reduced there by up to 12 pp. The most distinct increase (8-12 pp), can be found over the same region in

the upper troposphere between 350 and 250 hPa. Moreover, there is a slight decrease of unstable conditions by 2-4 pp in the middle and upper troposphere over mid- and high latitudes and a very slight decrease by 1-2 pp in the range of the tropopause over all latitudes.

Both the temperature of an air parcel as well as its moisture content influence its buoyancy and the atmospheric stability. The profile of the zonal mean nudging impact on the specific humidity (see Appendix, Figure G.2) reveals that nudging significantly decreases the moisture content in the lower and middle troposphere near to the equator. The specific humidity is decreased by about 1 g/kg between 900 and 600 hPa on zonal and annual average. This constitutes a relatively small change in lower altitudes but between 700 and 600 hPa this corresponds to a decrease of 12%. The reduced moisture content potentially causes more frequent stable conditions in the middle troposphere and suppresses vertical exchange to higher altitudes. Instabilities in higher altitudes are consequently balanced less frequently by deep convection and the number of unstable conditions is increased. However, the profile of zonal mean specific humidity reveals no significant increases of moisture in higher altitudes over the equator that would explain the increase of unstable conditions. On the one hand various regional effects can have a strong effect that is not significant on zonal average. On the other hand the impact of nudging on both the temperature of the buoyant air parcel and the environment turns out to be more decisive in the upper troposphere where the moisture content is generally low. The stability of dry air is generally specified by the vertical gradient of the potential temperature. The corresponding profile (see Appendix, Figure G.6) shows a significant increase of unstable conditions at 300 hPa over the equator and a decrease of unstable conditions in the range of the tropopause. The latter observation agrees well with the previously observed slight stabilisation in the range of the tropopause. However, the increase of unstable conditions for dry air at 300 hPa over the equator is about one order of magnitude smaller than the previously observed increase for moist air at this altitude. The area of increased unstable conditions in the lower troposphere between 65°S to 55°S is not remarkable neither in the profile of the specific humidity nor in the profile of the gradient of the potential temperature. The larger proportion of instability is probably caused by displacements of the southern west wind drift.

In the following three cross sections across the lower (at 850 hPa), middle (at 550 hPa), and upper troposphere (at 300 hPa) are considered to analyse the impact on the distribution of the degree of static stability as well as regional differences of the proportion of unstable conditions at these levels. The respective altitudes are marked in both profiles of Figure 7.1.

Lower Troposphere

At first, the impact of nudging on the degree of static stability is considered. The vertical gradient of the equivalent potential temperature is a good measure to represent the degree of static stability as outlined above.

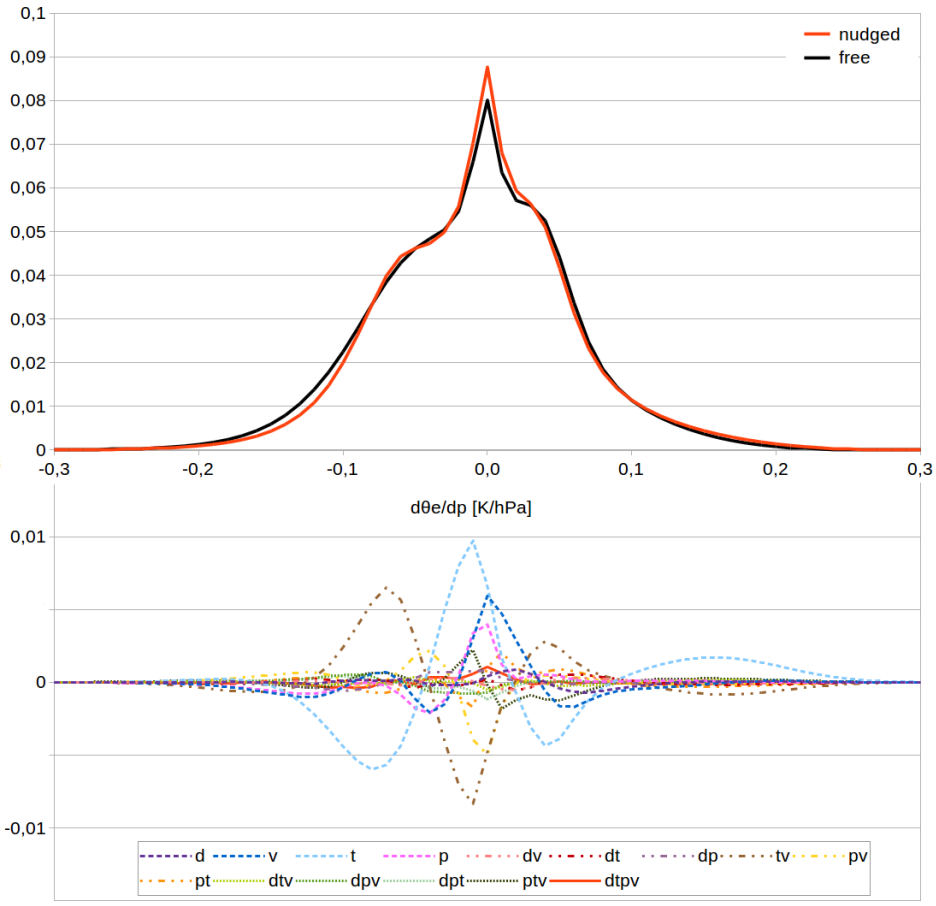

Figure 7.2.: Impact of nudging on static stability in the lower troposphere at 850 hPa: The upper curves show the frequency distribution of the vertical gradient in terms of pressure of the equivalent potential temperature from the entire Earth with respect to the simulated period of 9 years. The negative gradient indicates stable conditions whereas the positive gradient indicates instabilities. The red line represents the fully-nudged scenario and the black line represents the free model scenario. The lower curves break down the isolated and interactive contributions to the nudging impact.

Figure 7.2 shows the corresponding frequency distribution at 850 hPa from the entire Earth with respect to the simulated period for both the fully-nudged and the free scenario. The general shape of the distribution is very similar for both scenarios. The degree of stability appears virtually normally distributed around the neutral metastable case ($\frac{\partial \theta_e}{\partial p} = 0$) with a small bias towards stable conditions. There is an additional strong peak at neutral metastable conditions. The distribution shows that metastable and weakly stable or unstable conditions predominate in the lower troposphere from a global point of view. This is not affected by the nudging in general and only small effects can be obeserved: The integrated proportion of unstable conditions is increased from 41.68% for the free scenario to 42.32% for the nudged scenario and the same is true for the mean (-0.009 $^{\mathrm{K}}/_{\mathrm{hPa}}$ for the free scenario and -0.056 $^{\mathrm{K}}/_{\mathrm{hPa}}$ for the nudged

case). Both indicate that the distribution of the nudged scenario is shifted very slightly towards instability. Furthermore, the metastable peak is slightly more pronounced, the distribution is slightly more smooth, distinct instabilities are slightly preferred, whereas distinctly stable conditions are slightly less frequent.

The lower part of Figure 7.2 breaks down the separated contributions from the single nudged variables and their interactive effects. In agreement with the previous findings, the isolated contributions themselves are relatively small. The nudging of temperature and vorticity as well as the interaction between these two and the interaction between vorticity and surface pressure provide the strongest impact. The other contributions are negligibly small. The small augmentation of metastable or weakly stable and unstable conditions is mainly induced by nudging of temperature and vorticity. Nudging of temperature appears more important for the increase of weakly stable conditions, whereas the nudging of vorticity provokes the increase of instabilities. Both impacts are counterbalanced for the most part by the resulting interactive effect of temperature and vorticity, but also of the interaction of vorticity and surface pressure. The nudging of temperature is also responsible for the slight increase of distinct stabilities and instabilities. However, the interaction of temperature and vorticity counteracts again.

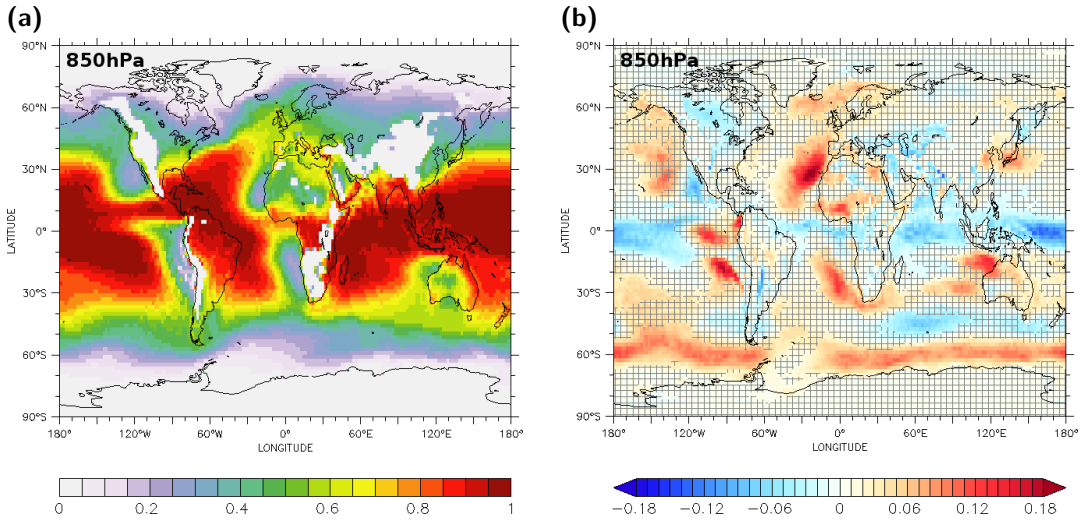

Figure 7.3.: Impact of nudging on the proportion of unstable conditions in the lower troposphere at an altitude of 850 hPa: (a) Proportion of unstable conditions with respect to the simulated period of 9 years. The cross section shows the annual average for the free scenario. (b) Impact by nudging: The simulated proportion of unstable conditions on annual average that results for the fully-nudged scenario is compared to the free model scenario. In hatched areas the difference is not highly significant based on an unpaired Student's t test and on a significance level of 95%.

The previous analysis has revealed that the impact of nudging on the distribution of the degree of stability is generally relatively small in the lower troposphere on a global

scale. However, the difference can be far more distinct depending on the region. The regional impact on the appearance of unstable conditions is examined in the following.

The proportion of unstable conditions for the free scenario at 850 hPa is shown in Figure 7.3(a). Unstable conditions occur very frequently (relative frequency > 75%) over the warm oceans between 35°S and 35°N except for the areas dominated by cold ocean currents along the west coasts of North and South America, Africa, and Australia. Very high frequencies can be found as well over the tropical regions of the continents, i.e. over South-East Asia, India, Central Africa, Central America, and northern South America. The range where unstable conditions generally predominate (frequency > 50%) stretches from 45°S to 40°N over the oceans and coastal areas on the continents. Central Asia appears very stable, however, whereas the Gulf Stream extends the predominantly unstable area up to 60°N in western Europe. Over the southern oceans unstable conditions occur with a frequency of 20% at 60°S. In summary, the regional distribution of predominantly unstable areas is mainly determined by the oceans and their surface temperature in the lower troposphere. The asymmetry with respect to the Asian continent in the North and the Indian Ocean in the South probably causes the asymmetry observed in the distribution of the zonal mean.

The impact of nudging is depicted in Figure 7.3(b). In general, destabilisation occurs more frequently in areas that are predominantly stable in the free scenario. The nudging reduces the frequency of unstable conditions near to the equator, primarily over the oceans. The Indo-Pacific Warm Pool exhibits the most pronounced decrease (∼8-14 pp) while the impact is less strong (∼6-10 pp) over the other near-equatorial regions of the Atlantic, Indian, and central Pacific Ocean. The area of more frequent stable conditions extends further to the eastern Pacific Ocean, east of Central America. Further to the North or South, in the range of the tropics, unstable conditions are significantly more frequent over areas influenced by cold ocean currents in the east of the oceans. The frequency is increased by up to 18 pp over the Northern Atlantic Ocean, east of Africa, and Southern Europe, and up to 12 pp in the Southern Atlantic Ocean, east of Africa, the Indian Ocean, east of Australia, and the Pacific Ocean, east of South America. The nudging augments unstable conditions as well over areas influenced by warm ocean currents in higher mid- and high latitudes: the Norwegian Sea (8 pp), Alaska and the Northern Pacific Ocean east of North America (10 pp), but also over Japan and the Japanese Sea (10 pp). Over the Southern Ocean unstable conditions are reduced in a belt between 40°S to 50°S south of Africa and Australia (5-10 pp), but they are also increased by up to 12 pp further south in a belt between 65°S to 55°S. Both of these are relatively strong changes for this region.

The analysis of the global frequency distribution has revealed that the nudging of temperature and vorticity provides the main impact. The regional distribution of the dominant contribution is shown in Figure 7.4 for areas with significant change. The analysis of the dominant contribution of one region does not provide any information about whether other contributions have a similar size or whether there is only one

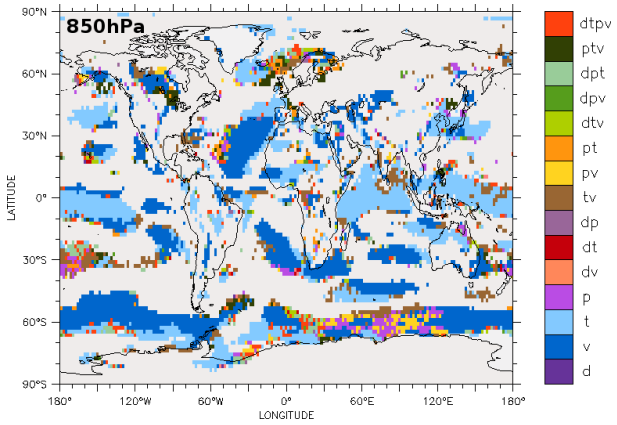

Figure 7.4.: The factor separation method allows to isolate the single and interactive contributions to the nudging impact. For each region the dominant contribution to the impact on static stability in the lower troposphere at 850 hPa is highlighted. Only areas with significant difference are included.

dominant contribution and all others are very small. However, the comparison of the dominant contributions with the global frequency distribution of the isolated impacts (see Figure 7.2) can indicate the range in which the degree of stability is affected most. These indications are subsequently verified by means of the frequency differences for the corresponding range (not shown). The nudging of vorticity and temperature as well as their interactive effect also have the strongest impact. In higher mid- and high latitudes there are significant contributions by nudging the vorticity, temperature and surface pressure, but also various interactive contributions from vorticity with temperature or pressure. This suggests an increase mainly in the range of weak instabilities (gradient between 0 and 0.03 $^{\mathrm{K}}/_{\mathrm{hPa}}$) because the mentioned contributions exhibit a significant impact within this range. The areas of increased frequency of unstable conditions over cold-water tropical oceans are mainly influenced by nudging of vorticity, whereas the stabilisation near the equator is mainly triggered by nudging the temperature. Here, the nudging mostly affects moderate instabilities related to a gradient between 0.03 and 0.09 $^{\mathrm{K}}/_{\mathrm{hPa}}$.

The comparison with the changes of specific humidity at 850 hPa caused by nudging (see Appendix, Figure G.3) confirms that the changes of static stability are correlated with changes of moisture in most regions, especially in low and lower mid-latitudes. Due to nudging, the annual mean of the specific humidity is significantly reduced in the range of the equator where also significant decreases of unstable conditions have been observed. The impact is strongest in the area of the Indo-Pacific Warm Pool which is also in agreement with the pronounced stabilisation in this region. Moreover, the cold water regions in the East of the tropical oceans, where unstable conditions occur more frequently, exhibit increased moisture.

Since unstable conditions facilitate convection, the alteration of static stability should also affect the frequency and type of the triggered convection events. The corresponding

collection of plots is presented in the Appendix. Figures G.13 to G.15 show the proportion of all triggered shallow, mid-level, and deep convection events, and the proportion of respective convection events at 850 hPa is presented in Figure G.10. The impact of nudging on frequency and type of triggered convection events seems to disagree with the observed alterations of static stability in some regions at first glance. At 850 hPa the frequency of triggered shallow convection events is significantly reduced over the tropical oceans on the one hand, especially over the Indo-Pacific Warm Pool. Deep convection events are significantly less frequent there as well. However, on the other hand deep convection is enhanced over the near-equatorial Atlantic and Indian Ocean, where the proportion of unstable conditions is actually reduced. The comparison of the frequency distributions of the degree of stability for both regions reveals the difference. For the Indo-Pacific Warm Pool (see Appendix, Figure G.16) the distribution is smoothed by nudging in such a way that weakly unstable conditions are less frequent and strongly stable and unstable conditions are enhanced. As a consequence, the mean is even slightly increased from 0.046 $^{\mathrm{K}}/_{\mathrm{hPa}}$ to 0.047 $^{\mathrm{K}}/_{\mathrm{hPa}}$, but the proportion of unstable conditions is decreased from 97.15% to 89.97%. For the near-equatorial Atlantic Ocean (see Appendix, Figure G.17), the peak of the distribution is also shifted slightly towards more stable conditions and the proportion of unstable conditions is decreased from 91.17% to 90.58%. However, the frequency distribution of the fully-nudged scenario exhibits a pronounced plateau between 0.1 and 0.15 $^{\mathrm{K}}/_{\mathrm{hPa}}$ that implies a strong enhancement of distinctly unstable conditions and thus explains the increase of triggered deep convection events. The mean of the distribution is consequently increased from 0.048 $^{\mathrm{K}}/_{\mathrm{hPa}}$ to 0.053 $^{\mathrm{K}}/_{\mathrm{hPa}}$. The factor separation eventually reveals that the shift of the peak and the frequency decrease of unstable conditions is essentially caused by nudging of the vorticity, whereas the nudging of the temperature causes the increase of distinctly stable conditions.

Due to nudging, shallow convection events are triggered more frequently over the cold water regions of the eastern tropical oceans (see Figure G.13). This agrees well with the observed increase of unstable conditions in these areas. The triggered convection events do not reach high altitudes, however, and that is why the frequency of shallow convection events is not significantly increased at 850 hPa. Over the Southern Ocean both the stabilisation between 40°S to 50°S and the destabilisation between 65°S to 55°S agree with the frequency changes of triggered shallow and also deep convection events. In this region vertical motion is essentially triggered by the large-scale lifting in the range of the warm and cold sectors of the low pressure systems as well as updraughts at the fronts. Hence, the poleward shift of increased instability and convective activity indicate a poleward shift of the southern storm track.

Middle Troposphere

The following analysis refers to an altitude of 550 hPa. Again, the impact of nudging on the degree of static stability is considered at first. The respective frequency distributions of the vertical gradient of equivalent potential temperature of both scenarios are presented in Figure 7.5. The distributions are essentially similar to a normal distribution again.

In contrast to the distributions of the lower troposphere, there are no additional peaks or plateaus. Both distributions are located clearly in the stable range. The nudging causes a further shift towards more stable conditions: The mean is only shifted from -0.041 K/hPa to $-0,042$ K/hPa, but the proportion of unstable conditions is reduced from 11.6% to 8.6%. For the nudged scenario the distribution exhibits a smaller width (full width at half maximum: -0.070 K/hPa (free), -0.075 K/hPa (nudged)), i.e. the degree of stability is distributed over a smaller range.

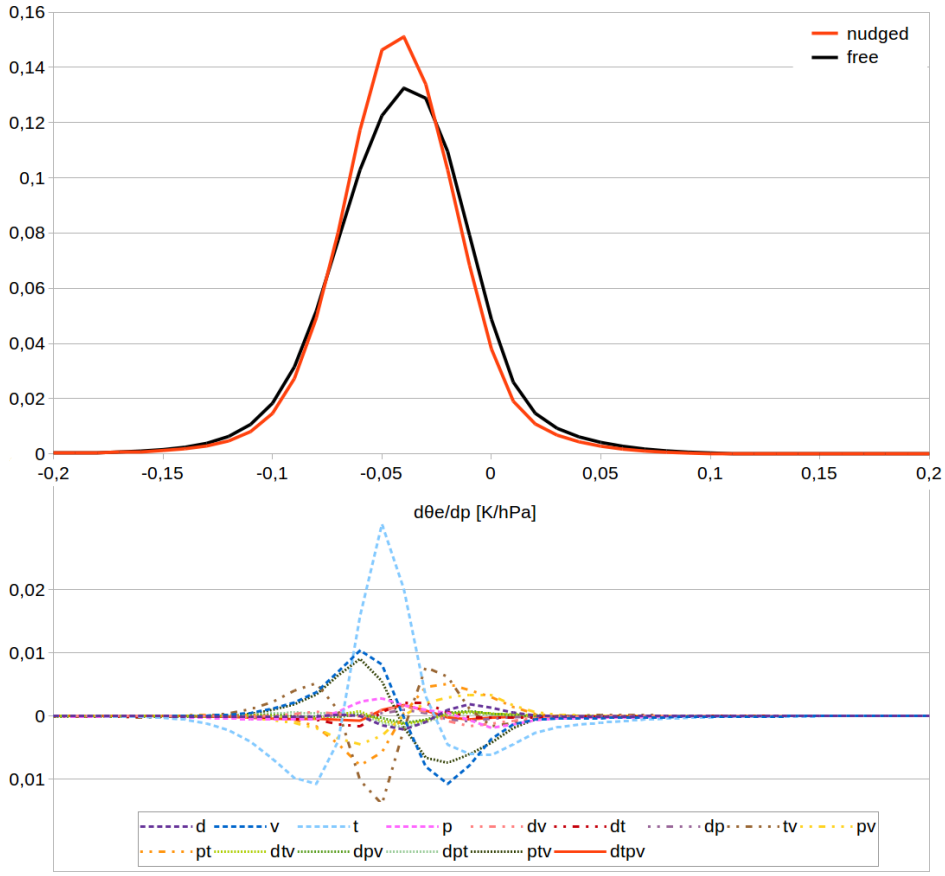

Figure 7.5.: Impact of nudging on static stability in the middle troposphere at 550 hPa: The upper curves show the frequency distribution of the vertical gradient in terms of pressure of the equivalent potential temperature from the entire Earth with respect to the simulated period of 9 years. The negative gradient indicates stable conditions whereas the positive gradient indicates conditional instabilities. The red line represents the fully-nudged scenario and the black line represents the free model scenario. The lower curves break down the isolated and interactive contributions to the nudging impact.

The separated contributions are again depicted in the lower part. The amplification of moderately stable conditions and the general shift is induced for the most part by nudging the temperature, vorticity and the triple interaction of pressure, temperature, and vorticity. The effect is reduced by the corresponding dual effects temperature-

pressure, vorticity-pressure, and temperature-vorticity. The influence of the temperature on the amplification of moderately stable conditions is very strong. For more stable conditions (< -0.07 K/hPa) the negative impact on the temperature is balanced by the other contributions.

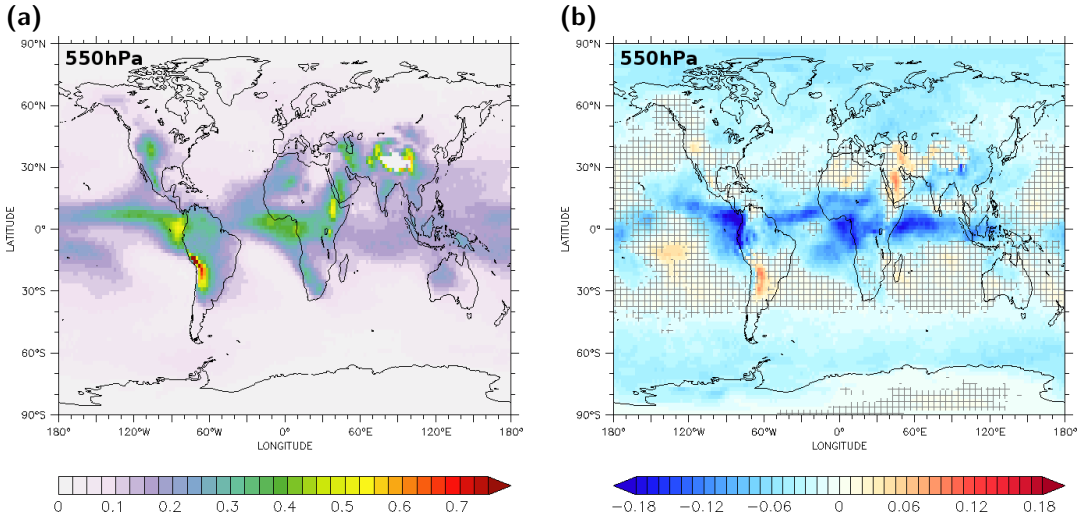

Figure 7.6.: Impact of nudging on the proportion of unstable conditions in the middle troposphere at an altitude of 550 hPa: (a) Proportion of unstable conditions with respect to the simulated period of 9 years. The cross section shows the annual average for the free scenario. (b) Impact of nudging: The simulated proportion of unstable conditions on annual average that results for the fully-nudged scenario is compared to the free model scenario. In hatched areas the difference is not highly significant based on an unpaired Student's t test and on a significance level of 95%.

The regional distribution of the free scenario, that is shown in Figure 7.6(a), also reflects the predominance of stable conditions. The belt of unstable conditions of a frequency higher than 20% is basically restricted between 15°S and 15°N. Over the continents there are extensions up to 40° of latitude. Relative frequencies of more than 30% occur over the equatorial eastern Pacific and Atlantic Ocean as well as over prominent mountain ranges, like the Rocky Mountains, the Andes, the Atlas Mountains, the Ethiopian Highlands, the Zagros Mountains, or the Himalaya and the Plateau of Tibet. Predominantly unstable regions are very rare and can merely be found over the Andes, the Plateau of Tibet and the Ethiopian Highlands.

The nudging impact on the proportion of unstable conditions in the middle troposphere at 550 hPa is presented in Figure 7.6(b). The distribution shows a decrease in almost every region. This agrees well with the shift towards more stable conditions that has been observed for the global frequency distribution of the gradient of the equivalent potential temperature. The most distinct decrease of unstable conditions can be observed along the equator, over the eastern Pacific Ocean, South America, Central Africa, and the Indian Ocean. In these areas the frequency of unstable conditions is reduced by

15-18 pp. This belt is also noticable in the mean zonal impact (see Figure 7.1(b)). In the adjacent regions to the North or South the impact of nudging is not significant in most parts. There are merely small regions over central South America and the Arabian peninsula that show a slight increase of instabilities by up to 8 pp, whereas parts of Autralia and South-East Asia show a slight decrease by 6 pp. Both hemispheres exhibit a significant decrease of unstable conditions by 3-6 pp in higher mid- and high latitudes poleward of 45° of latitude.

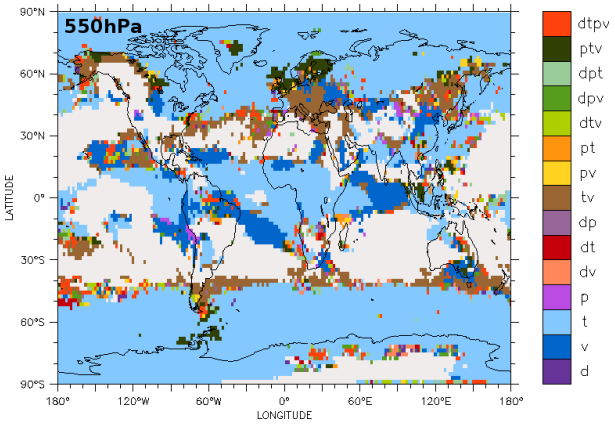

Figure 7.7.: The factor separation method allows to isolate the single and interactive contributions to the nudging impact. For each region the dominant contribution to the impact on static stability in the middle troposphere at 550 hPa is highlighted. Only areas with significant difference are included.

Figure 7.7 indicates the dominant contributions to the nudging impact. The belt of strong decrease of unstable conditions over the equator is primarily caused by nudging of the temperature while the impact by nudging of the vorticity merely predominates directly over the Andes and over the eastern Indian Ocean. In higher mid- and higher latitudes the nudging of the temperature provides the dominant impact again. The nudging of the temperature, vorticity, and the triple interaction of pressure, temperature, and vorticity also primarily affects the global frequency distribution within the stable range. This agrees well with the observed dominant contributions in the considered regions.

In this altitude the influence of moisture on atmospheric stability is basically restricted to lower latitudes since the moisture content is generally very low in mid- and high latitudes. The pattern of the nudging impact on specific humidity (see Appendix, Figure G.4) and the pattern observed for the proportion of unstable conditions match well for most regions. The specific humidity is decreased over most of the low-latitude oceans and continents where lower frequencies of unstable conditions have been found. However, discrepancies occur in the range of the equator. The humidity is significantly increased over the Atlantic Ocean, the Gulf of Guinea, and central Africa by 0.5-0.8 g/kg which corresponds to an increase of 20-25% in these regions. The humidity is also increased slightly over the Indian Ocean, but the effect is not significant there. In contrast, a strong

decrease of more than 1.2 $^{g}/_{kg}$ can be found over the Indo-Pacific Warm Pool. Both alterations agree with the observed pattern of triggered convection events (see Appendix, Figure G.11). The frequency of deep convection events is considerably increased over the Atlantic Ocean, and to a slight extent also over the Indian Ocean, while deep convection is significantly suppressed over the Indo-Pacific Warm Pool. The regional frequency distributions of the gradient of the equivalent potential temperature do not indicate any destabilisation due to nudging, however (not shown). Hence, the higher frequency of deep convection events, that have been triggered by nudging in the lower troposphere, increase the moisture content in the middle and upper troposphere over the near-equatorial Atlantic Ocean, but do not affect the frequency of unstable conditions in the middle troposphere. The humidity profiles of both regions (see Appendix) enlighten the difference: The nudging decreases the specific humidity at all altitudes over the Indo-Pacific Warm Pool (see Figure G.18). The nudging of temperature and vorticity provide the main impact while their interactive effect counteracts. Over the Atlantic Ocean the nudging, especially the nudging of the temperature, decreases the humidity up to an altitude of 650 hPa (see Figure G.19). The counter-effect by the nudging of the vorticity and several dual and the quadruple interaction predominate in higher altitudes and lead to the observed increase of humidity. The latter contributions are far larger than over the Warm Pool area. However, it is not directly obvious whether the nudging causes higher moisture content in the middle and upper troposphere over this area followed by increased frequency of instability and convection, or whether the nudging increases the frequency of deep convection that brings more moisture to higher altitudes. This issue is not examined further in this study, however. The strong decrease of unstable conditions in the eastern Pacific Ocean to the west of South America coincide with a significantly increased frequency of triggered mid-level convection events in this area (see Appendix, Figure G.14). In high latitudes both the decrease of the already-low moisture content as well as the reduced frequency of unstable conditions with respect to dry air (see Appendix, Figure G.8) contribute to the observed stabilisation. This agrees well with the observed decrease of triggered mid-level convection events in polar regions.

Upper Troposphere

The following analysis of static stability in the upper troposphere focusses on the cross section at an altitude of 300 hPa. The degree of static stability is again analysed by means of the vertical gradient of the equivalent potential temperature. The global frequency distributions of both scenarios are shown in Figure 7.8. Both distributions show significant predominance of stable conditions like in the middle troposphere. The degree of stability is not distributed normally, however, but exhibits a pronounced peak at moderately stable conditions and exhibits an elongated slope towards very stable conditions due to the impact of stratospheric air with high stability. This applies for both scenarios, although the peak as well as the pronounced slope is significantly more distinct for the nudged scenario. The nudging enhances the frequency of very stable conditions (< -0.2 $^{K}/_{hPa}$) and slightly shifts the peak towards instability. This implies a slight increase of unstable conditions and a significant decrease of stability of medium

degree (between -0.2 and -0.05 K/hPa) due to nudging. As a consequence, the mean is decreased from -0.090 K/hPa to -0.097 K/hPa on the one hand, but on the other hand the peak is shifted from -0.050 K/hPa to -0.040 K/hPa and the proportion of unstable conditions is increased from 6.1% to 7.3%.

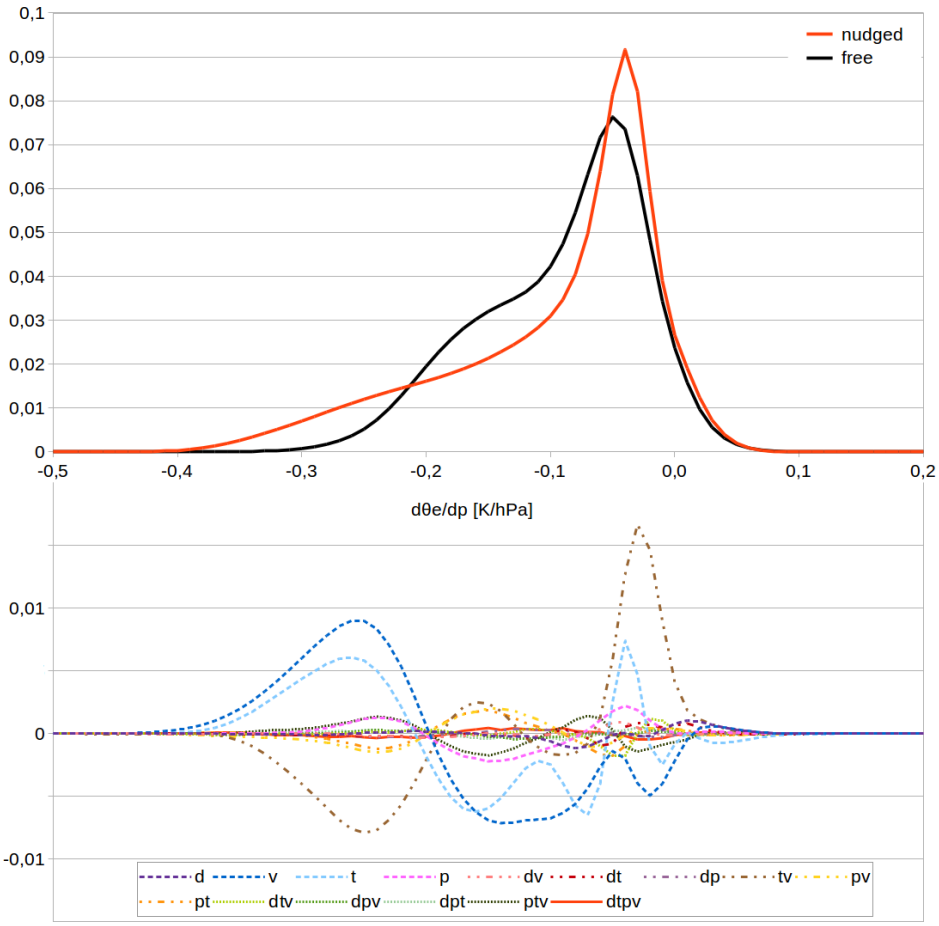

Figure 7.8.: Impact of nudging on static stability in the upper troposphere at 300 hPa: The upper curves show the frequency distribution of the vertical gradient in terms of pressure of the equivalent potential temperature from the entire Earth with respect to the simulated period of 9 years. The negative gradient indicates stable conditions whereas the positive gradient indicates conditional instabilities. The red line represents the fully-nudged scenario and the black line represents the free model scenario. The lower curves break down the isolated and interactive contributions to the nudging impact.

The nudging of vorticity and temperature as well as their interactive effect are again the main causes of these alterations. The corresponding contributions are depicted in the lower part of Figure 7.8. In the very stable range, the nudging of vorticity provides the strongest positive impact. The impact of nudging the temperature is also positive but less strong, whereas the interaction of nudging both variables counteracts and reduces the total impact. This behaviour is similar in the medium range where the negative

contributions of vorticity and temperature are counterbalanced to the most part by their interaction. In contrast, the shift of the peak and the enhancement of weakly stable and unstable conditions is mainly caused by the interactive effect of temperature and vorticity and the nudging of temperature itself.

The regional distribution of the proportion of unstable conditions in the upper troposphere, that is presented in Figure 7.9(a), reveals that unstable conditions are very rare in mid- and high latitudes in both hemispheres. The highest frequencies occur again near the equator over northern South America (∼28%), central Africa (∼25%), the Indian Ocean (∼25%), and over the Indo-Pacific Warm Pool (∼28%). Frequencies of up to 15% occur in the adjacent regions between 30°S and 30°N. Unstable conditions are nearly totally absent from polar regions.

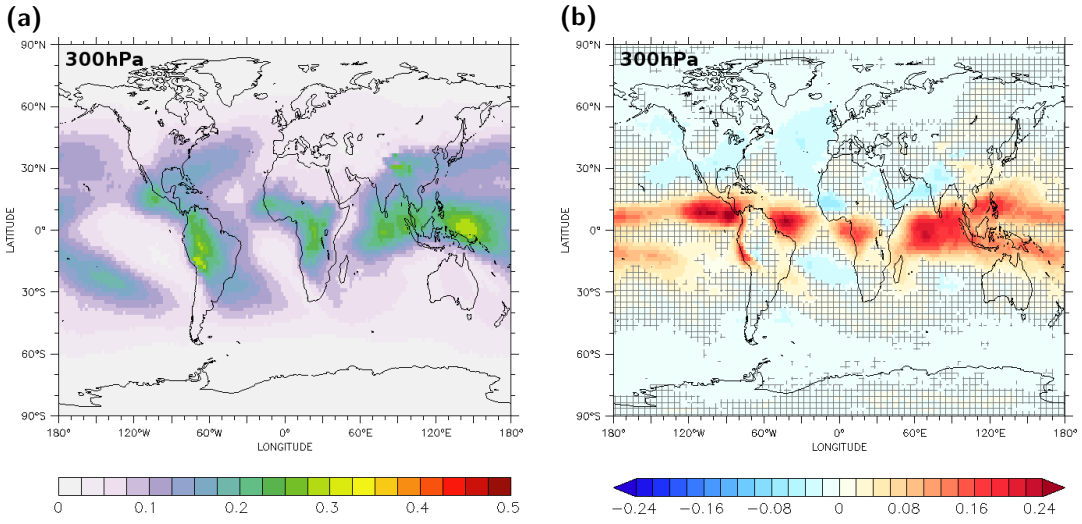

Figure 7.9.: Impact of nudging on the proportion of unstable conditions in the upper troposphere at an altitude of 300 hPa: (a) Proportion of unstable conditions with respect to the simulated period of 9 years. The cross section shows the annual average for the free scenario. (b) Impact by nudging: The simulated proportion of unstable conditions on annual average that results for the fully-nudged scenario is compared to the free model scenario. In hatched areas the difference is not highly significant based on an unpaired Student's t test and on a significance level of 95%.

Figure 7.9(b) depicts the impact of nudging on the mean proportion of unstable conditions in the upper troposphere. The nudging mainly causes a strong increase of unstable conditions over equatorial regions and merely provides a small impact in other parts. The area exposed to the increase of instabilities stretches from the eastern Pacific Ocean to the Atlantic and Indian Ocean up to Melanesia and Micronesia in the Indo-Pacific Warm Pool, but also affects South America along the Andes and Central Africa. The increase is strongest over the oceans (up to 25 pp) and slightly less distinct over the continents and island regions (14-18 pp). Slight decreases (2-6 pp) occur over the Atlantic Ocean between western Africa and north-west Europe as well as Southern

Africa and South America, and the Arabian Sea and India. There are no significant changes of static stability over most of the central Indo-Pacific Warm Pool at this altitude.

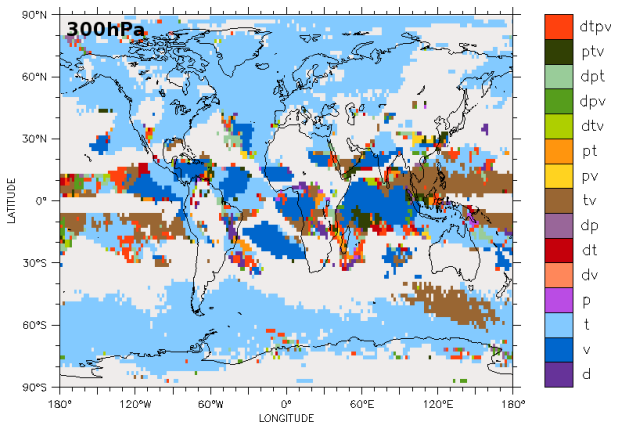

Figure 7.10.: The factor separation method allows to isolate the single and interactive contributions to the nudging impact. For each region the dominant contribution to the impact on static stability in the upper troposphere at 300 hPa is highlighted. Only areas with significant difference are included.

The dominant contributions to the nudging impact are presented in Figure 7.10. The nudging of vorticity, temperature as well as their dual and the quadruple interactive effect predominates in low latitudes between 20°S and 10°N. The nudging of the temperature has the dominant impact in nearly all of the remaining areas.

The pronounced increase of unstable conditions in this altitude due to nudging is also noticable in the patterns of triggered deep convection, moisture content, and the proportion of unstable conditions for dry air. The nudging basically causes higher or more frequent deep convection, increased moisture content, and an increase of unstable conditions with respect to dry air in several regions close to the equator. Again, it is not directly obvious whether the nudging triggers more convection that brings moisture to high altitudes, or whether the nudging increases the moisture content in the middle and upper troposphere and the resulting instabilities enhance convection. Areas of significantly increased specific humidity occur over the near-equatorial Atlantic Ocean, the Gulf of Guinea and central Africa, a belt at 10°N in the eastern Pacific Ocean and along the west coast of South America (see Appendix, Figure G.5). Most areas over the Atlantic and eastern Pacific Ocean also exibit more frequent and higher deep convection, whereas over the Gulf of Guinea and Central Africa the frequency is not altered and the convection height is merely increased slightly (see Appendix, Figure G.12). Over the near-equatorial Atlantic Ocean the nudging induces a strong enhancement of distinctly unstable conditions (see above or Figure G.17) in the lower troposphere at 850 hPa. This effect does not occur over the Gulf of Guinea as revealed by the regional frequency distributions of the gradient of the equivalent potential temperature (not shown). The nudging merely leads to very slight enhancement of instabilities in the lower troposphere

in this area and the triggering of convection is hardly affected. This is an indication that increased deep convection is generally not necessary for more unstable conditions in the upper troposphere. The nudging still can lead to higher moisture content and induce instability. Moreover, increased instability in high altitudes does not necessarily trigger deep convection when the instability is not increased in lower altitudes. The convection is consequently not triggered more frequenctly, but reaches higher altitudes. Over the Indian Ocean the nudging strongly increases the frequency and height of deep convection while the specific humidity is not affected significantly. The instability with respect to dry air is also distinctly increased over this region (see Appendix, Figure G.9). Although this increase is weaker by about one order of magnitude, the combination with slightly increased moisture content seems to be sufficient for extensive destabilisation over the Indian Ocean. There are no significant impacts on stability due to nudging over the Indo-Pacific Warm Pool in this altitude. The frequency distribution of convection height (see Appendix, Figure G.20) reveals that the proportion of convection to the upper troposphere is not affected by nudging in this region while the proportion of the middle troposphere is significantly increased. The lower absolute frequency of deep convection and the decreased moisture content is balanced by an increase of the frequency of unstable conditions for dry air, however. The areas of increased instability over the Northern and Southern Atlantic Ocean, the Arabian Sea, and India coincide with slightly decreased specific humidity.

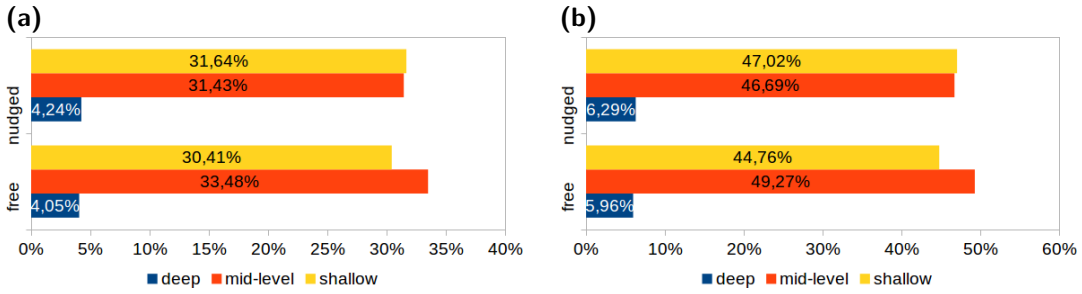

Figure 7.11.: Impact of nudging on the frequency of triggered convection events for the different types of convection: (a) The relative frequency with respect to the simulated period of 9 years is shown for both the fully-nudged and the free scenario. (b) The proportion of each type with respect to all triggered convection events is shown for both the fully-nudged and the free scenario.

The previous analysis has revealed that the impact of nudging on atmospheric stability is generally correlated to the impact on the frequency of triggered convection events. This is definitely not true for all regions since the occurence of unstable conditions does not necessarily induce convection. In lower layers of the troposphere the degree of stability appears to be decisive for the triggering of convection events while upper layers influence the height of the convection. Figure 7.11 summarises the nudging impact on the frequency of triggered convection events. While the left panel considers the relative frequency with respect to the entire simulation period, the right panel

enlightens the fraction of the different convections types. In general, the nudging slightly decreases the frequency of triggered convection events from 67.94% of the time on global average in the free scenario to 67.31% in the fully-nudged scenario. The impact is not equal for the different convection types, however. Mid-level convection is decreased by 2.05 pp, whereas shallow and deep convection are even increased by 1.23 pp or 0.19 pp, respectively. This corresponds to a decrease of about 6% for mid-level convection and an increase of about 4% for both shallow and deep convection. As a consequence, the fractions of shallow and mid-level convection are almost equal at 47.02% and 46.69%, and the fraction of deep convection is increased to 6.29%.

7.5.2. Impact of Nudging on the Intensity of Convection

The analysis has focussed so far on the impact of nudging on the frequency of instabilities and the triggering of convection. In the following the impact on the intensity of the triggered convection event will be analysed by means of two different measures: First, the impact of nudging on the convective upward mass transport is considered, and second, the analysis deals with the impact on the available energy, i.e. more precisely CAPE.

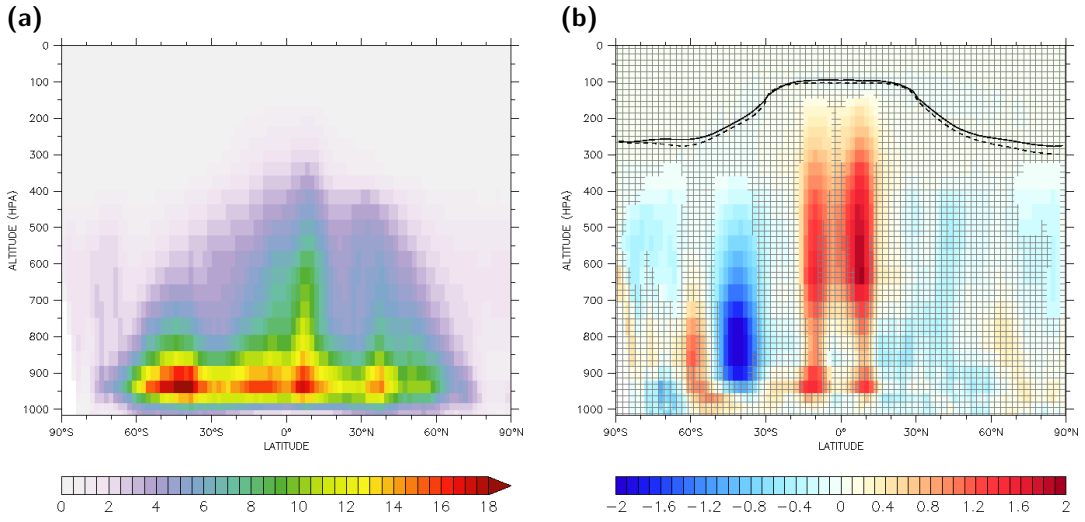

Figure 7.12.: Impact of nudging on convective mass flux: (a) Mean convective upward mass flux [g/m²] for free model. The mass flux is averaged zonally and annually over all convection events. (b) Impact by nudging: The simulated mean convective upward mass flux [g/m²] that results for the fully-nudged scenario is compared to the free model scenario.In hatched areas the difference is not highly significant based on an unpaired Student's t test and on a significance level of 95%.

Figure 7.12(a) shows the mean convective upward mass flux on annual and zonal average for the free scenario. The upward mass transport is strongest in the lower troposphere

between 950 and 850 hPa and it is distinctly stronger in the Southern Hemisphere. The mean upward mass transport reflects the mean global circulation patterns. It is relatively strong ($\sim$ 15 g/m^2 in the lower troposphere) over the equator and the adjacent latitudes where it reaches the highest altitudes. It is about 8 g/m^2 in the middle troposphere at 550 hPa and still about 2 g/m^2 in the upper troposphere at 300 hPa. In the range of the Hadley downwelling the downward motion generally predominates and thus the upward mass flux is significantly lower in the edges of the tropics. The resulting zonal mean mass flux is about 11 g/m^2 on the Northern Hemisphere and 13 g/m^2 in the Southern Hemisphere at maximum in the lower troposphere and about 4 g/m^2 at 550 hPa. The upward mass flux is stronger again in mid-latitudes in the range of the westerlies and fronts of the low pressure systems. This is pronounced weakly in the Northern Hemisphere where the mass flux reaches 14 g/m^2 in the lower troposphere but declines rapidly northward of 45°N. In contrast, the upward mass flux reaches the highest values of more than 28 g/m^2 in the range of the southern storm track and the zone of strong upward mass flux in the lower troposphere extends as far as 60°S. The mass flux in the middle troposphere is slightly weaker in the Southern Hemisphere (5 and 3 g/m^2, respectively). It is lower than 2 g/m^2 in high latitudes and higher altitudes.

The impact of nudging on the convective upward mass flux is depicted in Figure 7.12(b). Again, the zonal and annual average is considered. The nudging significantly increases the convective upward mass flux in low latitudes. There are two branches that exhibit enhanced mass flux, both at about 10° of latitude. The mass flux is not altered significantly over the equator. The increase is stronger in the Northern Hemisphere and the strongest increase can be found in the middle troposphere. The zonal mean mass flux is increased by about 2 g/m^2 at 550 hPa and about 1 g/m^2 at 300 hPa in the Northern Hemisphere, and about 1.6 g/m^2 at 550 hPa and 0.8 g/m^2 at 300 hPa in the Southern Hemisphere. This corresponds to an increase of about 30% in the middle troposphere and 40-50% in the upper troposphere. The upward mass flux is generally increased from the upper part of the boundary layer up to the tropopause. The strong increase in this zone agrees very well with the observed destabilisation in the upper troposphere and the increase of triggered convection and convection height in several regions along the equator. There are no significant changes in mid-latitudes in the Northern Hemisphere, but the upward mass flux is distinctly decreased in the lower and middle troposphere between 50°S and 30°S. The impact is most pronounced in lower altitudes where the mean zonal mass flux is decreased by more than 2 g/m^2, i.e. about 30%. Further poleward the mass flux is increased again by 1.2 g/m^2 ($\sim$25%) in the lower tropopause between 60°S and 50°S. Both effects agree also with the observed impact on the atmospheric stability. The previous analysis has revealed that the frequency of unstable conditions is reduced in the range between 40°S and 30°S, especially between Africa, Australia, and New Zealand. Furthermore, significantly less deep, shallow, and mid-level convection events have been observed. More frequent instabilities and enhanced convection have been observed further south in agreement with the increased upward mass flux between 60°S and 50°S. The middle and upper troposphere also exhibit decreased mass flux in high latitudes (0.5 g/m^2, 30-40%) that coincides with increased stabilisation in these

zones. The factor separation indicates that the nudging of the temperature provides the dominant impact for nearly all affected regions (not shown).

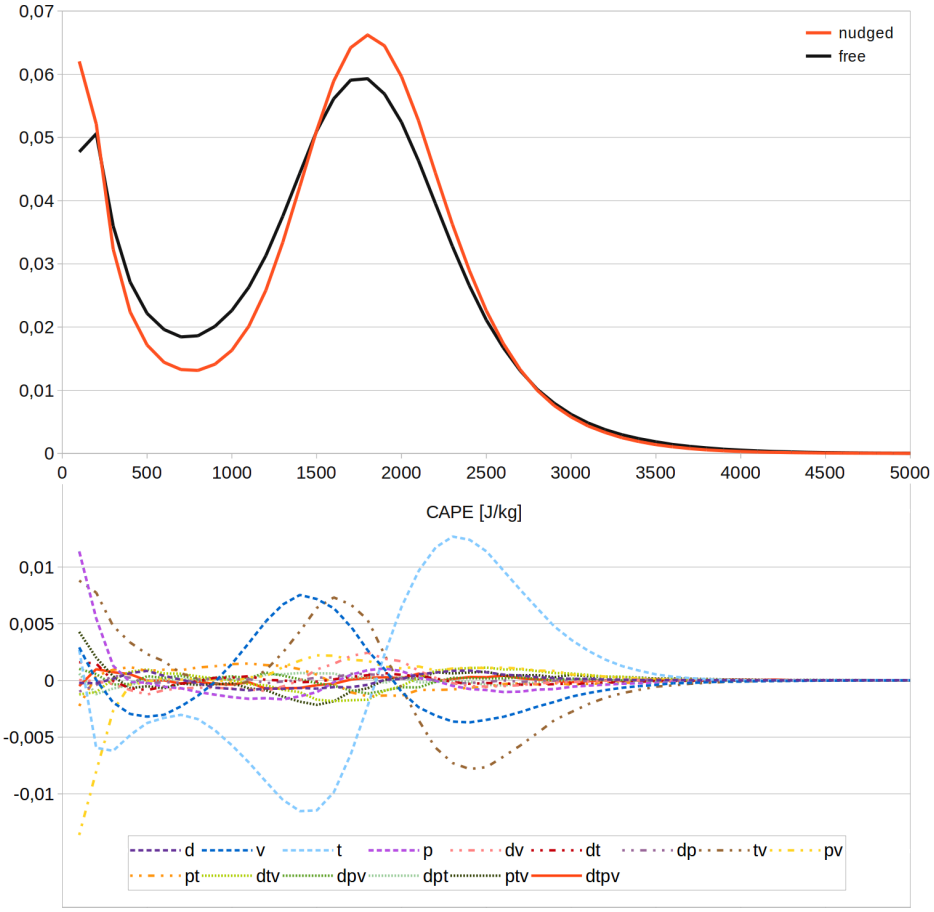

Figure 7.13.: Impact of nudging on convection processes: The upper curves show the global frequency distribution of CAPE at deep convection events with respect to the simulated period of 9 years. The red line represents the fully-nudged scenario and the black line represents the free model scenario. The lower curves break down the isolated and interactive contributions to the nudging impact.

The analysis of CAPE provides further information on the impact of nudging on convection. CAPE measures the amount of energy available for convection and is directly related to the maximum potential vertical speed within an updraught (see Section 1.3). That is why CAPE is an appropriate measure for the intensity of convection. The following analysis considers the maximum CAPE within an air column, i.e. the respective value of CAPE does not necessarily correspond to the air parcel at the surface or at the level where the convection has eventually been triggered.

Figure 7.13 depicts the global frequency distributions for CAPE in case of deep convection events for both scenarios. The general shape of the distribution is similar for both

scenarios and not affected by the nudging. Both distributions show high frequencies for low values of CAPE of less than 250 J/kg. Deep convection events with moderate CAPE in the range between 500 and 1000 J/kg are relatively rare, whereas high values of CAPE of about 2000 J/kg are most frequent. The distributions decline rapidly and events with CAPE of more than 3500 J/kg are very rare. On the one hand the nudging enhances the frequency of deep convection events at very low values of CAPE, but on the other hand CAPE is shifted towards higher energies for deep convection events. Deep convection events with moderate values of CAPE are significantly less frequent, but the frequency of events with high values is increased. The position of the minimum, 700 J/kg (free) and 800 J/kg (nudged), as well as position of the maximum, 1800 J/kg for both, are virtually not affected. The mean is increased by about 30 J/kg from 1493.77 J/kg for the free scenario to 1523.92 J/kg for the fully-nudged scenario. There is virtually no difference for very high values of CAPE.

The lower part of Figure 7.13 shows the separated contributions of the nudged quantities and their interactive effects on the global frequency distribution of CAPE. Again, the nudging of the temperature, vorticity, and their interaction basically determine the size of the impact. The nudging of the temperature essentially induces the decrease of moderate values of CAPE as well as the increase of high values. The nudging of the vorticity and the interaction provide a counter-effect that reduces the resulting impact. The nudging of the surface pressure and the interaction with the nudging of the vorticity strongly affect the increase of very low values of CAPE, but apart from that the other contributions are very small.

In addition to the nudging impact on the global frequency distribution the different regional impact on CAPE is considered in the following. Figure 7.14(a) shows the annual mean CAPE for triggered convective events of all types. Convective events with very low CAPE of less than 100 J/kg are excluded to focus on convective activities related to surface heating and instabilities and to neglect destabilisations in the middle and upper troposphere due to the advection of moisture or warmer air. The areas of high mean CAPE of more than 1500 J/kg are basically restricted to tropical oceans and continents in low latitudes. They appear in Central America and the Caribbean, South America, in Africa south of the Sahara and north of the Kalahari desert, India, the maritime continent, as well as over the Indian and the western Pacific Ocean. In North America the area extends as far as the Great Lakes at 45°N and as far as the River Plate at 35°S in South America. Very high mean CAPE can be merely found in small areas in northern South America, central Africa, the Bay of Bengal, the Indo-Pacific Warm Pool, and along the north-west coast of Australia. Especially in the Northern Hemisphere the large continents facilitate moderate mean CAPE of more than 400 J/kg over wide areas up to the Hudson Bay at 60°N in North America or the coast of the Arctic Ocean at 70°N north of Asia. Moderate mean CAPE further appears in East Asia and most of Australia. It reaches up to 40° of over most of the oceans except for the cold-water areas in the west of Southern Africa, North and South America.

Figure 7.14(b) presents the different regional alterations in annual mean CAPE due to

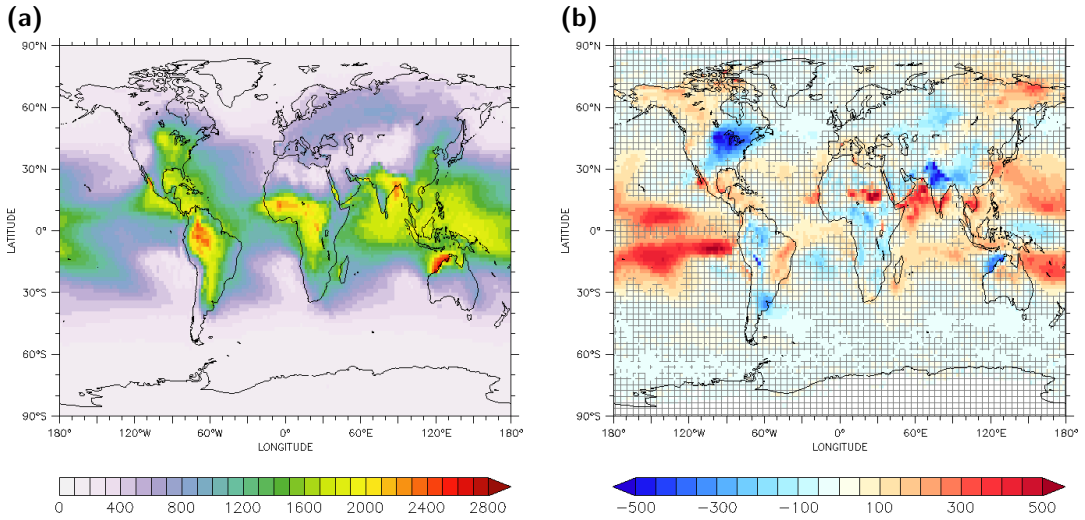

Figure 7.14.: Impact of nudging on convection processes: (a) Annual mean CAPE [J/kg] for free model. The annual mean is prefiltered with a minimum of 100 J/kg to exclude non-convective events. (b) Impact by nudging: The simulated annual annual CAPE [J/kg] that results for the fully-nudged scenario is compared to the free model scenario. The filter for convective events is applied again. In hatched areas the difference is not highly significant based on an unpaired Student's t test and on a significance level of 95%.

nudging. In low latitudes most of the significant changes are located over the oceans. There are essentially two belts at about 10° of latitude where the nudging leads to higher mean CAPE. The strength of the impact as well as the width of the influenced belt vary depending on the region, but they can be observed over all oceans and marginal seas on both hemispheres. In contrast, CAPE is not affected or even reduced directly at the equator. The most pronounced increases of more than 500 J/kg appear over the Pacific Ocean and the Arabian Sea. Moreover, there are similarly strong increases in Northern Africa whereby the area of high mean CAPE is extended further to the north. The increase of CAPE is of moderate strength over the western Pacific Ocean (∼300 J/kg), the southern Indian Ocean, and the Caribbean Sea (both 250 J/kg). The effect is merely weakly pronounced over the Atlantic Ocean (100 J/kg), and furthermore, the belt is more close to the equator there. In between these belts the most distinct decrease appears over the Indo-Pacific Warm Pool area where the annual mean CAPE is reduced by 150 J/kg. Significant decreases of similar strength can also be found over the continents in low and mid-latitudes. The nudging strongly reduces CAPE over the Himalaya and along the north-west coast of Australia by 400-500 J/kg. The extension of areas of high CAPE in North and South America is also restricted to lower latitudes and as a consequence the mean CAPE is decreased very strongly by more than 500 J/kg around the Great Lakes in North America. In high latitudes the annual mean CAPE is increased by 200-300 J/kg in north-western America and north-eastern Asia.

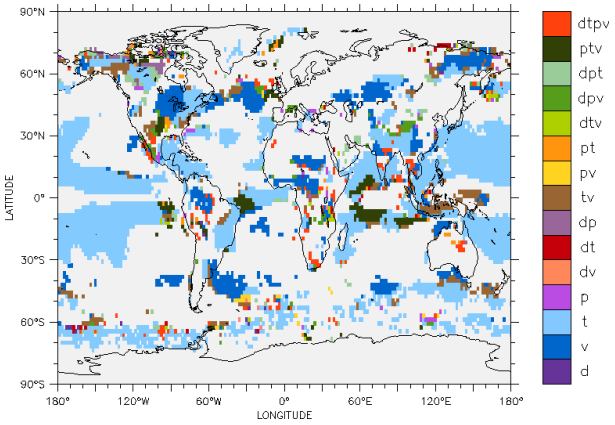

Figure 7.15.: Impact of nudging on CAPE: For each region the dominant isolated or interactive contribution to the nudging impact is highlighted. Only areas with significant difference are included.

The two marked belts of strong increase of CAPE across the tropical oceans agree well with the observed nudging impact on upward convective mass transport. As discussed above the upward mass flux is increased in the same latitude range where the two belts are located. Moreover, the analysis of atmospheric stability has revealed destabilisation over the tropical oceans in the upper troposphere accompanied by more frequent deep convection that also reaches higher altitudes. The destabilised area also exhibits two branches over the Pacific Ocean at about 10° of latitude (see Figure 7.9(b)). Over the Indian and Atlantic Ocean the southern belt of increased CAPE, that is pronounced less strongly, coincides with the areas of increased unstable conditions at 300 hPA. However, unstable conditions occur much more frequent in these regions while the annual mean CAPE is merely increased slightly. The comparison of the respective regional frequency distributions of CAPE (not shown) reveals that the nudging enhances convective activity for CAPE in the range between 1200 and 2000 $^{J}/_{kg}$, whereas convective activity is suppressed for very high CAPE. The mean is consequently increased only slightly. Over the Indo-Pacific Warm Pool the decrease of CAPE and the observed stabilisation also agree well. The range where the two belts of increased CAPE are located lies approximately in the range where the ITCZ is expected during the summer season on the respective hemisphere. Hence, the observed impact is potentially either the result of a stronger poleward shift of the ITCZ during summer due to nudging or the nudging enhances convective activity in the range of the ITCZ off the equator. The analyses of the mean monthly impact on CAPE (not shown) indicates that there is only one belt where CAPE is increased at a time. This belt lies not in the range of the ITCZ, however, but in the opposite hemisphere. Thus, the nudging rather enhances convective activity in lower latitudes in ranges off the ITCZ. The strong increase of mean CAPE over the Arabian Sea and southern India also turns out to be a seasonal effect. The nudging leads to higher CAPE during summer, i.e. during the wet season of the monsoon, while CAPE is not affected significantly there during the dry season. The analysed cross-sections of the proportion of static instabilities have not revealed any

noticable alterations for this region. However, the impact on the equivalent potential temperature also indicates an increase of unstable conditions in the lower tropsphere between 800 and 700 hPa that appears mainly during the wet season (not shown). The comparison of the respective frequency distributions of the vertical gradient (not shown) discloses that the nudging significantly increases the frequency of moderately and strongly unstable conditions with a gradient larger than 0.03 $^{K}/_{hPa}$ while weakly unstable conditions are suppressed. This increases the proportion of unstable conditions only slightly by about 5 pp to 59.00%, but the mean is increased significantly from 0.006 $^{K}/_{hPa}$ to 0.015 $^{K}/_{hPa}$. The strong decrease of CAPE near the Great Lakes coincides with significantly decreased moisture content in the boundary layer in this area (not shown). Thus, CAPE appears to be primarily affected close to the surface. The majority of convective activities is triggered in higher altitudes in this region, however, since the mean altitude for triggered convection events is around 850-900 hPa for shallow and deep convection events and around 700 hPa for mid-level convection. That is why this significant decrease of mean CAPE does not coincide with significant decreases in the frequency of instabilities or triggered convection in higher altitudes. The strong decrease merely appears during summer and autumn when CAPE is generally high in this area and strong thunderstorms and tornados are likely. Hence, the nudging reduces the simulated intensity of convective activities in the range of the tornado alley.

The nudging of the temperature provides again the dominant contributions to the impact (see Figure7.15), especially over the oceans, although the nudging of vorticity, the dual interactive between temperature and vorticity, and the triple interaction between surface pressure, vorticity and temperature also predominates in some regions. The influence is less evident on the continents.

7.5.3. Impact of Nudging on the Tropopause Height

The tropopause constitutes the uppermost boundary for most of the convective motion in the troposphere. The dry and very stable conditions as well as the positive temperature lapse rate in the lower stratosphere prevent any further ascent. By that means the height of the tropopause determines the maximal level of vertical exchange and thus has a significant impact on the atmospheric mixing. Shallow and mid-level convection processes generally do not reach such high altitudes and in many cases the energy of the updraughts of deep convection is not sufficient either, especially in higher latitudes. Only very energy-rich convection is able to overshoot into the lower stratosphere. The previous analyses have shown that the nudging affects both the frequency and the intensity of convection, including the cloud top height. That is why the height of the tropopause is presumably altered as well. In the following the impact of nudging on the mean tropopause height is examined.

Figure 7.16(a) presents the mean seasonal tropopause height for winter and summer for the free scenario. The upper panel corresponds to northern winter while the lower

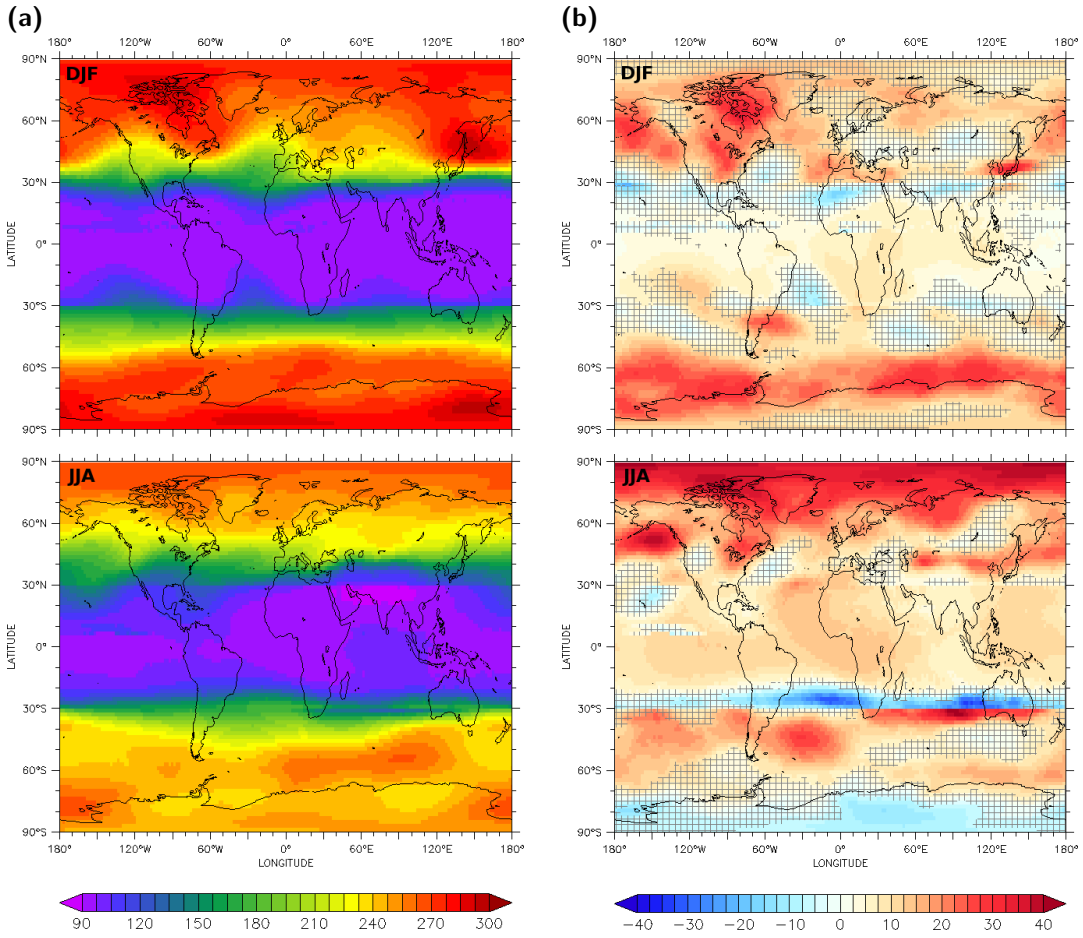

Figure 7.16.: Impact of nudging on tropopause height: (a) Seasonal mean tropopause height [hPa] for free model for winter and summer. The upper panel depicts the seasonal mean for northern winter or southern summer, the lower panel shows the mean for northern summer or southern winter. (b) Impact by nudging: The simulated mean seasonal tropopause height [hPa] that results for the fully-nudged scenario is compared to the free model scenario. Again the seasonal means for summer and winter season are shown. In hatched areas the difference is not highly significant based on an unpaired Student's t test and on a significance level of 95%.

panel considers the tropopause height for the northern summer. EMAC determines the tropopause height according to the WMO definition depending to the temperature lapse rate in low latitudes between 30°S and 30°N, and by the potential vorticity iso-surface of 3.5 PVU at latitudes poleward of 30° of latitude [96]. There is no smoothing applied at the transition and therefore inconsistencies can appear at 30° of latitude. In low latitudes the tropopause height is between 90 and 120 hPa on average and the variability between the seasons is about 15 hPa. Differences between the different continents and oceans are rather small. The 200 hPa-line is located at about 35°N in winter and 45°N

in summer and exhibits some fluctuations of up to 10° depending on the temperature of the underlying continent or ocean. In the Southern Hemisphere the line is closer to the equator, i.e. 30°S in winter and 40°S in summer. The fluctuations are less distinct due to the smaller fraction of land masses. The 240 hPa-line is about 65°N in summer while it meanders between 35°N and 55°N in winter. The warmer areas of the continents, like western North America and western Europe, go with higher tropopause heights in winter. The Southern Hemisphere exhibits the 240 hPa-line also more equatorward at 55°S and in winter the meandering appears between 40° latitude and 60°S with a leap between Australia and New Zealand. In high latitudes the tropopause is generally lower between December and February than between June and August. This is true for both hemispheres. The tropopause over the northern polar region is between 250-260 hPa in summer and 270-290 hPa in winter. In contrast, the southern polar tropopause is between 260-280 hPa in summer and 240-270 hPa in winter.

The nudging impact is shown in Figure 7.16(b) for both seasons. The nudging basically reduces the height of the tropopause for all latitudes. The impact is more distinct in high latitudes, especially in summer. There are only very few regions where the tropopause height is significantly increased. Again, discontinuities appear around 30° of latitude at the transition of the two different definitions of the tropopause. The tropopause height is lowered by 8-12 hPa in low latitudes. The impact extends to 30° of latitude on the summer hemisphere and 10°-20° of latitude on the winter hemisphere. It is generally stronger from June to August, particularly over Africa and the Atlantic Ocean. At the southern transition area the tropopause is lowered by 30 hPa according to the WMO definition in winter while it is increased by 30 hPa according to the PV definition. The free scenario exhibits a rather abrupt transition for that season that is smoothed by nudging. The effect is generally less pronounced in the Northern Hemisphere. In mid-latitudes there are only some regions where the tropopause is lowered significantly. The affected areas are the same for both seasons. Strong impact appears over North America (25-30 hPa), the Gulf of Alaska and parts of the Bering Sea (25-30 hPa in winter, 35-40 hPa in summer), the Japanese Sea and East Asia (20-25 hPa in summer, 30-35 hPa in winter), and the Southern Atlantic Ocean and southern South America (25-30 hPa). The nudging affects the tropopause over high latitudes mainly in summer. The impact is generally stronger in northern polar regions (up to 40 hPa) where it also extends up to the North Pole. In contrast, the tropopause is merely lowered by 30 hPa in southern polar regions. The impact appears to be restricted to the Southern Ocean and coastal regions while the area around the South Pole is not affected. In winter the tropopause is only lowered significantly over North America, the Labrador and the Bering Sea ($\sim$ 30 hPa). Antarctica even exhibits an increase of 10 hPa in winter.

The stratosphere is resolved very coarsely by means of the T63L31 atmospheric grid and several stratospheric processes are only approximated. The upper branch of the Brewer-Dobson circulation is not resolved at all, for example, and as a consequence transport along the lower branch is considerably exaggerated. Thus, the observed alterations of the tropopause height can be interpreted as corrections to the simulation

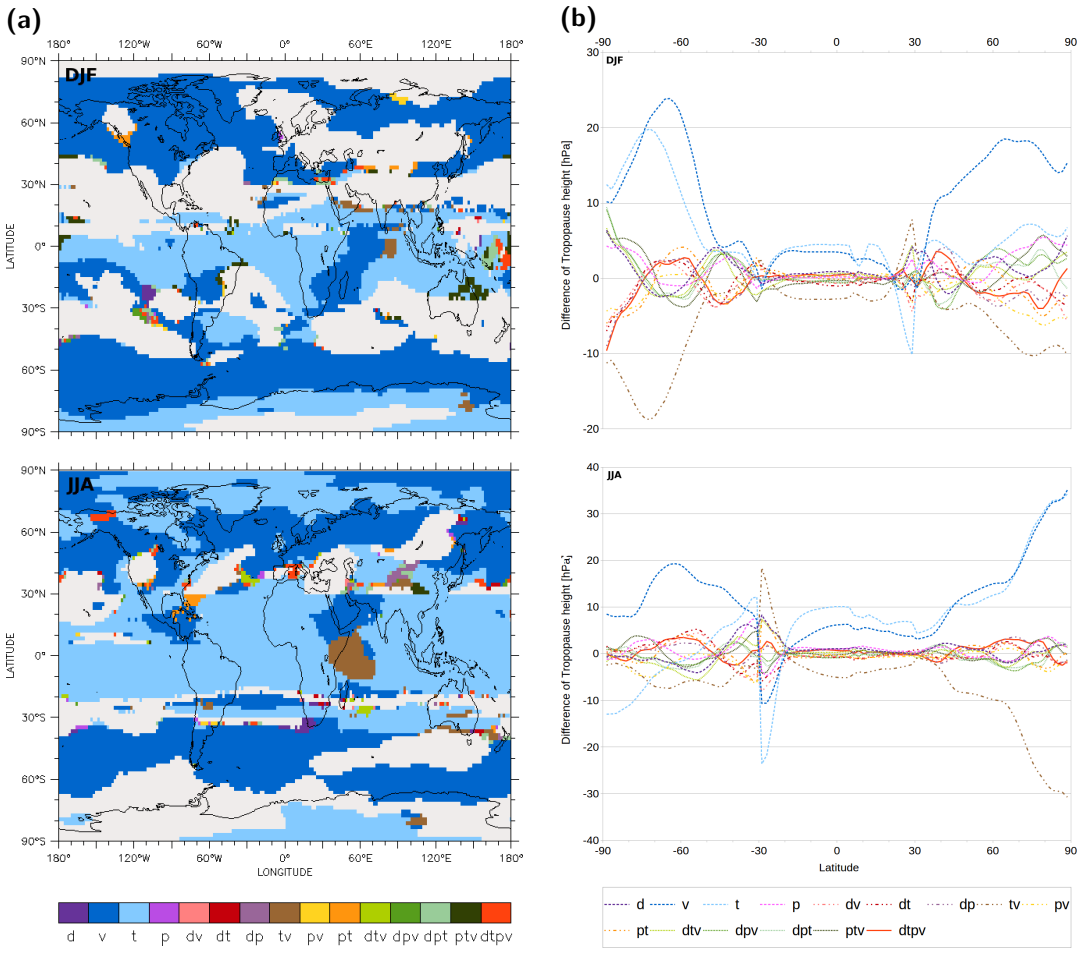

Figure 7.17.: Impact of nudging on tropopause height: (a) For each region the dominant isolated or interactive contribution to the nudging impact is highlighted. Only areas with significant difference are included. Again the upper panel represents the northern winter and the lower panel the northern summer seasonal mean. (b) The curves show the isolated and interactive contributions to the shift of mean seasonal tropopause height on zonal average for both winter and summer due to the nudging of the prognostic variables.

of the free scenario with respect to subgrid-scale processes. The nudging impact is damped, however, since nudging is faded out in higher levels and even not employed at all in the three uppermost levels.

The dominant contributions to the nudging impact are depicted in Figure 7.17(a). The nudging of the temperature provides the dominant impact in most areas in low latitudes. This is basically true for both seasons. The nudging of the vorticity and the interaction of temperature and vorticity merely predominate in some smaller areas depending on the season. In mid- and high latitudes the nudging of the vorticity provides the strongest

impact on the tropopause height in most areas on both hemispheres during winter. The temperature is merely predominant in Antarctica where the most significant increase of the tropopause height has been observed. The nudging of vorticity also provides the strongest impact in most areas of mid- and high latitudes during summer, however, the temperature predominates close to the pole at that time. Figure 7.17(b) breaks down the separated zonal mean impacts. The previous observations are generally confirmed: The nudging of temperature, vorticity, and their interaction mainly affect the alteration of the tropopause height. They induce raising as well as lowering of the tropopause by 5-10 hPa in low latitudes and 10-20 hPa or 20-30 hPa in southern or northern high latitudes, respectively. The other contributions are relatively small. In higher mid- and high latitudes the lowering during winter is mainly caused by the vorticity alone. Temperature and the interaction counteract and reduce the strength of the impact. In contrast, both temperature and vorticity strongly lower the tropopause during summer and outweigh the counter-effect by their interaction. The behaviour is generally similar in low latitudes, but the strength of the impact is smaller there. Temperature and vorticity mainly lower the tropopause while their interaction induces an increase. The smoothing at the transition at 30° of latitude appears in both winter hemispheres and is mainly triggered by nudging the temperature.

7.5.4. Conclusions

The previous analysis has shown that the forcing of the nudging constitutes a significant impact on atmospheric stability and vertical motion. The impact is strongest in low latitudes within the troposphere while the tropopause height is affected the most in high latitudes. The consequences vary depending on the region. Significant stabilisation occurs over the Indo-Pacific Warm Pool area. The convection top height is not altered, but the intensity as well as the frequency of both deep and shallow convection is considerably reduced. In contrast, the area over the near-equatorial Atlantic Ocean between South America and Africa and over the Gulf of Guinea exhibits a distinct destabilisation. There the nudging induces more frequent deep convection that also reaches higher altitudes. In general, the stability of the atmosphere is significantly increased in the middle troposphere, whereas the upper troposphere is destabilised in low latitudes. The intensity of convective activity is increased over two belts at about 10° of latitude. This leads to enhanced upward mass flux in the respective areas. Strong seasonal effects occur near the Great Lakes in North America and during the wet monsoon season over India and the Arabian Sea. Significant destabilisation and enhanced convection also appears at the southern range of the southern storm track. The tropopause is raised in most regions. The strongest impact can be found over high latitudes during summer. The factor separation has revealed that the nudging of the temperature, vorticity, as well as their interaction provide the main impact. In most cases the interaction counteracts and reduces the strength of the impact. This analysis has focussed on the time span from 1996 to 2004. Similar behaviour is very likely also

for other periods but has not been examined. Moreover, the dependence on different relaxation times has not been part of this study either.

8

Conclusions and Outlook

The established atmosphere-ocean general circulation model EMAC-MPIOM has been applied to simulate a palaeoclimate for the Kazanian stage (270-260 mya) of the Middle Permian. The Earth's surface as well as the composition of the atmosphere and the astronomical configuration of that period differ considerably from the present-day environment. That is why the modelling of the Permian atmosphere and the simulation of the mean Permian climate have required the generation of a full land surface data set and estimates of the fraction of various greenhouse gases and solar irradiation to take altered boundary conditions into account. This comprises the general shape and structure of the ground that affect the atmospheric flow, the reflection of the incoming radiation, the storage and conduction of heat, and the storage and availability of water. The reconstructions of the Permian environment are generally supported by means of different proxies within the geologic record and additional modelling of sources and sinks of different atmospheric gases. However, they bear non-negligible uncertainties.

The generated land surface data set describes the mean orography on selected model grids as well as subgrid-scale orography variations within the corresponding grid cell that characterise the shape and distribution of mountain ranges and the roughness of the surface. Moreover, structure and colour of the soil, the occurence of glaciers and lakes, and the vegetation coverage are specified. The orography of the Permian Earth has basically been derived from reconstructions based on palaeomagnetic data, while the vegetation distribution has been estimated by means of statistical and taxonomic analyses of the fossil record in terms of morphologies of leaves, stems, and roots with respect to phytogeographic distributions. The Permian topography is generally dominated by the supercontinent of Pangaea and the surrounding Panthalassic Ocean. Pangaea nearly stretches from pole to pole and encloses the smaller Tethys Ocean on three sides. The resulting model of the orography predicts widespread plains for most of Pangaea traversed by the Ural Mountains in Western Angara, the South Gondwanan Mountains, the Appalachian Mountains near the equator, and further minor mountain

ranges. The vegetation coverage is high on the Tethysian microcontinents throughout the year and moderately high with seasonal variations in Central Pangaea near the equator, along the Tethys coast, and in Angara and Southern Gondwana. The soil properties have been assumed generically as medium values since comprehensive soil data is rare.

The appropriate modelling of the SSTs requires considering the interaction and balancing of the ocean with the overlying atmosphere instead of using reanalysed monthly climatologies like it is common for simulations of the present-day environment. That way, feedback by the ocean can be taken into account directly and the coupled atmosphere-ocean system freely moves to its thermodynamic and dynamic equilibrium state. The coupled hydrological discharge model further ensures the clousure of the hydrological cycle and handles the run-off of water into the ocean. In contrast to the dynamic equilibrium of the atmosphere-ocean system, the concentrations of greenhouse gases have been fixed and their exposition and deposition is not considered. In agreement with geochemical models and proxies, the concentration of carbon dioxide has been prescribed to four times of the present-day value, the concentration of methane has been set to about half of its present-day value and nitrous oxyde (N_2O) has been assumed to be slightly less concentrated than at the present day. Further greenhouse gases, like e.g. chlorofluorocarbon, and aerosols have not been considered. Moreover, the oxygen concentration has been assumed to be on the present-day level and the content of ozone has been approximated by an idealised meridionally symmetric distribution. The eccentricity of the Earth's orbit as well as its obliquity and its rotation velocity have been kept at their present-day values, while the solar luminosity has been reduced by 2.6%.

The diagnostic simulations for the Permian palaeoclimate have been preceeded by spin-up simulations to make the coupled atmosphere-ocean system find an equilibrium state under the altered boundary conditions. The response stage of the atmosphere has been relatively short in the magnitude of weeks to a few months. The upper ocean layers have shown a response stage of a few years, whereas the deep ocean exhibited a response stage lasting several thousand years of simulation due to the slow ocean overturning circulation. The spin-up has been performed on a coarser atmospheric grid in order to save computation time. The coupled model has revealed to react sensitively to the tuning of free parameters describing processes related to clouds on a subgrid scale. The insufficient optimisation of these parameters with respect to radiative balancing has caused large discrepancies of mean global temperature for the transition from the coarse T21L19 grid to the finer T63L31 grid. However, these parameters have turned out to be optimised for the T31L19 grid. Only slight impacts on the mean global temperature have been observed at the transition to the T63L31 grid. The deep ocean response has still been active after 2500 years of simulation on the T21L19 grid and another 1000 years on a T31L19, but without affecting the SST and the surface air temperature significantly. The observed net radiation imbalance of 1.17 ± 0.06 W/m^2 at TOA is smaller than the imbalance detected by Jöckel et al. [159] for EMAC-MPIOM for a

present-day setup. Moreover, the found equilibrium state has proven to be unique and independent of the initialisation of atmosphere and ocean.

The simulated mean climate for the Middle Permian is characterised by warm temperatures, especially in high latitudes as well as extreme saisonality and dry conditions in the continental interior. The global annual mean surface air temperature is 18.4°C. Gondwana exhibits the most extreme temperatures due to its large extent. The annual mean temperature ranges between about −10°C in the South Gondwanan Mountains to about +34°C near the Tropic of Cancer in the continental interior. The temperature distribution is similar for Laurasia, but less extreme. The annual mean temperature varies between 32°C in the interior of Euramerica to −2°C at the northern island arc. Seasonal temperature differences are small near the equator (2 K) and the Tethysian microcontinents (12 K), but they reach 20 K in Laurasia and even 40 K in Southern Gondwana. The Tethysian microcontinents and coastal areas are subjected to a monsoonal climate including dry and humid seasons. The strong summer monsoon low and winter monsoon high pressure system over Northern Gondwana and Euramerica impact on the northern and southern trade winds and generate a cross-equatorial current that provides moisture to the coastal regions during the wet summer season. The monsoon is more pronounced on the Southern Hemisphere. Most of Euramerica and Northern Gondwana are dry throughout the year, whereas there is moderate precipitation all year round in Angara and in mid-latitude Gondwana from the Paraná-Karoo-Inland Sea to the southern Tethys coast. Southern Gondwana is arid during winter and moderately humid during summer. The ITCZ is significantly pronounced in the range of its northern and southern displacements, though there is virtually no precipitation over the Panthalassic Ocean directly at the equator. The seasonal breakdown has elucidated that this behaviour reflects a northward and southward shift during the corresponding seasons rather than a splitting into two separate branches of a double ITCZ. The interannual variability of the precipitation is generally smaller than 25% of the annual mean in most regions. There is no permanent sea ice coverage on both hemispheres of the Permian Earth. In the North the sea ice has melted completely by July and starts to re-form by November and in the south it starts growing by July and is melted again by November. The southern icesheets reach a thickness of only a few centimetres, whereas the northern icesheets grow to a thickness of about 60 cm.

Sensitivity studies with respect to a number of different parameters and assumptions have indicated the uncertainty range of the simulated mean climate and have allowed to evaluate these assumptions by the comparison with data of the geologic record. These studies have revealed a variation of annual mean temperature by 5-7 K (smaller over the ocean, even larger near the poles) and by about 250 mm for the precipitation amount. Altering radiative forcing impacts evenly on the mean annual temperature and only the sea ice in polar latitudes amplifies the deviations for colder scenarios due to the albedo-temperature feedback. The precipitation amount basically increases with higher radiative forcing near the equator and in mid- and high latitudes and the poleward extent of the subtropical arid areas grows.

The large uncertainty regarding the atmospheric carbon dioxide concentration of the Middle Permian contributes considerably to these relatively large uncertainty ranges. Within a spectrum from 355 to 3550 ppm ($1\times CO_2$ to $10\times CO_2$) the global annual mean temperature varies by about 13 K, which corresponds to local temperature variations up to 15-20 K in most parts of Pangaea. For rising atmospheric carbon dioxide concentrations the total annual precipitation amount increases, by about 30% on global average for a tenfold increase. The low-latitude trade winds are strengthened and the mid-latitude westerlies are weakened. Permanent polar sea ice coverage on both hemispheres only exists for the coldest scenario, whereas the warmer scenarios exhibit merely seasonal or even no sea icesheets.

The fluctuation of solar irradiation in the course of the Milankovitch cycles primarily affects the temperature in polar latitudes. The effect on the mean annual temperature is in the range of ± 1 K in most cases, but the effect on the mean monthly temperature can also reach up to ± 4 K, especially when the sea ice formation is affected. The impact of differently strong solar irradiation is more crucial during summer than during winter. The precipitation formation is not altered significantly. Higher solar luminosity causes considerably higher temperatures and increases the annual precipitation amount in most regions. Increasing to the present-day solar radiation intensity resembles the effect of doubling the atmospheric carbondioxide to $8\times CO_2$, for both temperature and precipitation.

The self-established vegetation increases the vegetation density in near-equatorial Pangaea and in mid-latitude forests, while the leaf area is reduced in temperate and boreal forests. Subtropical deserts are extended further to the North and South, and the eastern polar regions are virtually unvegetated. Reduced evaporative cooling increases the mean temperature in most parts of Gondwana and Angara, whereas cooling is observed near the equator. The difference can reach up to 2 K on annual average. The altered vegetation distribution also affects the available moisture and causes differences of the mean annual precipitation of up to 350 mm.

In addition to alterations of the Permian environment, the simulated mean climate has also revealed to be sensitive to model-intrinsic assumptions. The choice of the convection parameterisation affects the amount and the distribution of precipitation. The heavy precipitation along the ITCZ over the near-equatorial ocean seems to be an artefact of the Tiedtke scheme. The Zhang, McFarlane, and Hack scheme generates a more balanced distribution of precipitation across the Permian oceans, although the total precipitation amount is strongly decreased in most areas. The mean annual global temperature is virtually not affected, but local changes of up to 8 K occur in some areas.

The comparison with the geographic distribution pattern of biomes derived from lithological and floral data has revealed that the climate of the $4\times CO_2$ scenario simulated by EMAC-MPIOM reproduces well the indicated climate conditions in Euramerica and Gondwana, but tends towards cooler temperatures in Angara. Furthermore, the

simulated climate seems too dry in northern mid-latitudes and on the Tethysian microcontinents. The temperature distribution of Angara agrees well with results from other models ([74], [8]). However, the employed setup of EMAC-MPIOM has generated cooler conditions over the Northern Panthalassic Ocean, while warmer conditions are found in Gondwana and to some extent in Euramerica. The precipitation amount is increased in mid- and high latitudes compared to results from other models. The ocean circulation simulated by EMAC-MPIOM restricts poleward oceanic heat transport basically to lower latitudes, especially in the Northern Hemisphere where the Cathaysian landmass blocks warm inflow from the Tethys ocean. This causes enhanced warming of low-latitude regions, in particular in the tropical desert regions, and explains the lower temperatures in Angara. The effect is compensated in the Southern Hemisphere where the warm Tethysian current continues into the Panthalassic Ocean. Hence, the Tethys Ocean has turned out to be an important warm water source. The summer monsoon low is shifted further polward in Gondwana than expected for a symmetric continent. In contrast, the winter monsoon highs and the summer monsoon low over Euramerica are located closer to the equator.

The evaluation of the simulated Permian palaeoclimate has disclosed that the weakness of the northward oceanic heat transport is the major issue of the simulation to match the data-indicated distribution of biomes in the Northern Hemisphere. Increasing the number of vertical levels leads to a better resolution of vertical mixing of the ocean and is presumed to enhance the oceanic overturning circulation. This would also affect the global ocean circulation pattern and potentially improve the heat transport to the North. The presence of ocean ridges is proven to increase poleward heat transport [23, 167] as well. Hence, the modelling of a more realistic bathymetry - though speculative - and a better representation of vertical mixing of the ocean represent promising approaches to overcome this issue.

The rotation of the Earth was provably faster during the Middle Permian and one day had about 23 hours [63]. This reduces the daily duration of solar irradiation on the one hand, but on the other hand it increases the Coriolis parameter by about 4%. The Coriolis force has great influence on the atmospheric flow. That is why significant effects on the circulation pattern, the distribution of climate zones and biomes, and especially the Tethysian monsoon are expected. However, the implementation requires expensive changes to EMAC-MPIOM.

The altered climatic conditions of the Permian have affected the atmospheric mixing and several effects on atmospheric stability and vertical transport have been found. Higher temperatures throughout the troposphere and increased moisture content destabilise the atmosphere and lead to enhaced convective activity. The effect is generally stronger in the Southern Hemisphere due to the weaker poleward oceanic heat transport in the Northern Hemisphere. High latitudes exhibit significantly increased frequency of all types of convection events and increased upward mass flux. In southern mid-latitudes the lower and middle troposphere are more unstable and deep convection is triggered

more frequently which leads to stronger upward mass transport in the middle and upper troposphere. Deep convection is triggered less frequently in northern low latitudes in favour of shallow convection. The intensity of convective processes is enhanced in the entire Southern Hemisphere and in northern low latitudes in agreement with the observed weakness of northward heat transport. Events involving high energies occur more frequently, but the stabilisation in the upper troposphere between 300 and 400 hPa suppresses deep convection events in the medium-energy range and consequently upward mass transport is decreased in low latitudes. There are no exceptionally unstable areas like the Indo-Pacific Warm Pool in the present-day reference scenario. Furthermore, the Permian topography prevents the formation of a strong storm track in the range of the westerlies that favours instabilities and enhances convective activity in the PBL and lower troposphere. The tropopause is lifted mainly by 10-20 hPa in low and even by up to 50 hPa in high latitudes.

Some aspects of atmospheric mixing have not been considered in this work. A higher vertical resolution in the range of the upper troposphere and lower stratosphere could provide more information about changes with respect to the injection of water into the stratosphere and the exchange between stratosphere and troposphere. Morever, tracer studies can be performed to compare the atmospheric mixing rates of the Permian and present-day. The balanced model further offers to study entirely different processes in the Permian atmosphere and under the conditions of the Permian environment.

The forcing of nudging, as it is commonly employed to simulate the present-day atmosphere, provides a significant impact on atmospheric stability and vertical motion as well. The impact on the present-day atmosphere is strongest in low latitudes within the troposphere while the tropopause height is affected the most in high latitudes. The consequences vary depending on the region. Significant stabilisation occurs over the Indo-Pacific Warm Pool area where the intensity as well as the frequency of both deep and shallow convection is considerably reduced. The areas over the near-equatorial Atlantic Ocean between South America and Africa and over the Gulf of Guinea exhibit a distinct destabilisation and more frequent deep convection that also reaches higher altitudes. In general, the stability of the atmosphere is significantly increased in the middle troposphere, whereas the upper troposphere is destabilised in low latitudes. Strong seasonal effects occur near the Great Lakes in North America and during the wet monsoon season over India and the Arabian Sea. Significant destabilisation and enhanced convection also appears at the southern range of the southern storm track. The tropopause is raised in most regions. The strongest impact can be found over high latitudes during summer. The factor separation has revealed that the nudging of the temperature, vorticity, as well as their interaction provide the main impact. In most cases the interaction counteracts and reduces the strength of the impact.

The implementation of the nudging has not been varied in this work. Further studies can examine whether refining the implementation leads to different impact patterns. This refinement includes a more diverse variation of the nudging weights, instead of

prescribing fixed relaxation coefficients, and the introduction of additional rebalancing steps (see Section 7.1). So far the default relaxation times have been used for the nudging of the prognostic variables. However, the variation of the relaxation times and also prescribing equal relaxation times for all variables provides more information about the response behaviour of the atmosphere to the nudging of each of the prognostic variables. Tost, Jöckel, and Lelieveld [117] have shown that the choice of convection scheme influences the simulated precipitation pattern due to different triggering and depth of convection. The sensitivity studies of the Permian palaeoclimate have further confirmed this observation for a coupled ocean-atmosphere GCM. All simulations in this work to analyse the nudging impact have employed the Tiedtke convection scheme that shows good agreement with observations [117]. Comparisons with simulations utilising other convection schemes can elucidate how well the continuous nudging impact is balanced by these schemes and whether the strongest effects can be found in similar regions.

A

Geologic time scale

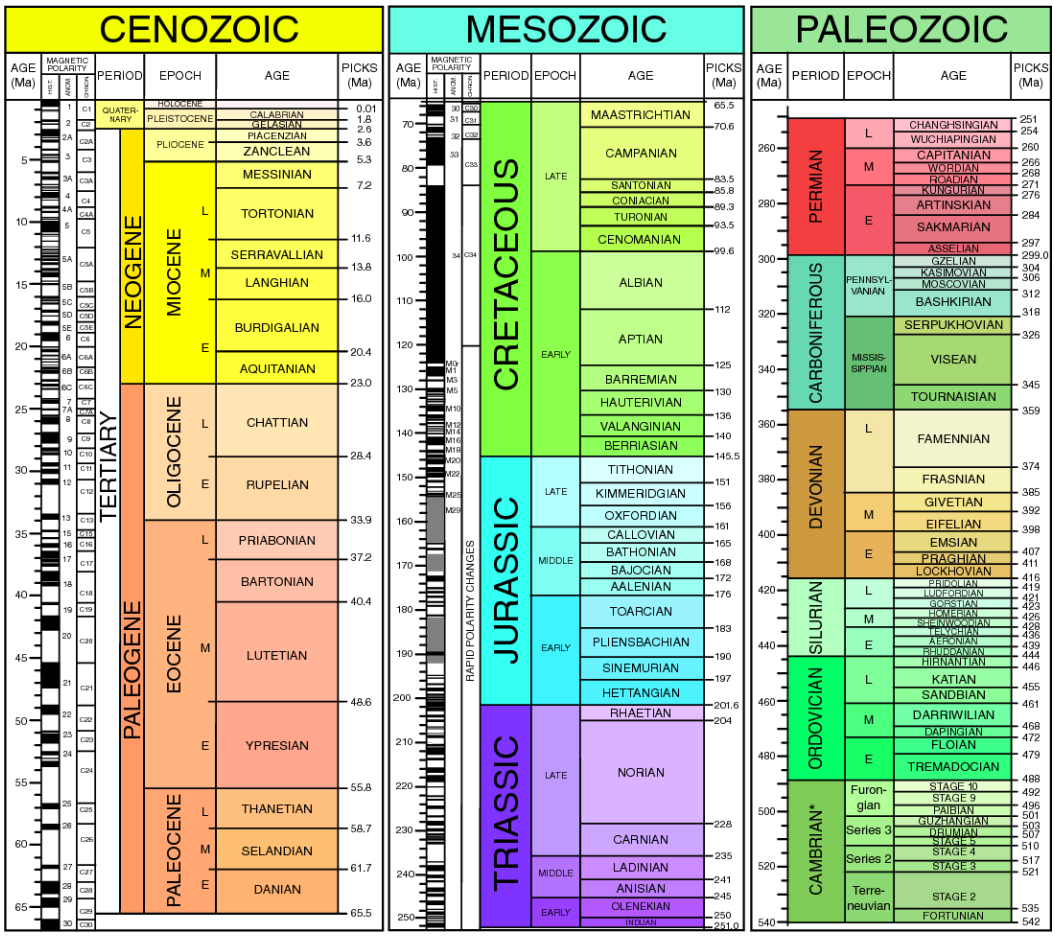

Figure A.1.: Geologic time scale. From Geological Society of America, 2009 [13].

B

Biomes Classification System

The biome classification system has been developed by Walter [80] to categorise the climate of the present-day Earth. The original classification depends on rather qualitative criteria. Kutzbach and Ziegler [36] and Rees et al. [73] applied this scheme for the Permian Earth and developed quantitative criteria on the basis of monthly averaged temperature and precipitation for the evaluation of their simulation results. The classification is summarised in Table B.1. The criteria of '40 mm' and '> 10 °C' "were arrived by trial-and-error approximations" [36].

Number of months having 40 mm or more of precipitation													Number of months
0	1	2	3	4	5	6	7	8	9	10	11	12	temp. >10 °C
3	3	3	3	2a	2	2	2	2	2	2	1	1	12
3	3	3	3	2a	4	4	4	4	4	4	5	5	11
7a	7a	7a	7	7	7	4	4	4	5	5	5	5	10
7a	7a	7a	7	7	5	5	5	5	5	5	5	5	9
7a	7a	7a	7	7	5	5	5	5	5	5	5	5	8
7a	7a	7a	7	7	5	5	5	5	5	5	5	5	7
7a	7a	7a	7	7	6	6	6	6	6	6	6	6	6
7a	7a	7	7	7	6	6	6	6	6	6	6	6	5
7	7	7	7	7	8	8	8	8	8	8	8	8	4
7	7	8	8	8	8	8	8	8	8	8	8	8	3
8	8	8	8	8	8	8	8	8	8	8	8	8	2
9	9	9	9	9	9	9	9	9	9	9	9	9	1
9	9	9	9	9	9	9	9	9	9	9	9	9	0

Table B.1.: Criteria to determine the Walter biomes [80] for the simulation results. From Kutzbach and Ziegler [36] and Rees et al. [73].

Additionally, two further criteria are necessary to distinguish between biomes 1 and 5 as

well as 2 and 4 because both tropical and temperate climate biomes may have all mean monthly temperatures above 10 °C but the temperate winter is significantly colder, whereas tropical climate biomes stay evenly warm. The quantity 'growing season degree months' (GDSM) is defined as:

$$\begin{aligned} \text{GDSM} &= \sum_{\text{months}=1}^{12} (\text{Mean Monthly Temperature } [^\circ\text{C}] - 10\ ^\circ\text{C}) \\ \text{GDSM}_0 &= 115 \end{aligned}$$

For GDSM $<$ GDSM$_0$ biome 5 is chosen instead of biome 1, and biome 4 instead of biome 2 [36, 73].

Furthermore, the Koeppen criterion for Mediterranean climate is applied. For biome 4 the rainfall of the wettest winter month is at least three times that for the driest summer month [36, 73]. Otherwise the warm temperate biome 5 is chosen.

Hereafter, the properties of the biomes are briefly summarised following the characterisation of Ziegler [76].

Biome 1: Equatorial and tropical everwet biome. Tropical rainforests with large trees and lianas dominate the landscape. The climate is characterised by constant hot temperatures ($T_{\text{mean}} = 26 - 29$ °C) and constant heavy rainfall ($10 - 20$ mm/month).

Biome 2: Tropical and subtropical summerwet biome. The alternation of wet and dry seasons is typical for this biome. The vegetation varies from deciduous forests to savannahs. Sufficient soil moisture ensures the survival of the forests in the dry period. The biome occurs along the margin of the ITCZ and in monsoonal areas.

Biome 3: Coastal and inland tropical desert biome. In every month there is a deficit of water and vegetation is not very productive or diverse. Plants are hardly preserved due to a lack of soil. Evaporite deposits and aeolian sands occur in the geological record. The biome is distributed in the areas of the Hadley cell descends and where cold oceanic upwelling occurs.

Biome 4: Winterwet biome. At the present day this biome is developed in the subtropics between 30° to 40° N and S on the west margin of the continents. It is characterised by hot and dry summers and cool and wet winters. The vegetation predominantly consists of low trees with leathery leaves whose preservation potential is low.

Biome 5: Western and eastern warm temperate biome. Temperate evergreen forests with a mixture of angiosperm and gymnosperm forests are typical of this biome. The precipitation is equally distributed throughout the year and the daily temperature minimum of the coldest month is above freezing.

Biome 6: Western and eastern cool temperate biome. This biome is also characterised by extended angiosperm and gymnosperm forests and an equally distributed

precipitation. However, the winter is cold and hard frosts are possible. Angiosperm forests shed their leaves during the cold season.

Biome 7: Mid-latitude desert biome. Being too remote from moisture sources or isolated by precipitation shadows, this biome is characterised by an annual soil-water deficiency. The landscape is dominated by grass prairies or deserts. Plants are hardly preserved, but evaporites are common.

Biome 8: Cold temperate biome. Extended evergreen coniferous forests with mosses and lichens covering the ground are typical of this biome. The growing season is short ($1 - 4$ months) and the amount of precipitation is rather low.

Biome 9: Artic biome. This biome is characterised by an extremely short growing season and the absence of trees. The landscape is dominated by tundra vegetation, i.e. grasses, mosses and lichens.

Biome 10: Glacial biome. Extended glaciers and ice fields are typical for this biome. This biome is virtually abiotic but it is represented in the geological record via tillites and dropstones.

C

Land surface parameter dataset for Permian Earth

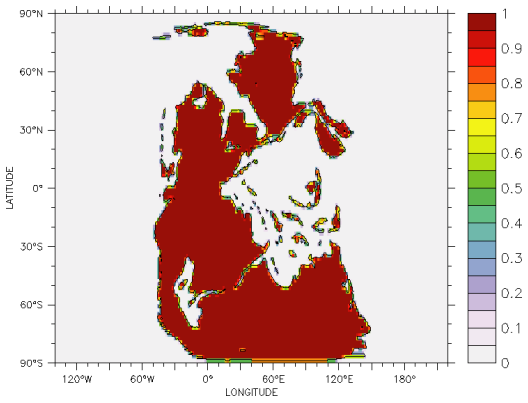

Figure C.1.: Sea-land mask [0 = sea, 1 = land] (`slm`) for T63 grid.

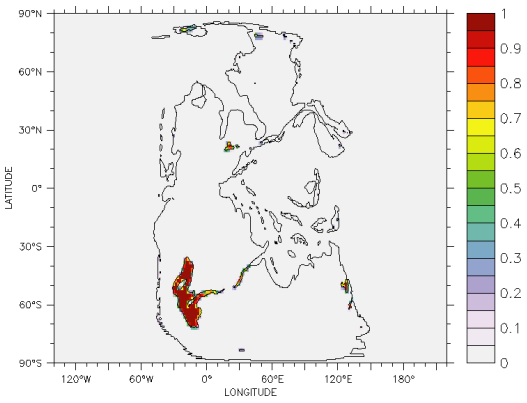

Figure C.2.: Lake mask [fractional] (`alake`) for T63 grid.

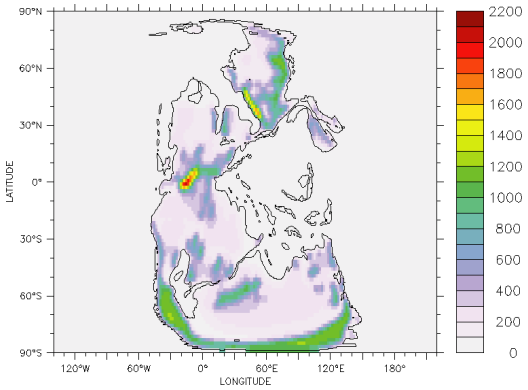

Figure C.3.: Mean orography [m] (`oromea`) for T63 grid.

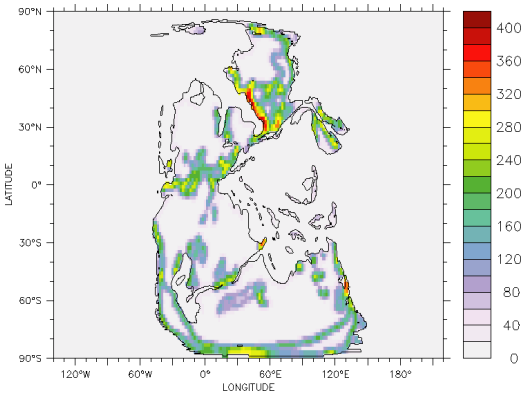

Figure C.4.: Standard deviation of orography [m] (`orostd`) for T63 grid.

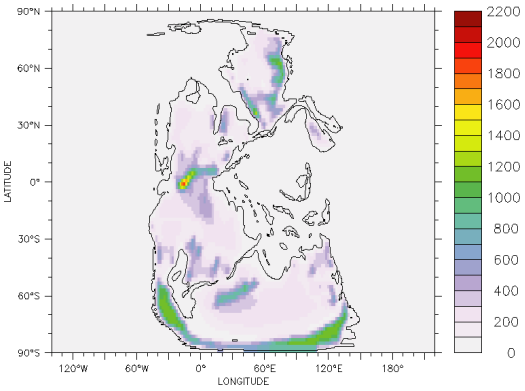

Figure C.5.: Orographic valleys elevation [m] (`oroval`) for T63 grid.

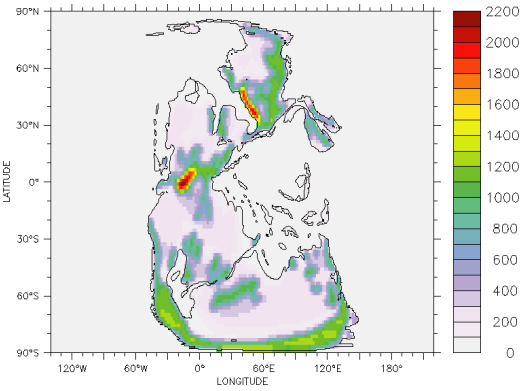

Figure C.6.: Orographic peaks elevation [m] (`oropic`) for T63 grid.

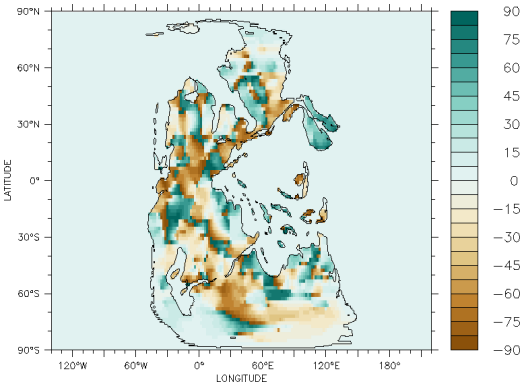

Figure C.7.: Orographic orientation θ [°] (`orothe`) for T63 grid.

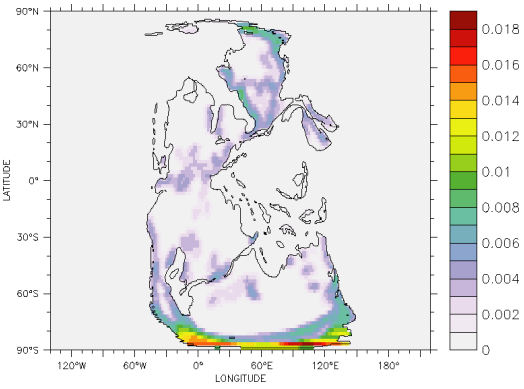

Figure C.8.: Orographic slope σ [°] (`orosig`) for T63 grid.

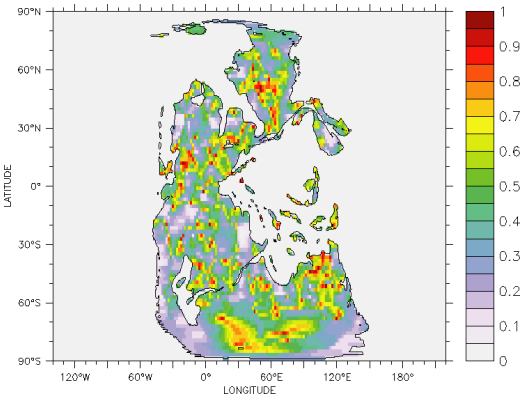

Figure C.9.: Orographic anisotropy γ (`orogam`) [0 = ridge, 1 = circular] for T63 grid.

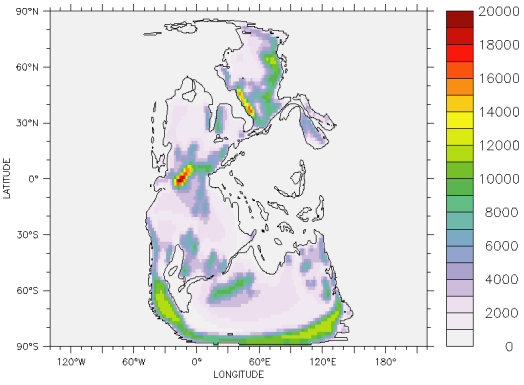

Figure C.10.: Surface geopotential [m^2s^{-2}] (`geosp`) for T63 grid.

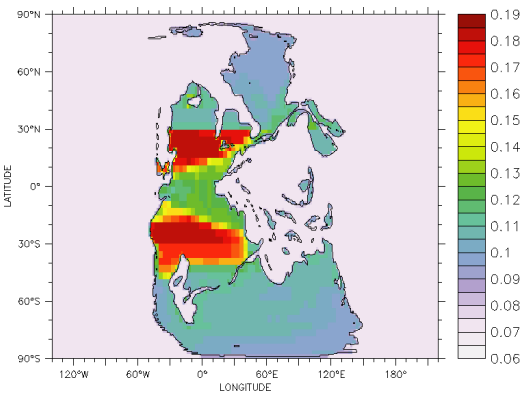

Figure C.11.: Surface background albedo [fractional] (`alb`) for T63 grid.

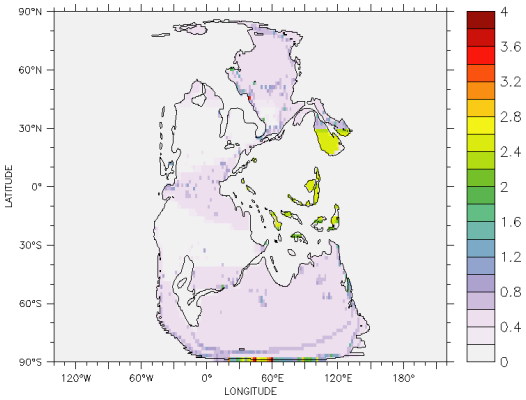

Figure C.12.: Surface roughness length [m] (`az0`) for T63 grid.

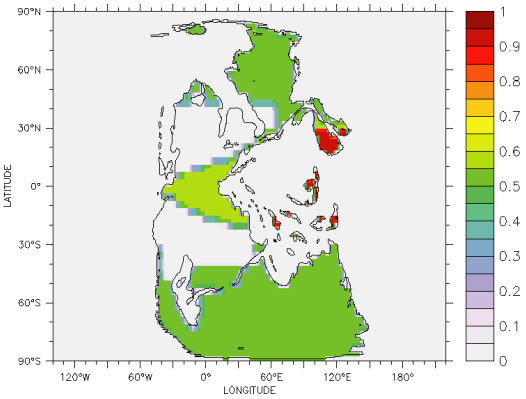

Figure C.13.: Forest ratio [fractional] (`forest`) for T63 grid.

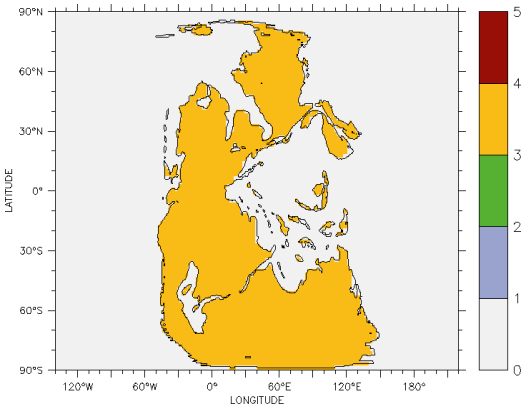

Figure C.14.: Soil type according to FAO dataset [0,...,5] (`fao`) for T63 grid.

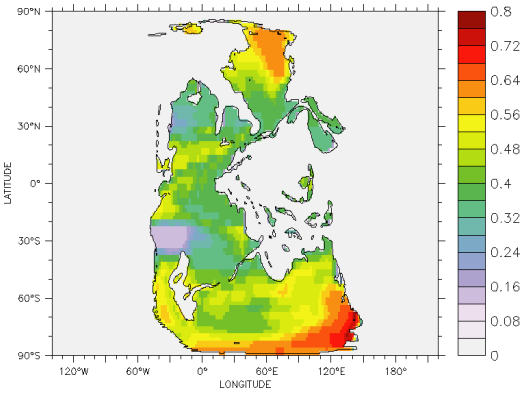

Figure C.15.: Soil wetness [m] (`ws`) for T63 grid.

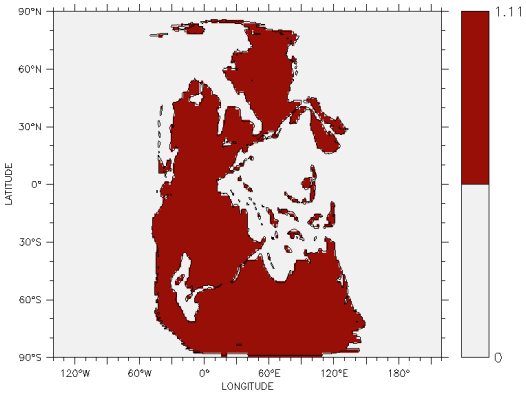

Figure C.16.: Field capacity of soil [m] (`wsmx`) for T63 grid.

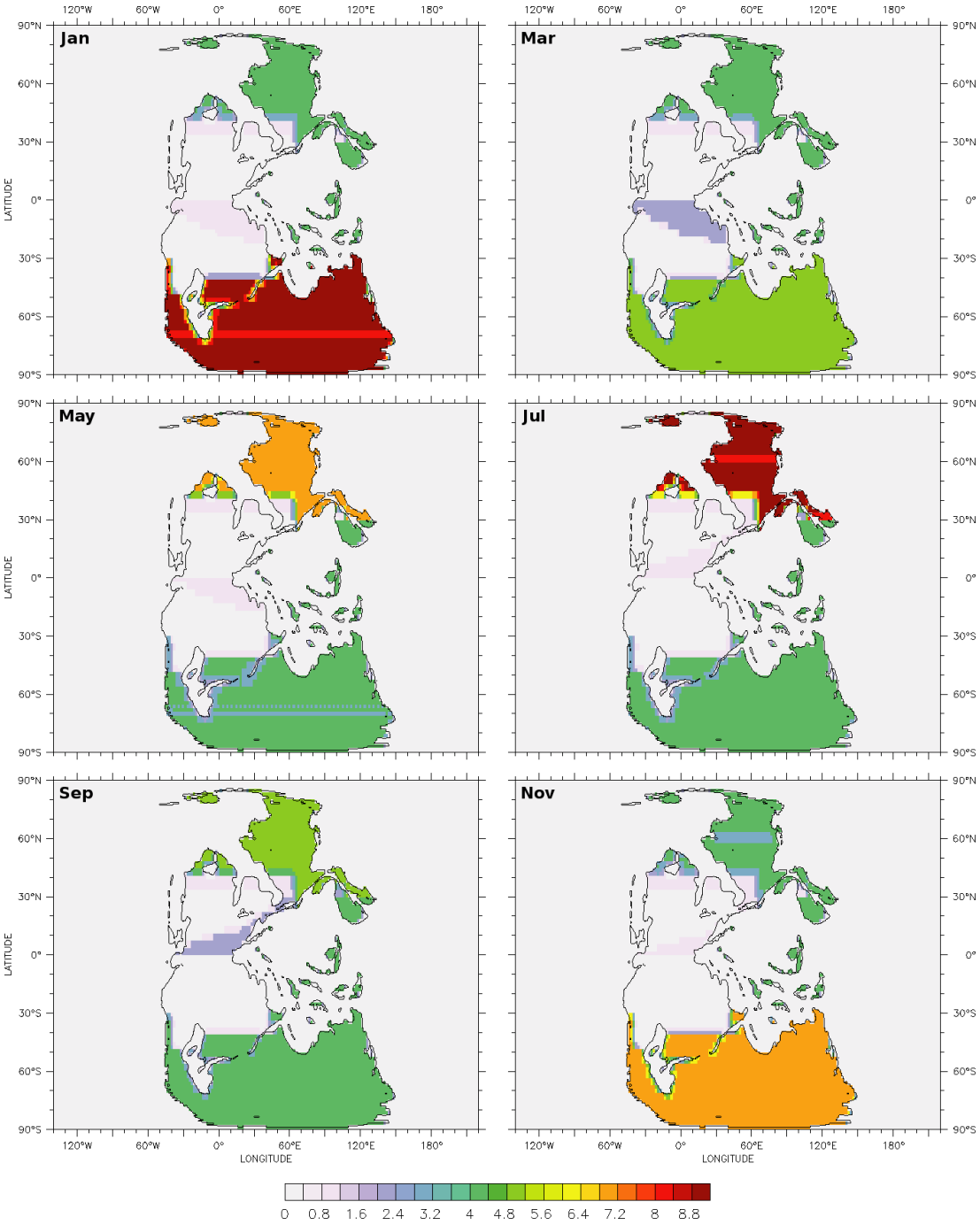

Figure C.17.: Climatology of leaf area index $[\frac{m^2}{m^2}]$ (`vltclim`) for T63 grid.

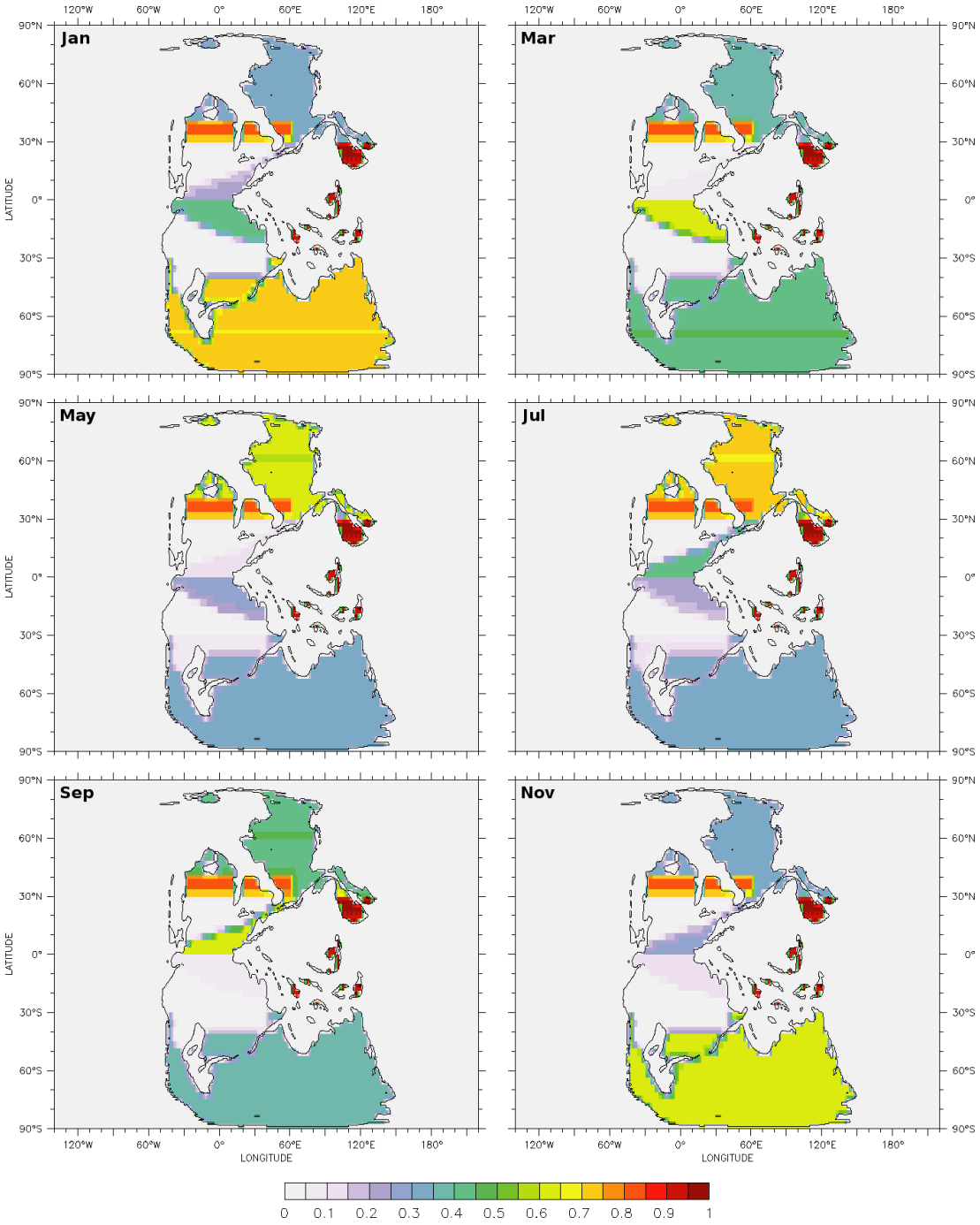

Figure C.18.: Climatology of vegetation ratio (`vgratclim`) for T63 grid.

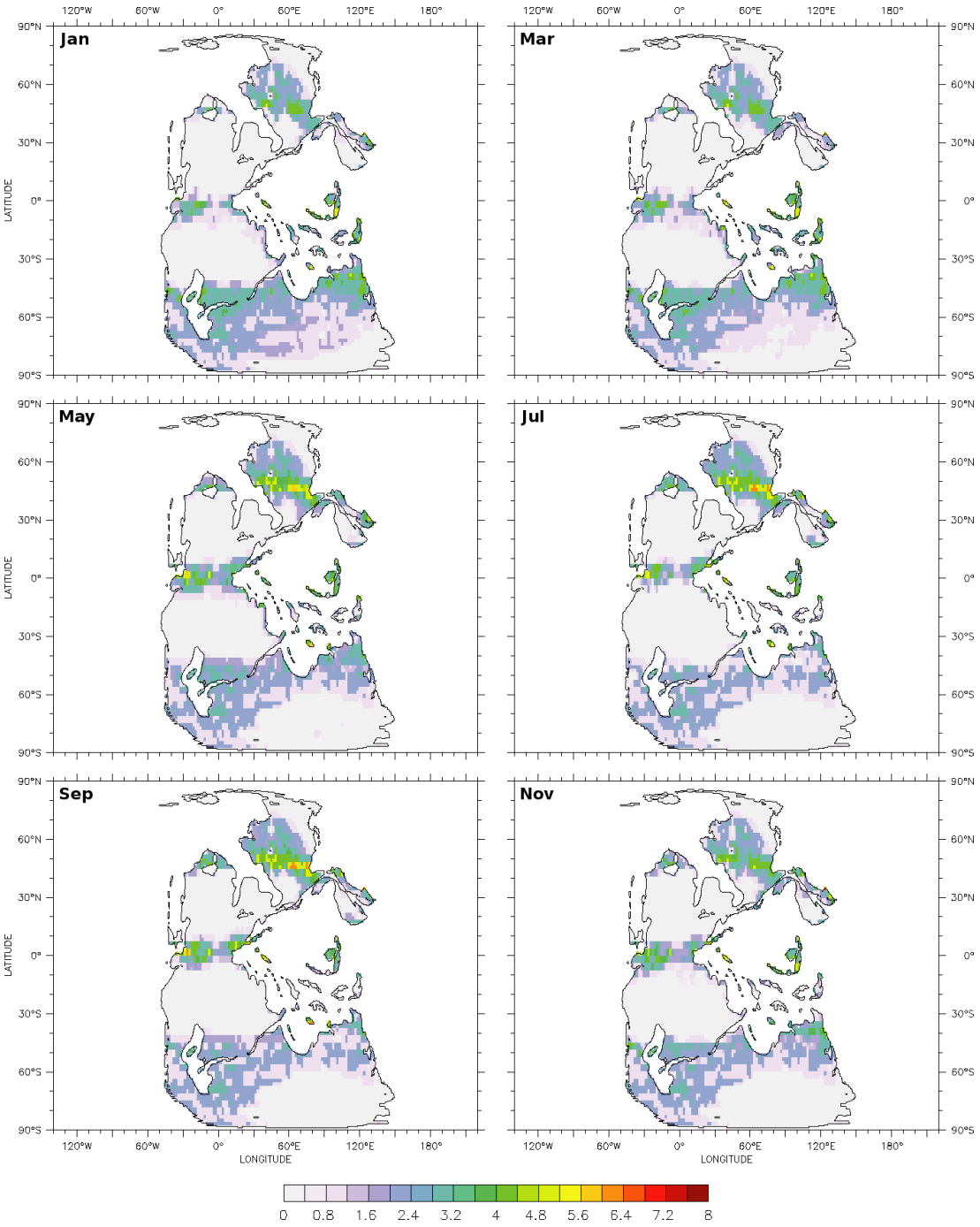

Figure C.19.: Climatology of leaf area index $[\frac{m^2}{m^2}]$ (`vltclim`) for T63 grid based on dynamically grown vegetation after 200 years of spin-up simulation for $4\times CO_2$ scenario.

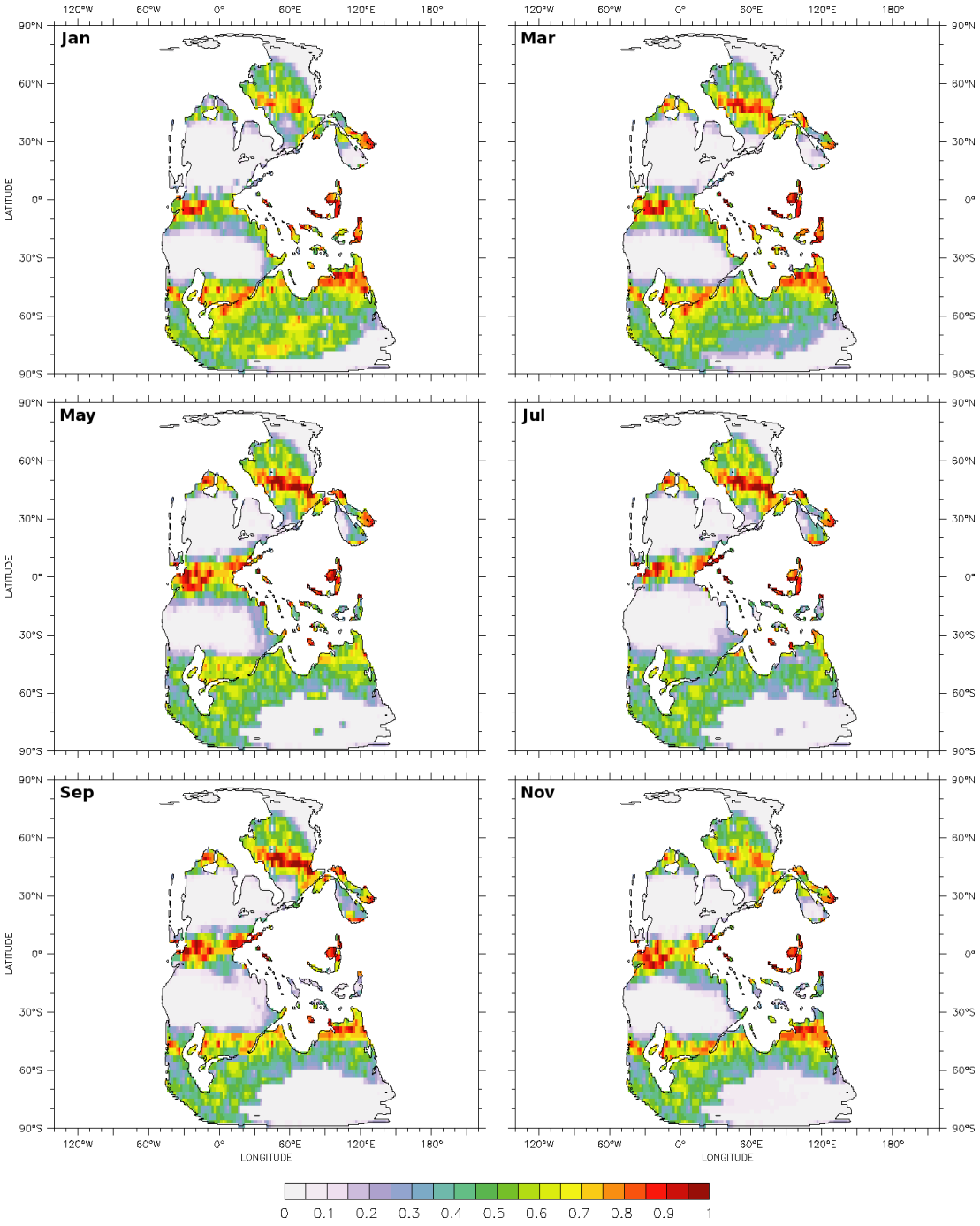

Figure C.20.: Climatology of vegetation ratio (`vgratclim`) for T63 grid based on dynamically grown vegetation after 200 years of spin-up simulation for $4\times CO_2$ scenario.

D

Sea ice coverage on Permian Earth

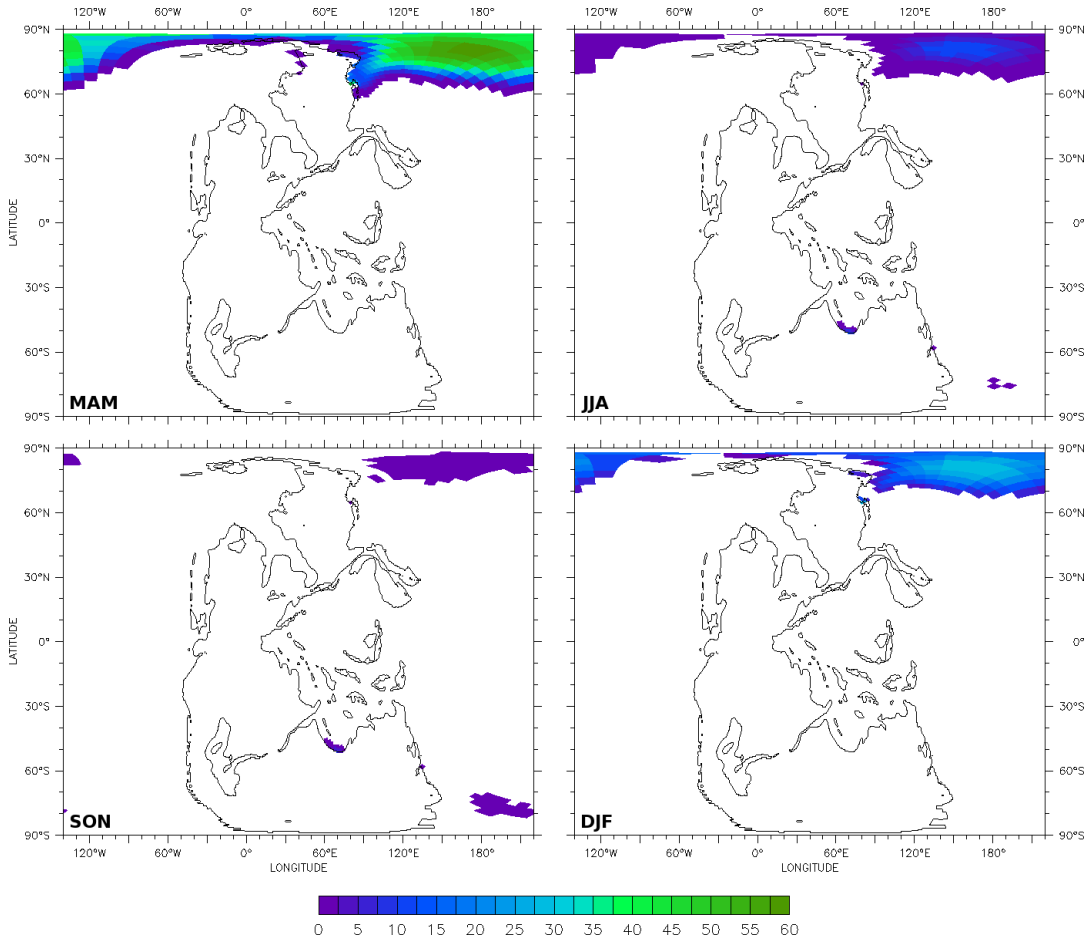

Figure D.1.: Mean seasonal sea ice extent and thickness [cm] for $4\times CO_2$ scenario.

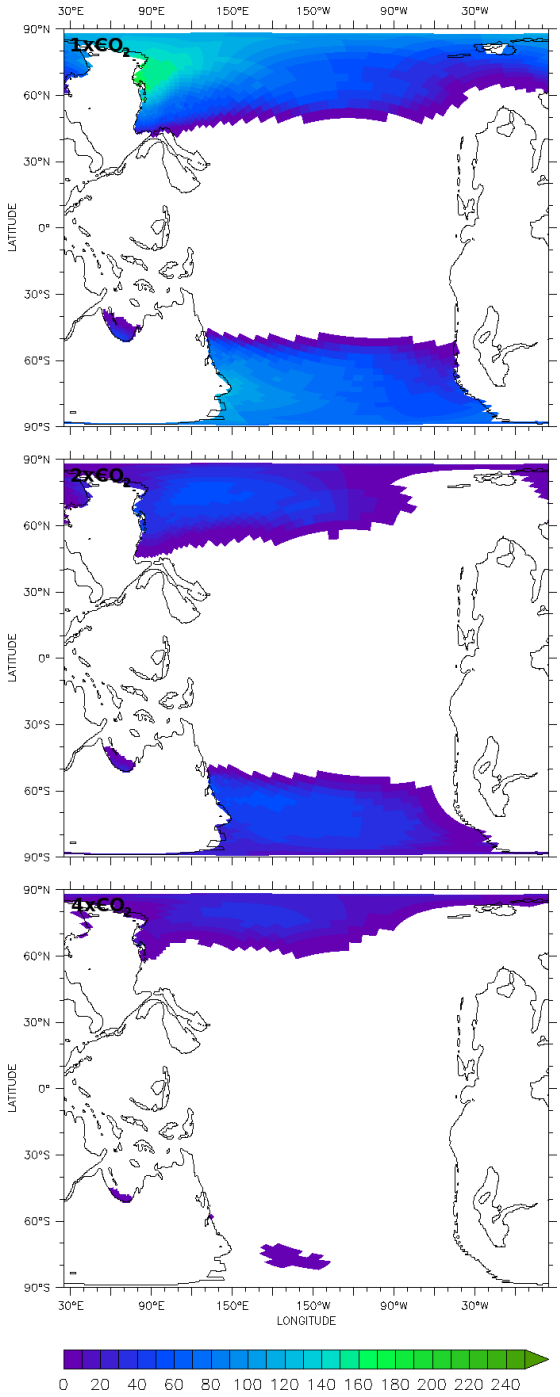

Figure D.2.: Mean annual sea ice extent and thickness [cm] for $1\times CO_2$(top), $2\times CO_2$(center), and $4\times CO_2$ scenario (bottom). There is no permanent sea ice coverage on yearly average for the $6\times CO_2$, $8\times CO_2$, and $10\times CO_2$ scenario.

E

Transport Processes in Permian and Present-Day Atmosphere

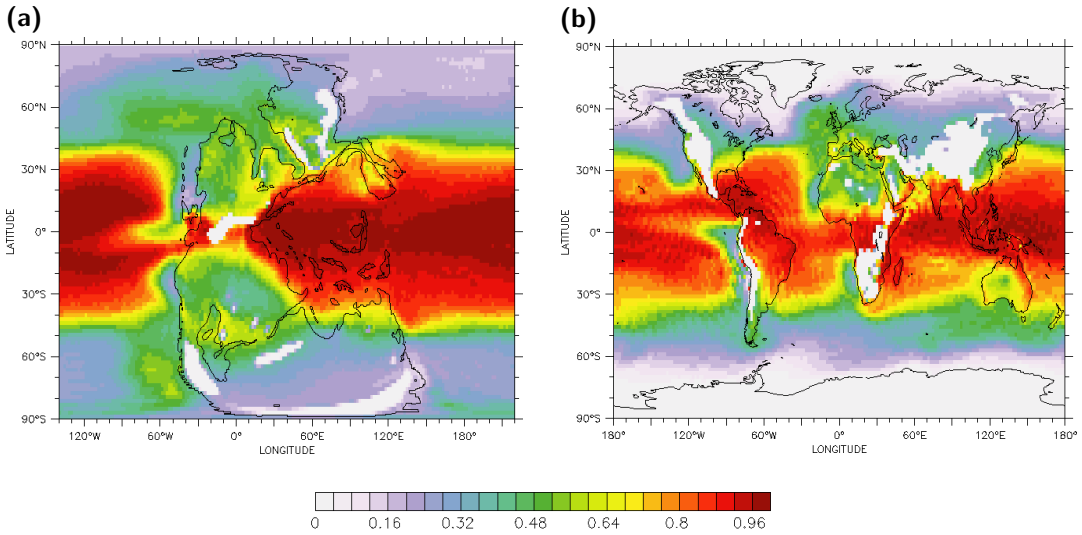

Figure E.1.: Mean proportion of unstable conditions in lower troposphere at 850 hPa. The cross section shows the annual average for the (a) Permian and (b) present-day reference scenario.

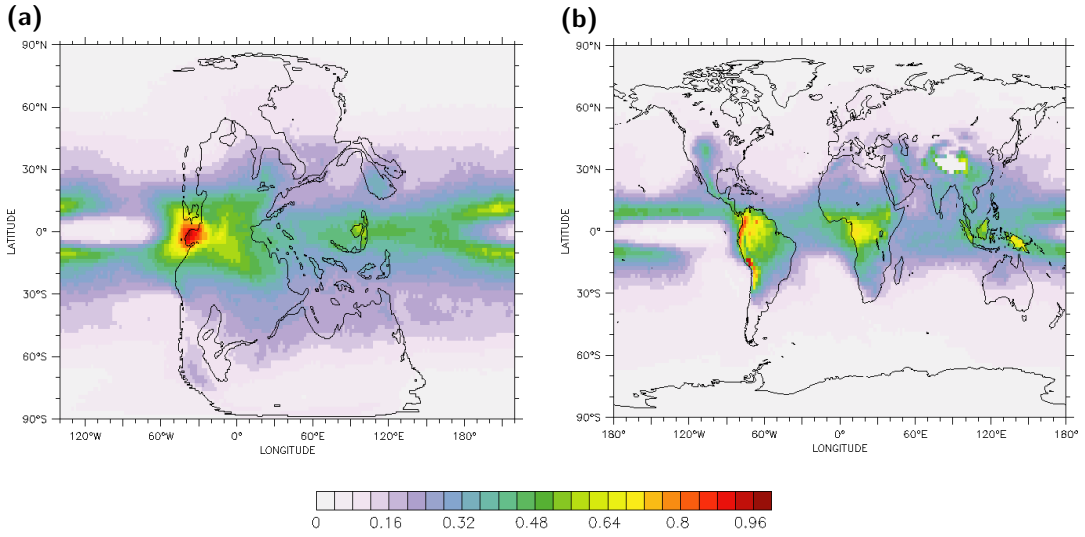

Figure E.2.: Mean proportion of unstable conditions in middle troposphere at 550 hPa. The cross section shows the annual average for the (a) Permian and (b) present-day reference scenario.

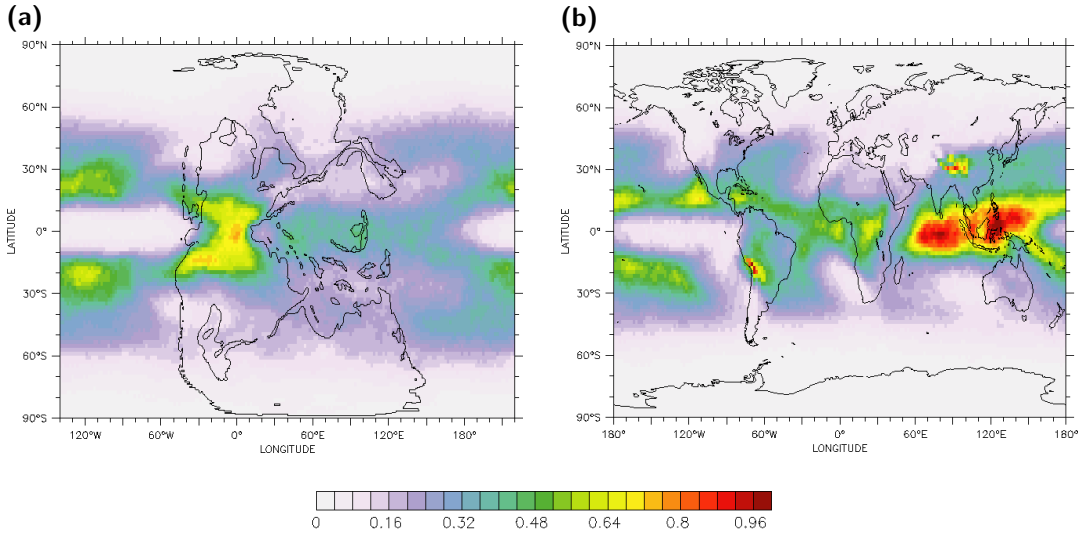

Figure E.3.: Mean proportion of unstable conditions in upper troposphere at 300 hPa. The cross section shows the annual average for the (a) Permian and (b) present-day reference scenario.

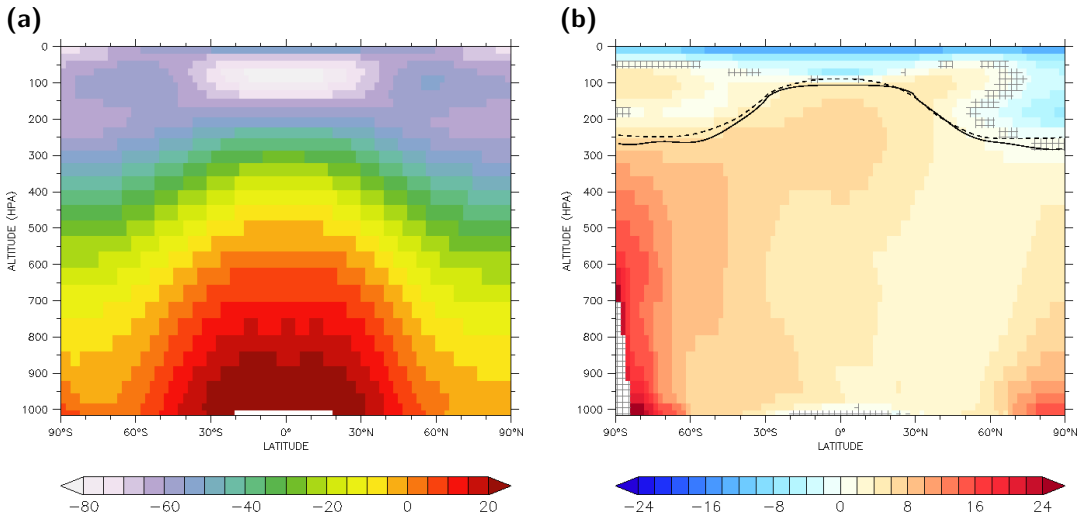

Figure E.4.: Mean temperature on annual and zonal average [°C]: (a) Annual average for the Permian 4×CO_2 scenario. (b) Comparison between the Permian and the present-day reference scenario. In hatched areas the difference is not highly significant based on an unpaired Student's t test and on a significance level of 95%. In addition the mean altitude of the tropopause is marked for both scenarios (solid: Present scenario, dashed: Permian scenario).

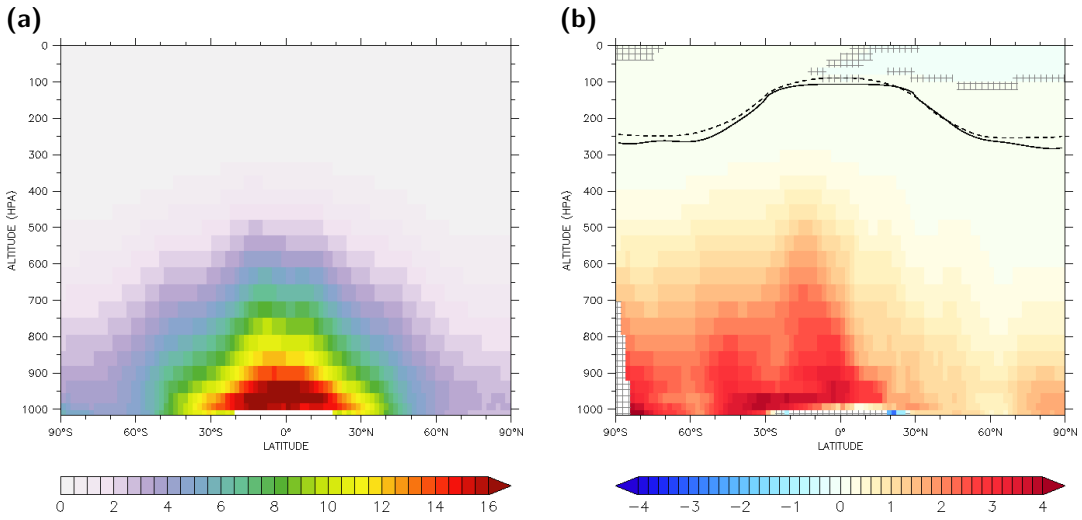

Figure E.5.: Mean specific humidity on annual and zonal average [g/kg]: (a) Annual average for the Permian 4×CO_2 scenario. (b) Comparison between the Permian and the present-day reference scenario. In hatched areas the difference is not highly significant based on an unpaired Student's t test and on a significance level of 95%. In addition the mean altitude of the tropopause is marked for both scenarios (solid: Present scenario, dashed: Permian scenario).

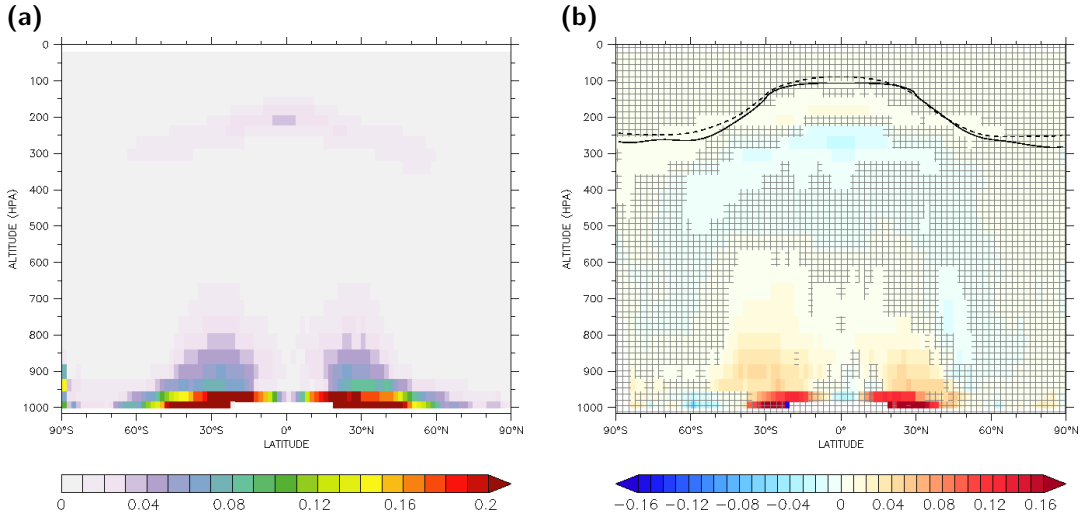

Figure E.6.: Proportion of unstable conditions in terms of potential temperature on zonal average: (a) Annual average for the Permian $4\times CO_2$ scenario. (b) Comparison between the Permian and the present-day reference scenario. In hatched areas the difference is not highly significant based on an unpaired Student's t test and on a significance level of 95%. In addition the mean altitude of the tropopause is marked for both scenarios (solid: Present scenario, dashed: Permian scenario).

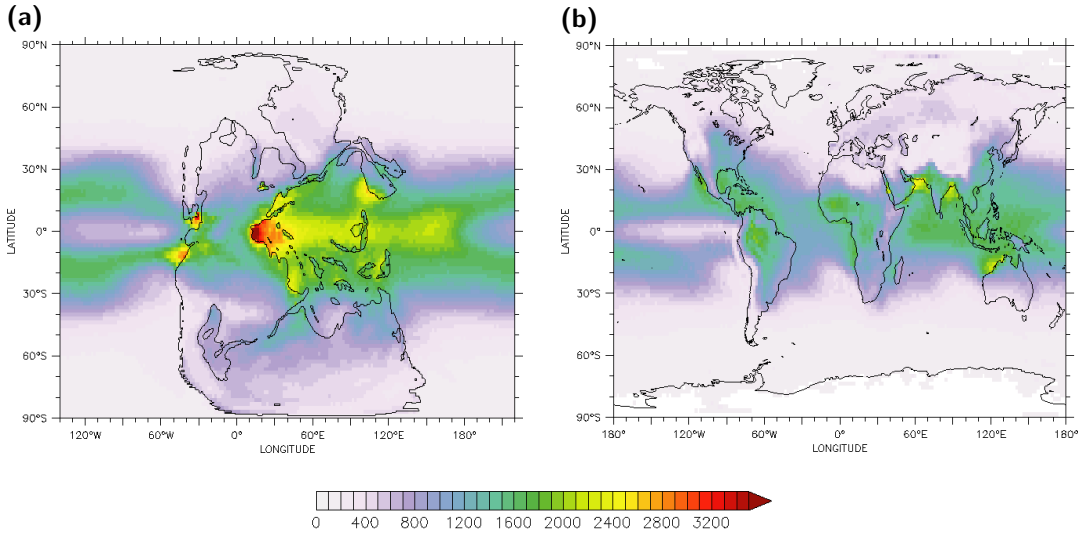

Figure E.7.: Annual mean CAPE [J/kg] for the (a) Permian and (b) present-day reference scenario. The annual mean is prefiltered with a minimum of 100 J/kg to exclude non-convective events.

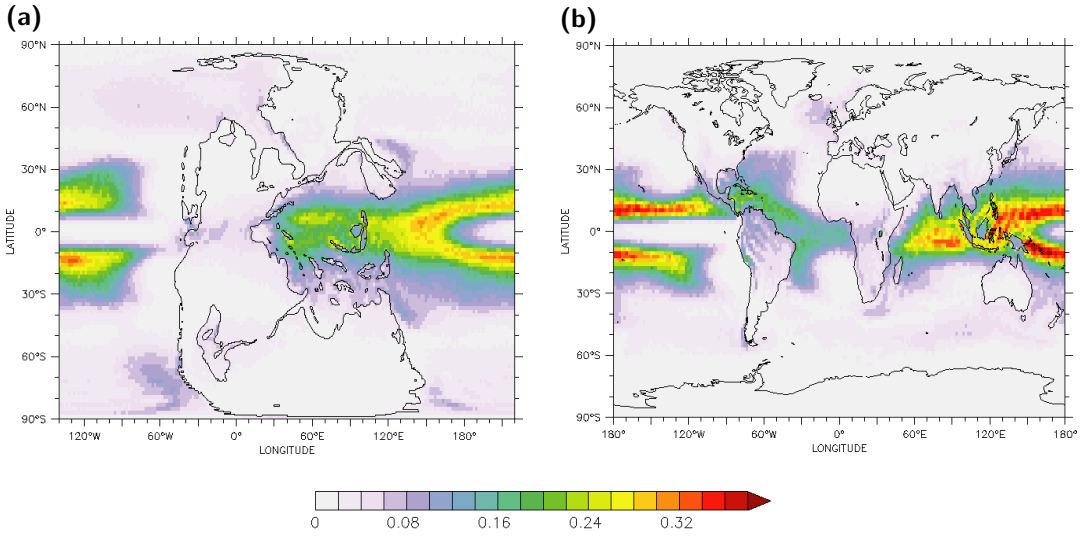

Figure E.8.: Mean proportion of triggered deep convection events on annual average for the (a) Permian and (b) present-day reference scenario.

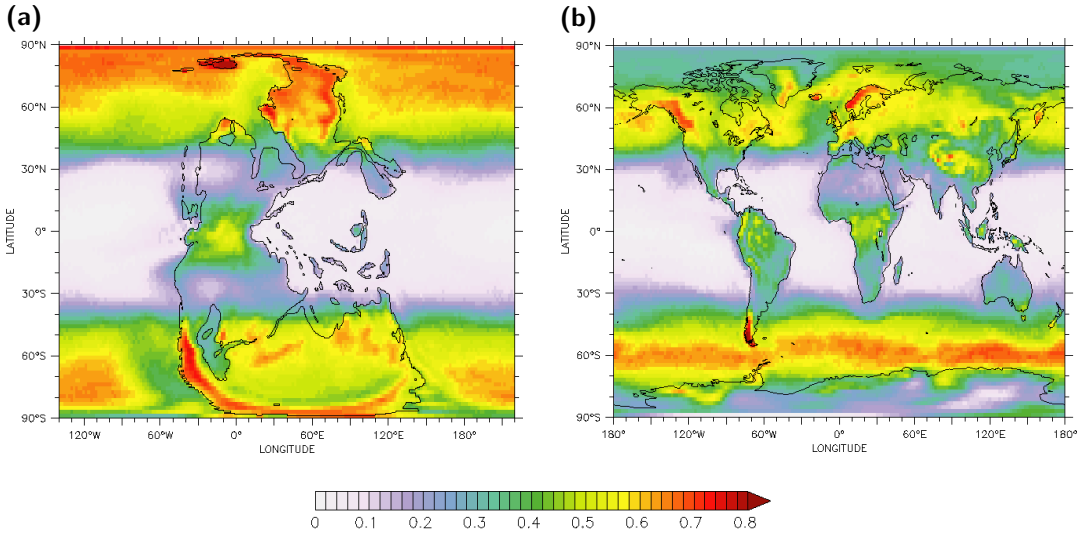

Figure E.9.: Mean proportion of triggered mid-level convection events on annual average for the (a) Permian and (b) present-day reference scenario.

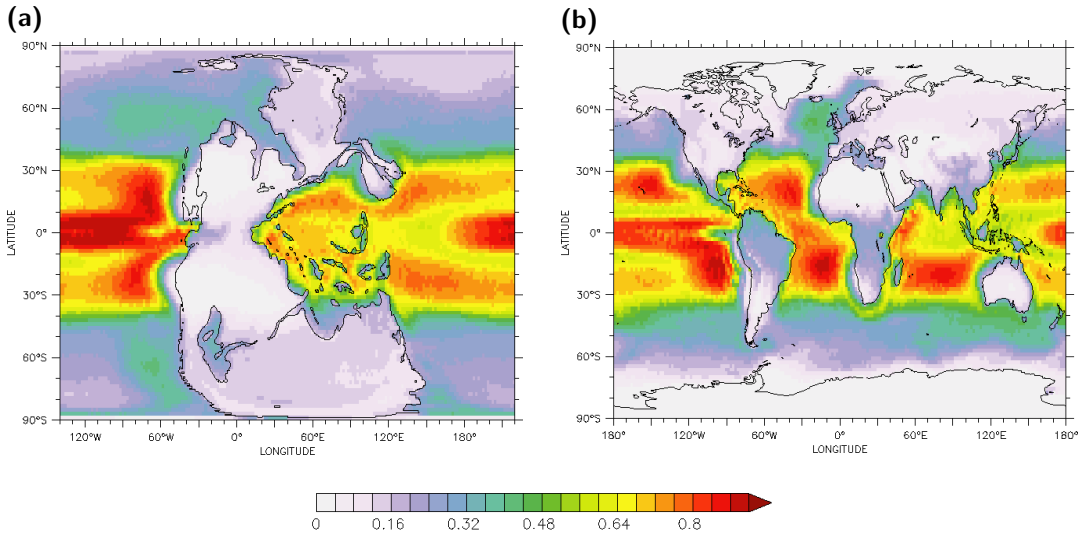

Figure E.10.: Mean proportion of triggered shallow convection events on annual average for the (a) Permian and (b) present-day reference scenario.

F

Derivation of the Factor Separation Method

Stein and Alpert [178] consider a field f that depends on n factors ψ_i where $i \in [1, n]$. If ψ_i is changed in a continuous manner this entails a continuous change of the field as well. The change can be written as multiplication by a changing coefficient c_i:

$$\psi_i(c_i) = c_i \psi_i, \quad 0 \leq c_i \leq 1. \tag{F.1}$$

Hence, the resulting field is a continuous function of the changing coefficients c_i:

$$f = f(c_1, c_2, c_3, \ldots, c_n). \tag{F.2}$$

The field function f can be decomposed and written as series expansion in such a way that the dependencies of the changing coefficients are separated:

$$\begin{aligned} f(c_1, c_2, c_3, \ldots, c_n) = \hat{f}_0 + \sum_{i=1}^{n} \hat{f}_i(c_i) + \sum_{i,j=1,2}^{n-1,n} \hat{f}_{ij}(c_i, c_j) + \\ \sum_{i,j,k=1,2,3}^{n-2,n-1,n} \hat{f}_{ijk}(c_i, c_j, c_k) + \cdots + \hat{f}_{123\ldots n}(c_1, c_2, c_3, \ldots, c_n) \end{aligned} \tag{F.3}$$

Here $\hat{f}$ denotes the part of f that is independent of all change coefficients and the second term is the sum of all parts, $\hat{f}_i$, that depend on one change coefficient c_i only. The third term of Equation F.3 merely contains dependencies of two change coefficients, c_i and c_j, and is a sum of all sorted pairs, whereas the forth terms is a sum of all sorted trios depending on three coefficients only etc.

In the following the change coefficients are restricted to either $c_i = 0$ or $c_i = 1$, i.e. the data is simulated or recorded either under the influence of this factor or without but the size of the factor is generally kept constant. This reduces the number of combinations

of possible simulations or records to 2^n. The equation set of the corresponding field functions is given by:

$$f_0 \equiv f(0,0,0,\ldots,0) = \hat{f}_0, \tag{F.4}$$

$$f_i = \hat{f}_i + \hat{f}_0, \quad i \in [1,n], \tag{F.5}$$

$$f_{ij} = \hat{f}_{ij} + \hat{f}_i + \hat{f}_j + \hat{f}_0, \quad i,j \in [1,n], \tag{F.6}$$

$$f_{ijk} = \hat{f}_{ijk} + \hat{f}_{ij} + \hat{f}_{jk} + \hat{f}_{ik} + \hat{f}_i + \hat{f}_j + \hat{f}_k + \hat{f}_0, \quad i,j,k \in [1,n], \tag{F.7}$$

$$f_{123\ldots n} = \hat{f}_{123\ldots n} + \cdots + \sum_{i,j,k=1,2,3}^{n-2,n-1,n} \hat{f}_{ijk} + \sum_{i,j=1,2}^{n-1,n} \hat{f}_{ij} + \sum_{i=1}^{n} \hat{f}_i + \hat{f}_0, \tag{F.8}$$

where $\hat{f}_{ij}$ considers the case with $c_i = c_j = 1$ and all remaining coefficients are set to zero.

The equation set can be solved by recursive elimination. The general solution for the isolated parts is:

$$\hat{f}_{i_1 i_2 \ldots i_l} = \sum_{m=0}^{l} (-1)^{l-m} \left(\sum_{j_1,j_2,j_3,\ldots,j_m=i_1,i_2,\ldots,i_m}^{i_{l-m+1},i_{l-m+2},\ldots,i_l} f_{j_1 j_2 j_3 \ldots j_m} \right) \tag{F.9}$$

where $j_1, j_2, j_3, \ldots, j_m \in \{i_1, i_2, i_3, \ldots, i_l\}$ $\forall$ $0 \leq l \leq n$ and the second sum is over all groups of m sorted indices.

G

Impact of Nudging on Transport in Present-Day Atmosphere

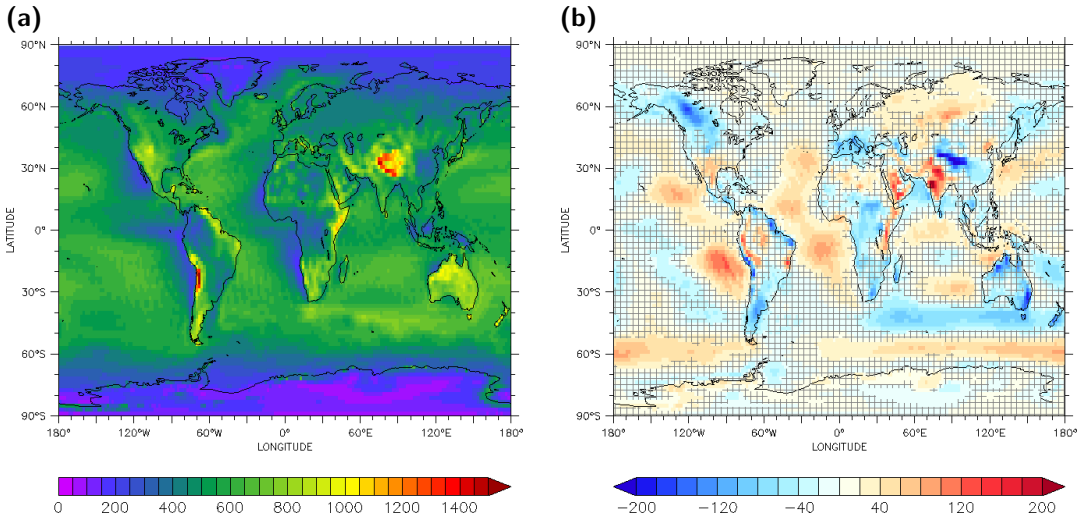

Figure G.1.: Impact of nudging on the planetary boundary layer height: (a) Mean planetary boundary layer height [m] on annual average for the free scenario. (b) Impact of nudging: The simulated mean boundary layer height that results for the fully-nudged scenario is compared to the free model scenario. In hatched areas the difference is not highly significant based on an unpaired Student's t test and on a significance level of 5%.

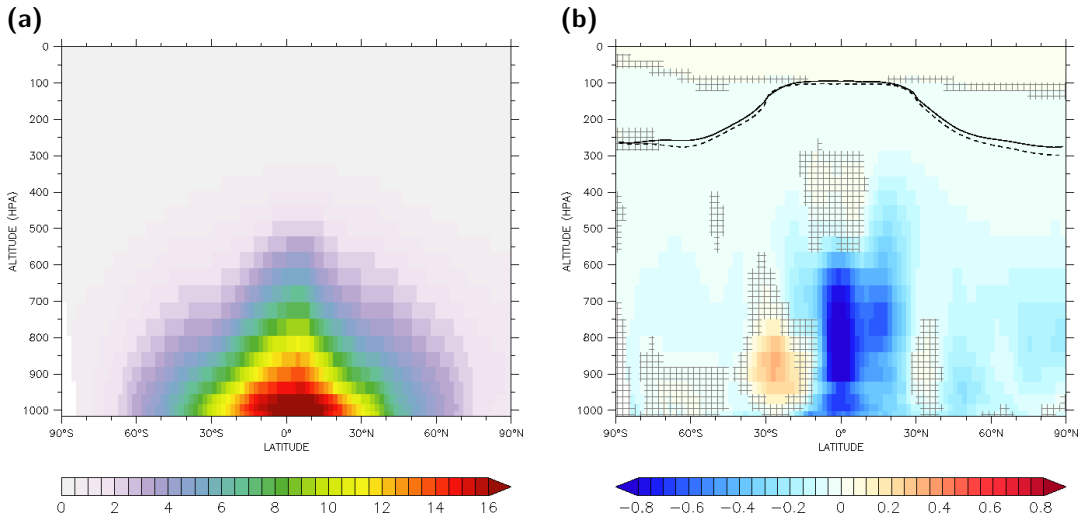

Figure G.2.: Impact of nudging on mean zonal specific humidity [g/kg]: (a) Mean specific humidity on annual and zonal average for the free scenario. (b) Impact of nudging: The simulated mean specific humidity that results for the fully-nudged scenario is compared to the free model scenario. In hatched areas the difference is not highly significant based on an unpaired Student's t test and on a significance level of 5%. In addition the mean altitude of the tropopause is marked for both scenarios (solid: free scenario, dashed: fully-nudged scenario).

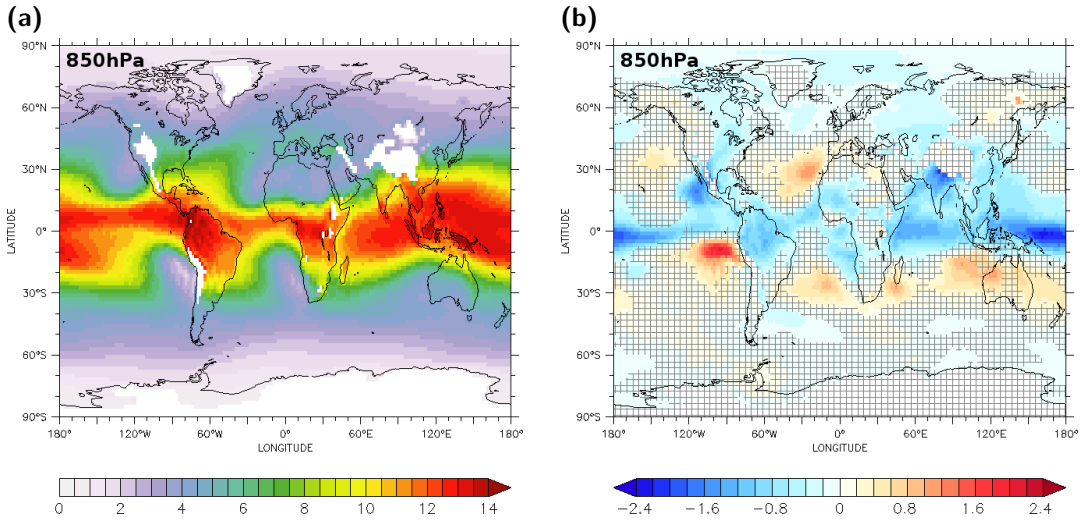

Figure G.3.: Impact of nudging on mean specific humidity [g/kg] in the lower troposphere at 850 hPa: (a) Mean specific humidity on annual for the free scenario. (b) Impact of nudging: The simulated mean specific humidity that results for the fully-nudged scenario is compared to the free model scenario. In hatched areas the difference is not highly significant based on an unpaired Student's t test and on a significance level of 5%.

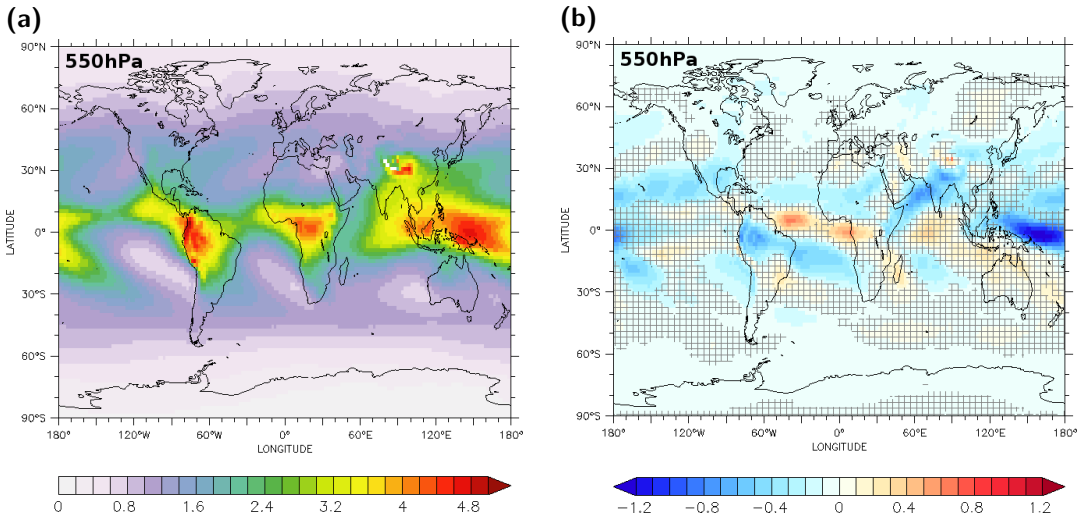

Figure G.4.: Impact of nudging on mean specific humidity [g/kg] in the middle troposphere at 550 hPa: (a) Mean specific humidity on annual for the free scenario. (b) Impact of nudging: The simulated mean specific humidity that results for the fully-nudged scenario is compared to the free model scenario. In hatched areas the difference is not highly significant based on an unpaired Student's t test and on a significance level of 5%.

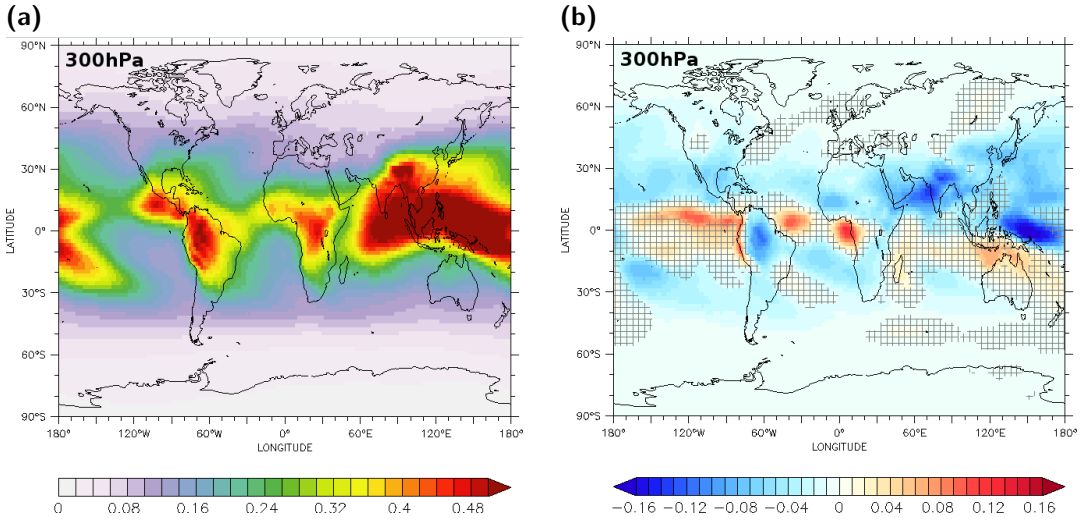

Figure G.5.: Impact of nudging on mean specific humidity [g/kg] in the upper troposphere at 300 hPa: (a) Mean specific humidity on annual for the free scenario. (b) Impact of nudging: The simulated mean specific humidity that results for the fully-nudged scenario is compared to the free model scenario. In hatched areas the difference is not highly significant based on an unpaired Student's t test and on a significance level of 5%.

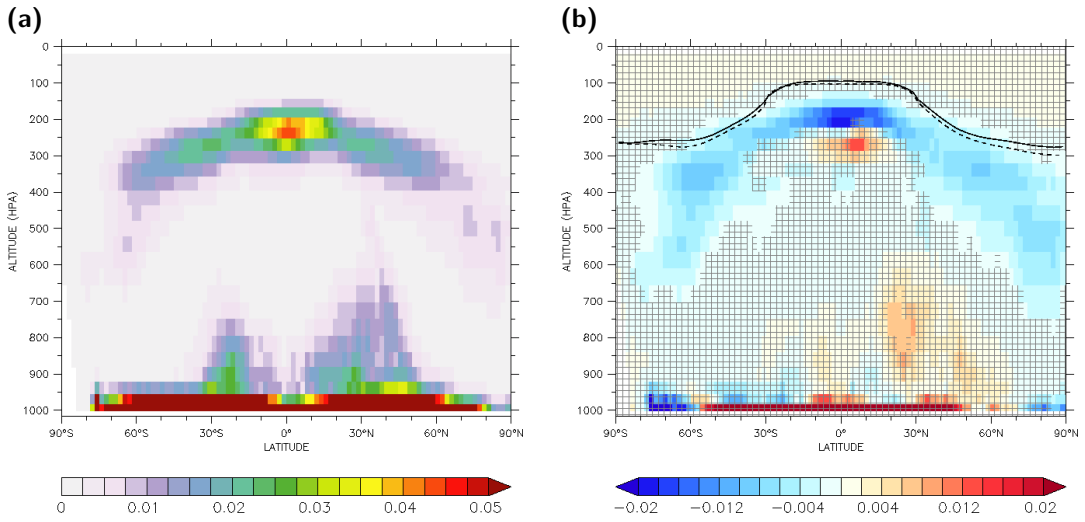

Figure G.6.: Impact of nudging on the proportion of unstable conditions in terms of potential temperature on zonal average: (a) The profile shows the annual average for the free scenario. (b) Impact of nudging: The mean proportion of unstable conditions for the fully-nudged scenario is compared to the free model scenario. In hatched areas the difference is not significant based on an unpaired Student's t test and on a level of 5%. In addition the mean altitude of the tropopause is marked for both scenarios (solid: free scenario, dashed: fully-nudged scenario).

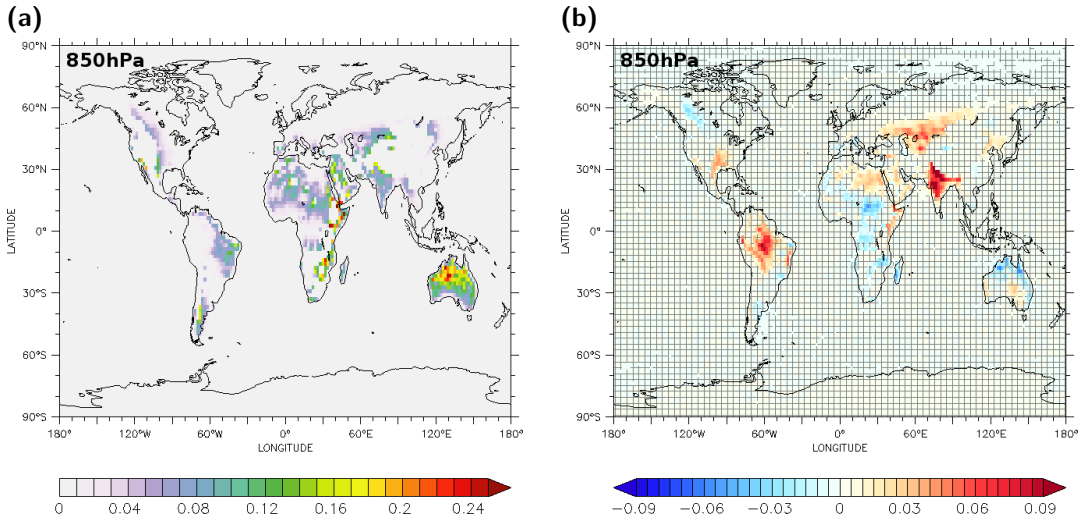

Figure G.7.: Impact of nudging on the proportion of unstable conditions in terms of potential temperature in the lower troposphere at an altitude of 850 hPa: (a) The cross section shows the annual average for the free scenario. (b) Impact of nudging: The proportion of unstable conditions for the fully-nudged scenario is compared to the free model scenario. In hatched areas the difference is not significant based on an unpaired Student's t test and on a level of 5%.

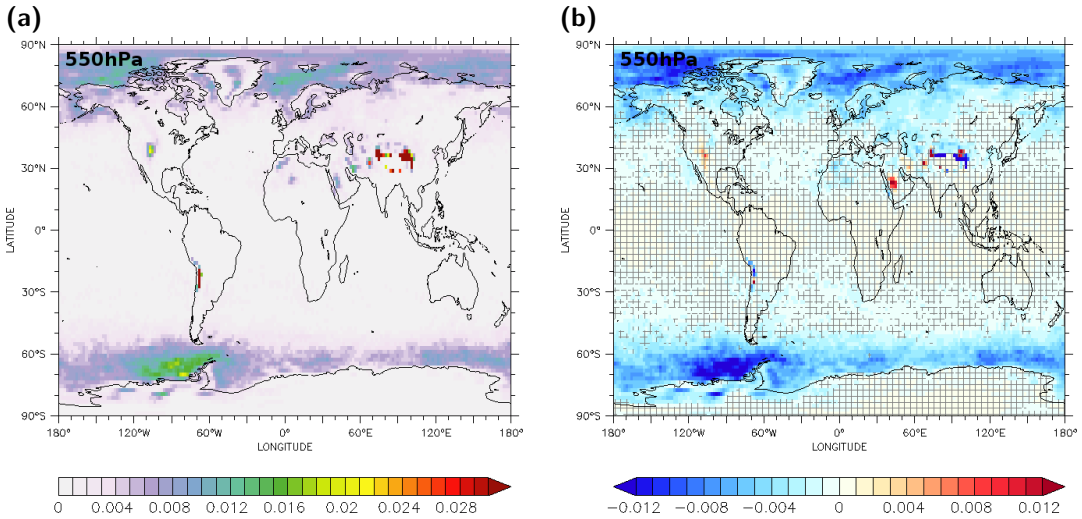

Figure G.8.: Impact of nudging on the proportion of unstable conditions in terms of potential temperature in the middle troposphere at an altitude of 550 hPa: (a) The cross section shows the annual average for the free scenario. (b) Impact of nudging: The proportion of unstable conditions for the fully-nudged scenario is compared to the free model scenario. In hatched areas the difference is not significant based on an unpaired Student's t test and on a level of 5%.

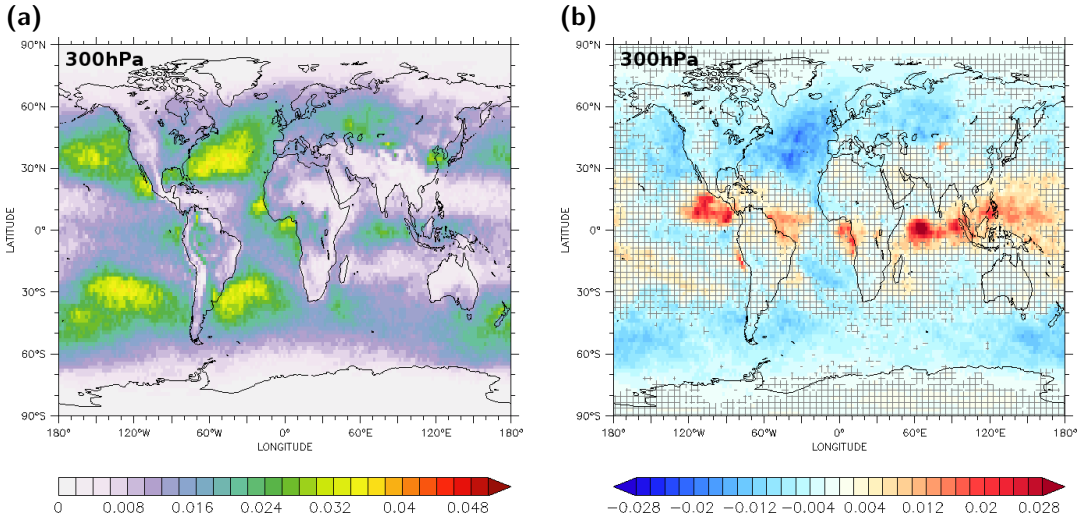

Figure G.9.: Impact of nudging on the proportion of unstable conditions in terms of potential temperature in the upper troposphere at an altitude of 300 hPa: (a) The cross section shows the annual average for the free scenario. (b) Impact of nudging: The proportion of unstable conditions for the fully-nudged scenario is compared to the free model scenario. In hatched areas the difference is not significant based on an unpaired Student's t test and on a level of 5%.

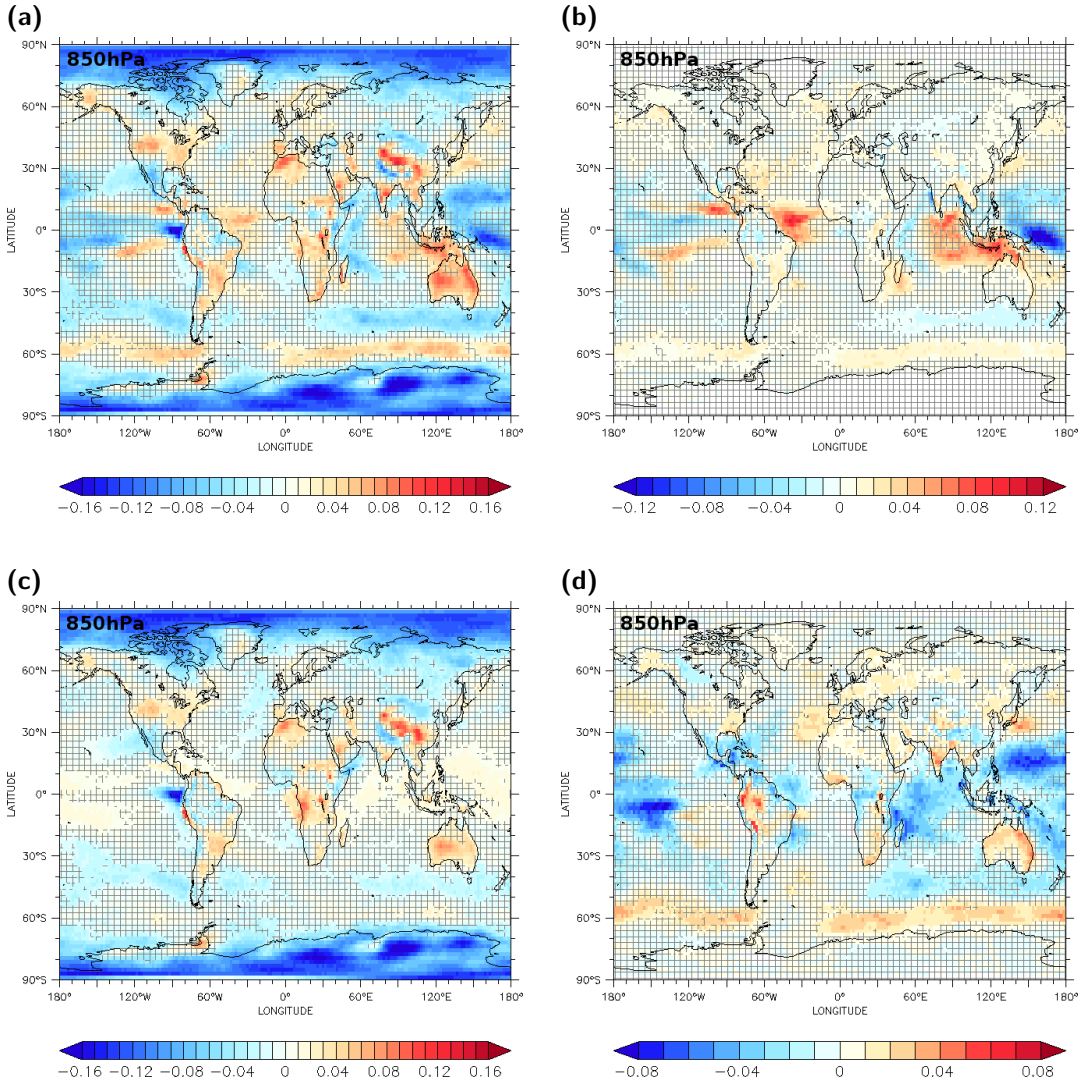

Figure G.10.: Impact of nudging on the mean proportion of convection events of an altitude higher than 850 hPa in the lower troposphere: In the cross sections the mean proportion of triggered convection events for the fully-nudged scenario is compared to the free model scenario. (a) All types, (b) deep convection, (c) mid-level convection, and (d) shallow convection. In hatched areas the difference is not significant based on an unpaired Student's t test and on a level of 5%.

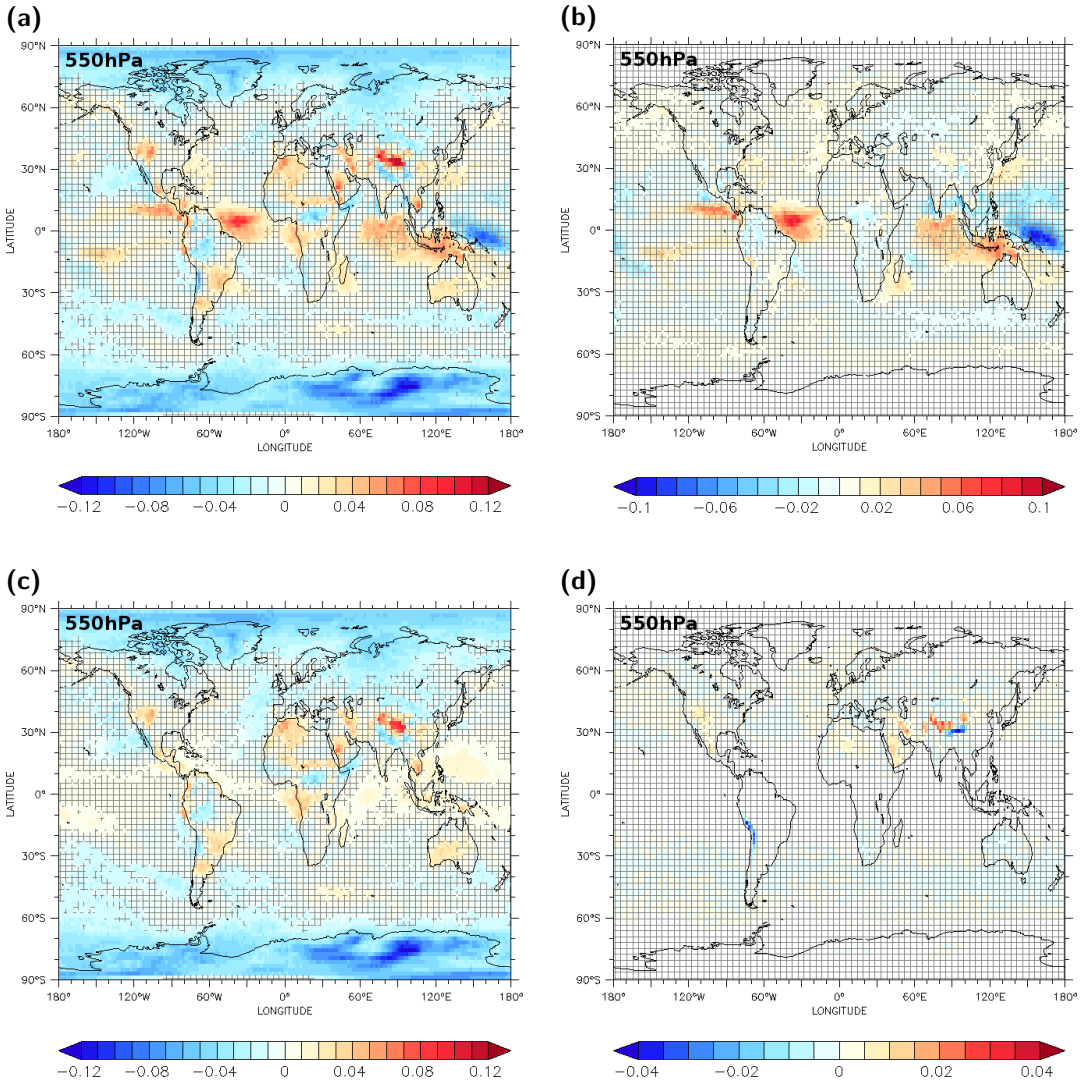

Figure G.11.: Impact of nudging on the mean proportion of convection events of an altitude higher than 550 hPa in the middle troposphere: In the cross sections the mean proportion of triggered convection events for the fully-nudged scenario is compared to the free model scenario. (a) All types, (b) deep convection, (c) mid-level convection, and (d) shallow convection. In hatched areas the difference is not significant based on an unpaired Student's t test and on a level of 5%.

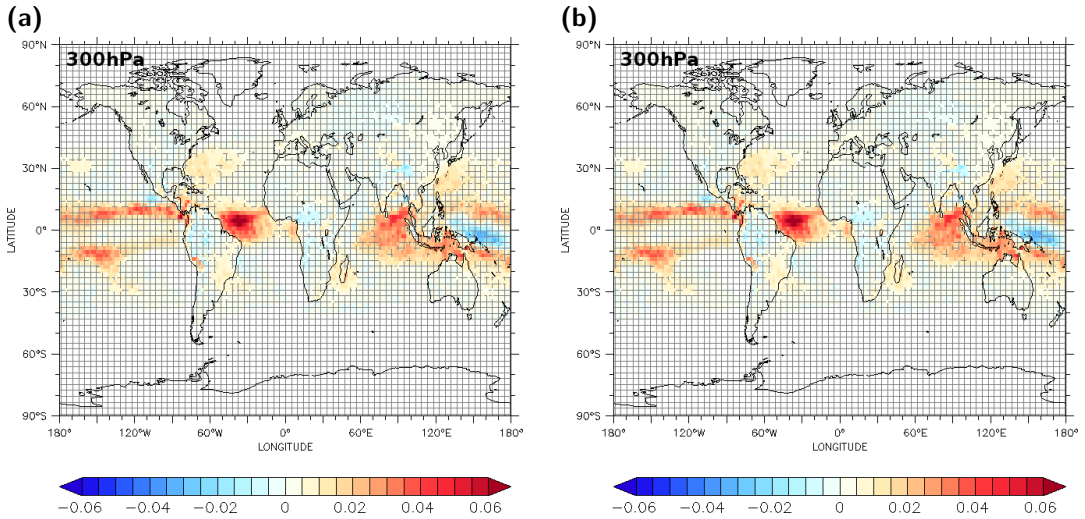

Figure G.12.: Impact of nudging on the mean proportion of convection events of an altitude higher than 300 hPa in the upper troposphere: In the cross sections the mean proportion of triggered convection events for the fully-nudged scenario is compared to the free model scenario. (a) All types, and (b) deep convection. In hatched areas the difference is not significant based on an unpaired Student's t test and on a level of 5%.

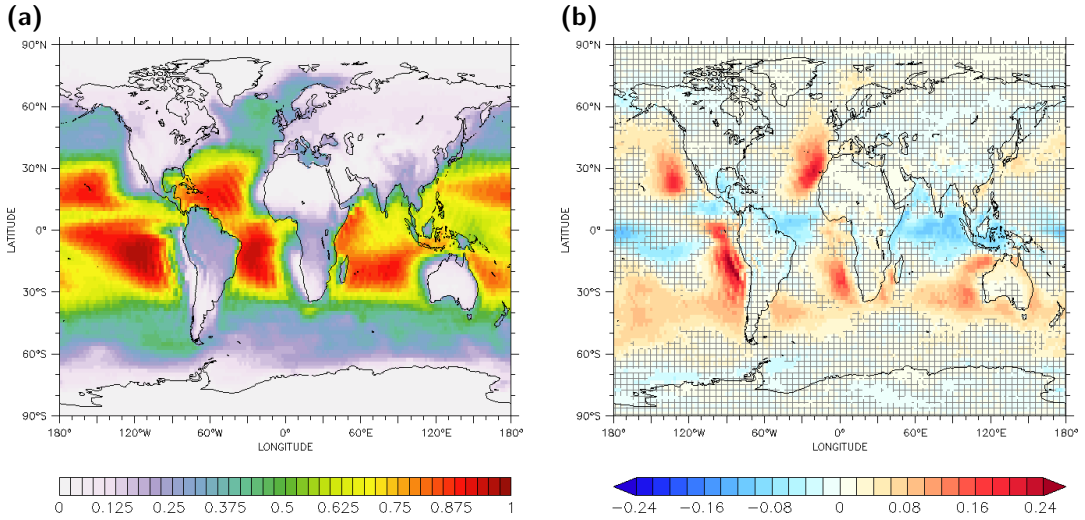

Figure G.13.: Impact of nudging on the proportion of triggered shallow convection events: (a) Mean propotion with respect to the simulated period of 9 years for the free scenario. (b) Impact of nudging: The simulated mean proportion that results for the fully-nudged scenario is compared to the free model scenario. In hatched areas the difference is not highly significant based on an unpaired Student's t test and on a significance level of 5%.

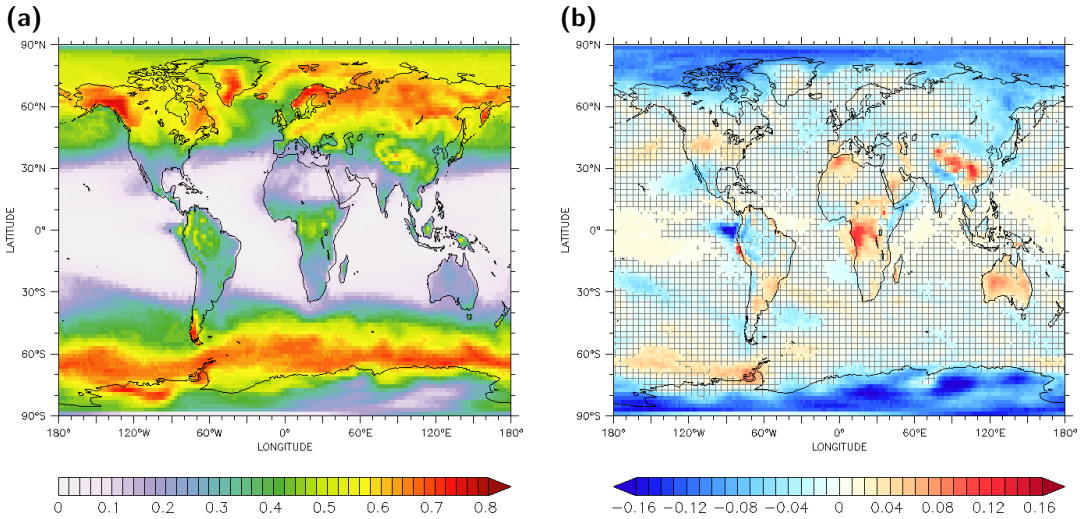

Figure G.14.: Impact of nudging on the proportion of triggered mid-level convection events: (a) Mean propotion with respect to the simulated period of 9 years for the free scenario. (b) Impact of nudging: The simulated mean proportion that results for the fully-nudged scenario is compared to the free model scenario. In hatched areas the difference is not highly significant based on an unpaired Student's t test and on a significance level of 5%.

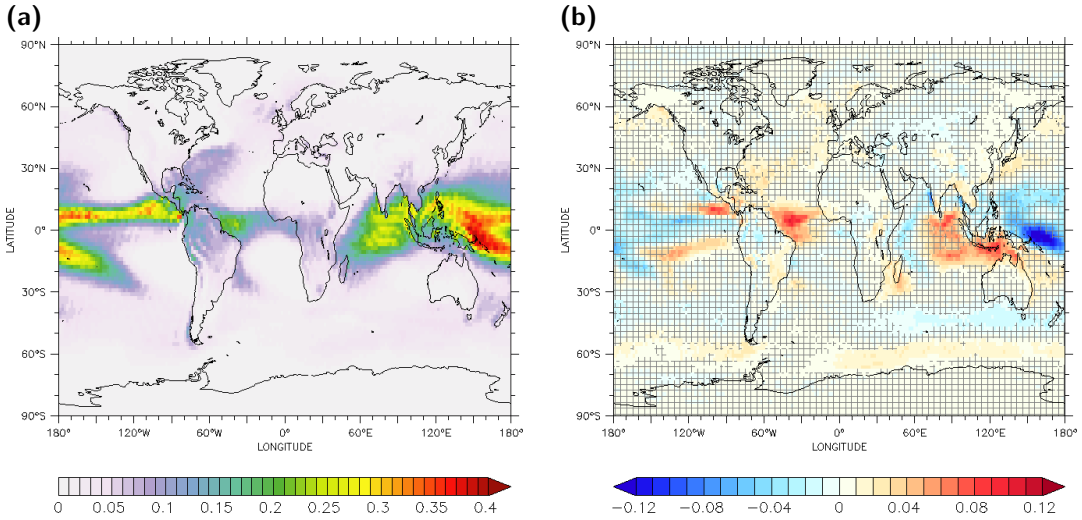

Figure G.15.: Impact of nudging on the proportion of triggered deep convection events: (a) Mean propotion with respect to the simulated period of 9 years for the free scenario. (b) Impact of nudging: The simulated mean proportion that results for the fully-nudged scenario is compared to the free model scenario. In hatched areas the difference is not highly significant based on an unpaired Student's t test and on a significance level of 5%.

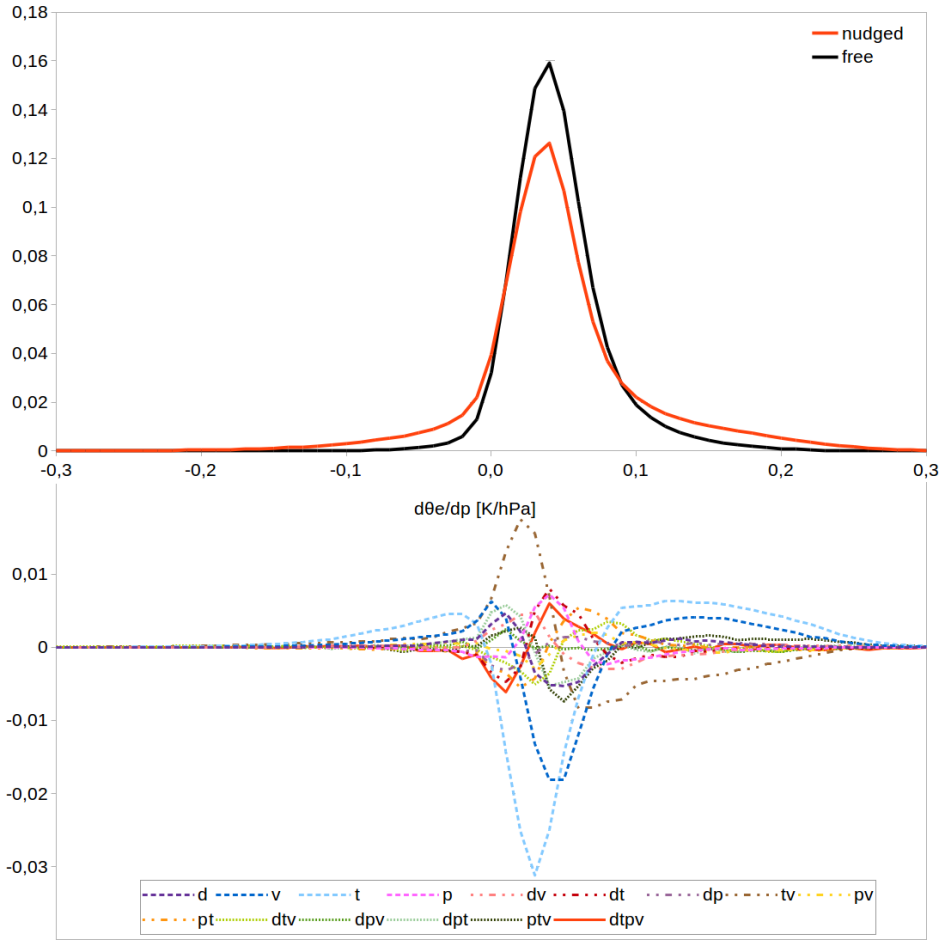

Figure G.16.: Impact of nudging on static stability over the Indo-Pacific Warm Pool [5°S-5°N; 140°E-160°E] in the lower troposphere at 850 hPa: The upper curves show the frequency distribution of the vertical gradient of the equivalent potential temperature in terms of pressure from the entire region with respect to the simulated period of 9 years. The negative gradient indicates stable conditions whereas the positive gradient indicates conditional instabilities. The red line represents the fully-nudged scenario and the black line represents the free model scenario. The lower curves break down the isolated and interactive contributions to the nudging impact.

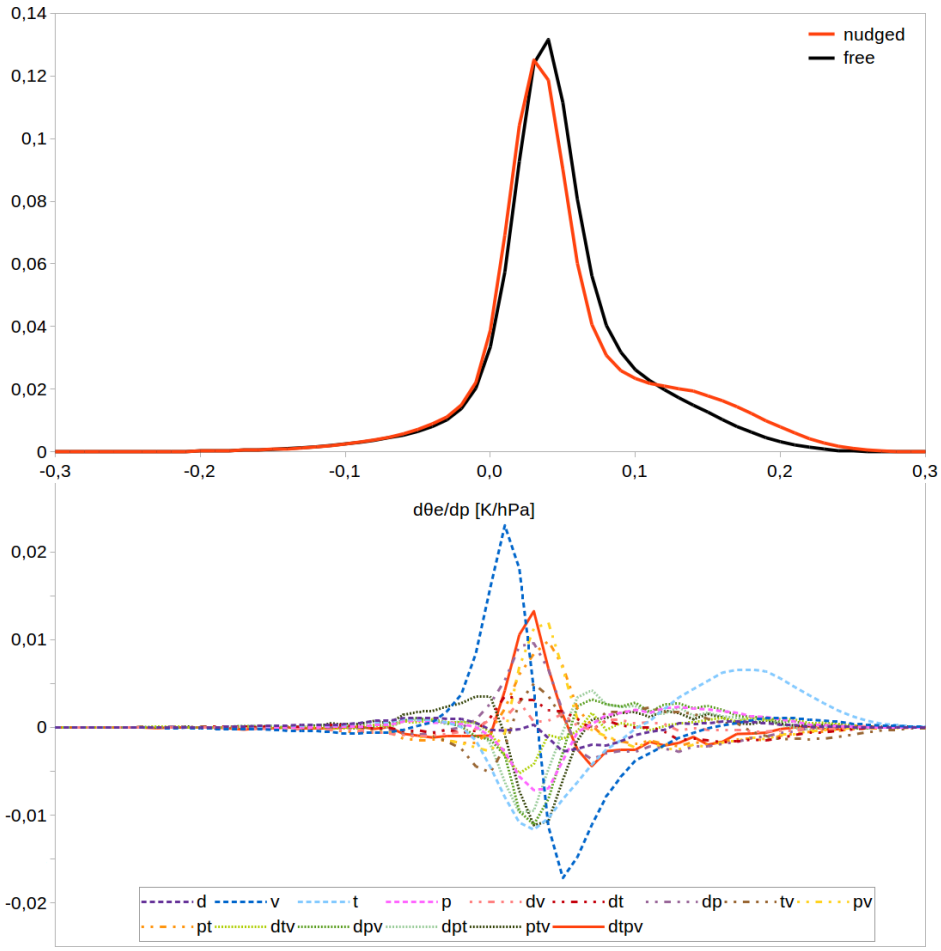

Figure G.17.: Impact of nudging on static stability over the Central Atlantic Ocean [$0°$-$10°$N; $50°$W-$30°$W] in the lower troposphere at 850 hPa: The upper curves show the frequency distribution of the vertical gradient of the equivalent potential temperature in terms of pressure from the entire region with respect to the simulated period of 9 years. The negative gradient indicates stable conditions whereas the positive gradient indicates conditional instabilities. The red line represents the fully-nudged scenario and the black line represents the free model scenario. The lower curves break down the isolated and interactive contributions to the nudging impact.

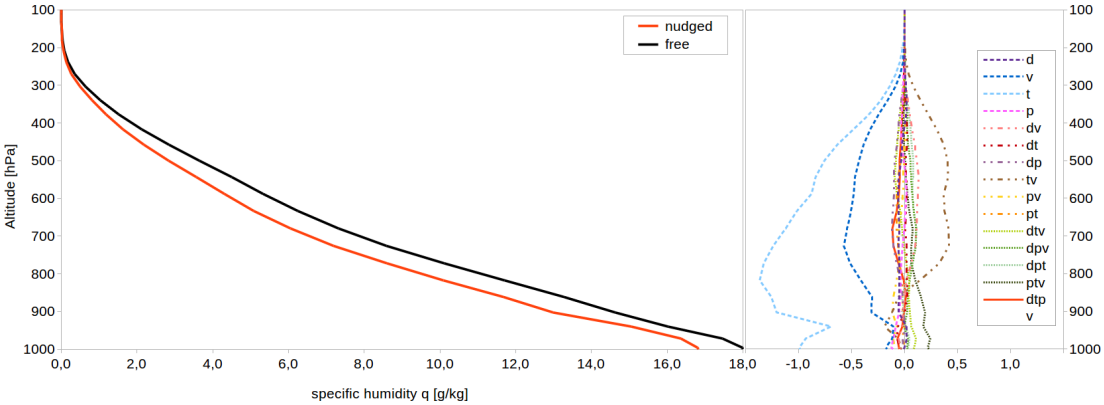

Figure G.18.: Impact of nudging on specific humidity over the Indo-Pacific Warm Pool [5°S-5°N; 140°E-160°E]: The left curves show the mean profile from the entire region with respect to the simulated period of 9 years. The red line represents the fully-nudged scenario and the black line represents the free model scenario. The right curves break down the isolated and interactive contributions to the nudging impact.

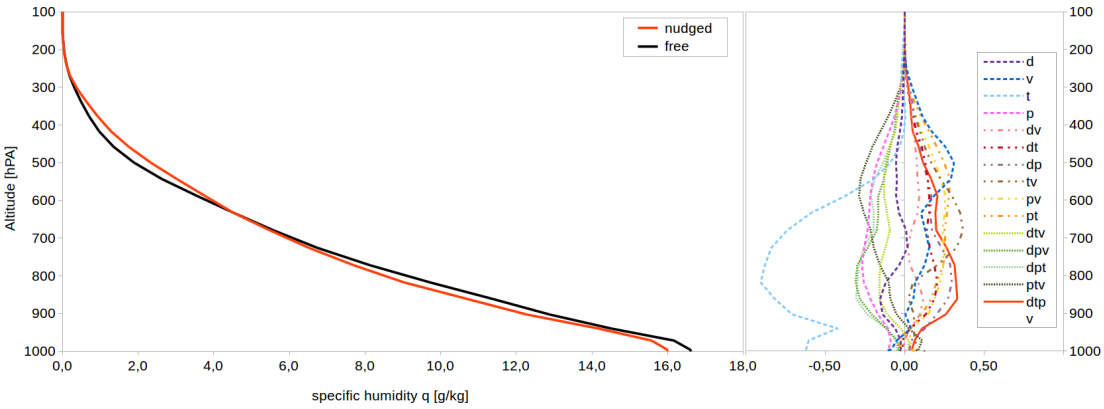

Figure G.19.: Impact of nudging on specific humidity over the Central Atlantic Ocean [0°-10°N; 50°W-30°W]: The left curves show the mean profile from the entire region with respect to the simulated period of 9 years. The red line represents the fully-nudged scenario and the black line represents the free model scenario. The right curves break down the isolated and interactive contributions to the nudging impact.

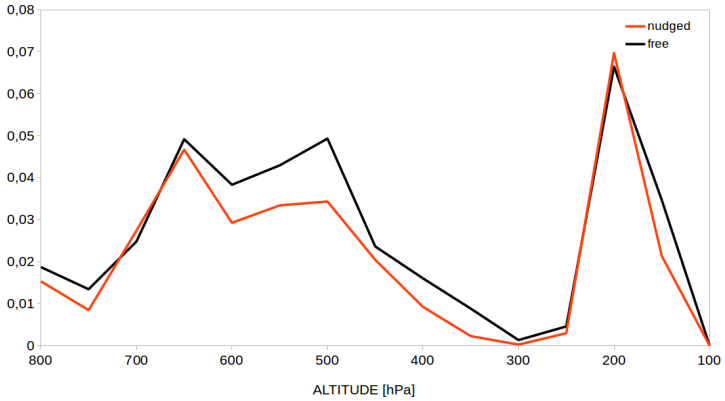

Figure G.20.: Impact of nudging on convection top height over the Indo-Pacific Warm Pool [$5°$S-$5°$N; $140°$E-$160°$E]: The curves show the frequency distributions of the convection top height from the entire region with respect to the simulated period of 9 years. The red line represents the fully-nudged scenario and the black line represents the free model scenario.

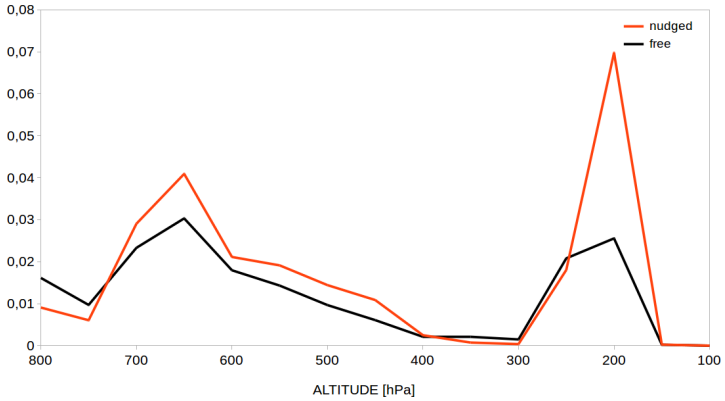

Figure G.21.: Impact of nudging on convection top height over the Central Atlantic Ocean [$0°$-$10°$N; $50°$W-$30°$W]: The curves show the frequency distributions of the convection top height from the entire region with respect to the simulated period of 9 years. The red line represents the fully-nudged scenario and the black line represents the free model scenario.

List of Figures

List of Tables

Bibliography

[1] Christopher R. Scotese and W. S. McKerrow. "Revised World maps and introduction". In: *Palaeozoic Palaeogeography and Biogeography*. Ed. by W. S. McKerrow and Christopher R. Scotese. Memoirs. Vol. 12. 1. London: Geological Society of London, 1990, pp. 1–21. ISBN: 0435-4052. DOI: 10.1144/GSL.MEM.1990.012.01.01.

[2] Alfred M. Ziegler, Michael L. Hulver, and David B. Rowley. "Permian World Topography and climate". In: *Late Glacial and Postglacial Environmental Changes - Quaternary, Carboniferous - Permian, and Proterozoic*. Ed. by I. Peter Martini. New York: Oxford University Press, 1997, pp. 111–146.

[3] Alfred M. Ziegler, Mark T. Gibbs, and Michael L. Hulver. "A mini-atlas of oceanic water masses in the Permian period". In: *Proceedings of the Royal Society of Victoria* 110.1-2 (1998), pp. 323–343. ISSN: 00359211.

[4] Robert A. Berner and Zavareth Kothavala. "GEOCARB III: A revised model of atmospheric CO2 over Phanerozoic time". In: *American Journal of Science* 301.2 (2001), pp. 182–204.

[5] Dana L. Royer. "CO2-forced climate thresholds during the Phanerozoic". In: *Geochimica et Cosmochimica Acta* 70.23 SPEC. ISS. (2006), pp. 5665–5675. ISSN: 00167037. DOI: 10.1016/j.gca.2005.11.031.

[6] Dana L. Royer et al. "CO2 as a primary driver of Phanerozoic climate". In: *Geological Society of America Today* 14.9 (2004), pp. 4–10. DOI: 10.1130/1052-5173(2004)014<4.

[7] D.H. Erwin. "The End-Permian Mass Extinction". In: *The Permian of Northern Pangea, Vol. 1*. Ed. by P.A. Scholle. Berlin: Springer Verlag, 1995. Chap. 2, pp. 20–34.

[8] Jeffrey T. Kiehl and Christine A. Shields. "Climate simulation of the latest Permian: Implications for mass extinction". In: *Geology* 33.9 (2005), pp. 757–760. ISSN: 00917613. DOI: 10.1130/G21654.1.

[9] Secretariat of the World Meteorological Organization. *International Meteorological Vocabulary*. 2nd. Geneva: World Meteorological Organization, 1992, p. 636. ISBN: 92-63-02182-1.

[10] R. H. Simpson. "Simpson, 1978..pdf". In: *Monthly Weather Review* 106.1 (1978), pp. 124–130.

[11] David Bolton. "The Computation of Equivalent Potential Temperature". In: *Monthly Weather Review* 108.7 (July 1980), pp. 1046–1053. ISSN: 0027-0644. DOI: 10.1175/1520-0493(1980)108<1046:TCOEPT>2.0.CO;2.

[12] Thomas R. Worsley and R. Damian Nance. "Carbon redox and climate control through earth history: A speculative reconstruction". In: *Global and Planetary Change* 1.4 (1989), pp. 259–282. ISSN: 0921-8181. DOI: http://dx.doi.org/10.1016/0921-8181(89)90006-4.

[13] J.D. Walker and J.W. Geissman. *Geologic Time Scale*. Boulder, Colorado, 2009. DOI: 10.1130/2009.CTS004RC.

[14] Roderick Impey Murchison. "First sketch of the principal results of a second geological survey of Russia". In: *Philosophical Magazine* 19.3 (1841), pp. 417–422.

[15] S. G. Lucas, J. W. Schneider, and G. Cassinis. "Non-marine Permian biostratigraphy and biochronology: an introduction". In: *Geological Society, London, Special Publications* 265.1 (2006), pp. 1–14. ISSN: 0305-8719. DOI: 10.1144/GSL.SP.2006.265.01.01.

[16] J. C. Crowell. "The Ending of the Late Paleozoic Ice Age During the Permian Period". In: *The Permian of Northern Pangea, Vol. 1*. Ed. by P.A. Scholle. Berlin: Springer Verlag, 1995. Chap. 5, pp. 62–74.

[17] J. C. Crowell. "Ice Ages Recorded on Gondwanan Continents". In: *Transactions of The Geological Society of South Africa* 86.3 (1983), pp. 237–262.

[18] S. Sahney and M. J. Benton. "Recovery from the most profound mass extinction of all time". In: *Proceedings of the Royal Society B: Biological Sciences* 275.1636 (2008), pp. 759–765. ISSN: 0962-8452. DOI: 10.1098/rspb.2007.1370.

[19] David L. Kidder and Thomas R. Worsley. "Causes and consequences of extreme Permo-Triassic warming to globally equable climate and relation to the Permo-Triassic extinction and recovery". In: *Palaeogeography, Palaeoclimatology, Palaeoecology* 203.3-4 (2004), pp. 207–237. ISSN: 00310182. DOI: 10.1016/S0031-0182(03)00667-9.

[20] Yukio Isozaki. "Permo-Triassic Boundary Superanoxia and Stratified Superocean: Records from Lost Deep Sea". In: *Science* 276.5310 (1997), pp. 235–238. ISSN: 00368075. DOI: 10.1126/science.276.5310.235.

[21] Bärbel Hönisch et al. “The Geological Record of Ocean Acidification”. In: *Science* 335.6072 (2012), pp. 1058–1063. ISSN: 0036-8075. DOI: 10.1126/science.1208277.

[22] Roberta M. Hotinski et al. “Ocean stagnation and end-Permian anoxia”. In: *Geology* 29.1 (2001), pp. 7–10. ISSN: 00917613. DOI: 10.1130/0091-7613(2001)029<0007:OSAEPA>2.0.CO;2.

[23] A. Montenegro et al. “Climate simulations of the Permian-Triassic boundary: Ocean acidification and the extinction event”. In: *Paleoceanography* 26.3 (2011), pp. 1–19. ISSN: 08838305. DOI: 10.1029/2010PA002058.

[24] Benjamin A. Black et al. “Acid rain and ozone depletion from pulsed Siberian Traps magmatism”. In: *Geology* 42.1 (2013), pp. 67–70. DOI: 10.1130/G34875.1.

[25] Jean-Francois Lamarque et al. “Modeling the response to changes in tropospheric methane concentration; Application to the Permian-Triassic boundary”. In: *Paleoceanography* 21.3 (2006), pp. 1–15. ISSN: 08838305. DOI: 10.1029/2006PA001276.

[26] Peter McAllister Rees. “Land-plant diversity and the end-Permian mass extinction”. In: *Geology* 30.9 (2002), pp. 827–830. ISSN: 00917613. DOI: 10.1130/0091-7613(2002)030<0827:LPDATE>2.0.CO;2.

[27] A. M. E. Winguth et al. “Simulated warm polar currents during the middle Permian”. In: *Paleoceanography* 17.4 (2002), pp. 1–19. ISSN: 0883-8305. DOI: 10.1029/2001PA000646.

[28] G. M. Stampfli et al. “The formation of Pangea”. In: *Tectonophysics* 593 (2013), pp. 1–19. ISSN: 00401951. DOI: 10.1016/j.tecto.2013.02.037.

[29] R. P. Langford et al. *Permian Coal and Palaeogeography of Gondwana (BMR Record 1991/95)*. Palaeogeography 39. Canberra: Bureau of Mineral Resources, Geology and Geophysics, 1992, pp. 1–136.

[30] L. R. M. Cocks and T. H. Tosvik. “European geography in a global context from the Vendian to the end of the Palaeozoic”. In: *European Lithosphere Dynamics*. Ed. by D. G. Gee and R. A. Stephenson. Memoirs Vo. London: Geological Society of London, 2006, pp. 83–95. DOI: 10.1144/GSL.MEM.2006.032.01.05.

[31] Christopher R. Scotese and R. P. Langford. “Pangea and the Paleogeography of the Permian”. In: *The Permian of Northern Pangea, Vol. 1*. Ed. by P.A. Scholle. Berlin: Springer Verlag, 1995. Chap. 1, pp. 3–19.

[32] Christopher R. Scotese. “Development of the Circum-Pacific Panthallassic Ocean During the Early Paleozoic”. In: *Circum-Pacific Orogenic Belts and Evolution of the Pacific Ocean Basin*. American Geophysical Union, 2013, pp. 49–57. ISBN: 9781118669860. DOI: 10.1029/GD018p0049.

[33] R. D. Jr. Hatcher et al. “Alleghanian orogen”. In: *The Appalachian-Ouachita Orogen in the United States*. Ed. by R. D. Jr. Hatcher, W. A. Thomas, and G. W. Viele. Geological Society of America, 1989, pp. 233–318. ISBN: 0813752094, 9780813752099. DOI: 10.1130/DNAG-GNA-F2.233.

[34] W. C. Pitman and X. Golovchenko. “The effect of sea level changes on the morphology of mountain belts”. In: *Journal of Geophysical Research: Solid Earth* 96.B4 (1991), pp. 6879–6891. ISSN: 2156-2202. DOI: 10.1029/91JB00250.

[35] Keddy Yemane. “Contribution of Late Permian palaeogeography in maintaining a temperate climate in Gondwana”. In: *Nature* 361.6407 (Jan. 1993), pp. 51–54.

[36] John E. Kutzbach and Alfred M. Ziegler. “Simulation of Late Permian Climate and Biomes with an Atmosphere-Ocean Model: Comparisons with Observations”. In: *Philosophical Transactions of the Royal Society of London B: Biological Sciences* 341.1297 (Aug. 1993), pp. 327–340.

[37] Keddy Yemane, Christoph Siegenthaler, and Kerry Kelts. “Lacustrine environment during Lower Beaufort (Upper Permian) Karoo deposition in Northern Malawi”. In: *Palaeogeography, Palaeoclimatology, Palaeoecology* 70.1-3 (1989), pp. 165–178. ISSN: 00310182. DOI: 10.1016/0031-0182(89)90087-4.

[38] Alfred M. Ziegler et al. “Meszoic assembly of Asia: contraints from fossil floras, tectonics, and paleomagnetism.” In: *The Tectonic Evolution of Asia*. Ed. by A. Yin and M. Harrison. Cambridge: Cambridge University Press, 1996, pp. 371–400.

[39] Dana L. Royer, Robert A. Berner, and David J. Beerling. “Phanerozoic atmospheric CO2 change: Evaluating geochemical and paleobiological approaches”. In: *Earth-Science Reviews* 54.4 (2001), pp. 349–392. ISSN: 00128252. DOI: 10.1016/S0012-8252(00)00042-8.

[40] D. J. Lunt et al. “Warm climates of the past – a lesson for the future?” In: *Philosophical transactions. Series A, Mathematical, physical, and engineering sciences* 371.2001 (2013), pp. 1–13. ISSN: 1364-503X. DOI: 10.1098/rsta.2013.0146.

[41] IPCC. *Climate Change 2001: The Physical Science Basis*. Ed. by J. T. Houghton et al. Cambridge; NewYork: Cambridge University Press, 2001, p. 881. ISBN: 0521-80767-0.

[42] Thomas R. Worsley and David L. Kidder. “First-order coupling of paleogeography and CO2, with global surface temperature and its latitudinal contrast”. In: *Geology* 19.12 (1991), pp. 1161–1164. DOI: 10.1130/0091-7613(1991)019<1161:FOCOPA>2.3.CO;2.

[43] Thomas R. Worsley et al. “Phanerozoic CO2 levels and global temperatures inferred from changing paleogeography”. In: *Pangea; paleoclimate, tectonics, and sedimentation during accretion, zenith and breakup of a supercontinent*. Ed. by George D. Klein. Boulder, Colorado: Geological Society of America Special Paper 288, 1994, pp. 57–73.

[44] William T. Hyde et al. “Siberian glaciation as a constraint on Permo-Carb\-oni\-fer\-ous CO2 levels”. In: *Geology* 34.6 (2006), pp. 421–424. ISSN: 00917613. DOI: 10.1130/G22108.1.

[45] Claudia I. Mora, Steven G. Driese, and Paula G. Seager. "Carbon dioxide in the Paleozoic atmosphere: Evidence from carbon-isotope compositions of pedogenic carbonate". In: *Geology* 19.10 (1991), pp. 1017–1020. DOI: 10.1130/0091-7613(1991)019<1017:CDITPA>2.3.CO;2.

[46] Robert A. Berner. "Atmospheric carbon dioxide levels over phanerozoic time." In: *Science (New York, N.Y.)* 249.4975 (1990), pp. 1382–1386. ISSN: 0036-8075. DOI: 10.1126/science.249.4975.1382.

[47] Robert A. Berner. "A model for atmospheric CO2 over Phanerozoic time". In: *American Journal of Science* 291.4 (1991), pp. 339–376.

[48] Robert A. Berner. "GEOCARB II: A revised model of atmospheric CO2 over Phanerozoic time". In: *American Journal of Science* 294.1 (1994), pp. 56–91.

[49] Robert A. Berner. "Examination of hypotheses for the Permo-Triassic boundary extinction by carbon cycle modeling". In: *Proceedings of the National Academy of Sciences of the United States of America* 99.7 (2002), pp. 4172–4177. ISSN: 00278424. DOI: 10.1073/pnas.032095199.

[50] Robert A. Berner. "Drying, O2 and mass extinction". In: *Nature* 340.8 (1989), pp. 603–604.

[51] Robert A. Berner. "Modeling atmospheric O2 over Phanerozoic time". In: *Acta Geochimica et Cosmochimica* 65.5 (2001), pp. 685–694.

[52] Robert A. Berner and Donald E. Canfield. "A new model for atmospheric oxygen over Phanerozoic time". In: *American Journal of Science* 289.4 (1989), pp. 333–361. DOI: 10.2475/ajs.289.4.333.

[53] IPCC. *Climate Change 2007: The Physical Science Basis*. Ed. by S. Solomon et al. Cambridge; NewYork: Cambridge University Press, 2007, p. 996. ISBN: 978-0-521-88009-1.

[54] James Hansen and Makiko Sato. "Greenhouse gas growth rates." In: *Proceedings of the National Academy of Sciences of the United States of America* 101.46 (2004), pp. 16109–16114. ISSN: 0027-8424. DOI: 10.1073/pnas.0406982101.

[55] J. Hansen et al. "Climate change and trace gases". In: *Philosophical Transactions of the Royal Society A: Mathematical, Physical and Engineering Sciences* 365.1856 (2007), pp. 1925–1954. ISSN: 1364-503X. DOI: 10.1098/rsta.2007.2052.

[56] David J. Beerling et al. "Methane and the CH4-related greenhouse effect over the past 400 million years". In: *American Journal of Science* 309.2 (2009), pp. 97–113. ISSN: 00029599. DOI: 10.2475/02.2009.01.

[57] Martin Schwarzschild. *Structure and Evolution of the Stars*. New York, New Jersey: Princeton University Press, 1958. ISBN: 0883072475.

[58] Michael J Newman and Robert T Rood. "Implications of Solar Evolution for the Earth's Early Atmosphere". In: *Science*. New Series 198.4321 (Dec. 1977), pp. 1035–1037. ISSN: 00368075. DOI: 10.2307/1745351.

[59] A. S. Endal and S. Sofia. “Rotation in solar-type stars. I - Evolutionary models for the spin-down of the sun”. In: *The Astrophysical Journal* 243 (1981), pp. 625–640. DOI: 10.1086/158628.

[60] Thomas J. Crowley and Steven K. Baum. “Toward reconciliation of Late Ordovician (˜440 Ma) glaciation with very high CO2 levels”. In: *Journal of Geophysical Research* 96.D12 (1991), pp. 22597–22610. ISSN: 0148-0227. DOI: 10.1029/91JD02449.

[61] Thomas J. Crowley, Steven K. Baum, and William T. Hyde. “Climate model comparison of Gondwanan and Laurentide glaciations”. In: *Journal of Geophysical Research* 96.D5 (1991), pp. 9217–9226. ISSN: 0148-0227. DOI: 10.1029/91JD00530.

[62] Thomas J. Crowley. “Pangean climates”. In: *Pangea: Paleoclimate, Tectonics, and Sedimentation During Accretion, Zenith and Breakup of a Supercontinent*. Ed. by G. D. Klein. Boulder, Colorado: Geological Society of America Special Paper 288, 1994, pp. 25–39.

[63] George E. Williams. “Geological constraints on the Precambrian history of Earth’s rotation and the Moon’s orbit”. In: *Reviews of Geophysics* 38.1 (2000), pp. 37–59. ISSN: 8755-1209. DOI: 10.1029/1999RG900016.

[64] Giorgio Pannella. “Paleontological evidence on the Earth’s rotational history since early precambrian”. English. In: *Astrophysics and Space Science* 16.2 (1972), pp. 212–237. ISSN: 0004-640X. DOI: 10.1007/BF00642735.

[65] Victor Zemtsov. “Evolution of Rotation Structures in the Earth’s Geological History”. In: *New Frontiers in Tectonic Research - General Problems, Sedimentary Basins and Island Arcs*. Ed. by Evgenii Sharkov. InTech, 2011. Chap. 3, pp. 39–72. ISBN: 978-953-307-595-2. DOI: 10.5772/21305.

[66] Milutin Milanković. *Mathematische Klimalehre und astronomische Theorie der Klimaschwankungen*. Ed. by W. Köppen and R. Geiger. Handbuch der Klimatologie, Bd. 1: Allgemeine Klimalehre. Berlin: Gebrüder Borntraeger, 1930.

[67] Vivien Gornitz, ed. *Encyclopedia of Paleoclimatology and ancient environments*. Dordrecht: Springer Netherlands, 2009. ISBN: 978-1-4020-4551-6.

[68] R. Y. Anderson. “Enhanced climate variability in the tropics: a 200 000 yr annual record of monsoon variability from Pangea’s equator”. In: *Climate of the Past* 7.3 (2011), pp. 757–770. DOI: 10.5194/cp-7-757-2011.

[69] John E. Kutzbach. “Idealized Pangean climates: Sensitivity to orbital changes”. In: *Pangea: Paleoclimate, Tectonics, and Sedimentation During Accretion, Zenith and Breakup of a Supercontinent*. Ed. by G.D. Klein. Boulder, Colorado: Geological Society of America Special Paper 288, 1994, pp. 41–55. DOI: 10.1130/SPE288-p41.

[70] Thomas J. Crowley, Steven K. Baum, and William T. Hyde. “Milankovitch fluctuations on supercontinents”. In: *Geophysical Research Letters* 19.8 (1992), pp. 793–796. ISSN: 00948276. DOI: 10.1029/92GL00561.

[71] Ján Veizer et al. "87Sr/86Sr, δ13C and δ18O evolution of Phanerozoic seawater". In: *Chemical Geology* 161.1-3 (1999), pp. 59–88. ISSN: 00092541. DOI: 10.1016/S0009-2541(99)00081-9.

[72] Ján Veizer, Y. Godderis, and L. M. François. "Evidence for decoupling of atmospheric CO2 and global climate during the Phanerozoic eon." In: *Nature* 408.6813 (2000), pp. 698–701. ISSN: 0028-0836. DOI: 10.1038/35047044.

[73] Peter McAllister Rees et al. "Permian Phytogeographic Patterns and Climate Data/Model Comparisons". In: *The Journal of Geology* 110.1 (2002), pp. 1–31. DOI: 10.1163/_afco_asc_2291.

[74] Mark T. Gibbs et al. "Simulations of Permian Climate and Comparisons with Climate-Sensitive Sediments". In: *The Journal of Geology* 110.1 (2002), pp. 33–55. ISSN: 0022-1376. DOI: 10.1086/324204.

[75] J. T. Parrish. "Geologic Evidence of Permian Climate". In: *The Permian of Northern Pangea, Vol. 1.* Ed. by P. A. Scholle. Berlin: Springer Verlag, 1995. Chap. 4, pp. 53–61.

[76] Alfred M. Ziegler. "Phytogeographic patterns and continental configurations during the Permian Period". In: *Palaeozoic Palaeogeography and Biogeography.* Ed. by W. S. McKerrow and Christopher R. Scotese. London: Geological Society Memoir No. 12, 1990, pp. 363–379. ISBN: 0435-4052. DOI: 10.1144/GSL.MEM.1990.012.01.35.

[77] Peter McAllister Rees et al. "Permian climates: Evaluating model predictions using global paleobotanical data". In: *Geology* 27.10 (1999), pp. 891–894. ISSN: 00917613. DOI: 10.1130/0091-7613(1999)027<0891:PCEMPU>2.3.CO;2.

[78] J. Eder-Kovar and Z. Kvacek. "Towards vegetation mapping based on the fossil plant record". In: *Neogene Vegetation and Climate Reconstructions.* Ed. by J. Eder-Kovar. Prague: Acta Universitatis Carolinae, Geologica 46, 2003, pp. 7–13.

[79] Torsten Utescher, Volker Mosbrugger, and Abdul R. Ashraf. "Terrestrial Climate Evolution in Northwest Germany over the Last 25 Million Years". In: *Palaios* 15.5 (2000), pp. 430–449. ISSN: 08831351, 19385323. DOI: 10.2307/3515514.

[80] Heinrich Walter. *Vegetation of the earth and ecological systems of the geo-biosphere.* 3rd Edit. Heidelberg science library. Berlin: Springer-Verlag, 1985, pp. 1–318. ISBN: 9783540137481.

[81] William T. Hyde et al. "The Pangean ice age: studies with a coupled climate-ice sheet model". In: *Climate Dynamics* 15.9 (1999), pp. 619–629. ISSN: 0930-7575. DOI: 10.1007/s003820050305.

[82] Elizabeth M. Truswell. "Antarctica: a history of terrestrial vegetation". In: *The geology of Antarctica.* Ed. by R. J. Tingey. Oxford: Clarendon Press, 1991. Chap. 14, pp. 499–537. ISBN: 978-0198544678.

[83] Edith L. Taylor, Thomas N. Taylor, and N. Rubén Cúneo. "The Present Is Not the Key to the Past: A Polar Forest from the Permian of Antarctica". In: *Science* 257.5077 (1992), pp. 1675–1677. DOI: 10.1126/science.257.5077.1675.

[84] Eric J. Barron and P. J. Fawcett. "The Climate of Pangaea: A Review of Climate Model Simulations of the Permian". In: *The Permian of Northern Pangea, Vol. 1*. Ed. by P.A. Scholle. Berlin: Springer Verlag, 1995. Chap. 3, pp. 37–52.

[85] John E. Kutzbach and R. G. Gallimore. "Pangaean climates: Megamonsoons of the megacontinent". In: *Journal of Geophysical Research* 94.D3 (1989), pp. 3341–3357. ISSN: 0148-0227. DOI: 10.1029/JD094iD03p03341.

[86] John E. Kutzbach and P. J. Guetter. "Simulated circulation of an idealized ocean for Pangaean time". In: *Paleoceanography* 5.3 (1990), pp. 299–317. DOI: 10.1029/PA005i003p00299.

[87] F. Fluteau et al. "The late Permian climate. What can be inferred from climate modelling concerning Pangea scenarios and Hercynian range altitude?" In: *Palaeogeography, Palaeoclimatology, Palaeoecology* 167.1-2 (2001), pp. 39–71. ISSN: 00310182. DOI: 10.1016/S0031-0182(00)00230-3.

[88] Bette L. Otto-Bliesner and Garland R. Upchurch. "Vegetation-induced warming of high-latitude regions during the Late Cretaceous period". In: *Nature* 385.6619 (1997), pp. 804–807. DOI: 10.1038/385804a0.

[89] Marco Roscher, Frode Stordal, and Henrik Svensen. "The effect of global warming and global cooling on the distribution of the latest Permian climate zones". In: *Palaeogeography, Palaeoclimatology, Palaeoecology* 309.3-4 (2011), pp. 186–200. ISSN: 00310182. DOI: 10.1016/j.palaeo.2011.05.042.

[90] Starley L. Thompson and David Pollard. "Greenland and Antarctic Mass Balances for Present and Doubled Atmospheric CO2 from the GENESIS Version-2 Global Climate Model". In: *Journal of Climate* 10.5 (1997), pp. 871–900. ISSN: 08948755. DOI: 10.1175/1520-0442(1997)010<0871:GAAMBF>2.0.CO;2.

[91] G. R. North, J. G. Mengel, and D. A. Short. "Simple energy balance model resolving the seasons and the continents: Application to the astronomical theory of the ice ages". In: *Journal of Geophysical Research* 88.C11 (1983), pp. 6576–6586. ISSN: 0148-0227. DOI: 10.1029/JC088iC11p06576.

[92] U. Mikolajewicz. *A meltwater induced collapse of the "conveyor belt" thermohaline circulation and its influence on the distribution of Delta14C and delta18O in the oceans*. MPI Report 189. Hamburg: Max-Planck-Institut for Meteorology, 1996.

[93] William D. Collins et al. "The Community Climate System Model Version 3 (CCSM3)". In: *Journal of Climate* 19.11 (2006), pp. 2122–2143. ISSN: 0894-8755. DOI: 10.1175/JCLI3761.1.

[94] Patrick Jöckel et al. "Technical Note: The Modular Earth Submodel System (MESSy) – a new approach towards Earth System Modeling". In: *Atmospheric Chemistry and Physics* 5 (2005), pp. 433–444. DOI: 10.5194/acp-5-445-2005.

[95] Erich Roeckner et al. *The atmospheric general circulation model ECHAM5: Part 1: Model description*. MPI Report No. 349. Hamburg: Max-Planck-Institut for Meteorology, 2003, pp. 1–140.

[96] Patrick Jöckel et al. "The atmospheric chemistry general circulation model ECHAM5/MESSy1: consistent simulation of ozone from the surface to the mesosphere". In: *Atmospheric Chemistry and Physics Discussions* 6.4 (2006), pp. 6957–7050. ISSN: 1680-7375. DOI: 10.5194/acpd-6-6957-2006.

[97] S. J. Marsland et al. "The Max-Planck-Institute global ocean / sea ice model with orthogonal curvilinear coordinates". In: *Ocean Modelling* 5.2 (2003), pp. 91–127. ISSN: 1463-5003.

[98] Andrea Pozzer et al. "The Atmosphere-Ocean General Circulation Model EMAC-MPIOM". In: *Geoscientific Model Development* 4.3 (2011), pp. 771–784. ISSN: 1991-9603. DOI: 10.5194/gmd-4-771-2011.

[99] S. Sitch, B. Smith, and I. C. Prentice. "Evaluation of ecosystem dynamics, plant geography and terrestrial carbon cycling in the LPJ dynamic global vegetation model". In: *Global Change Biology* 9 (2003), pp. 161–185.

[100] Patrick Jöckel et al. "Development cycle 2 of the Modular Earth Submodel System (MESSy2)". In: *Geoscientific Model Development* 3.2 (2010), pp. 717–752. ISSN: 1991959X. DOI: 10.5194/gmd-3-717-2010.

[101] André Robert, John Henderson, and Colin Turnbull. "An Implicit Time Integration Scheme for Baroclinic Models of the Atmosphere". In: *Monthly Weather Review* 100.5 (1972), pp. 329–335. ISSN: 0027-0644. DOI: 10.1175/1520-0493(1972)100<0329:AITISF>2.3.CO;2.

[102] André Robert. "A stable numerical integration scheme for the primitive meteorological equations". In: *Atmosphere-Ocean* 19.1 (1981), pp. 35–46. ISSN: 0705-5900. DOI: 10.1080/07055900.1981.9649098.

[103] André Robert. "A Semi-Lagrangian and Semi-Implicit Numerical Integration Scheme for the Primitive Meteorological Equations". In: *Journal of the Meteorological Society of Japan. Ser. II* 60.1 (1982), pp. 319–325.

[104] Richard Asselin. "Frequency Filter for Time Integrations". In: *Monthly Weather Review* 100.6 (1972), pp. 487–490. ISSN: 0027-0644.

[105] S.-J. Lin and R. B. Rood. "Multidimensional Flux-Form Semi-Lagrangian Transport Schemes". In: *Monthly Weather Review* 124 (1996), pp. 2046–2070. ISSN: 0027-0644. DOI: 10.1175/1520-0493(1996)124<2046:MFFSLT>2.0.CO;2.

[106] Patrick Wetzel et al. *The Max-Planck-Institute Global Ocean/Sea-Ice Model MPI-OM*. Technical Report. Hamburg: Max-Planck-Institute for Meteorology, 2008, pp. 1–84.

[107] Jörg-Olaf Wolff, Ernst Maier-Reimer, and Stephanie Legutke. *The Hamburg Ocean Primitive Equation Model (HOPE)*. Technical Report No. 13. Hamburg: German Climate Computer Center (DKRZ), 1997, pp. 1–98.

[108] Akio Arakawa and Vivian R. Lamb. *General Circulation Models of the Atmosphere*. Vol. 17. Methods in Computational Physics: Advances in Research and Applications. New York: Elsevier, 1977, pp. 173–265. ISBN: 9780124608177. DOI: 10.1016/B978-0-12-460817-7.50009-4.

[109] A. Beckmann and R. Döscher. "A Method for Improved Representation of Dense Water Spreading over Topography in Geopotential-Coordinate Models". In: *Journal of Physical Oceanography* 27.4 (1997), pp. 581–591. ISSN: 0022-3670. DOI: 10.1175/1520-0485(1997)027<0581:AMFIRO>2.0.CO;2.

[110] Martha H. Redi. "Oceanic Isopycnal Mixing by Coordinate Rotation". In: *Journal of Physical Oceanography* 12.10 (1982), pp. 1154–1158. ISSN: 0022-3670. DOI: 10.1175/1520-0485(1982)012<1154:OIMBCR>2.0.CO;2.

[111] Stephen M. Griffies. "The Gent-McWilliams Skew Flux". In: *Journal of Physical Oceanography* 28.5 (1998), pp. 831–841. ISSN: 0022-3670. DOI: 10.1175/1520-0485(1998)028<0831:TGMSF>2.0.CO;2.

[112] Peter R. Gent et al. "Parameterizing eddy-induced tracer transports in ocean circulation models". In: *Journal of Physical Oceanography* 25 (1995), pp. 463–474.

[113] R. C. Pacanowski and S. G. H. Philander. "Parameterization of Vertical Mixing in Numerical Models of Tropical Oceans". In: *Journal of Physical Oceanographygraphy* 11.11 (1981), pp. 1443–1451. ISSN: 0022-3670. DOI: 10.1175/1520-0485(1981)011<1443:POVMIN>2.0.CO;2.

[114] W. D. Hibler. "A Dynamic Thermodynamic Sea Ice Model". In: *Journal of Physical Oceanography* 9.4 (1979), pp. 815–846. ISSN: 0022-3670. DOI: 10.1175/1520-0485(1979)009<0815:ADTSIM>2.0.CO;2.

[115] Patrick Jöckel et al. "Technical note: Coupling of chemical processes with the modular earth submodel system (MESSy) submodel TRACER". In: *Atmospheric Chemistry and Physics* 8.6 (2008), pp. 1677–1687. ISSN: 1680-7316. DOI: 10.5194/acp-8-1677-2008.

[116] Erich Roeckner et al. "Sensitivity of simulated climate to horizontal and vertical resolution in the ECHAM5 atmosphere model". In: *Journal of Climate* 19.16 (2006), pp. 3771–3791. ISSN: 08948755. DOI: 10.1175/JCLI3824.1.

[117] Holger Tost, Patrick Jöckel, and Jos Lelieveld. "Influence of different convection parameterisations in a GCM". In: *Atmospheric Chemistry and Physics* 6.12 (2006), pp. 5475–5493. ISSN: 1680-7375. DOI: 10.5194/acp-6-5475-2006.

[118] Holger Tost. "Global Modelling of Cloud, Convection and Precipitation Influences on Trace Gases and Aerosols". PhD thesis. Rheinische Friedrich-Wilhelms-Universität Bonn, 2006, pp. 1–198.

[119] Stefan Hagemann and Lydia Dümenil. "A parametrization of the lateral waterflow for the global scale". In: *Climate Dynamics* 14.1 (1998), pp. 17–31. ISSN: 0930-7575. DOI: 10.1007/s003820050205.

[120] Holger Tost and Matthew Forest. "Coupling LPJ-GUESS to EMAC (in Prep.)" 2016.

[121] Hilding Sundqvist. "A parameterization scheme for non-convective condensation including prediction of cloud water content". In: *Quarterly Journal of the Royal Meteorological Society* 104.441 (July 1978), pp. 677–690. ISSN: 00359009. DOI: 10.1002/qj.49710444110.

[122] Adrian M. Tompkins. "A Prognostic Parameterization for the Subgrid-Scale Variability of Water Vapor and Clouds in Large-Scale Models and Its Use to Diagnose Cloud Cover". In: *Journal of the Atmospheric Sciences* 59.12 (2002), pp. 1917–1942. ISSN: 0022-4928. DOI: 10.1175/1520-0469(2002)059<1917:APPFTS>2.0.CO;2.

[123] Erich Roeckner et al. *The atmospheric general circulation model ECHAM-4: Model description and simulation of present-day climate*. MPI Report No. 218. Hamburg: Max-Planck-Institute for Meteorology, 1996, pp. 1–171.

[124] Mark G. Lawrence and Philip J. Rasch. "Tracer Transport in Deep Convective Updrafts : Plume Ensemble versus". In: *Journal of the Atmospheric Sciences* 62.1982 (2005), pp. 2880–2894. ISSN: 0022-4928. DOI: 10.1175/JAS3505.1.

[125] Stefan Hagemann and Lydia Dümenil. *Documentation for the Hydrological Discharge Model*. Technical Report. No. 17. Hamburg: Max Planck Institute for Meteorology, 1998, pp. 1–42.

[126] Stefan Hagemann and Lydia Dümenil Gates. "Validation of the hydrological cycle of ECMWF and NCEP reanalyses using the MPI hydrological discharge model". In: *Journal of Geophysical Research* 106.D2 (2001), pp. 1503–1510. ISSN: 0148-0227. DOI: 10.1029/2000JD900568.

[127] Y. Fouquart and B. Bonnel. "Computations of solar heating of the Earth's atmosphere: A new parameterization". In: *Beiträge zur Physik der Atmosphäre* 53 (1980), pp. 35–62.

[128] Eli J. Mlawer et al. "Radiative transfer for inhomogeneous atmospheres: RRTM, a validated correlated-k model for the longwave". In: *Journal of Geophysical Research* 102.D14 (1997), pp. 16663–16682. ISSN: 0148-0227. DOI: 10.1029/97JD00237.

[129] M. Tiedtke. "A Comprehensive Mass Flux Scheme for Cumulus Parameterization in Large-Scale Models". In: *Monthly Weather Review* 117.8 (1989), pp. 1779–1800. ISSN: 0027-0644. DOI: 10.1175/1520-0493(1989)117<1779:ACMFSF>2.0.CO;2.

[130] G. J. Zhang and N. A. McFarlane. "Sensitivity of climate simulations to the parameterization of cumulus convection in the Canadian climate centre general circulation model". In: *Atmosphere-Ocean* 33.3 (Sept. 1995), pp. 407–446. DOI: 10.1080/07055900.1995.9649539.

[131] James J. Hack. "Parameterization of moist convection in the National Center for Atmospheric Research community climate model (CCM2)". In: *Journal of Geophysical Research* 99.D3 (1994), pp. 5551–5568. ISSN: 0148-0227. DOI: 10.1029/93JD03478.

[132] T E. Nordeng. *Extended versions of the convective parametrization scheme at ECMWF and their impact on the mean and transient activity of the model in the tropics*. Technical Memorandum No. 206. Reading: European Centre for Medium-Range Weather Forecasts, 1994, pp. 1–41.

[133] U.S. Navy Fleet Numerical Meteorology and Oceanography Center U. S. Department of Defense. *U.S. Navy 10-Minute Global Elevation and Geographic Characteristics*. Boulder, CO, 1980.

[134] J. C. Eidenshink and J. L. Faundeen. "The 1-km AVHRR global land dataset: first stages in implementation". In: *International Journal of Remote Sensing* 15.17 (1994). ISSN: 3443-3462.

[135] U.S. Geological Survey. *Global land cover characteristics data base*. 1997.

[136] Jerry S. Olson. *Global Ecosystem Framework 1. Definitions*. USGS EROS Data Center Internal Report 1. Sioux Falls, SD, 1994, pp. 1–37.

[137] Jerry S. Olson. *Global Ecosystem Framework 2. Translation Strategy*. USGS EROS Data Center Internal Report 2. Sioux Falls, SD, 1994, pp. 1–39.

[138] Stefan Hagemann et al. *Derivation of global GCM boundary conditions from 1km land use satellite data*. MPI Report No. 289. Hamburg: Max-Planck-Institute for Meteorology, 1999, pp. 1–34.

[139] Stefan Hagemann. *An Improved Land Surface Parameter Dataset for Global and Regional Climate Models*. MPI Report No. 336. Hamburg: Max-Planck-Institute for Meteorology, 2002, pp. 1–21.

[140] Martin Claussen et al. *A Global Data Set of Land-Surface Parameters*. MPI Report No. 135. Hamburg: Max-Planck-Institute for Meteorology, 1994, pp. 1–30.

[141] L. Zobler. *A world soil file for global climate modeling*. National Aeronautics and Space Administration Technical Memorandum 87802. Washington D.C., 1986.

[142] W. Lawrence Gates. "AMIP: The Atmospheric Model Intercomparison Project". In: *Bulletin of the American Meteorological Society* 73.12 (1992), pp. 1962–1970. ISSN: 0003-0007.

[143] François Lott and M. J. Miller. "A new subgrid-scale orographic drag parametrization: Its formulation and testing". In: *Quarterly Journal of the Royal Meteorological Society* 123.537 (1997), pp. 101–127. ISSN: 1477870X. DOI: 10.1002/qj.49712353704.

[144] François Lott. "Alleviation of Stationary Biases in a GCM through a Mountain Drag Parameterization Scheme and a Simple Representation of Mountain Lift Forces". In: *Monthly Weather Review* 127.5 (1999), pp. 788–801. ISSN: 0027-0644. DOI: 10.1175/1520-0493(1999)127<0788:AOSBIA>2.0.CO;2.

[145] P. G. Baines and T. N. Palmer. *Rationale for a new physically based parametrization of subgrid-scale orographic effects*. Technical Memorandum No. 169. Reading: European Centre for Medium-Range Weather Forecasts, 1990, pp. 1–11.

[146] K. Oleson et al. *Technical Description of the Community Land Model (CLM)*. NCAR Technical Note 461. Boulder, Colorado: Terrestrial Sciences Section, Climate and Global Dynamics Division, National Center for Atmospheric Research, 2004, pp. 1–174. DOI: 10.5065/D6N877R0.

[147] Diana Rechid, Thomas J. Raddatz, and Daniela Jacob. "Parameterization of snow-free land surface albedo as a function of vegetation phenology based on MODIS data and applied in climate modelling". In: *Theoretical and Applied Climatology* 95.3-4 (2009), pp. 245–255. ISSN: 0177798X. DOI: 10.1007/s00704-008-0003-y.

[148] Stefano Tibaldi and J.-F. Geleyn. *The production of a new orography, land sea mask and associated climatological surface fields for operational purpose*. Technical Memorandum No. 40. Reading: European Centre for Medium-Range Weather Forecasts, 1981, pp. 1–73.

[149] Gordon B. Bonan. "Landscapes as patches of plant functional types: An integrating concept for climate and ecosystem models". In: *Global Biogeochemical Cycles* 16.2 (2002), pp. 5.1–5.18. ISSN: 0886-6236. DOI: 10.1029/2000GB001360.

[150] Lydia Dümenil and E. Todini. "A rainfall-runoff scheme for use in the Hamburg climate model". In: *Advances in Theoretical Hydrology - A Tribute to James Dooge*. Ed. by J. P. O'Kane. Elsevier Science Ltd, 1992. Chap. 9, pp. 129–157. ISBN: 978-0444898319. DOI: 10.1016/B978-0-444-89831-9.50016-8.

[151] D. J. Houlbrooke and S. Laurenson. "Effect of sheep and cattle treading damage on soil microporosity and soil water holding capacity". In: *Agricultural Water Management* 121 (2013), pp. 81–84. ISSN: 03783774. DOI: 10.1016/j.agwat.2013.01.010.

[152] Soil Classification Working Group. *The Canadian system of Soil classification*. Agriculture and Agri-Food Canada Publication (Revised) 1646. 1998, pp. 1–158.

[153] Pankaj Kumar et al. "Impact of modified soil thermal characteristic on the simulated monsoon climate over south Asia". In: *Journal of Earth System Science* 123.1 (2014), pp. 151–160. ISSN: 02534126. DOI: 10.1007/s12040-013-0381-0.

[154] Bjorn Stevens et al. "Atmospheric component of the MPI-M Earth System Model: ECHAM6". In: *Journal of Advances in Modeling Earth Systems* 5.2 (June 2013), pp. 146–172. ISSN: 19422466. DOI: 10.1002/jame.20015.

[155] Bastian Kern. "Chemical interaction between ocean and atmosphere". PhD thesis. Johannes Gutenberg-Universität Mainz, 2013, pp. 1–257.

[156] Z. Liu et al. "Modeling long-term climate changes with equilibrium asynchronous coupling". In: *Climate Dynamics* 15.5 (1999), pp. 325–340. ISSN: 09307575. DOI: 10.1007/s003820050285.

[157] Hugues Goosse et al. "Modelling past sea ice changes". In: *Quaternary Science Reviews* 79 (2013), pp. 191–206. ISSN: 02773791. DOI: 10.1016/j.quascirev.2013.03.011.

[158] Anne De Vernal et al. "Sea ice in the paleoclimate system: The challenge of reconstructing sea ice from proxies - an introduction". In: *Quaternary Science Reviews* 79 (2013), pp. 1–8. ISSN: 02773791. DOI: 10.1016/j.quascirev.2013.08.009.

[159] Patrick Jöckel et al. "Earth System Chemistry Integrated Modelling (ESCiMo) with the Modular Earth Submodel System (MESSy, version 2.51)". In: *Geoscientific Model Development Discussions* 8.10 (2015), pp. 8635–8750. ISSN: 1991-962X. DOI: 10.5194/gmdd-8-8635-2015.

[160] Xiaoxiao Zhang, Hailong Liu, and Minghua Zhang. "Double ITCZ in Coupled Ocean-Atmosphere Models: From CMIP3 to CMIP5". In: *Geophysical Research Letters* 42.20 (2015), pp. 8651–8659. ISSN: 19448007. DOI: 10.1002/2015GL065973.

[161] F. I. Woodward, M. R. Lomas, and R. A. Betts. "Vegetation-climate feedbacks in a greenhouse world". In: *Philosophical Transactions of the Royal Society B: Biological Sciences* 353.1365 (1998), pp. 29–39. ISSN: 0962-8436. DOI: 10.1098/rstb.1998.0188.

[162] Alfred Wegener. *Die Entstehung der Kontinente und Ozeane*. Braunschweig: Friedrich Vieweg & Sohn Akt. Ges., 1922, pp. 18–22. ISBN: 3-443-01056.

[163] E Irving. "Drift of the continental blocks since the Devonian". In: *Nature* 270 (1977), pp. 304–309. ISSN: 00280836. DOI: doi:10.1038/270304a0.

[164] Marco Roscher and Joerg W. Schneider. "Permo-Carboniferous climate: Early Pennsylvanian to Late Permian climate development of central Europe in a regional and global context". In: *Nonmarine Permian chronology and correlation*. Ed. by S. G. Lucas, G. Cassinis, and Joerg W. Schneider. Special Pu. Vol. 265. London: Geological Society of London, 2006, pp. 95–136. ISBN: 0305-8719/06.

[165] Christophe Sturm, Georg Hoffmann, and Bärbel Langmann. "Simulation of the stable water isotopes in precipitation over South America: Comparing regional to global circulation models". In: *Journal of Climate* 20.15 (2007), pp. 3730–3750. ISSN: 08948755. DOI: 10.1175/JCLI4194.1.

[166] Maisa Rojas and Anji Seth. "Simulation and sensitivity in a nested modeling system for South America. Part II: GCM boundary forcing". In: *Journal of Climate* 16.15 (2003), pp. 2454–2471. ISSN: 08948755. DOI: 10.1175/1520-0442(2003)016<2454:SASIAN>2.0.CO;2.

[167] Maura Brunetti, Christian Vérard, and Peter O. Baumgartner. "Modelling the Middle Jurassic ocean circulation". In: *Journal of Palaeogeography* 4 (2015). ISSN: 20953836. DOI: 10.1016/j.jop.2015.09.001.

[168] C. Brühl et al. “The role of carbonyl sulphide as a source of stratospheric sulphate aerosol and its impact on climate”. In: *Atmospheric Chemistry and Physics* 12.3 (2012), pp. 1239–1253. ISSN: 16807316. DOI: 10.5194/acp-12-1239-2012.

[169] R. A. Muller and G. J. MacDonald. “Spectrum of 100-kyr glacial cycle: orbital inclination, not eccentricity.” In: *Proceedings of the National Academy of Sciences of the United States of America* 94.16 (1997), pp. 8329–8334. ISSN: 00278424. DOI: 10.1073/pnas.94.16.8329.

[170] Kenneth A. Farley. “Cenozoic variations in the flux of interplanetary dust recorded by 3He in a deep-sea sediment”. In: *Nature* 376 (1995), pp. 153–156. ISSN: 0028-0836. DOI: 10.1038/376153a0.

[171] P. Rampal et al. “IPCC climate models do not capture Arctic sea ice drift acceleration: Consequences in terms of projected sea ice thinning and decline”. In: *Journal of Geophysical Research: Oceans* 116.9 (2011), pp. 1–17. ISSN: 21699291. DOI: 10.1029/2011JC007110.

[172] Nikolay V. Koldunov, Detlef Stammer, and Jochem Marotzke. “Present-day arctic sea ice variability in the coupled ECHAM5/MPI-OM model”. In: *Journal of Climate* 23.10 (2010), pp. 2520–2543. ISSN: 08948755. DOI: 10.1175/2009JCLI3065.1.

[173] Michael Hübner. “Evaluation of Sea-ice in the Max Planck Institute Earth System Model”. Bachelor thesis. Ludwig-Maximilians-Universität München, 2013, pp. 1–34.

[174] J. H. Jungclaus et al. “Characteristics of the ocean simulations in the Max Planck Institute Ocean Model (MPIOM) the ocean component of the MPI-Earth system model”. In: *Journal of Advances in Modeling Earth Systems* 5.2 (2013), pp. 422–446. ISSN: 19422466. DOI: 10.1002/jame.20023.

[175] Michael Ghil and Paola Malanotte-Rizzoli. *Data Assimilation in Meteorology and Oceanography*. Tech. rep. Cambridge, Massachusetts, United States: Department of Earth Atmospheric and Planetary Sciences, Massachusetts Institute of Technology, 1991, pp. 141–266. DOI: DOI:10.1016/S0065-2687(08)60442-2.

[176] Rebecca A. Woodgate and Peter D. Killworth. “The Effects of Assimilation on the Physics of an Ocean Model. Part I: Theoretical Model and Barotropic Results”. In: *Journal of Atmospheric and Oceanic Technology* 14.4 (Aug. 1997), pp. 897–909. ISSN: 0739-0572. DOI: 10.1175/1520-0426(1997)014<0897:TEOAOT>2.0.CO;2.

[177] A. B. M. Jeuken et al. “On the potential of assimilating meteorological analyses in a global climate model for the purpose of model validation”. In: *Journal of Geophysical Research: Atmospheres* 101.D12 (1996), pp. 16939–16950. ISSN: 2156-2202. DOI: 10.1029/96JD01218.

[178] U. Stein and P. Alpert. “Factor Separation in Numerical Simulations”. In: *Journal of the Atmospheric Sciences* 50.14 (1993), pp. 2107–2115. ISSN: 0022-4928. DOI: 10.1175/1520-0469(1993)050<2107:FSINS>2.0.CO;2.

[179] R. Jastrow and M. Halem. "Simulation Studies and Design of First Garp Global Experiment". In: *Bulletin of the American Meteorological Society* 54.1 (1973), pp. 13–21.

[180] Lennart Bengtsson. "4-Dimensional Assimilation Of Meteorological Observations". In: *GARP Publications Series* 15.WMO/ICSU (1975), pp. 1–76.

[181] Dewey E. Harms, Sethu Raman, and Rangarao V. Madala. "An Examination of Four-Dimensional Data-Assimilation Techniques for Numerical Weather Prediction". In: *Bulletin of the American Meteorological Society* 73.4 (1992), pp. 425–440. DOI: 10.1175/1520-0477(1992)073<0425:AEOFDD>2.0.CO;2.

[182] François-Xavier Le Dimet and Olivier Talagrand. "Variational algorithms for analysis and assimilation of meteorological observations: theoretical aspects". In: *Tellus A* 38A.2 (Mar. 1986), pp. 97–110. ISSN: 02806495. DOI: 10.1111/j.1600-0870.1986.tb00459.x.

[183] William Carlisle Thacker and Robert Bryan Long. "Fitting dynamics to data". In: *Journal of Geophysical Research* 93.C2 (Feb. 1988), pp. 1227–1240. ISSN: 0148-0227. DOI: 10.1029/JC093iC02p01227.

[184] R. E. Kalman. "A New Approach to Linear Filtering and Prediction Problems". In: *Transactions of the ASME - Journal of Basic Engineering* 82.1 (1960), pp. 35–45. ISSN: 00219223. DOI: 10.1115/1.3662552.

[185] R. E. Kalman and R. S. Bucy. "New Results in Linear Filtering and Prediction Theory". In: *Journal of Basic Engineering* 83.1 (1961), p. 95. ISSN: 00219223. DOI: 10.1115/1.3658902.

[186] Geir Evensen. "Sequential data assimilation with a nonlinear quasi-geostrophic model using Monte Carlo methods to forecast error statistics". In: *Journal of Geophysical Research* 99.C5 (May 1994), pp. 10143–10162. ISSN: 0148-0227. DOI: 10.1029/94JC00572.

[187] Geir Evensen. "The Ensemble Kalman Filter: Theoretical formulation and practical implementation". In: *Ocean Dynamics* 53.4 (2003), pp. 343–367. ISSN: 16167341. DOI: 10.1007/s10236-003-0036-9.

[188] P. L. Houtekamer and Fuqing Zhang. "Review of the Ensemble Kalman Filter for Atmospheric Data Assimilation". In: *Monthly Weather Review* 144.12 (2016), pp. 4489–4532. ISSN: 0027-0644. DOI: 10.1175/MWR-D-15-0440.1.

[189] P. L. Houtekamer et al. "Data Assimilation Using an Ensemble Kalman Filter Technique". In: *Monthly Weather Review* 126.3 (1998), pp. 796–811. ISSN: 0027-0644. DOI: 10.1175/1520-0493(1998)126<0796:DAUAEK>2.0.CO;2.

[190] G. A. Gottwald. "Controlling balance in an ensemble Kalman filter". In: *Nonlinear Processes in Geophysics* 21.2 (2014), pp. 417–426. ISSN: 16077946. DOI: 10.5194/npg-21-417-2014.

[191] Lili Lei and Jeffrey S. Whitaker. "A Four-Dimensional Incremental Analysis Update for the Ensemble Kalman Filter". In: *Monthly Weather Review* 144.7 (2016), pp. 2605–2621. ISSN: 0027-0644. DOI: 10.1175/MWR-D-15-0246.1.

[192] Richard A. Anthes. "Data Assimilation and Initialization of Hurricane Prediction Models". In: *Journal of the Atmospheric Sciences* 31.3 (Apr. 1974), pp. 702–719. ISSN: 0022-4928. DOI: 10.1175/1520-0469(1974)031<0702:DAAIOH>2.0.CO;2.

[193] James E. Hoke and Richard A. Anthes. "The Initialization of Numerical Models by a Dynamic-Initialization Technique". In: *Monthly Weather Review* 104.12 (Dec. 1976), pp. 1551–1556. ISSN: 0027-0644. DOI: 10.1175/1520-0493(1976)104<1551:TIONMB>2.0.CO;2.

[194] Didier Auroux and Jacques Blum. "Back and forth nudging algorithm for data assimilation problems". In: *Comptes Rendus Mathematique* 340.12 (2005), pp. 873–878. ISSN: 1631073X. DOI: 10.1016/j.crma.2005.05.006.

[195] Arthur Vidard, François-Xavier Le Dimet, and Andrea Piacentini. "Optimal Determination Of Nudging Coefficients". In: *Tellus A, Co-Action Publishing* 55.1 (2003), pp. 1–15.

[196] S. Lakshmivarahan and John M. Lewis. "NudgingMethods: A Critical Overview". In: *Data Assimilation for Atmospheric, Oceanic and Hydrologic Applications (Vol. II)*. Ed. by S.K. Park and L. Xu. Vol. II. Berlin Heidelberg: Springer-Verlag, 2013. Chap. 2, pp. 27–57. ISBN: 9783642350887. DOI: 10.1007/978-3-642-35088-7_2.

[197] Jian-Wen Bao and Ronald M. Errico. "An Adjoint Examination of a Nudging Method for Data Assimilation". In: *Monthly Weather Review* 125.6 (1997), pp. 1355–1373. ISSN: 0027-0644. DOI: 10.1175/1520-0493(1997)125<1355:AAEOAN>2.0.CO;2.

[198] Erich Roeckner et al. *Simulation of the present-day climate with the ECHAM model: Impact of model physics and resolution*. MPI Report No. 93. Hamburg: Max-Planck-Institute for Meteorology, 1992, pp. 1–110.

[199] Martina Schubert-Frisius et al. "Optimal Spectral Nudging for Global Dynamic Downscaling". In: *Monthly Weather Review* 145.3 (2017), pp. 909–927. ISSN: 0027-0644. DOI: 10.1175/MWR-D-16-0036.1.

[200] C. Timmreck and M. Schulz. "Significant dust simulation differences in nudged and climatological operation mode of the AGCM ECHAM". In: *Journal of Geophysical Research D: Atmospheres* 109.13 (2004), pp. 1–12. ISSN: 01480227. DOI: 10.1029/2003JD004381.

[201] Patrick Jöckel et al. "Earth System Chemistry integrated Modelling (ESCiMo) with the Modular Earth Submodel System (MESSy) version 2.51". In: *Geoscientific Model Development* 9.3 (2016), pp. 1153–1200. ISSN: 19919603. DOI: 10.5194/gmd-9-1153-2016.

[202] A. J. G. Baumgaertner et al. “Energetic particle precipitation in ECHAM5/MESSy â€“ Part 2: Solar Proton Events”. In: *Atmospheric Chemistry and Physics Discussions* 10.2 (2010), pp. 4501–4542. ISSN: 1680-7375. DOI: 10.5194/acpd-10-4501-2010.

[203] Sebastian Rast et al. *ECHAM6 User manual*. Tech. rep. Hamburg: Max Planck Institute for Meteorology, 2013, pp. 1–220.

[204] D. P. Dee et al. “The ERA-Interim reanalysis: configuration and performance of the data assimilation system”. In: *Quarterly Journal of the Royal Meteorological Society* 137.656 (Apr. 2011), pp. 553–597. ISSN: 00359009. DOI: 10.1002/qj.828.

Acknowledgements

There are a number of people that I want to thank a lot for their support, their inspirations, and their encouragement.

First, I want to thank [redacted] for offering me a position as doctoral candidate in his working group and for the freedom I had to define the research topics of my interest for this work. He supported me whenever I needed it, provided advice and inspirations in many aspects as well as technical help.

Thanks a lot to [redacted] and [redacted] for their support for technical issues related to ECHAM/MESSY and its execution on the computer clusters in Mainz and Hamburg.

Moreover, I like to thank [redacted] for the introduction into MPIOM and for assisting me to run the coupled model for the Permian environment.

Thanks to [redacted] from MPIM for applying the hydrologic discharge model to the Permian environment and generating the respective data set. I am thankful as well to [redacted] from NCAR for offering me her data set of Permian vegetation and Permian soils.

I like to thank all my colleagues at the institute of physics of the atmosphere for their ideas, their inspirations, and the pleasant time we had together. Especially I like to thank [redacted] and [redacted] for the daily discussions and the nice atmosphere we had in our working group.

I am very thankful to everyone who assisted me with corrections of this work.

And last but not least, I want to thank my parents, my brother [redacted], my friends, and my fiancee [redacted] for their support at home, their encouragement to finish this thesis, and for caring about me.